Preliminary Sizing of Balance-of-Plant Systems for Liquid Hydrogen Fuel Cell-Electric Propulsion in Regional Retrofitted Aircraft

Martijn Vroom

Delft University of Technology

TU Delft

nlr

Preliminary Sizing of Balance-of-Plant Systems for Liquid Hydrogen Fuel Cell-Electric Propulsion in Regional Retrofitted Aircraft

by

Martijn Vroom

to obtain the degree of Master of Science
at the Delft University of Technology,
to be defended publicly on Wednesday January 29th, 2025 at 14:30 PM.

Student number:	4666372	
Project duration:	December 1, 2023 – January 29, 2025	
Thesis committee:	Prof.dr.ir. P. Colonna	TU Delft, chair
	Dr. ir. C.M. de Servi,	TU Delft, supervisor
	Dr.ir. W.J. Baars	TU Delft, committee
	Ir. T.P. Dotman,	NLR, daily supervisor

Data in thesis is confidential until 2031 and will be removed from the public version.

Cover:	Porter Bombardier Dash8 Q300
Style:	TU Delft Report Style, with modifications by Daan Zwaneveld

An electronic version of this thesis is available at http://repository.tudelft.nl/.

TU Delft

Preface

It has been a great privilege to conduct this thesis as a graduate intern at the Netherlands Aerospace Centre (NLR). During my time at NLR, I had the unique opportunity to define my own thesis topic by undertaking an extensive literature review on the use of liquid hydrogen in aviation, which ultimately led to the formulation of the specific research objectives and questions. I am very grateful to the many experts who shared their valuable insights and provided guidance on decisions regarding the scope, modeling, and interpretation of the results.

I am especially thankful to my day-to-day supervisor, Thom Dotman, for his enthusiastic and engaging mentorship throughout the thesis. His thought-provoking questions consistently challenged me to refine my approach and deepen my understanding. A special thanks also goes to Pieter-Jan Dewitte for his thorough review of my model, along with his insightful suggestions to enhance its clarity and robustness. I extend my gratitude to my TU Delft supervisor, Carlo de Servi, for offering valuable feedback and direction during each review meeting.

Finally, I would like to pay a tribute to my grandfather, who sadly passed away just a month before the defense. He, too, studied at TU Delft, became a distinguished physics researcher at TNO specializing in acoustics, and even performed studies into aircraft noise. As a student, he once flew in a De Havilland Tiger Moth with his brother—De Havilland, a company that, remarkably, provided the reference aircraft for this thesis. His legacy will continue to provide inspiration in my career.

Martijn Vroom
Rotterdam, January 2025

Abstract

The aviation sector faces growing pressure to reduce greenhouse gas emissions, while projections are suggesting that emissions could double by 2050 to account for increases in passengers. Liquid hydrogen fuel cell-electric (LH2FCE) propulsion offers a promising solution, with the potential to reduce climate impact by up to 90% compared to conventional turboprop engines. However, significant challenges exist, including heat dissipation, increased drag, and increased weight penalties from heavy fuel cell stacks, cryogenic hydrogen storage and thermal management systems.

This thesis evaluates the impact on payload and range of retrofitting a regional turboprop aircraft with an LH2FCE propulsion system, by performing the preliminary design of the balance-of-plant systems, and assessing system performance by means of steady state analyses in take-off, top-of-climb and cruise conditions. A lumped parameter model was developed to simulate the fuel cell and balance-of-plant components, including an air supply and thermal management system and ram air ducts. Results show that payload reductions of approximately 58-71% are expected for a 1500 km range compared to current turboprop aircraft, primarily due to increased mass and drag penalties, which reduce the propulsion system's specific power and lift-to-drag ratio. Sensitivity analyses were conducted, highlighting the effects of fuel cell operational parameters. It was revealed that adjustments in fuel cell temperature, pressure, and current density in the different operating conditions can enhance system performance. Additionally, it was found that most systems must be sized for top-of-climb, except for the ram air duct, which is constrained by take-off conditions. Incorporating a variable inlet design may eliminate ram air drag in cruise, although detailed drag analysis is recommended. Integration of a turbine and halving the rate-of-climb demonstrated that achieving a 1500 km range with a competitive payload (>3000 kg, 35 passengers) is feasible for retrofits, while reserving mass for non-modeled systems such as batteries. Moreover, projections for 2030 suggest that the performance of current turboprop aircraft could be matched by LH2FCE systems.

These findings highlight that LH2FCE propulsion is a viable and sustainable alternative for regional aviation, provided the reduction in payload is acceptable. With advancements in fuel cells, heat exchangers, electric motors, and liquid hydrogen storage, LH2FCE aircraft could achieve performance of current kerosene-powered turboprop aircraft by 2030.

Contents

List of Figures

List of Tables

Nomenclature

Table 1: List of Abbreviations

Symbols	Explanation	Symbols	Explanation
AC	Alternating Current	LNG	Liquid Natural Gas
APU	Auxiliary Power Unit	LT-PEMFC	Low-Temperature Proton Exchange Membrane Fuel Cell
AR	Area Ratio (in the diffuser)	LHV	Lower Heating Value
ASS	Air Supply System	LPM	Liters Per Minute
ATAG	Air Transport Action Group	MDA	Multi-Disciplinary Analysis
AVG	Average	MF	Fuel Mass
BOP	Balance-Of-Plant	MFR	Mass Flow Ratio
CF	Critical Heat Flux	MPL	Mechanically Pumped Loop
CFD	Computational Fluid Dynamics	MTOM	Maximum Take-Off Mass
CHF	Critical Heat Flux	MLM	Maximum Landing Mass
CO_2	Carbon Dioxide	N/A	Not Applicable
DC	Direct Current	NACA	National Advisory Committee for Aeronautics Airfoils
DLR	Deutsches Zentrum für Luft- und Raumfahrt	NFPA	National Fire Protection Association
EM	Electric Motors	NIST	National Institute of Standards and Technology
FC	Fuel Cell	NTU	Number of Transfer Units
FCS	Fuel Cell System	OEM	Operational Empty Mass
GB	Gearbox	PCA	Pressure Controlled Accumulator
GH_2	Gaseous Hydrogen	PAX	Passengers
GWP	Global Warming Potential	PS	Propulsion System
HHV	Higher Heating Value	PSFC	Power-Specific Fuel Consumption
HT-PEMFC	High-Temperature Proton Exchange Membrane Fuel Cell	RAD	Ram Air Duct
HX	Heat Exchanger	ROC	Rate-Of-Climb
IC	Intercooler	RPM	Revolutions Per Minute
ICCT	International Council on Clean Transportation	SAF	Sustainable Aviation Fuel
ISA	International Standard Atmosphere	SBC	Synthetic Blend Component
L/D	Lift-To-Drag Ratio	SOFC	Solid Oxide Fuel Cell
LH_2	Liquid Hydrogen	SOFC-GT	Solid Oxide Fuel Cell Gas Turbine
LH2FCE	Liquid Hydrogen Fuel Cell Electric	TMS	Thermal Management System
LHP	Loop-Heat Pipes	TR	Thrust-To-Drag Ratio
LPM	Liters Per Minute	TRL	Technology Readiness Level
MDA	Multi-Disciplinary Analysis	XDSM	Extended Design Structure Matrix
N/A	Not Applicable	W/EG	Water-Ethylene-Glycol
NM	Nautical Miles	lb	Lower Bounds
NFPA	National Fire Protection Association	ub	Upper Bounds

Table 2: List of Symbols

Symbol	Explanation	Unit	Symbol	Explanation	Unit
A	Area	m^2	a	Acceleration	m/s^2
C	Heat Capacity Rate	W/K	C_{pressure}	Diffuser Pressure Coefficient	-
C_r	Heat Capacity Ratio	-	CTE	Coefficient of Thermal Expansion	1/K
D	Diameter	m	Δp	Pressure Gradient	Pa
ΔT	Temperature Gradient	K	ϵ	Effectiveness	-
ϕ_{rel}	Relative Humidity	%	f	Friction Factor	-
G	Mass Flux	$kg/s/m^2$	g	Gravitational Acceleration	m/s^2
γ	Ratio of Specific Heats	-	H	Enthalpy	J/kg
H_0	Standard Enthalpy	J/kg	H_{lv}	Enthalpy of Vaporization	J/kg
h	Height	mm	i	Current Density	A/cm^2
J_g	Dimensionless Vapor Quality	-	K	Loss Factor	-
k	Thermal Conductivity	W/(m·K)	L	Length	m
M	Mach Number	-	m	Mass	kg
m_{fin}	Fin Effectiveness	-	N	Amount	-
Nu	Nusselt Number	-	P	Perimeter	m
P/A	Power Density	W/m^2	p_{t}	Total Pressure	Pa

Continued on next page

Symbol	Explanation	Unit	Symbol	Explanation	Unit
p_v	Vapor Pressure	Pa	p_X	Partial Pressure	Pa
Pr	Prandtl Number	-	Q	Heat Flux	W/m^2
R	Gas Constant	J/(kg·K)	r	Radius	m
ρ	Density	kg/m^3	$\dot{m}$	Mass Flow Rate	kg/s
Re	Reynolds Number	-	σ	Smoothing Function	-
t	Thickness	mm	T_0	Static Temperature	K
UA	Heat Transfer Coefficient · Area	W/K	u	Velocity	m/s
u_0	Bulk Velocity	m/s	U	Heat Transfer Coefficient	$W/(m^2 \cdot K)$
W	Work	J	W	Width	m
χ	Quality	-	x	Mole Fraction	-
Z	Shah's Correlating Parameter	-	z	Length	-

1 Introduction

Air pollution from the aviation industry is an urgent environmental concern, with aviation emissions currently contributing up to 3.5% of global greenhouse gases [1]. Without significant decarbonization efforts, the share of aviation emissions can rise drastically as demand for air travel is evergrowing. Projections indicate that emissions could double by 2050 [2]. The regional aviation sector, while responsible for only about 3% of total industry CO_2 emissions, provides an opportunity to pioneer green aviation technologies [3].

One promising solutions for reducing emissions is liquid hydrogen fuel cell electric (LH2FCE) propulsion, having the potential to reach a 90% reduction in climate impact compared to turboprop engines [4]. Research into LH2FCE propulsion for aviation is gaining interest, with multiple flight tests already conducted in the commuter [5, 6, 7, 8] and regional aircraft segment [9]. Various companies and organizations are actively engaged in developing larger-scale concepts for hydrogen-powered aviation, either by retrofitting existing turboprop aircraft [7, 8, 9, 10] or developing entirely new aircraft [11].

However, significant challenges remain. Heat dissipation poses a significant challenge in LH2FCE propulsion. In state of the art fuel cells, approximately half of the energy input is converted into low-grade heat, which must be dissipated via thermal management systems. This can result in significant weight and drag penalties. Also, while hydrogen is a lighter fuel than kerosene, it is expected that current cryogenic storage technologies reduce performance compared to kerosene aircraft [12]. While storing hydrogen as a cryogenic liquid is most efficient [13], heating to appropriate temperatures is required for fuel cell operation [14]. For this, utilization of fuel cell waste heat can be efficient [15], but precautions against coolant freezing in cryogenic environments is essential [16]. Furthermore, fuel cells performance decreases at lower air pressure, necessitating adaptations to the air supply system for flying at high altitude. Compressors required to provide the necessary pressure ratio might increase fuel cell mass, especially when high climb rates are required. To decrease fuel cell mass, it can be designed for a higher current density at the design power output, but this decreases efficiency [17]. Employment of current fuel cell technologies (LT-PEM) also results in large amounts of relatively low-grade heat, requiring sophisticated thermal management systems, especially at MW power levels. To dissipate this heat, large radiators can be placed inside ram air ducts. This may increase the zero-lift-drag coefficient of the aircraft by at least 5%, and decrease the lift-to-drag ratio by more than 2% [10]. Careful design of these ram air ducts may result in net-zero drag by implementing the so-called Meredith effect, with potentially a small of thrust (5% of the ram air drag) [18]. Nevertheless, the impact on propeller blockage of such a duct may be significant [19].

Given the adverse effects on weight and drag, preliminary studies suggest that range and payload capacity of regional LH2FCE aircraft may be affected substantially [20]. Retrofitting existing turboprop aircraft will demonstrate whether LH2FCE propulsion can enhance sustainability and establish itself as a viable alternative in the regional aviation sector. Therefore, the following research objective is proposed:

Research Objective

The objective is to evaluate the impact of retrofitting a regional turboprop aircraft with a liquid hydrogen fuel cell-electric propulsion system on payload and range.
This will be achieved through the development of a lumped parameter model for preliminary sizing of the air supply system, thermal management system, and ram air duct integrated with the fuel cell system, assessing performance under take-off, top-of-climb, and cruise conditions.

This thesis is structured as follows. Chapter 2 provides a comprehensive literature study on LH2FCE propulsion, after which the research questions are introduced. Chapter 3 presents the methodology for modelling and simulation of the different propulsion architectures. Chapter 4 will discuss verification and validation methods and Chapter 5 will focus on results and discussion. Finally, Chapter 6 closes off this thesis with conclusions and recommendations.

2

Literature Study

This chapter presents the findings of a literature survey on liquid hydrogen fuel cell electric (LH2FCE) propulsion systems to retrofit existing regional aircraft.

First, it will be discussed why LH2FCE propulsion is one of the promising solutions for decarbonization in the aviation sector in Section 2.1. Then the subsystems of such a propulsion system are discussed in Sections 2.2 to 2.6. After each subsystem section, a summary of the scope and research question(s) is given. Finally in Section 2.7, the main research question is stated.

2.1. Background

Air pollution has been a focal point of concern regarding environmental issues. With the ever growing aviation industry being one of the key contributors, sustainable innovation is required. As aviation is still thriving on kerosene-powered propulsion, it may account for about 3.5 percent of global emissions [1]. Without any efforts to decarbonize aviation and considering air traffic growth, emissions could double by 2050 as shown in Figure [2].

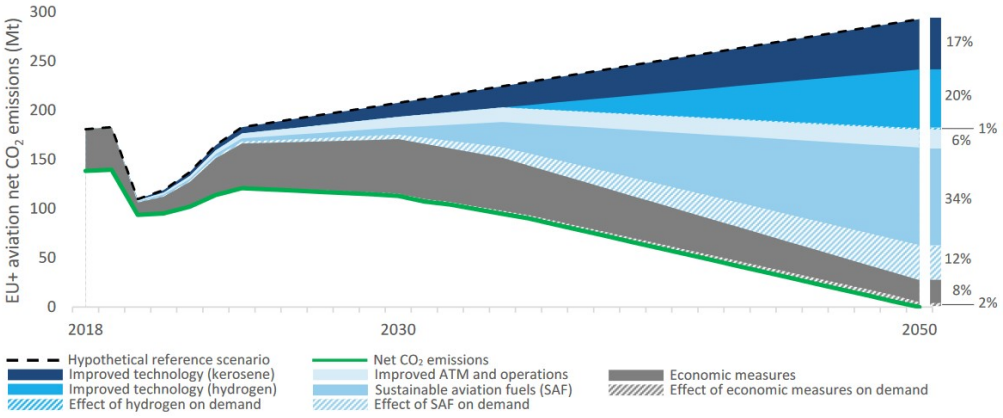

Figure 2.1: Decarbonization roadmap for European aviation. Reproduced from [2].

As a result of these major concerns, in 2011, environmental goals were set by the European Commission for aviation by launching Flightpath 2050 [21]. Research programs such as Clean Sky 2 (first Clean Sky) embody these objectives by developing new aircraft and propulsion technologies to reduce CO_2, NO_x and noise emissions [22]. In 2015, the Paris agreement was announced. The participating countries set the "overarching goal to hold the increase in the global average temperature to well below 2°C above pre-industrial levels and pursue efforts to limit the temperature increase to 1.5°C above pre-industrial levels [23]." Later, in 2019, the European Commission through its Green Deal announced the goal of Europe becoming the first carbon-neutral continent by 2050 [24]. Recently, efforts towards carbon-neutral aviation have been accelerated by Destination 2050 [2] and the Clean Aviation Strategic Research and Innovation Agenda [25] in Europe, and by the Air Transport Action Group [3] and the International Air Transport Association [26] globally.

Implementing novel technologies such as electric propulsion, sustainable aviation fuel (SAF), hydrogen combustion or hydrogen fuel cell propulsion present the opportunity to address these challenging targets across all segments of aviation. An indicative overview on which technologies might become commercially available at what time and in which segment was provided by ATAG in 2021 [3].

	2020	2025	2030	2035	2040	2045	2050
Commuter » 9-19 seats » < 60 minute flights » <1% of industry CO_2	SAF	Electric or Hydrogen fuel cell and/or SAF	Electric or Hydrogen fuel cell and/or SAF	Electric or Hydrogen fuel cell and/or SAF	Electric or Hydrogen fuel cell and/or SAF	Electric or Hydrogen fuel cell and/or SAF	Electric or Hydrogen fuel cell and/or SAF
Regional » 50-100 seats » 30-90 minute flights » ~3% of industry CO_2	SAF	SAF	Electric or Hydrogen fuel cell and/or SAF	Electric or Hydrogen fuel cell and/or SAF	Electric or Hydrogen fuel cell and/or SAF	Electric or Hydrogen fuel cell and/or SAF	Electric or Hydrogen fuel cell and/or SAF
Short haul » 100-150 seats » 45-120 minute flights » ~24% of industry CO_2	SAF	SAF	SAF	SAF potentially some Hydrogen	Hydrogen and/or SAF	Hydrogen and/or SAF	Hydrogen and/or SAF
Medium haul » 100-250 seats » 60-150 minute flights » ~43% of industry CO_2	SAF	SAF	SAF	SAF	SAF potentially some Hydrogen	SAF potentially some Hydrogen	SAF potentially some Hydrogen
Long haul » 250+ seats » 150 minute + flights » ~30% of industry CO_2	SAF	SAF	SAF	SAF	SAF	SAF	SAF

Figure 2.2: An indicative overview of where low- and zero-carbon energy could be deployed in commercial aviation. Reproduced from [3].

As indicated in figure 2.2, SAF is currently used in aviation, but for a very small amount (0.2% in 2023 [27]). SAF is a hydrocarbon based fuel with an alternative feedstock to fossil fuels, such as biofuel or synthesis gas. Currently, aircraft are certified to fly with a blend of conventional aviation fuel (Jet-A1) and up to 50% SAF. When 100% SAF is used, CO_2 emission reductions of up to 80% are possible [28]. Also, a 100% based SAF fuel has potentially higher gravimetric energy density and decreased formation of contrails.

Despite the environmental benefits, SAF has high production costs and is not currently economically competitive, having a price around 3 times higher than Jet-A1 [29]. Furthermore, for some routes of SAF production a large amount of hydrogen is required, which only makes sense if electricity is only produced via renewable sources [30]. Still, with current projections, SAF will become a major resource for aviation fuels to enable the decarbonization of long-haul flights. Also, SAF can make use of existing kerosene infrastructure [4].

Another novel technology is battery-electric propulsion, which has the highest emission reduction potential (up to 93%) as it has no in-flight emissions [31]. Still, battery production and electricity used for power also require to be green [4]. While it is indicated in figure 2.2 that electric flight is not expected to reach the regional segments, there are studies stating that electric flight could eventually expand to cover longer range segments of aviation. Wolleswinkel et al. [32] re-examined the assumptions that lead to the conclusion of limited applicability of battery-electric aircraft, and claim that battery-electric passenger aircraft can play a larger role in climate-neutral aviation than was previously envisioned. In a second study, de Vries et al. [33] argued that the addressable market is actually substantial by conducting a conceptual study on a 90-Seater with 800 km range. Still, thus far only small battery-electric aircraft have been developed, such as the Pipistrel Velis Electro [34] and the Eviation Alice [35]. Mukhopadhaya and Graver argues that, electric aircraft will be limited to small and short-range missions [36]. Even if power density of batteries continues to improve as forecast, Staack et al. argue [37] that electric propulsion might mostly play a role in hybrid-electric configurations. Thonemann et al. [38] conclude that in the short- and medium-term, hybridization with Li-ion and Li-S batteries may be regarded as transitioning solutions toward commercial hydrogen fuel cell aircraft.

Using hydrogen as a fuel is the other promising option. The gravimetric energy density of hydrogen is significantly larger than kerosene (LHV = 120 MJ/kg vs 43.2 MJ/kg). However, the volumetric energy density of hydrogen at ambient temperature and pressure is extremely low. Even when it is stored as a cryogenic liquid (LH_2), kerosene only requires a third of the volume for the same energy content (8.5 MJ/L vs. 34.9 MJ/L). Actually, hydrogen and kerosene should be compared in terms of tank gravimetric efficiency (η_{gr}). Below $\eta_{gr} \approx 55\%$, hydrogen performs slightly worse than kerosene in regional flights and significantly worse for longer flights. For values large than $\eta_{gr} \approx 55\%$, hydrogen outperforms kerosene and the advantage increases with range. As preliminary gravimetric efficiencies of LH_2 tanks range between 25-40%, with some extreme predictions reaching up to 70%, some argue hydrogen only fits lower range aircraft while others argue it gets even more attractive for longer range aircraft [12].

Hydrogen can be combusted in a jet engine just as kerosene. This has been researched already some time ago such as in the Soviet experimental Tupolev-155, which performed over 100 test flights since 1988 with a LH_2 tank in the

back of the aircraft and one of three engines running on H_2 [39] (see figure 2.3). The project was discontinued due to the fall of the Soviet Union. Another attempt was the Cryoplane study by Airbus and DLR [40], which led to the conclusion the required energy would increase by 10% and enormous LH_2 tanks would be needed (see figure 2.4).

Figure 2.3: Soviet experimental Tupolev-155, powered partially on LH_2. [41]

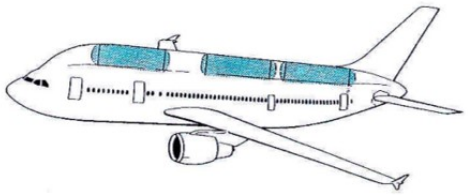

Figure 2.4: Cryoplane by Airbus, with unconventional LH_2 tank placement. Reproduced from [42]

Although the regional sector accounts for only 3% of aviation industry CO_2, these type of aircraft might see the first major technology improvements by 2030 [3]. The regional sector presents the opportunity to develop the first revolutionary technology for green aviation. As argued by, among others, Fuel Cells and Hydrogen 2 JU and Clean Sky 2 JU [4] and Adler and Martins [12] these regional aircraft will be most efficiently powered by hydrogen fuel cells with hydrogen stored as a cryogenic liquid.

In fuel cells, hydrogen reacts with oxygen generating water and electricity. Climate impact reduction potential of hydrogen fuel cells is estimated at up to 90%, while hydrogen combustion does not reach higher than 75%. This is due to NO_x formation in combustion chambers and more contrail formation in hydrogen turbines [4].

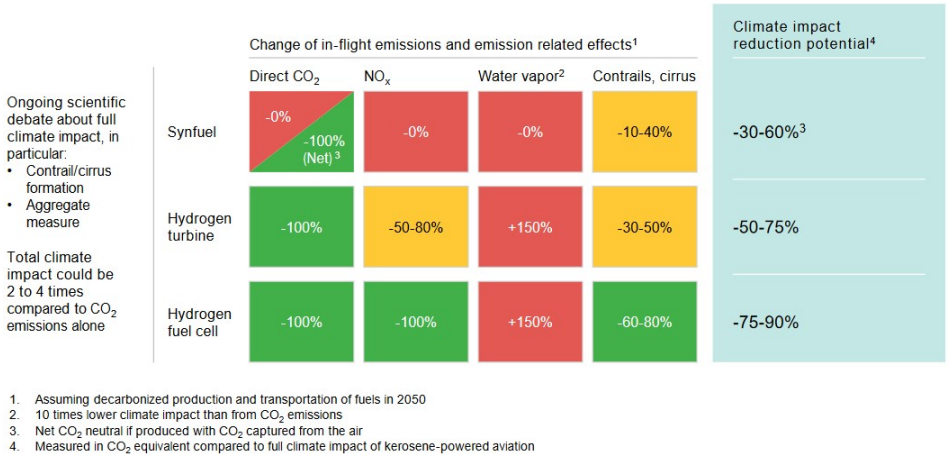

Figure 2.5: Comparison of climate impact from hydrogen propulsion and SAF (Synfuel), compared to kerosene-powered aircraft. Reproduced from [4]

Still, to reach the potential indicated in Figure 2.5, production has to be green. In a hydrogen-based economy, aviation accounts for 10 million tons of H_2 by 2040, which is 5% of the global demand projected by the Hydrogen Council [4]. In the same study it is argued that fuel cell systems are unfit for short-range aircraft (165 passengers, 2000 km), since fuel cell systems are relatively large due to their large cooling requirements, unless design range is reduced by up to 50% and flight time is increased by up to 15%. For longer ranges, hydrogen combustion becomes a more viable opportunity even though climate impact reduction potential is decreased. It is therefore argued that hydrogen fuel cell propulsion will be mainly applicable in the commuter and regional sector.

In aviation, liquid hydrogen fuel cell electric propulsion remains an active field of research. Several ground and flight demonstration tests have been performed in the commuter and regional aircraft segment with limited payload and passengers. Some OEMs also envision larger concepts on which they are actively working. In figure 2.6 a few of these demonstrators and concepts are shown.

Figure 2.6: Hydrogen fuel cell propulsion demonstrators and concepts: Boeing first ever manned fuel cell aircraft, ENFICA-FC, H2FLY HY4, ZeroAvia Do228, Universal Hydrogen, Airbus. Reproduced from [5, 6, 7, 8, 9, 11]

While Boeing came with the first fuel cell manned aircraft in 2008 powered by gaseous hydrogen at a pressure of 350 bars [43], they believe that aviation will be largely powered by SAF in 2050, which is in line with the vision of the Air Transport Action Group [3]. Boeing is thus not focusing as much on hydrogen fuel cell technology at the moment, as they believe it will only start playing a role after 2050 [44]. Romeo et al. flew a small two-seater in 2013 powered by GH_2 (the ENCICA-FC), setting a speed record at that time [6]. H2FLY performed the first piloted flight of a 4-seater LH_2 fuel cell electric aircraft, which can reach twice the range their earlier GH_2 demonstrator could. H2FLY and Deutsche Aircraft plan to retrofit a 40-seater Dornier 328 with hydrogen fuel cell propulsion, carrying 40 PAX up to 1150 miles [7].

ZeroAvia performed a first test flight in January 2023 with a 19-seat Dornier 228, where one of the engines was replaced with a fuel cell. Current tests have been limited to altitudes of merely 5000 feet, with an endurance of only 23 minutes. The company targets to retrofit DeHavilland DHC-8 Q400 and ATR72 aircraft with fuel cell electric retrofit with their ZA2000 engine platform [8]. In March 2023, Universal Hydrogen demonstrated an operational fuel cell powered by GH_2 on an ATR 72, having replaced one of the engines. The company also recently performed a 1h40m ground test with a 1MW iron bird powered by LH_2. Universal Hydrogen plans to produce a conversion kit for the ATR72 and the DHC-8 to fly on LH_2. The LH_2 tanks will be modular capsules that are refueled at specific hubs and can be delivered to whichever airport necessary, at least for the first generation [9].

Airbus has set itself the goal of putting a hydrogen-powered aircraft on the market by 2035. Several variants are being investigated, one of which is a variant with fuel cells in pods under the wing. The six modular pods contain hydrogen tanks, fuel cells and electric motors. Recently, Airbus performed the most powerful ground-test ever with a 1.2 MW fuel cell system designed for aviation. Airbus aims to test and this system on their A380 demonstrator by 2026 [11]. Conscious Aerospace together with a consortium of parties from the Netherlands plans to provide a means to retrofit DHC-8 Q300 aircraft with fuel-cell electric propulsion and LH_2 storage in their hydrogen aircraft powertrain and storage system (HAPSS) project [10].

In a study by Fuel Cells and Hydrogen 2 and Clean Sky 2 Joint Undertaking (European Union), a regional concept with distributed propulsion on the wings and LH_2 tanks is envisioned [4], reaching 540 NM with 80 PAX. Mukhopadhaya argues in a conceptual performance analysis for ICCT that hydrogen fuel cell aircraft will compromise on passengers and range, with LH_2 performing slightly better [20].

A key selling point of current regional aircraft is short runway take-off distance. For instance, the DHC-8 Q400 has a minimum take-off distance of 1300m [45]. Keeping to this distance puts a strict requirement on power delivery from the fuel cells, which can pose a challenge with current fuel cell power density and increase system weight significantly [12]. It might be more realistic to construct a mission profile with longer take-off distances at larger (regional) airports. The HYPORT project was the first to construct green hydrogen production and distribution infrastructure at Toulouse-Blagnac airport (3500m runway) [46, 47]. The project will open a second hydrogen plant at Tarbes-Lourdes-Pyrenees airport (3000m runway).

An attempt has been made to summarize the commuter/regional hydrogen demonstrators and concepts mentioned above into a PAX-range diagram. For comparison some kerosene-powered turboprop aircraft have been added, from early to recent generations.

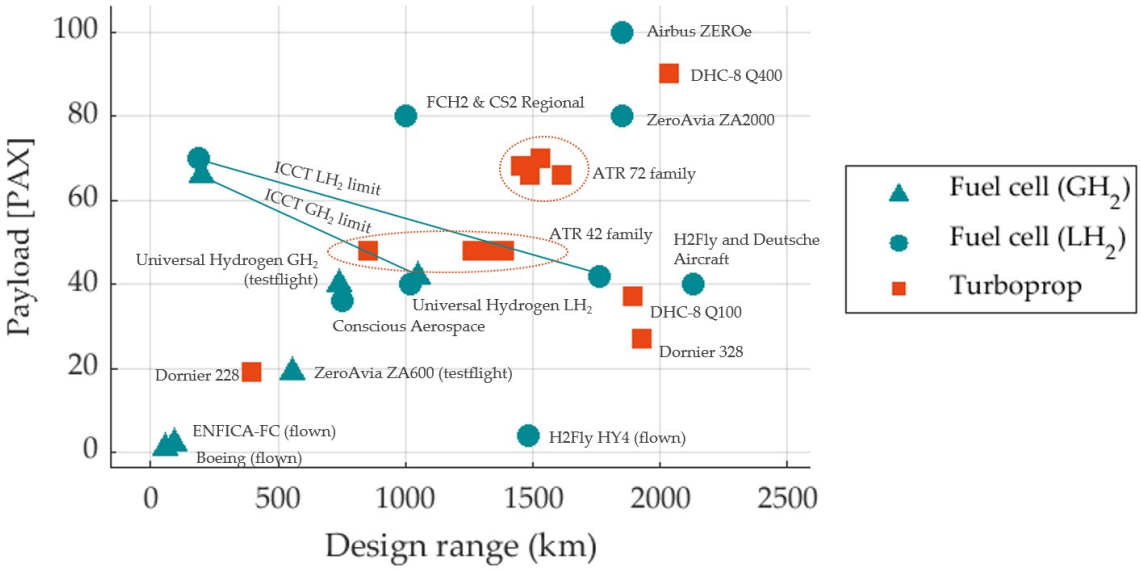

Figure 2.7: Regional hydrogen fuel cell-electric aircraft compared to kerosene-powered turboprop aircraft, in terms of payload (passengers, PAX) and design range.

Several conclusions can be drawn from figure 2.7:

- LH_2 storage increases payload-range compared to GH_2 storage.
- Hydrogen fuel cell powered aircraft seem to compromise on passengers or range compared to current kerosene-powered turboprop aircraft. Few argue that performance can be similar or even better.
- When comparing conceptual hydrogen fuel cell aircraft to older turboprop aircraft (DHC-8 Q100, Dornier 328, ATR 42 family) performance is similar.

While the mission requirements of state-of-the-art turboprop aircraft serve as the baseline for comparison with LH2FCE propulsion, modifications to these requirements may improve performance. For example, reducing the rate-of-climb can lower the required climb power, while a lower cruise altitude and speed can reduce power demand at top-of-climb. Additionally, sacrificing range for payload could enhance performance. These considerations lead to the following research question:

Background: Research Question

- "What modifications to the baseline mission can improve payload and range?"

2.2. Fuel Cell System

A hydrogen fuel cell is a device that generates electricity from hydrogen and oxygen. Hydrogen is consumed at the negative electrode (anode), while oxygen is consumed at the positive electrode. Oxygen is usually supplied through ambient air. Most common types of fuel cells considered for aircraft are low-temperature proton exchange membrane fuel cell (LT-PEMFC) and solid-oxide fuel cell (SOFC) [48]. A less mature technology fuel cell technology that is now emerging is the high temperature proton exchange membrane fuel cell (HT-PEMFC) [49].

2.2.1. Fuel Cell Types

In a LT-PEMFC, the following reactions takes place:

$$2H_2 \longrightarrow 4H^+ + 4e^- \text{ (anode)}$$
$$O_2 + 4H^+ + 4e^- \longrightarrow 2H_2O \text{ (cathode)}$$

A LT-PEMFC contains a polymer electrolyte membrane which allows only H^+ protons to pass. The H^+ protons recombine with oxygen to form water at the cathode, while the electrons can provide power to an external load. The LT-PEMFC has currently the highest technology readiness level (TRL) and power density [14], so this is likely to be implemented into the first generation of fuel cell aircraft [12]. LT-PEMFCs have a efficiencies up to 60% [50], which is substantial. However, heat from this type of fuel cells is low-grade as temperatures are 90°C at most, to not damage the membrane. Complex thermal management systems that increase system weight will be required [12].

LT-PEMFCs also require active water management as appropriate humidification of the membrane is essential to prevent dry-out. Challenges include dependence on expensive polymer membrane materials such as Nafion, expensive platinum catalysts and sensitivity to impurities in the hydrogen supply [14]. Figure 2.8 displays a LT-PEMFC. To increase voltage output, many cells are connected in series, forming a stack.

Currently, research into LT-PEMFCs with power levels required for aviation is gaining momentum. Up to 4 MW can be required to power regional aircraft [10], whereas one of the most powerful operational automotive fuel cell stacks, in the Toyota Mirai, only provides 128 kW at a specific power of about 2.0 kW/kg [12, 51]. Schröter reports a fuel cell with 2.4 kW/kg in his work [17] and recent ground tests with LT-PEMFC stacks carried out by Airbus and Universal Hydrogen demonstrated power levels up to 1.2 MW [52, 53]. According to the Aerospace Technology Institute, fuel cell specific power may increase to 9 kW/kg by 2030 [54], although this assumes HT-PEM technology.

In SOFC, another common type of fuel cells, the following reactions take place:

$$2H_2 + 2O^{2-} \longrightarrow 2H_2O + 4e^- \text{(anode)}$$
$$O_2 + 4e^- \longrightarrow 2O^{2-} \text{(cathode)}$$

A SOFC uses a solid oxide or ceramic electrolyte, which selectively allows only O^{2-} ions to pass. These ions migrate through the electrolyte to the anode, where they react with hydrogen to produce water. SOFCs operate at high temperatures, typically between 600-1000 °C [55], which reduces the cooling demands on the thermal management system. Unlike LT-PEMFCs, SOFCs do not require humidification of the membrane, eliminating the need for a water management system. Additionally, SOFCs are more tolerant to fuel impurities and can operate with hydrogen derived from kerosene reforming, whereas PEMFCs needs H_2 purity levels of over 99.7% [56]. However, SOFCs typically have low specific power, with current forecasts reaching up to only 0.5 kW/kg, making them less attractive for aviation unless future advancements significantly increase this metric [57].

The high operating temperature of SOFCs presents an opportunity to harness waste heat efficiently. For example, waste heat can preheat the air entering the combustor in a gas turbine, thereby lowering fuel utilization [12]. Many SOFC-GT (gas turbine) hybrid architectures have been proposed, though few experiments have been performed to validate claims [58]. Challenges remain related to managing the transient operation and control of SOFC-GT systems, an area of active research [59]. Additionally, SOFCs produce some NO_x, though using alternative hydrogen carriers such as ammonia or biofuels could mitigate these pollutants [60]. Among various fuels studied for SOFC-GT hybrids—such as ammonia, alkanes, and ethanol—liquid hydrogen (LH_2) generally delivers the best performance, albeit with a weight penalty [61].

In regional aviation applications, Choudhary et al. [62] found through modeling that integrating SOFCs into a hybrid turboprop system could improve performance by 12-13%, although this benefit is most effective when using Sustainable Aviation Fuel (SAF) in the turboprop. Figure 2.9 illustrates the structure of a single SOFC cell.

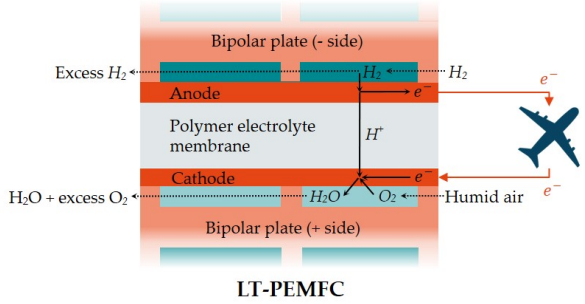

Figure 2.8: Low-temperature proton exchange membrane single fuel cell.

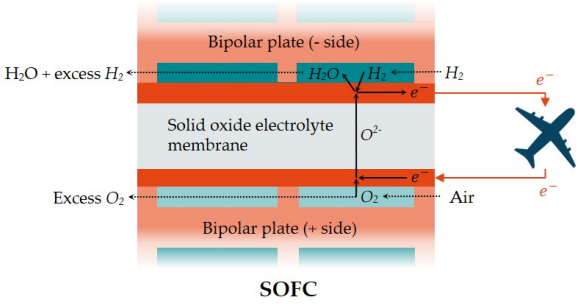

Figure 2.9: Solid oxide single fuel cell.

A HT-PEMFC operates at higher temperature (140-180 °C), reducing the cooling requirement of the fuel cell stack. The higher operating temperature also allows operation with solid acid membranes, eliminating the need for humidification. However, lifetime is expected to be shorter than LT-PEM [63]. The higher operating temperature allows the fuel cell to be cooled by the same compressed air used in the FC stack [12]. Hypoint, owned by ZeroAvia, wants to develop such an air-cooled HT-PEM propulsion system [64]. They claim such an architecture can reach four times more efficient cooling compared to liquid cooling, placing stacks in a radial fashion. Also, lower grade H_2 would be possible, as well as three times more specific power. Also Embraer is aiming to integrate a HT-PEM into a propulsion system in their Hydrogen Demo Family project [65]. The Aerospace Technology Institute claims that specific cooling powers of >10kW/kg are possible with HT-PEM technology [66].

2.2.2. Fuel Cell Characteristics

Electrical current is proportional to the amount of electrons traveling from the anode to the cathode [12]. Ideal reversible cell potential $E[V]$ that can be obtained in a fuel cell is dictated by the Nerst equation [14], which accounts for pressure effects and for temperature effects.

$$E = E^0 + \frac{\Delta\hat{s}}{nF}(T - T_0) - \frac{RT}{nF} \ln \frac{\prod a^{\nu_i}_{\text{products}}}{\prod a^{\nu_i}_{\text{reactants}}} \tag{2.1}$$

Where,

- $E^0 = \Delta\hat{g}/nF$, with $\Delta\hat{g}$ is the Gibbs free energy change, n the number of moles of electrons ($n = 2$ for H_2) and F the Faraday constant.
- $\frac{\Delta\hat{s}}{nF}(T - T_0)$ is a temperature-dependent term, where $\Delta\hat{s}$ represents the molar enthalpy term, and T_0 the standard temperature.
- $\frac{RT}{nF} \ln \frac{\prod a^{\nu_i}_{products}}{\prod a^{\nu_i}_{reactants}}$ is term dependant on the activity/partial pressure a^{ν_i} of the products and reactants. Increasing partial pressures of the reactants increases reversible voltage.

The theoretical maximum efficiency of a fuel cell is given by [14]

$$\eta_{FC} = \frac{\text{work}}{\text{energy input}} = \frac{\Delta\hat{g}}{\Delta\hat{h}}. \tag{2.2}$$

As Gibbs free energy $\Delta\hat{g}$ and reaction enthalpy $\Delta\hat{h}$ are pressure- and temperature-dependent, the efficiency definition depends on the reference value taken for these quantities. Also, $\Delta\hat{h}$ depends on whether the produced water remains a vapour (lower heating value, LHV) or condenses to a liquid (higher heating value, HHV) [17]. O'Hayre et al. [14] argue that the HHV should be used, as this represents the true theoretical energy that can be recovered from hydrogen oxidation. Using the LHV might lead to higher but misleading efficiencies. Theoretical cell potentials and efficiencies at standard conditions of 25°C and 1013 mbar(a) are shown in table 2.1.

Table 2.1: Theoretical cell potential and efficiency based on LHV and HHV at standard conditions of 25°C and 1013 mbar(a) [17]

Phase of produced water	Heating value water	$\Delta\hat{h}$	$\Delta\hat{g}$	Theoretical maximum efficiency
liquid	HHV	1.48V	1.23V	83.1%
gaseous	LHV	1.25V	1.18V	94.4%

While fuel cell current is solely determined by the reaction rate, actual voltage is lowered by three types of losses [14]:

- Activation losses, due to the voltage required to overcome the chemical reaction activation barrier.
- Ohmic losses, a result of the internal resistance of a fuel cell. This is mainly dependant on electrolyte type and thickness.
- Mass transport losses, dictated by limitations in the ability of reactants to reach reaction sites on the electrodes. This lowers the current density as it lowers the reaction rate.

A polarization curve relates cell potential (voltage) and current density, including the three regions aforementioned losses. As current density is increased, cell potential drops as well as fuel cell efficiency. This is shown in figure 2.10.

Fuel cells have interesting behaviour when specific power output is considered. While efficiency is lower at higher current density, specific power increases as shown in figure 2.11. Hence, when integrating a fuel cell into an aircraft, one can lower current density and increase fuel utilization efficiency, thereby lowering fuel mass. However this increases fuel cell size, mass and cost. Sizing the fuel cell to maximum specific power reduces fuel cell weight but increases fuel mass. The optimum point may be somewhere in between and can depend on the aircraft [12].

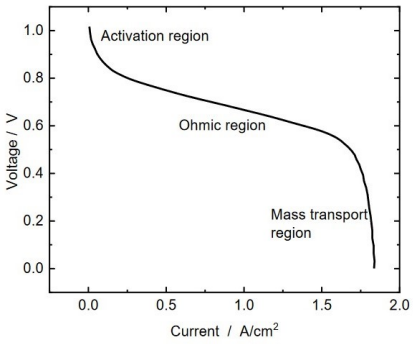

Figure 2.10: Polarization curve of a fuel cell. Regions of losses are indicated. Reproduced from [17].

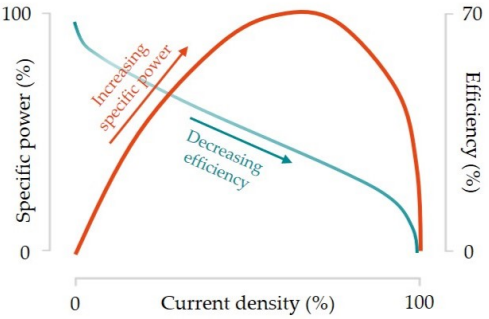

Figure 2.11: Specific power and efficiency of a fuel cell versus current density. Adapted from [12].

While polarization curves of fuel cells are often unavailable, some papers show these curves, often obtained experimentally. Figures 2.12 and 2.13 show the polarization curves at different operating pressures. Fuel cell efficiency seems to increase with increasing air pressure. This topic is discussed in greater detail in section 2.3.1.

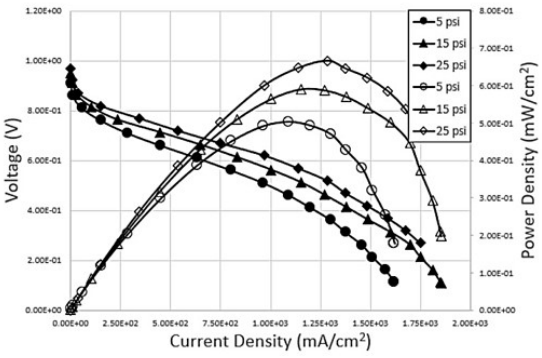

Figure 2.12: Polarization curve, at $RH = 75\%$ and fuel cell temperature of $74°C$ [67].

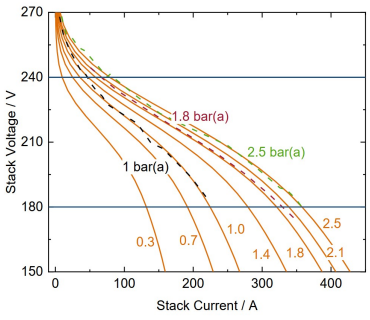

Figure 2.13: Polarization curve obtained by modelling, with experimental results added for an ElringKlinger NM5 300 cell stack [17].

2.2.3. Fuel Cell System: Key Takeaways and Research Questions

As a result of the key takeaways in the previous subsections, the technology considered for the fuel cell system is as follows.

Fuel Cell: Key Takeaways

- As LT-PEMFC has the highest TRL, with specific powers reaching up to 2.0 - 2.4 kW/kg, it is selected in this study.
- While SOFC has some advantageous over LT-PEMFC, it is excluded as specific power (<0.5 kW/kg) and TRL are low.
- HT-PEMFC has low TRL, but it should allow for a more effective and lighter thermal management system. The effect of the higher operating temperature can be considered in a sensitivity analysis. Also, the effect on payload and range of transition from LT-PEM to HT-PEM, increasing specific power, can be assessed, based on technology projections for 2030.

The corresponding research questions are:

Fuel Cell: Research Questions

- "To what extent does implementation of a HT-PEM fuel cell improve payload and range, when considering the increase in operating temperature?"
- "How do payload and range improve based on technology projections for 2030?"

2.3. Air Supply System

As flight altitude increases, ambient pressure drops. Air pressure, relative humidity and air excess ratio are three factors that influence fuel cell performance. As the effect of these parameters is strongly intertwined, Schröter (2023) argues that finding optimal values is not trivial [17]. Their relation can be expressed through the following equation [17].

$$\lambda_{O_2} = \frac{x_{O_2,\text{in}} \left(RH_{\text{out}} p_{\text{sat,out}} - 2p_{\text{out}} \right)}{\psi p_{\text{out}} - RH_{\text{out}} \left(1 + \psi \right) p_{\text{sat,out}}}, \tag{2.3}$$

where,

$$\psi = \frac{p_{\text{sat,in}} RH_{\text{in}}}{p_{\text{in}} - p_{\text{sat,in}} RH_{\text{in}}} \tag{2.4}$$

where:

- λ_{O_2}: stoichiometry,
- x_{O_2}: molar fraction of oxygen,
- RH: relative humidity,
- p_{sat}: saturation pressure,
- p: pressure.

First, insight on the effect of air pressure, relative humidity and air excess ratio is given in Sections 2.3.1 - 2.3.3. Thereafter, the essential and optional components of the air supply system are discussed in subsection 2.3.5.

2.3.1. Influence of Air Pressure

At elevated fuel cell air pressures, air density is higher, leading to a smaller air volume flow rates for the same mass flow. The reduction in air volume flow rate reduces the risk of membrane dehydration. Also, as mentioned in subsection 2.2.2, increasing partial pressure or activity a^{ν_i} of the reactants increases Nernst potential (Equation 2.1) and thus cell voltage and power density. The voltage required to overcome the chemical activation barrier is lowered, and ohmic and mass transport losses are lowered. In Figures 2.12 and 2.13 the effect of increasing pressure can be seen quite clearly.

While Schröter argues that increased pressure elevates fuel cell performance, compressor power also increases [17]. If the compressor is powered by the fuel cell, excessive pressurization can outweigh these performance gains by increasing system mass, as shown in preliminary research from the CATHINCA project at NLR [68]. Blunier and Miraoudi (2007) mention that compressor power can be 20-25% of the fuel cell gross power [69]. Therefore, there is a trade-off between performance and increased system mass.

2.3.2. Influence of Relative Humidity

Temperature and pressure variations influence the relative humidity: an increase in temperature decreases relative humidity as the ability of the air to hold water increases. An increase in pressure conversely increases relative humidity as the air is able to hold less water vapor [70]. However, temperature has a much larger effect [17].

Maintaining the correct relative humidity in a LT-PEMFC is crucial for its operation. The membrane in such a fuel cell is often made from Nafion. Nafion conductivity increases with increasing relative humidity [71, 14]. Insufficient water content can cause dry-out of the membrane, leading to damage in the long term. Conversely, too much water can flood the electrodes, preventing reactants from reaching reactant sites [12].

Studying water movements inside the fuel cell is of great importance for its design. Different mechanisms transport water back and forth between cathode and anode. These are electro-osmotic drag, thermal-osmotic drag, hydraulic permeation and back diffusion. Whereas the first mechanism transports water towards the cathode, the other three have a reverse effect [72]. While currently humidifiers are often used to maintain the correct relative humidity inside the fuel cell, in the future the water generated inside the cell may be sufficient to keep the membrane wet. However, more research is required to understand this so-called self-humidification in detail, according to Fan et al. (2021) [73].

Sanchez et al. (2014) constructed a diagram by conducting fuel cell humidity experiments, relating cathode and anode relative humidity for a single cell [74]. For a constant temperature of 80°C and p = 1.5 bar, they identified the regimes in which fuel cell performance drops drastically. Although no precise value is given, a high air excess ratio is mentioned. As can be seen in Figure 2.14, a cathode (air side) relative humidity of 50-100% is required for low

anode relative humidity. Cathode relative humidity can be slightly decreased by increasing the value on the anode side.

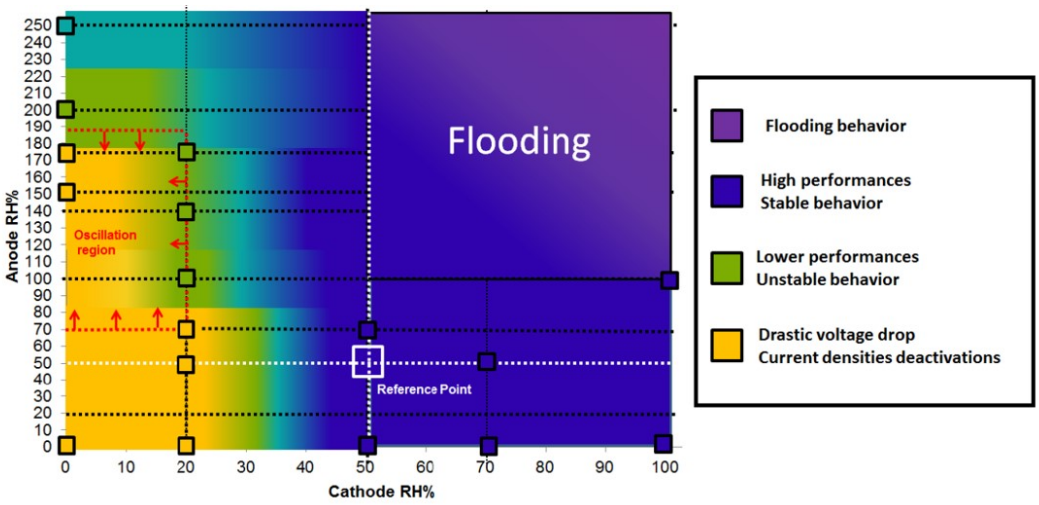

Figure 2.14: Relation between fuel cell stahbility and relative humidity on cathode and anode side. Reproduced from Sanchez et al. (2014) [74]

2.3.3. Influence of Air Excess Ratio

To prevent a loss of efficiency at the end of the plates, it is common to increase *air excess ratio* or *stoichiometry* of the incoming air. More air than required to reach the stoichiometric air to hydrogen ratio is provided. Especially at higher current densities, fuel cell performance increases with increasing air excess ratio [75]. The air excess ratio λ (similar to equivalence ratio in combustion) can be calculated with [70, 17]

$$\lambda = \frac{\text{mass flow of air}}{\text{usage of air}} = \frac{\dot{m}_{\text{air}}}{\frac{i_{FC} n_{O_2} M_{O_2}}{4F \chi_{O_2}}}, \tag{2.5}$$

where $\dot{m}_{\text{air}}$ is the air mass flow [kg/s], i_{FC} the current density [A/cm^2], n_{O_2} the number of moles in the equation, M_{O_2} the molar mass of air [mol], F the Faraday constant, χ_{O_2} the molar fraction of oxygen in air. In practice, less oxygen is consumed then expected as reaction rate decreases with oxygen concentration [70]:

$$\chi_{O_{2,\text{out}}} = \frac{\lambda - 1}{\frac{\lambda}{\chi_{O_{2,\text{in}}}} - 1} \tag{2.6}$$

With $\chi_{O_{2,\text{out}}}$ the oxygen molar fraction [-].

2.3.4. Optimal conditions

According to Schröter (2023) relative humidity at the fuel cell outlet should be 100% to prevent either dry-out or flooding of the membrane. To obtain a 100% outlet relative humidity, the air volume flow needs to be lowered, while still reaching the required air excess ratio. Increasing air pressure decreases volume flow. Also, increasing inlet relative humidity increases outlet relative humidity. For fuel cell powers higher than 45 kW, air pressure should be as high as possible, while the optimal air excess ratio is $\lambda = 1.7$ and inlet relative humidity is at 100%. The publication by Schröter is one of the few works in which cell and air supply system are modeled and validated through testing of a 68 kW fuel cell (ElringKlinger NM5 300), including conditions mimicking those encountered in operation at high altitudes. Along with the polarization curves at different fuel cell pressures, Schröter presents the relationship between the inlet air temperature, pressure, and relative humidity in his fuel cell model, as can be seen in Figure 2.15.

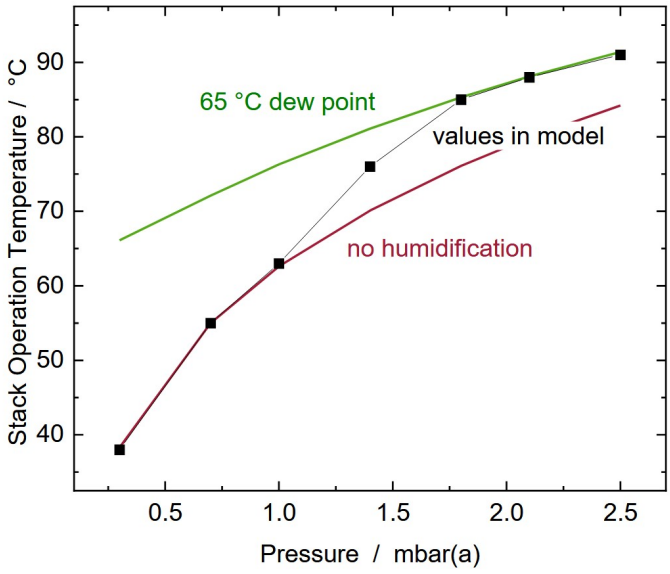

Figure 2.15: Fuel cell stack operating temperatures for different relative humidity conditions: no humidification (red line) and 98% RH (65°C dew point, green line). Modeled data values are shown in black. Reproduced from Schröter [17].

Figure 2.15 presents the fuel cell stack operating temperatures corresponding to no humidification (red line) at air pressures below 1.4 bar, 50% relative humidity at 1.4 bar, and 98% relative humidity at pressures higher than 1.4 bar (65°C dew point, green line). At higher pressures, the stack operating temperature increases due to improved heat transfer and reaction kinetics. When the inlet air is humidified to a dew point of 65°C, 98% RH can be maintained even as the stack temperature rises. Below 1.4 bar, the stack temperature is reduced, and no relevant humidification is observed. Therefore 0% humidification is assumed, as shown in the "no humidification" curve. The model predicts these trends and enables performance estimation for pressure levels not covered in the literature, with the modeled data plotted as black points.

In other studies, different combinations of optimal conditions are mentioned. Schröder et al. (2021) found optimal conditions for all three operating conditions - $\lambda = 1.8$, $\phi_{\text{rel}} = 38 - 49\%$ and $p = 1.59 - 1.90$. While an elaborate model including an air supply system and thermal management system is modeled for an APU system of 300 kW, experimental tests are conducted on a testbed of only 4 kW. Schröder et al. mention that the tested fuel cell stack is not particularly well-suited for aviation due to low its power density [76]. Kim et al. (2005) suggest that optimal system efficiency is achieved at $p = 2$ bar. A relative humidity at the cathode inlet of $\phi_{\text{rel}} = 70\%$ should be used as it yields $\phi_{\text{rel}} = 100\%$ at the outlet. However, air excess ratio λ is not optimized [77]. Blunier and Miraoudi (2007) found an optimum at 2.5 bar for an air excess ratio of 2 [69]. Beyond an air excess ratio of 3, the net voltage level was negative, as more voltage was required for compression of the air than the fuel cell can deliver. There is no mention of relative humidity in the paper. Ahmadi et al. (2016) find optimum pressures of 3-4 bar, but insights on air excess ratio and relative humidity are lacking. Janicka et al. (2021) mention optimal values for relative humidity at low and high current densities (i_{FC}). However, air excess ratio and operating pressure are not optimized.

2.3.5. Air Supply System Components

The basic architecture for the air supply of an aircraft fuel cell propulsion system includes several components [76, 17]:

- An **air intake**. Additional pressure losses should be considered if the mass flow of air is significant.
- An **air filter**, to remove harmful particles from the air.
- A **compressor**, to increase air pressure to the desired FC inlet value. This compressor is usually electrically driven.
- An **intercooler**, as the air heats up significantly after compression.
- A **humidifier**, which humidifies the relatively dry air to the desired value. The air is relatively dry as relative humidity drops when air temperature is increased due to compression in the compressor. Humidification is often done through a membrane, separating the exhaust gases and incoming air.

To control pressure inside the fuel cell, a pressure regulation valve at the outlet can be used. However, the air exiting the humidifier is still relatively hot compared to the environment, resulting in energy loss if vented through a valve. A number of components can be added to not only recover energy, but also ensure improved water management.

- A **turbine** can be used to extract energy from the relatively hot air exiting the fuel cell. It can be used in combination with centrifugal compressor to form a turbocharger. More than 30% of the compressor power may be recovered [78]. This is also being researched in the CATHINCA project at NLR [68].
- A **recuperator** can be employed to heat air entering the turbine with the hotter air exiting the compressor. This results in a power increase of the turbine, reducing system mass. The recuperator can also eliminate the risk of condensation inside the turbine. However, preliminary analysis in the CATHINCA project showed no substantial benefit of this configuration at system level [68].
- A **water separator**, which can be employed to remove liquid water particles from the exhaust gases. This can be achieved either through centrifugal force or by cooling, the latter being known as a **condenser**. Removing the liquid reduces the risk of freezing near the outlet to the environment. Also, if a turbine is implemented, damage to the turbine blades by liquid droplets is prevented. Furthermore, the recovered water can be used in the humidifier or elsewhere in the aircraft.

Table 2.2 provides an overview of several studies in which these components are implemented in fuel cell air supply systems. When applicable, the types of compressor and intercooler are specified.

Table 2.2: Literature reviw of studies dealing with various air supply system components. "X" indicates use of the component, while "-" indicates no use.

Source	Compressor type	Intercooler type	Recuperator	Water separator	Condenser	Pressure regulation valve	Turbine
[69]	Centrifugal, screw, scroll or rotary vane	Liquid-air	-	X	X	-	Optional
[79]	Centrifugal	-	-	X	X	-	-
[80]	- ($p < p_{amb}$)	-	-	X	X	X	-
[81]	Roots	Liquid-air	-	-	-	X	-
[82]	Centrifugal	Liquid-air	-	-	X	-	-
[83]	Centrifugal	Air-air	-	-	-	X	-
[76]	unknown	Air-air	-	-	-	-	Optional
[84]	Centrifugal	-	X	-	-	-	X
[17]	Centrifugal	Air-air	-	-	-	X	-
[85]	Centrifugal	Liquid-air	-	X	-	Optional	Optional
[86]	unknown	-	-	-	-	-	-

From the literature overview, it is evident that a centrifugal compressor is commonly employed, while both air-to-air and liquid-to-air intercoolers are valid options. In addition, the potential integration of a turbine is considered to increase system efficiency.

2.3.6. Air Supply System: Key Takeaways and Research Questions

Considering the literature study on air supply systems for fuel cells, several key considerations emerge:

Air Supply System: Key Takeaways

- Data from the publication by Schröter will be implemented as it provides the most complete data for optimal fuel cell temperature, pressure, current density and air excess ratio, validated for the largest fuel cell and air supply system testbed currently in use (65 kW) [17].
- Literature shows a large variety for optimal fuel cell inlet air pressure, relative humidity and air excess ratio. These parameters will be included in a sensitivity analysis of the preliminary design of the propulsion system.
- Essential components are the air filter, centrifugal compressor, intercooler, humidifier and air outlet. Preliminary design of these components can be affected by mission parameters such as air velocity, air pressure, humidity and air density. It will be essential to quantify the effect of such parameters in different operating conditions.
- While air-to-air and liquid-to-air intercoolers are both implemented in literature. The choice of the type of intercooler depends on the ease of integration with other systems.
- The addition of a turbine to the air supply system can decrease the power requirement of the compressor.
- While a recuperator can increase reduce system mass and eliminate the risk of condensation inside the turbine, preliminary analysis in literature showed no substantial benefit at system level. Therefore it is considered inessential to include in preliminary sizing of the air supply system.
- Components such a as a water separator, condenser and pressure regulation valve are not always included in studies detailing air supply systems for fuel cells. These components are considered inessential to include in preliminary sizing of the air supply system.

The following research questions arise are associated with the air supply system:

Air Supply System: Research Questions

- "To what extent do fuel cell operational parameters affect payload and range?"
- "What operating conditions are affecting the preliminary design of a fuel cell balance-of-plant?"
- "To what extent can the addition of a turbine enhance payload and range?"

2.4. Thermal Management System

This section discusses the literature review of thermal management of LH2FCE propulsion systems for regional aircraft. Cooling the fuel cell is critical, as these aircraft typically require power levels up to 4 MW [87]. With fuel cells operating at about 40-60% efficiency, approximately 4 MW of excess heat must be dissipated [50]. This is similar to heat dissipation from more than 1000 household electric ovens at the same time. Without adequate cooling, increased temperatures can degrade performance and damage the proton exchange membrane inside the fuel cell. LT-PEMFCs operate around 80°C, producing low-grade heat with a small temperature difference relative to the environment. This narrow difference complicates the design of effective heat rejection systems.

2.4.1. Fuel cell cooling

Three primary techniques are utilized to cool a fuel cell:

- **Air cooling:** The cathode air is employed to control the temperature of the fuel cell.
- **Liquid cooling:** Water or another coolant is employed to convect heat from the fuel cell, typically in a mechanically pumped loop.
- **Phase change cooling:** This technique uses the latent heat of water or another coolant [88].
- **Evaporative cooling** adds cooling water to the cathode air, removing heat from the fuel cell through water evaporation [88].

Air cooling is typically employed in relatively small fuel cells, such as in NLR's HYDRA-1 drone. This hydrogen drone is powered by fuel cells of only 800W [89]. In larger LT-PEMFCs with power outputs exceeding 5 kW, liquid cooling is the most common method. The standard coolant in the automotive industry is a water–ethylene-glycol mixture [90].

A liquid mechanically pumped loop consist of a pump and accumulator, expansion valve and radiator [88]. The accumulator is required to control thermal expansion and pressure of the working fluid [91]. There are multiple types of accumulator, such as a pressure controlled accumulator. Pressure can for instance be controlled by pushing a diaphragm inside the accumulator with pressurized nitrogen [92]. A heat controlled accumulator is another type of pressure device, in which pressure is maintained by keeping the accumulator above a certain saturation temperature. The corresponding vapor pressure regulates the accumulation of liquid. A porous filter can be exploited for vapor blocking [93].

Pump and accumulator are typically placed on the cold side of the system to prevent cavitation which can damage the pump [93]. However, if the lowest possible pressure is desired inside the fuel cell, the pump and accumulator can also be placed on the hot side. An overview of a liquid mechanically pumped loop is shown in Figure 2.16 with a T-S diagram for illustrative purposes.

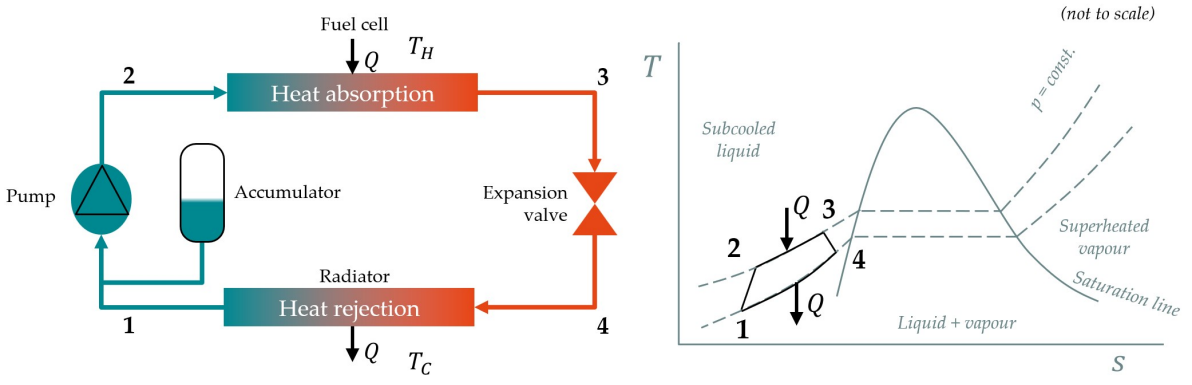

Figure 2.16: Liquid mechanically pumped loop (mechanically pumped loop). Own work based on [91].

To dissipate heat out of the fuel cell, the coolant can be pumped through small channels in the bipolar plates, mainly removing the heat through convection [94]. A small portion of the heat is convected or radiated via other paths, as shown in Figure 2.17.

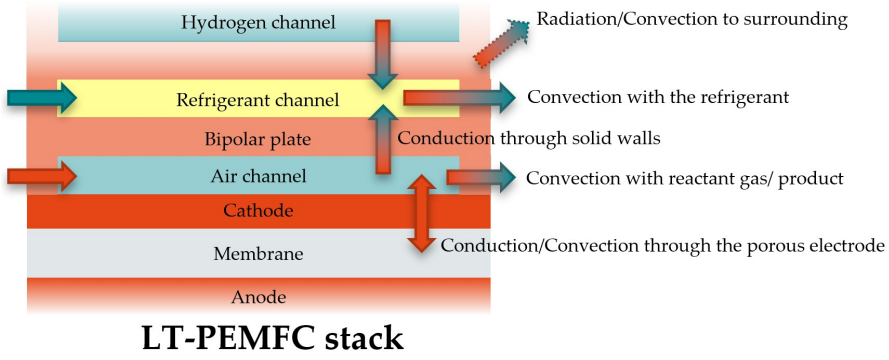

Figure 2.17: Heat paths inside a LT-PEMFC with coolant channel. Adapted from Bargal et al. (2020) [94].

An emerging technique for cooling fuel cells is employing a two-phase mechanically pumped loop [88]. Ellis and Kurwits (2016) found that a two-phase mechanically pumped loop is especially suited for high heat flux applications and temperature uniformity, e.g. space applications, as the latent heat of the cooling fluid is exploited [95]. However, LT-PEMFCs typically exhibit relatively low heat flux and non-uniform temperature distribution, making this approach less applicable. Current fuel cells generate about q=5 kW/m2 [96]. With low heat, a challenge arises. Superheated liquid can enter the fuel cell at the onset boiling without vaporizing significantly. This considerably decreases the heat transfer coefficient [97]. At heat fluxes of an order of magnitude larger (O(200 kW)), two-phase mechanically pumped loops are much more effective. Furthermore, a temperature difference of 10-15K is usually observed in LT-PEMFCs to prevent large coolant mass flow rates, resulting in a non-uniform temperature distribution [98]. Figure 2.18 illustrates how a two-phase mechanically pumped loop works.

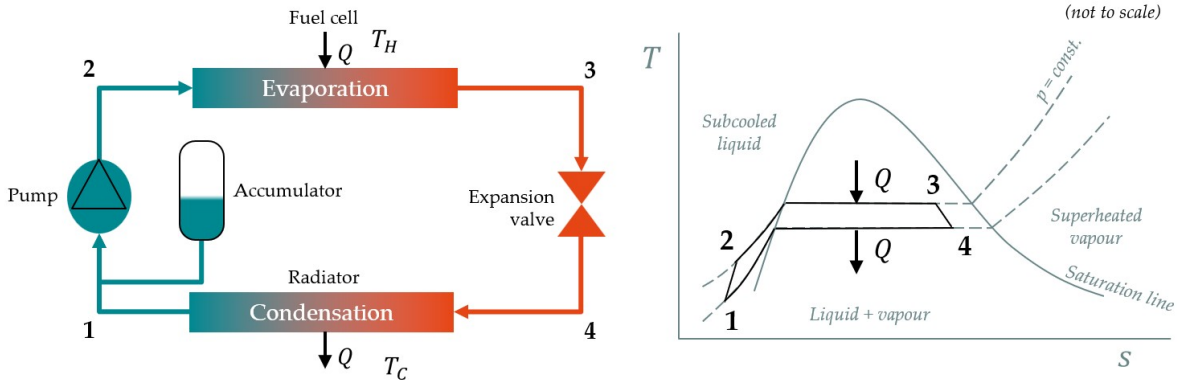

Figure 2.18: Two-phase mechanically pumped loop. Own work based on [91].

In two-phase cooling systems, a condition that must be avoided is critical heat flux (CHF), which results in flow instability and low heat transfer coefficient [99]. Figure 2.19 illustrates that the heat transfer coefficient is rather small beyond the CHF, when compared to a liquid-vapor mixture. Also, it can be seen that the HTC increases only for a specific region of liquid-vapor mixture, highlighting the essence of temperature uniformity. Scoccimarro (2023) argues that two-phase mechanically pumped loops probably outperform liquid cooling, but many challenges are to be solved and detailed analysis is lacking [85].

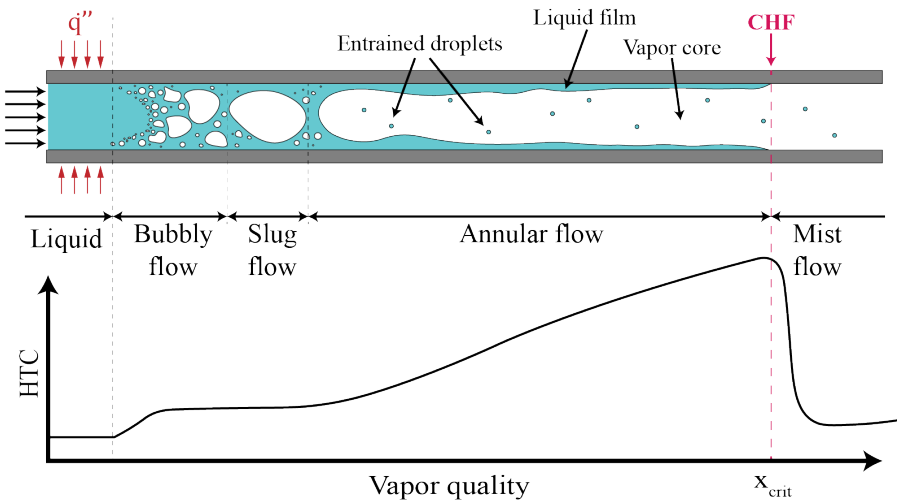

Figure 2.19: Heat transfer coefficient (HTC) for different flow regimes. The critical heat flux (CHF) condition is illustrated. Reproduced from Morse et al. (2021) [100]

Fly and Thring (2016) argue that evaporative cooling can be a very effective fuel cell cooling method, requiring a radiator frontal area of 27% less than required for liquid cooling [88]. Additionally, no cooling channels are required within the fuel cell, decreasing mass and increasing specific power. However, a highly efficient water removal system is needed to maintain the water cooling cycle, before exhausting the cathode air (> 90%). A cyclone water separator is mentioned as a potential solution. Otherwise, fuel cell temperature would have to be lowered to maintain water balance, as relative humidity and water production increase in the fuel cell. This increases required radiator area due to lower temperature difference. At water removal efficiencies below 90%, liquid mechanically pumped loop cooling is again the preferred method. Furthermore, the use of purified water in the evaporative cooling cycle forbids the use of aluminium radiators, as uncoated aluminium tubes can contaminate the condensing de-ionised water. [88]. Usage of e.g. stainless steel radiators would increase system mass. Concluding, evaporative cooling shows great potential but more research is required, as the disadvantages might outweigh the benefits.

2.4.2. Coolant Selection

Although an ethylene-glycol based water solution (water-eglycol for short) remains a widely used coolant, ongoing research aims to identify potentially more suitable alternatives. A notable limitation of water-eglycol is its freezing point of -37°C for a 50/50 mixture [**noauthor_ethylene_nodate**].

At the typical cruising altitude of regional aircraft (25,000 ft), the International Standard Atmosphere (ISA) temperature is approximately -35°C, which is too close to the freezing point of water-eglycol 50/50. Furthermore, this coolant exhibits significantly increased viscosity at temperatures below zero, becoming 22 times more viscous than water at 20°C when reaching -17.8°C [101]. The risk of freezing makes water-eglycol 50/50 less attractive, although this can be counteracted with e.g. battery powered heaters. To decrease the freezing point of water-eglycol, the mixture fraction of ethylene-glycol can be increased, but this increases viscosity at lower temperatures further, and the specific heat coefficient is reduced [102].

Consequently, exploration of alternative coolants is necessary. Building on a systematic approach that is used at NLR [91] for the selection of suitable coolants (e.g. Galden HT80, Methanol, Ammonia) across various cooling techniques, several mixtures of water-eglycol are added [103]. The approach is based on a "Figure of Merit", which incorporates coolant properties from the NIST Reference Fluid Thermodynamic and Transport Properties (REFPROP) database [104].

For the Figure of Merit calculation of coolants for a liquid mechanically pumped loop, the pressure drop is important. This can be determined by [91]:

$$\Delta p \propto \frac{\mu_l^{1/4}}{\rho_l C p^{7/4}} \frac{L}{d^{19/4}} \frac{P^{7/4}}{\Delta T^{7/4}} \tag{2.7}$$

In this equation,

- $\frac{\mu_l^{1/4}}{\rho_l C p^{7/4}}$ is a fluid dependant part.
- $\frac{L}{d^{19/4}}$ is a geometry dependant part.
- $\frac{p^{7/4}}{\Delta T^{7/4}}$ is determined by the heat input and sensible temperature difference of the fluid.

For a liquid mechanically pumped loop three Figures of Merit are important [91]:

- **Minimal pressure drop** in the system, which is the inverse of the fluid dependant part of the pressure drop. This is important as it determines maximum length and minimum diameter of the tubing [93]:

$$M_{\Delta p} = \frac{1}{\mu_l^{1/4}/(\rho_l c_p^{7/4})} \tag{2.8}$$

- **Minimal required pump power**, which is obtained through a small pressure drop and a low volume flow rate:

$$M_{\text{pump}} = \frac{\rho_l c_p}{\mu_l^{1/4}/(\rho_l c_p^{7/4})} \tag{2.9}$$

- **Minimal size of the accumulator**. The accumulator is quite a large part of the total mass of a liquid mechanically pumped loop. The figure of merit for accumulator size is based on the operational temperature range.

$$M_{\text{accu}} = \frac{\rho_l \text{ at } T_{\max}}{\rho_l \text{ at } T_{\min} - \rho_l \text{ at } T_{\max}} \tag{2.10}$$

These three Figures of Merit can be averaged, creating M_{weighted}. Additionally, the following criteria should be kept in mind [93, 103]:

- Operating pressure should be close to the fuel cell pressure, to limit structural stresses inside the cells.
- The critical temperature T_{crit} should be $< -40°\text{C}$, which is the EASA requirement for cold restart [105]. This prevents freezing of the coolant.
- NFPA (National Fire Protection Association) rating should not be too large for early generation retrofit aircraft [106]. The NFPA rates the coolants flammability, stability, and the impact on health.
- The global warming potential of the coolant should be GWP < 150. This is expressed as the equivalent effect of 1 kg CO_2. Therefore, often used coolants such as R134a are not considered, as their use is prohibited in new vehicles by the European commission, having a global warming potential GWP >150 that of CO_2 [107]. While there are replacements for high-GWP refrigerants like R1233ZD(E), it is likely that in the future only use of natural coolants such as Methanol will be permitted.

2.4.3. Heat Rejection

As mentioned before, a regional hydrogen fuel cell aircraft requires up to 4MW of power. If a fuel cell is 50% efficient, 4MW of heat will need to be rejected from the system. This section discusses several approaches to reach this objective.

Ram Air Duct with Radiator

Ambient air cools removes waste heat by flowing over a skin heat exchanger (HX) or through an air-to-air or air-to-liquid HX. In aircraft systems that require more heat dissipation a ram air duct is often implemented. A puller fan can be used to increase airflow during ground operation [108].

Schiltgen and Freeman (2016) proposed a tube-and-fin radiator placed inside a ram air duct to provide up to 1.49 MW cooling power at top of climb [109]. Their design incorporates the Meredith effect to reduce cooling drag and increase heat rejection [110].

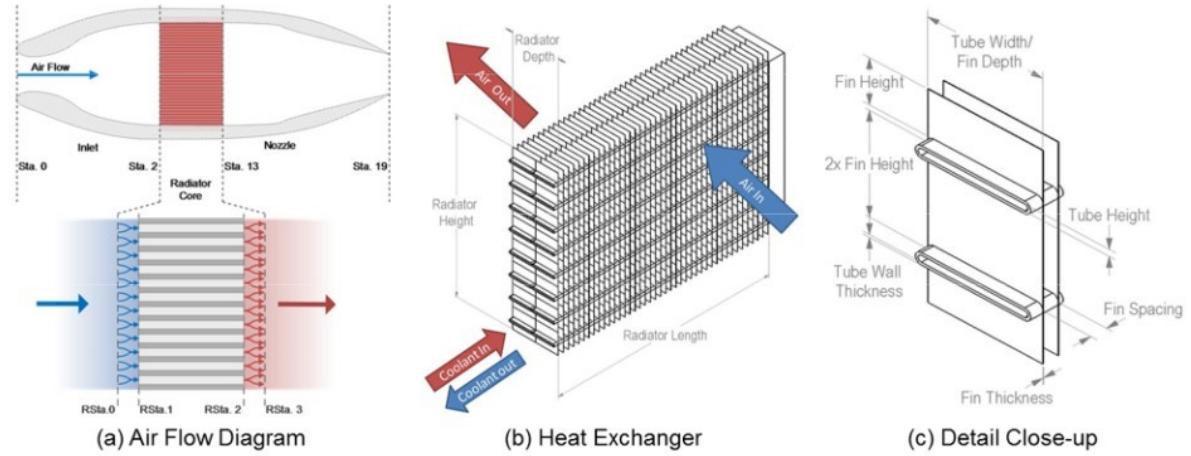

Figure 2.20: Ram air duct design with radiator to provide 1.5 MW cooling power. Reproduced from Schiltgen and Freeman (2016) [109]

The Meredith effect is essentially an open Brayton cycle, but only works as the inflowing air has significant speed. First the air is compressed in the diffuser due to the ram air effect. Then, the air is heated by flowing through the radiator and expanded and accelerated through the nozzle. From this acceleration a small portion of thrust can be generated [110]. The P-51 Mustang, a bomber used by the Americans during World War II, was one of the first aircraft to effectively exploit this effect, achieving a few hundred pounds of thrust and significantly lowering cooling drag [111]. In literature Meredith effect is mainly employed to cool piston engine [112]. Figure 2.21 shows how the P-51's cooling duct was designed.

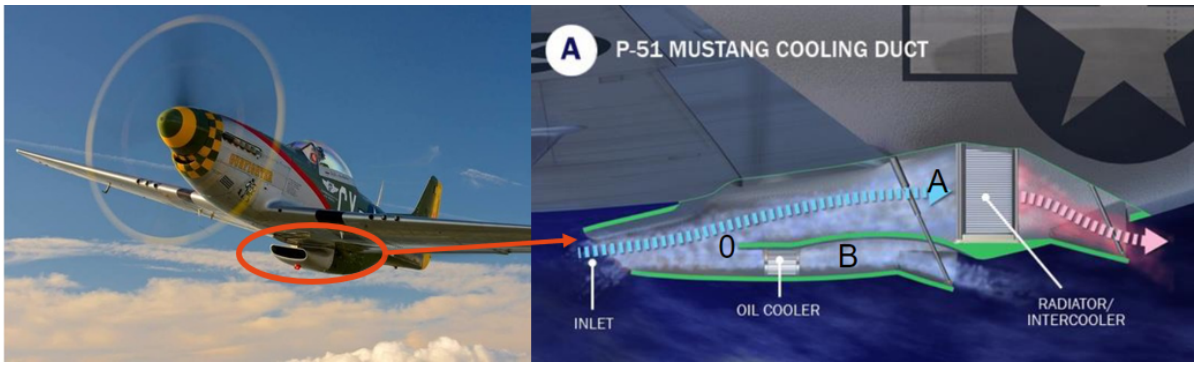

Figure 2.21: P-51 Mustang ram air cooling duct. Reproduced from [111, 113].

Kozulovic (2020) argues that if a fuel cell system would be installed on a A320neo or B737MAX with propulsive power of about 10 MW, the required radiator would increase power demand by 23.7%. Also in his design, the Meredith effect is exploited to reduce the cooling drag [114].

To improve heat transfer, the radiator can be placed under an angle, as a larger frontal area can be attained without a significant increase in pressure drop. This is true up to an air inflow angle of 70 degrees. After that, pressure drop increases significantly due to flow separation, as was found in experiments by NACA in 1942 [115] and Henriksson et al. (2015) [116]. This effect is visualized in Figure 2.22.

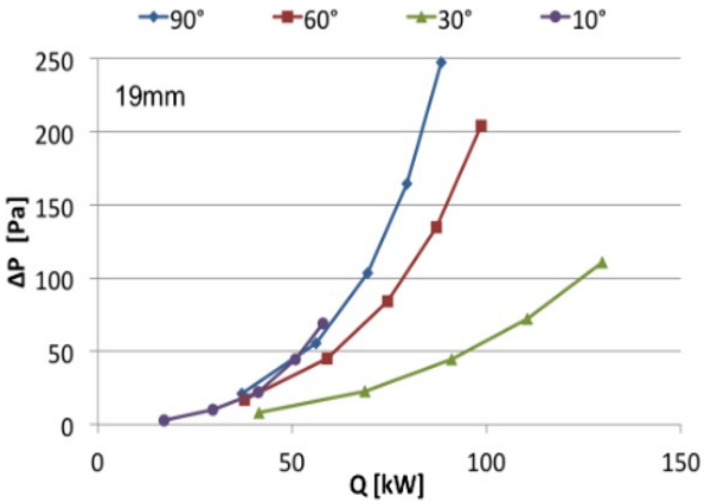

Figure 2.22: Static pressure drop as a function of heat transfer for a 19mm thick HX. Reproduced from Henriksson et al. (2015) [116].

Rietdijk and Selier (2024) present results of a feasibility study for a retrofit of a widely used regional aircraft, a DHC-8 Q300, with a LH2FCE propulsion system [10]. In the publication, they argue that four ram air ducts with a radiator under an angle of 65° will be able to dissipate all fuel cell heat effectively, given an air mass flow for the minimum control speed of the aircraft. They make a rough estimate of the cooling drag by assuming that the ducts increase the zero-lift drag coeffcient proportional to the increase in frontal area of the aircraft. The design of the cooling ducts is shown in Figure 2.23.

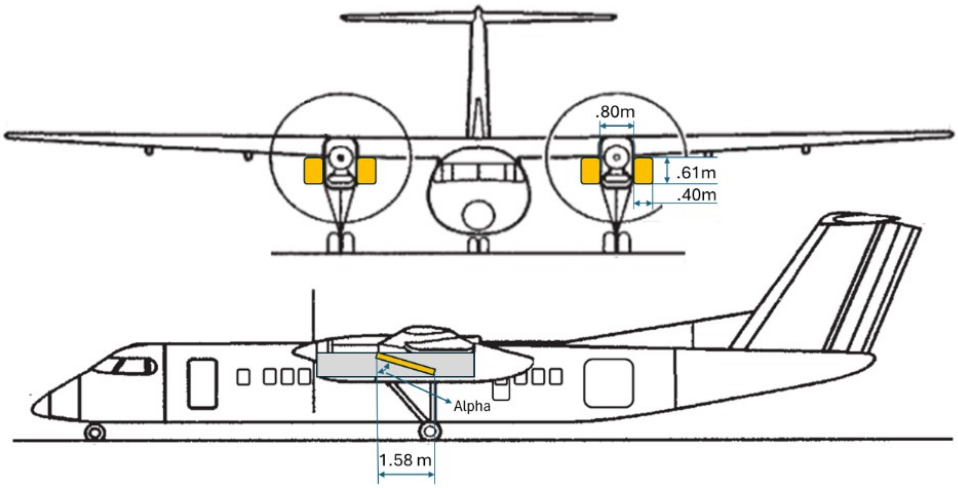

Figure 2.23: Positioning of the ram air ducts in the DHC-8 q300 retrofit with a LH2FCE propulsion system. Reproduced from Rietdijk and Selier (2024) [10].

Beltrame et al. argue that the Meredith effect can be achieved during cruise by integrating an inclined radiator in a ram air duct [18]. They simulate a ram air duct housing a condenser with a heat rejection of 740 kW. The duct design is visualized in Figure 2.24.

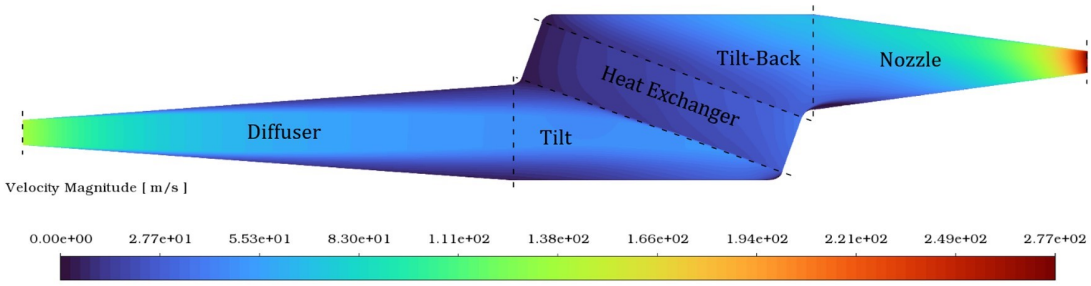

Figure 2.24: Velocity contour inside the optimized ram air duct. Reproduced from Beltrame et al. [18]

Results of a sensitivity analysis by Beltrame et al. on TR (thrust-to-drag ratio) are shown in Figure 2.25. Varied input parameters are the diffuser area ratio AR, the pre-diffusion mass flow ratio MFR and the heat exchanger inflow angle θ. With the condenser under an angle of $\theta = 70°$, AR of 4.0 and $MFR = 0.6$ a TR of at least 1.05 should be possible.

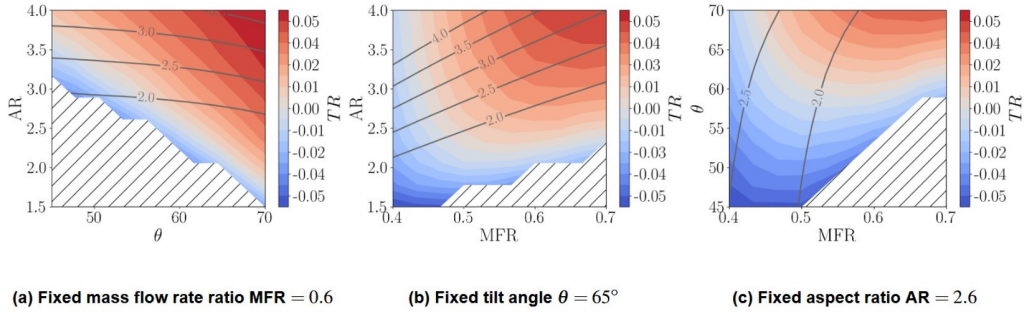

Figure 2.25: Ram air duct sensitivity analysis on radiator angle θ, diffuser area ratio AR, mass flow ratio MFR, and thrust ratio TR. Reproduced from Beltrame et al. [18]

An upcoming technology to replace state of the art fin and tube radiators are microtube or microchannel radiators. These have some advantages, according to Mezzotechnologies [117]:

- A reduction in air pressure drop of 30-40% compared to state of the art fin and tube radiators.
- Placing many microtubes enhances mixing of the flow inside the radiator due to the vortices (von Karman vortex street), resulting in improved heat transfer. Usually, the boundary layer growth of air between the tubes decreases the heat transfer coefficient.
- More surface area for heat rejection is available due to tubes having a smaller diameter and the significant increase in amount of tubes.
- Higher damage resistance than state of the art radiators (cracking of tubes instead of buckling of the entire assembly).

Overall, this would result in lower weight and less drag. Still, manufacturing requires more effort. While there is no existing literature to supports these claims, these microtube radiators are adopted in the high performance automotive racing and military industry [117]. The difference between tube-fin (in this case folded tube-louver fin) and microtube HX is illustrated in Figure 2.26.

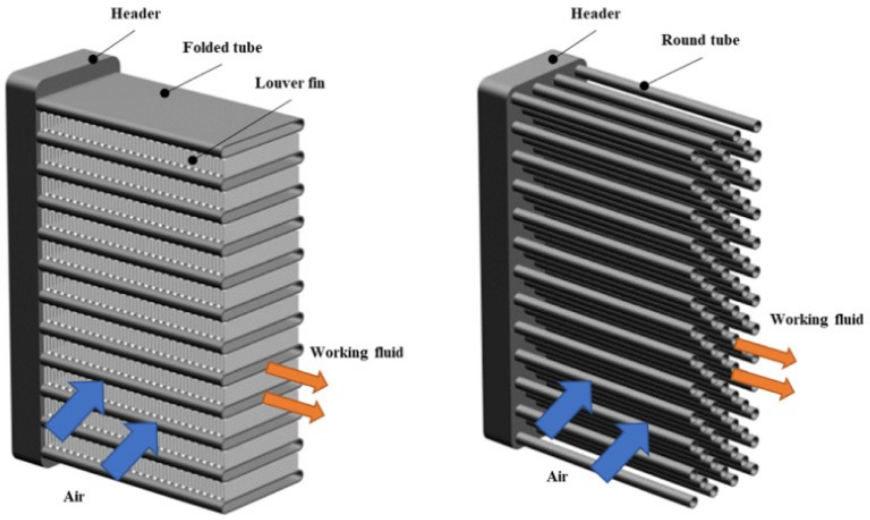

Figure 2.26: Cross sectional view of a folded tube-louver fin HX and bare-tube HX (comparable to microtube HX). Reproduced from [118].

Fan Heat Exchangers

Cranfield Aerospace Solutions employs a different methodology than a ram air duct. They are placing two ducted fans with radiators inside underneath the nacelle as can be seen in Figure 2.27. A round duct is more efficient than a rectangular one. Moreover, it is more suitable for integration with a fan. If air flow through the radiator is insufficient, this fan could be turned on. Kellermann et al. (2021) argue that a ram air inlet design with small puller propeller can be exploited to reach steady-state cooling requirements on a hot-day take-off. This was designed for a 180-passenger hybrid-electric aircraft. If the puller fan is omitted the thermal management system is oversized and fuel burn increases by 0.29% [119].

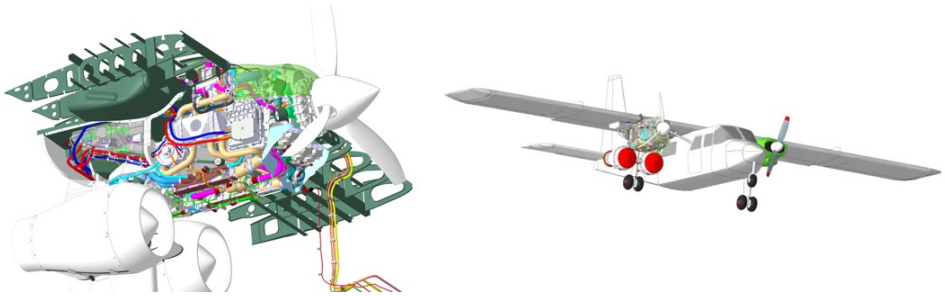

Figure 2.27: Cranfield Aerospace Solutions (CAES) design for a hydrogen fuel cell commuter aircraft. Two ducted fan radiators are placed under each nacelle. Reproduced from [120, 121]

Hydrogen Heat Exchanger

While hydrogen combustion requires high GH_2 injection pressures, the pressure in the tank may be sufficient to deliver the LH_2 to the fuel cell at the required temperature and pressure, eliminating the need for heavy cryogenic pumps [122]. The LH_2 needs to be vaporized and heated to $60 - 80°C$ for operation in a LT-PEMFC. For this, fuel cell waste heat could be exploited in a hydrogen heat exchanger (H2HX). This increases η_{shaft} by 11.4% according to De Boer (2024, unpublished) [15].

A risk that arises in a H2HX is freezing of the heat transfer fluid used to heat the hydrogen stream. Brenk et al. (2021) argue that in a shell-and-tube LNG heater, freezing of the heat transfer fluid in the shell can be allowed to a certain extent, without affecting pressure drop. Minimal impact on pressure drop was observed by optimizing the size and spacing of the tubes in the shell. The geometry is shown in Figure 2.28. However, the saturation temperature of LNG, consisting mostly of methane, at p=3 bar is higher than LH_2 (126.7K vs. 24.7K [123]). Also, the purpose is only related to re-gasification and not heating, as in the H2HX. Differences in overall heat transfer coefficient complicate comparison of the H2HX with the results in the study by Brenk et al. [124].

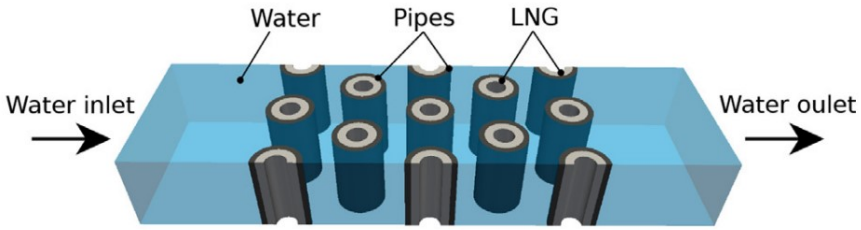

Figure 2.28: Modeled geometries of the shell-and-tube LNG heat exchanger reproduced from Brenk et al. (2021) [124].

Alternatively, to lower the risk of freezing, the coolant can be fed through a single tube, with auxiliary electrical heaters placed around the H2HX, powered by a battery. An illustration of such a heat exchanger concept is shown in Appendix B.1. The auxiliary heaters can be employed during start-up of the engine or in case of freezing of the heat transfer fluid (e.g. during re-start in cruise flight) [122]. A battery may be required in any case to assist with high transient power demands that the LT-PEMFC cannot deliver on its own [57]. In case of heat transfer fluid freezing during a re-start scenario, other methods to prevent freezing may be to increase coolant mass flow rate by increasing pump speed or partial closure of the radiator inside the ram air duct [122].

Skin Heat Exchangers

While Ahlers (2011) states that skin or surface HXs have less cooling potential than heat exchangers in ram air ducts [108], this is an emerging technique to reject heat to the environment. Instead of ingesting air into a duct, resulting in momentum loss and additional drag, the to-be-cooled coolant is in direct contact with the skin of the aircraft, which is in turn in contact with the ambient. Skin HXs have been used since the early days of flight, when piston-powered aircraft had strict cooling requirements. With the rise of turbine powered aircraft, skin HXs became less common as much of the heat is effectively rejected into the environment. Recent studies into skin HX include the combined use with ice-protection systems [125]. Aside from ice-protection, Wang et al. (1999) found that heating the boundary layer on the wing surface can result in earlier transition of the flow [126]. On the other hand, Kallath et al. (2020) found that heating the flow can reduce drag and increase lift by a few percent at an optimal combination of Reynolds number, angle of attack, HX location and heat flux magnitude [127].

A recent example of skin HX employment is that aboard the Airbus A320, where it is used to reject heat from the avionics cooling system, as shown in Figure 2.29.

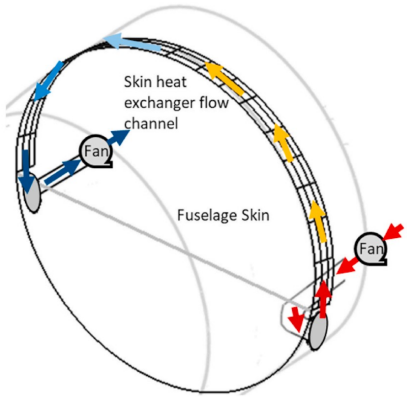

Figure 2.29: Skin heat exchanger system to reject heat from avionics, similar to that used in the Airbus A320 [125].

Considering all Airbus A320 surfaces, up to 7MW of cooling power is available during cruise, according to Kellermann et al. (2020) [128]. However, there is no mention of the added weight that skin HXs would have on the considered aircraft surfaces: the fuselage, wings, nacelles and horizontal/vertical tails. Also, during hot day take-off ($T_{\text{ambient}} \approx 47°C$) only 0.25 MW is available at most.

Recent developments investigate the implementation of loop-heat pipes for de-icing, a two-phase heat transfer system efficient over long distances [129]. However, given that heat transfer rates for de-icing systems of up to 8 kW/m^2 are required [130], and the wings of a DHC-8 Q300 have a surface area of 56.1 m^2 [10], maximum required heat flux is significant (561 kW, 11% of total cooling demand). When other aircraft surfaces are considered, the

potential for heat rejection increases.

However, Schaefer et al. (2022) used CFD and Aircraft Systems Design tools to demonstrate the drawbacks of the added mass of skin HXs in LH2FCE aircraft [131]. They simulated two concepts: In Concept 1, heat rejection is divided between ram air HXs and skin HXs (see Figure 2.30), leading to a total HX mass of 1126 kg. In concept 2, all heat rejection was managed by ram air HXs, significantly reducing HX mass to 215 kg. Maximum power levels were comparable to regional aircraft (3.65MW), while cruise altitude was slightly higher, increasing the temperature difference with the environment. While concept 2 has a slightly larger drag penalty, fuel mass is increased much more in concept 1 (5%) than in concept 2 (1%), due to the increased system mass. However, the skin HX tube material was aluminium material, while in the design by Su et al. (2017) [129], lighter composite materials are implemented. However, there is no mention for the mass of the skin HX system in this study. In conclusion, although skin HXs offer potential for integration with de-icing systems, the significant mass penalty from the associated tubing makes this technique less attractive.

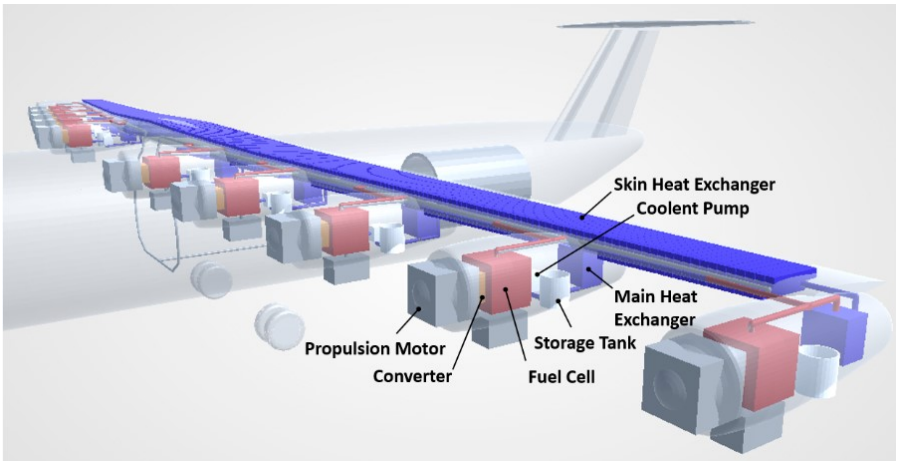

Figure 2.30: Illustration of the cooling architecture for Concept 1 in the study by Schaefer, with skin HX and ram air HX accounting for the required heat rejection [131].

2.4.4. Thermal Management System: Key Takeaways and Research Questions

From literature research on thermal management in fuel cell powered systems, the following considerations arise:

Thermal Management System: Key Takeaways

- Thermal management based on a liquid mechanically pumped loop chosen for the propulsion system model. Air cooling is discarded as it is only suitable low power fuel cells. Two-phase cooling is excluded as well, due to challenges with low heat flux, requirements for temperature uniformity and low technology readiness level. Evaporative cooling shows potential, but more research is required as the disadvantages might outweigh the benefits, and is therefore not considered in this work.
- Ram air ducts with radiators may be used for heat rejection from the thermal managenement system. Efficient ram air duct design can result in net zero drag and even a small amount of thrust.
- While microtube HX may provide improved heat transfer over tube-fin HX and enable weight savings, existing literature lacks conclusive evidence to support this claim.
- Employment of fan HXs decreases fuel burn by a negligible amount (0.29%) and thus this solution is not modeled.
- While usage of skin HXs in combination with de-icing systems shows potential (11% of the cooling demand), the significant mass penalty from the associated tubing makes this technique less attractive. In recent studies, skin HXs partially made of composites are mentioned, but exact mass estimates are not mentioned. Therefore skin HXs are not included in the modeled propulsion system.
- Heat rejection through a hydrogen heat exchanger (H2HX), thereby evaporating and heating the LH_2 is included among the investigated solutions, as a significant amount of the total heat can be rejected in such a system.
- As there are numerous ways to prevent freezing inside the thermal management system due to cryogenic hydrogen or cold outside air, this aspect is not considering critical to be included in the preliminary design of the LH2FCE propulsion system.

Thermal Management System: Research Questions

- "To what extent does ram air duct design affect payload and range?"
- "To what extent can a hydrogen heat exchanger be employed to reject heat from the thermal management system?"
- "To what extent can a small amount of thrust be generated from the ram air duct?"

2.5. Hydrogen Storage System

While hydrogen has about 4 times more energy per mass than kerosene, it has an extremely low volumetric energy density. This makes storage difficult, especially in aircraft. Storing hydrogen at ambient pressure requires about 500 fuselages for a Boeing 777-200ER. Hydrogen can be compressed to about 700 bar, as is done in the automotive industry (e.g. in the Toyota Mirai [132]), but this storage method still requires one full Boeing 777-200ER fuselage. The analogy here does not take into account aircraft design changes to accommodate for weight and volume changes but gives an idea how bulky the hydrogen tank can be [12].

Hydrogen can also be cooled to the liquid state ($T \approx 20K$), reducing the required volume by a factor 2, but these tanks require dedicated vacuum-insulation to limit boil-off of the liquid, increasing weight of the tank. An important metric when selecting storage method is the gravimetric efficiency:

$$\eta_{\text{gr}} = \frac{FM}{FM + m_{\text{tank}}} \tag{2.11}$$

Whereas gravimetric efficiency of gaseous hydrogen (GH_2) tanks is currently <10%, liquid hydrogen (LH_2) may reach values of over 50%, making storage of hydrogen as a cryogenic liquid the best option [12].

2.5.1. Liquid Hydrogen Storage

It is uncertain what a realistic gravimetric efficiency (η_{gr}) is for LH_2 tanks aboard aircraft. Below $\eta_{\text{gr}} \approx 55\%$, hydrogen performs slightly worse than kerosene in regional flights and significantly worse for longer flights. For values large than $\eta_{\text{gr}} \approx 55\%$, hydrogen outperforms kerosene and the advantage increases with range. As preliminary gravimetric efficiencies of LH_2 tanks range between 25-40%, with extreme predictions reaching up to 70%, some argue hydrogen propulsion only fits lower range aircraft while others argue it gets even more attractive for longer range aircraft [12]. This is visualized in Figure 2.31.

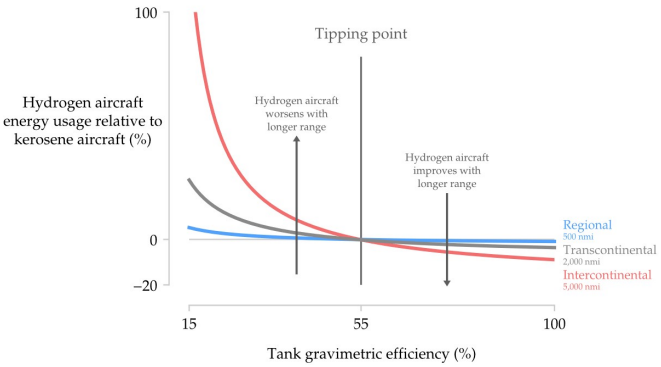

Figure 2.31: LH_2 tank gravimetric efficiency is an important metric for the feasibility in regional, medium and long range aircraft. Medium and long range become feasible around the tipping point of $\eta_{gr} \approx 55\%$. Reproduced from Adler and Martins (2023) [12].

In literature, LH_2 storage designs in aircraft often include large forward and/or aft integral tanks in the fuselage, meaning the fuselage is lengthened compared to kerosene aircraft, or a compromise on the number of passengers is made. Some concepts are shown in Figure 2.32.

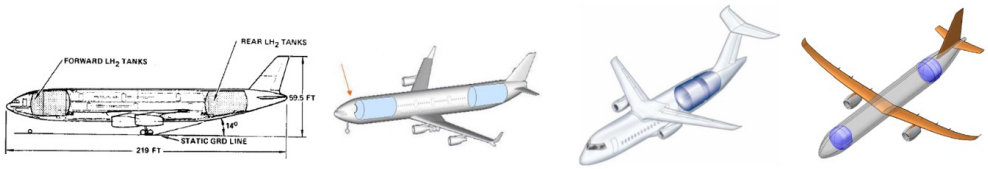

Figure 2.32: Different integral tank concepts. Reproduced from Brewer (1976) x2 [133], Cryoplane report [42] and Troelstch et al. (2020) [134].

Onorato et al. (2022) argue that large integral tanks in the front and back of regional aircraft enable weight savings, but that their suitability in aircraft has yet to be demonstrated [13]. Integral tanks carry additional structural loads of the fuselage, so comparison with non-integral in terms of gravimetric efficiency is difficult. For regional aircraft, these integral tanks will compromise on number of passengers and TRL is low.

Alternatively, wing-pods offer a solution, although it's important to note that this may increase drag [135]. Also, wing pods can cause ground clearance issues, but they can be swapped for larger ones when a longer range is needed and vice-versa [136].

An important advantage of storing kerosene in the wings is the fact that the bending moment caused by lift is counteracted by the weight of the fuel, enabling structural weight savings. In accordance with that consideration, Friedmann et al. (2023) designed high-pressure load bearing gaseous hydrogen tanks inside the wings. However, these tanks only reach $\eta_{gr} = 5 - 6\%$ [137].

Currently, only non-integral tanks have been built, which are easier to model as well [12]. Also, as envisioned by Universal Hydrogen, non-integral tanks can be modular [9]. Conceptual designs for early generations of regional retrofitted aircraft by Universal Hydrogen and Conscious Aerospace are shown in Figures 2.33 and 2.34, showing multiple smaller tanks. Rietdijk and Selier report for their retrofitted aircraft that a gravimetric efficiency of $\eta_{gr} = 23\%$ is currently feasible [10]. Rietdijk and Selier mention a fuel weight of 340 kg, for which gravimetric efficiencies of integral tanks can reach up to 35%, according to Saias et al. (2022) [138]. When the metal walls in the vacuum-insulated integral tanks are replaced by composites, a $\eta_{gr} = 61\%$ can be feasible, according to the Aerospace Technology Institute [139].

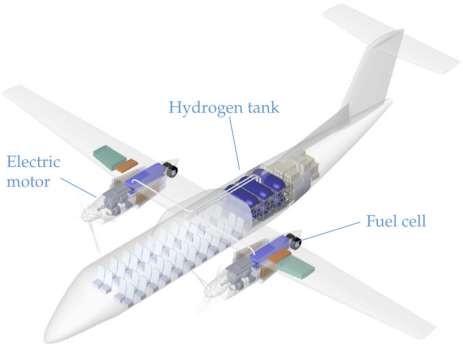

Figure 2.33: Regional aircraft concept by Universal Hydrogen. Reproduced from Adler and Martins (2023) [12].

Figure 2.34: Regional aircraft concept by Conscious Aerospace. Reproduced from Conscious Aerospace [140].

2.5.2. Tank Pressure Regulation

Pressure inside the fuel tank drops as LH_2 is drawn from it, so a pressure regulation device is essential. While in larger vertical tanks LH_2 could be drawn from the tank, heated and partly re-injected in the upper part of the tank, this pressure differential is too small for horizontal mobile tanks. Rather, electric heaters can be integrated inside the tank [141]. Boer et al. (2021) also implement this technique in their LH_2-based fuel cell system on the HYDRA-2 drone, by placing a polyimide heating element on the outside surface of the inner vessel in the vacuum jacket. They argue that a heater is required as passive heat leak from the tank is smaller than the heat needed to pressurize the tank [142]. However, Michel (1998) argues that electric heating elements have two disadvantages [141]. Electrical power is consumed from a battery, adding battery weight and replacement of defect cables inside the vacuum jacket lead to high repair costs. Instead, the most robust technique is to return a controlled amount of the heated gaseous hydrogen through the tank in enclosed tubing by means of a pressure controlled valve. The liquid hydrogen is heated using fuel cell waste heat through cooling water in a heat exchanger. The returned hydrogen gas can be heated again using fuel cell waste heat. Both tank pressure regulation techniques are visualized in Figure 2.36.

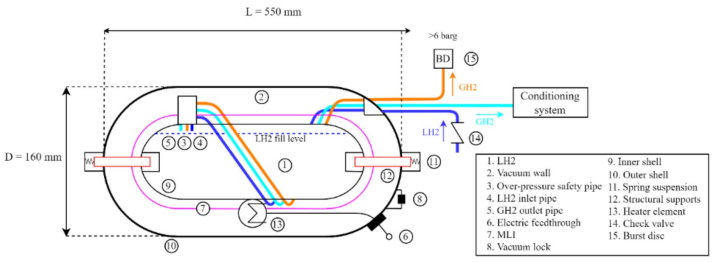

Figure 2.35: Pressurization by electric heating. Reproduced from Boer et al. (2021) [142]

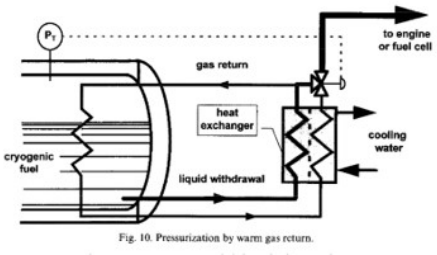

Figure 2.36: Pressurization by warm gas return. Reproduced from Michel (1998) [141]

2.5.3. Hydrogen Storage System: Key Takeaways

From literature research on the hydrogen storage system, the following key takeaways emerge:

Hydrogen Supply and Storage System: Key Takeaways

- A tank gravimetric efficiency of 23% is assumed to determine the mass of the liquid hydrogen storage system, based on an approximated fuel mass mostly based on cruise flight.
- The effects of gravimetric efficiencies up to 61% can be included in technology projections for 2030, assuming integral tanks made of composite materials.
- Although tank pressure regulation is essential, appropriate systems are presumably integrated in current non-integral hydrogen tanks. Therefore, this aspect is not investigated in the present work.
- Although tank volume has a large effect on payload space, a detailed design would be required to determine the integration in the aircraft.

2.6. Powertrain

The powertrain in LH2FCE aircraft includes:

- A propeller to convert shaft power to thrust.
- Electric motors to convert electric power from the fuel cells to shaft power.
- Inverters to convert DC power from the fuel cells to AC power.

And may include:

- A gearbox when propeller rotational speed is smaller than rotational speed of the electric motors.
- A battery to assist with high transient loads that the fuel cell cannot deliver.

Considering the publication by Quillet et al. (2021), propellers for regional turboprop aircraft, in this case a DHC-8 Q300, are quite efficient, reaching efficiencies up to 84% [87]. Cowlings are often placed directly behind the propeller, taking up a small portion of the air for engine cooling or for use in piston engines. However, placing objects behind the propeller such as large ram air ducts (see Section 2.4.3) might result in partial blockage of the propeller wake, decreasing thrust [19]. On the other hand, the propeller increases the mass flow through the ram air duct, which may be important in take-off conditions at recuded air velocity. Figure 2.37 highlights the size of the ram air duct compared to the propeller diameter, even though the test propeller is smaller than the original.

Figure 2.37: Propeller size compared to ram air duct size (left) for the Universal Hydrogen test aircraft [143].

The use of electric motors results in increased efficiency compared to piston and turbine engines, with current electric motors having more than 30% higher specific power [144]. Recently, researchers at MiT developed a 1 MW air-cooled electric motor for aviation, featuring a specific power of 17 kW/kg, efficiency of 97.3% with a rotational speed of 12,500 rpm [145] (see Figure 2.38). This motor assembly includes an air-cooled heat sink. Specific power may increase to 23 kW/kg by 2030 [146].

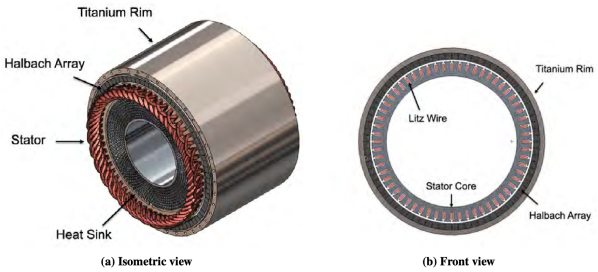

Figure 2.38: High power density electric motor developed by researchers at MiT [145].

Also, inverters and gearboxes are very efficient, having efficiencies of $\eta \approx 98\%$ [144]. Still, heat dissipation for electrical motors, converters, power electronics, batteries is at least one order of magnitude higher than conventional propulsion aircraft systems, requiring adequate cooling methods, according to Affonso et al. (2022) [147].

With powertrain cooling posing a challenge, the next generation of superconducting electric motors with cold power electronics might present a solution. Use could be made of cryogenic hydrogen to reject the heat to, while conditioning the fuel for further use [148]. Figure 2.39 highlights the use of cryogenic hydrogen to this purpose.

Two projects where such superconducting motors are being developed are Airbus ASCEND [149] and Rolls-Royce ASuMED [150], but technology is still in an early development phase.

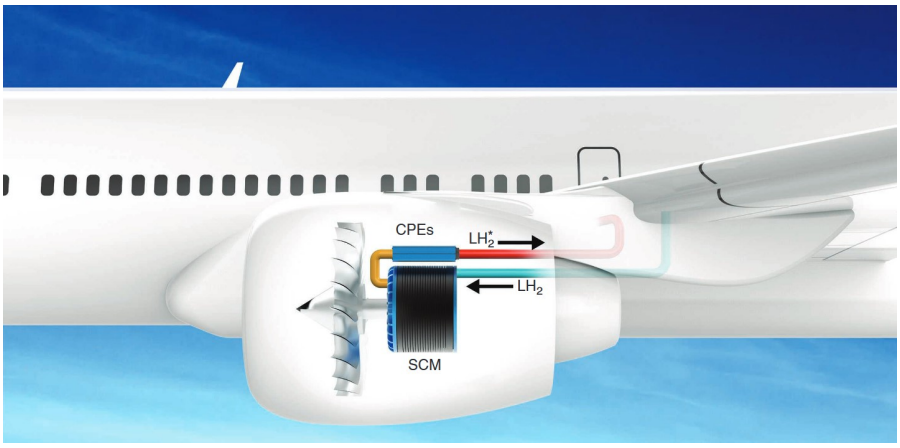

Figure 2.39: Liquid hydrogen as a means to provide cooling to superconducting electric motors and cold power electronics (CPE) in an aircraft [148].

Including a battery next to the fuel cell system may be required to cope with large power load transients [57]. Also, start-up processes might require the use of electric heaters to evaporate and preheat the hydrogen before its use, as waste heat is not yet available from the fuel cell. Also, electric heat from a battery may be required for freezing prevention in for instance a hydrogen heat exchanger (see Section 2.4.3) [16].

2.6.1. Powertrain: Key Takeaways

From the literature research on powertrain concepts, the following considerations are made:

Powertrain: Key Takeaways

- Detailed modeling of powertrain components is out of scope. To determine shaft power, the following efficiencies can be used:
  - Electric motor efficiency η_{EM} = 97.3%.
  - Gearbox efficiency η_{GB} = 98%
  - Inverter efficiency η_{INV} = 98%
- Since power electronics are very efficient, the corresponding cooling requirements are neglected in this research. A specific electric motor power of 17 kW/kg (including a air-cooled heat sink) can be used for current generation retrofits, and 23 kW/kg for 2030 projections.
- While batteries may be required in a LH2FCE aircraft, a full mission analysis and detailed fuel cell design would be required to determine peak loads. It is therefore assumed that all power is provided by the fuel cell system.
- The mass of inverters and power electronics is neglected.
- The feasibility of installing a large ram air duct behind a propeller is not investigated, as detailed flow analysis is required.

2.7. Research Questions

Considering the literature study, the following main research question is posed for this study:

Main research question

"How are payload and range affected when retrofitting a turboprop aircraft with a liquid hydrogen fuel cell electric propulsion system?"

The main research question shall be addressed by answering the following sub-questions, which were introduced in the previous literature sections:

Research Sub-questions

- "What modifications to the baseline mission can improve payload and range?"
- "To what extent does implementation of a HT-PEM fuel cell improve payload and range, when considering the increase in operating temperature?"
- "How do payload and range improve based on technology projections for 2030?"
- "To what extent do fuel cell operational parameters affect payload and range?"
- "What operating conditions are affecting the preliminary design of a fuel cell balance-of-plant?"
- "To what extent can the addition of a turbine enhance payload and range?"
- "To what extent does ram air duct design affect payload and range?"
- "To what extent can a hydrogen heat exchanger be employed to reject heat from the thermal management system?"
- "To what extent can a small amount of thrust be generated from the ram air duct?"

3 Methodology

To address the proposed research questions, it is essential to develop a model that can perform a preliminary design and assess the effects on payload and range of liquid hydrogen fuel cell electric (LH2FCE) aircraft. First of all, in Section 3.1 a reference aircraft is presented, as well as mission scenarios. Furthermore, it is explained how impact on payload and range are quantified.

Then in Section 3.2 the modeling strategy is presented. Afterwards, the ram air duct model (RAD), fuel cell system model (FCS), air supply system model (ASS) and thermal management system model (TMS) are discussed in Sections 3.3 to 3.6.

3.1. Mission Parameters

The DHC-8 Q300 is chosen as a reference aircraft (see Figure 3.1). This is the same aircraft as in the HAPSS retrofit project by Luchtvaart in Transitie [10].

Figure 3.1: Reference Aircraft, the DHC-8 Q300, adapted from [151].

When designing and sizing fuel cell balance-of-plant architectures, it is important to consider the worst-case scenarios during operation. These include the following conditions:

- **Hot-day conditions**, which is at ISA +30°C [10]. This is a constraining condition as the thermal management system will struggle to dissipate heat with a smaller temperature difference between the coolant and the ambient.
- **Take-off conditions**. The aircraft will be at its maximum weight, while also requiring high power levels to reach the required take-off velocity. Also, the air velocity is small, limiting air mass flow in the radiator and decreasing heat rejection.
- **Top-of-climb**. Air density will be smallest, while required power levels are still high to maintain the required rate of climb (1000 ft/min or 5 m/s for the final climb phase [152]). With lower air density, the compressor will struggle to elevate the air pressure, increasing required total fuel cell power. However, the radiator will struggle less to reject heat than in take-off, as air velocity is higher and ambient temperature lower.

Comparing preliminary designs for these mission conditions will determine for which scenario the system must be sized. After evaluating optimal on-design points for the limiting mission scenario, the system can be tested in off-design conditions. This includes cruise conditions, as the required fuel flow impacts the range and fuel mass in cruise.

Based on the original mission for the DHC-8 Q300 aircraft, altitude and velocity can be determined [152]. Using the drag polar of the aircraft [87], corresponding power settings (P_{shaft}, $P_{\text{net, FC}}$) are determined with the support of experts at NLR [153], using the NLR in-house MASS tool [154]. The mission input parameters to the model are presented in Table 3.1.

Table 3.1: Mission parameters.

Parameter	Take-off	Top-of-climb	Cruise
Altitude (h)	0 m	7620 m	7620 m
Temperature (ISA +30°C) (T)	45°C	-4.53°C	-4.53°C
Pressure (p)	101325 Pa	34712 Pa	34712 Pa
Density (ρ)	1.1095 kg/m^3	0.4502 kg/m^3	0.4502 kg/m^3
Relative Humidity (ϕ_{rel})	50%	50%	50%
Airspeed (TAS)	40 m/s	128.6 m/s	128.6 m/s
Rate of climb (ROC)	-	5 m/s	-
Fuel cell net output power ($P_{\text{net, FC}}$)	3.1 MW	3.9 MW	3.50 MW
Shaft power (P_{shaft})	2.90 MW	3.64 MW	3.27 MW

As can be seen, power required for top-of-climb is more than for take-off, so this might be the constraining design point. Furthermore, the minimum control velocity is chosen as design point for take-off (40 m/s), which is by regulation lower than the lift-off speed (56.6 m/s) [10]. Usually this is the minimum control speed in case one engine fails, but this requirement is not analyzed in detail in this thesis.

3.1.1. Payload Calculation

To quantify payload it is assumed that:

- Maximum take-off mass (MTOM) is 19051 kg. While the original MTOM is 19501 kg, the maximum landing mass (MLM) is assumed. In the event of immediate landing after take-off, a minor amount of fuel is used and dumping of liquid hydrogen is considered unfeasible [10].
- LH_2 tank mass is dependent on fuel mass. A realistic gravimetric efficiency of 23% is assumed [10].
- Operational empty mass (OEM) excludes the original PW123 engine system (950 kg) and excludes kerosene fuel system and tank mass, which is 5.5% of the MTOM [10]. This gives a specific power for the original propulsion system of about 1.16 kW/kg.
- Propulsion system mass m_{PS} includes the mass of the fuel cell, balance-of-plant components and powertrain components.

For total fuel mass, the fuel required for cruise can be determined given the fuel flow in cruise and the cruise time. The fuel mass for climb can be estimated by multiplying the average fuel flow between take-off and top-of-climb with the time it takes to reach cruise altitude.

$$m_{H_2,\text{climb}} = \left(\frac{\dot{m}_{H_2,\text{TO}} + \dot{m}_{H_2,\text{TOC}}}{2}\right)\left(\frac{h_{\text{cruise}}}{\text{ROC}}\right) \tag{3.1}$$

It is assumed that next to the fuel required for cruise and climb, 10% of the overall fuel mass is consumed in other mission phases than cruise $m_{H_2,\text{other}}$. This percentage should have minor influence on payload, as hydrogen is a lightweight fuel. The influence of the retrofitted propulsion system mass is expectedly much higher.

The MTOM breakdown of the original DHC-8 Q300 [155], the retrofit by Rietdijk and Selier (2024) and the mass budget considered in this study is shown in Figure 3.2. Note that the design range for the original turboprop is 1500 km (see Section B.4), while this is lowered to 750 km by Rietdijk and Selier. This is thought to be a commercially viable range for retrofits, probably due to increased payload and the consequent decrease in range. The fuel mass for the original aircraft is based on fuel capacity at design payload and range (see Figure B.4). The max fuel capacity is 2547 kg kerosene.

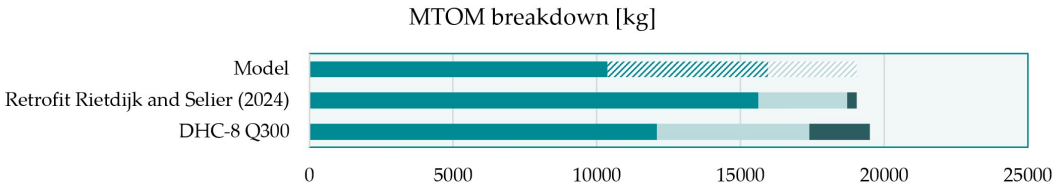

	DHC-8 Q300	Retrofit Rietdijk and Selier (2024)	Model
OEM	12103	15622	10383
Payload	5300	3089	
MF	2102	340	
Propulsion system budget			5579
Payload budget			3089

Figure 3.2: MTOM breakdown of the original DHC-8 Q300 [155], the retrofit by Rietdijk and Selier (2024) [10] and the mass budget for the model.

Note that the propulsion system budget includes fuel cell and balance-of-plant mass $m_{\text{FC+BoP}}$, tank mass m_{tank} and fuel mass m_{H_2}. The actual payload can then be determined according to:

$$\text{Payload} = \text{MTOM} - \text{OEM} - m_{\text{FC+BoP}} - m_{\text{tank}} - m_{H_2,\text{cruise}} - m_{H_2,\text{climb}} - m_{H_2,\text{other}} \tag{3.2}$$

Should the mass of the LH2FCE propulsion system be larger than the original, a compromise on payload is necessary. Note that the space left for payload has to account for passengers, cargo, crew and some auxiliary systems that are not included in the weight analysis, such as a battery, high-voltage inverters and tubing.

3.1.2. Range Calculation

To assess the effects on cruise range, the Breguet range equation is considered, modified for LH2FCE aircraft [156]. The Breguet range equation for propeller aircraft is:

$$R = \frac{\eta_{\text{prop}}}{g} \cdot \frac{1}{\text{PSFC}} \cdot \left(\frac{L}{D}\right) \cdot \ln\left(\frac{W_{\text{initial}}}{W_{\text{final}}}\right) \tag{3.3}$$

For reference, the maximum range of the original DHC-8 Q300 is up to 1707 km and the design range for the retrofit by Rietdijk and Selier is 750 km, as shown in Figure 2.7.

Given that power-specific fuel consumption (PSFC) is based on shaft power and fuel flow:

$$P_{\text{shaft}} = P_{\text{FC,net}} \cdot \eta_{\text{powertrain}} \tag{3.4}$$

$$\text{PSFC} = \frac{P_{\text{shaft}}}{\dot{m}_{\text{H}_2}}, \tag{3.5}$$

the following relation between fuel mass $m_{H_2,\text{cruise}}$ and design range is obtained:

$$R_{\text{cruise}} = \frac{P_{\text{FC,net}} \cdot \eta_{\text{powertrain}} \cdot \eta_{\text{prop}}}{g \cdot \dot{m}_{\text{H}_2}} \cdot \left(\frac{L}{D}\right)_{\text{cruise}} \cdot \ln\left(\frac{W_{\text{i,cruise}}}{W_{\text{i,cruise}} - m_{H_2,\text{cruise}}}\right)$$

where,

- $P_{\text{FC,net}}$ is the net required fuel cell power in cruise flight, delivered to the powertrain.
- η_{pt} is the powertrain efficiency, including the electric motors, gearbox and inverters, which is estimated at $\eta_{\text{pt}} = 95\% \cdot 97.3\% \cdot 98\%$ [144].
- η_{prop} is the propeller efficiency, estimated at 84% for the original propellers on the reference aircraft (see Section 2.6)
- $\dot{m}_{\text{H}_2}$ is the fuel flow in cruise.
- $W_{\text{i,cruise}}$ is the mass of the aircraft at the start of cruise, estimated as $W_{\text{i,cruise}} = \text{MTOM} - m_{H_2,\text{climb}}$. [10]

To determine the L/D in cruise, the drag polar for the aircraft is required. In literature, two sources were found mentioning a drag polar for the DHC-8 Q300, namely Rietdijk and Selier (2024) [10] and Quillet et al. (2021) [87]:

$$C_D = C_{D_0} + k \cdot C_L^2 \tag{3.6}$$

$$C_{D_0} = 0.0248, k = 0.0319 \text{ [Rietdijk and Selier (2024)]} \tag{3.7}$$

$$C_{D_0} = 0.0322, k = 0.0372 \text{ [Quillet et al. (2021)]} \tag{3.8}$$

The lift-to-drag ratio for different lift coefficients is determined according to:

$$L/D = \frac{C_L}{C_D} \tag{3.9}$$

The difference in drag polars and lift-to-drag ratio between the two sources is highlighted in Figure 3.3. The change in drag polar and lift-to-drag ratio for the retrofit in [10] is shown as well, for which an increase of 5% to the zero-lift-drag coefficient was assumed. This 5% increase in C_{D_0} stems from the increase in frontal area due to the addition of 4 ram air ducts, increasing parasite area. This assumption is probably optimistic, as ram air drag, interference drag and propeller blockage are neglected (see Section 3.3 for more details).

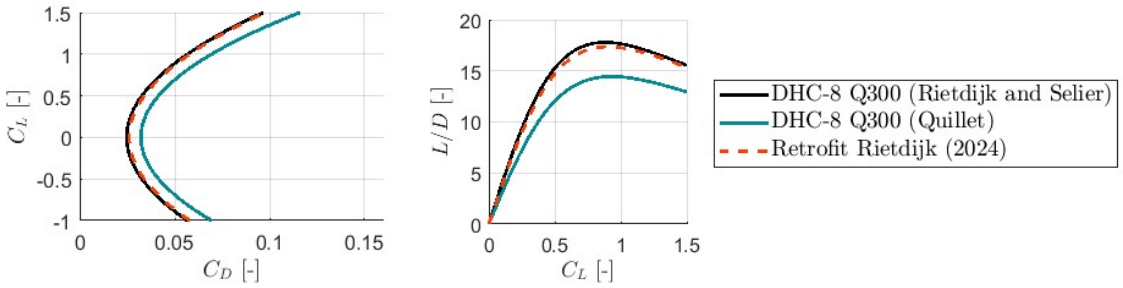

(a) Drag polar.

(b) Lift-to-drag ratio.

Figure 3.3: Differences in estimated drag polar and L/D for the original (black, blue lines) and retrofitted DHC-8 Q300 (red line), based on [10] and [87].

The maximum lift-to-drag ratio for the reference aircraft can be determined according to [10]:

$$\left(\frac{L}{D}\right)_{\text{max}} = \frac{1}{2\sqrt{C_{D_0} \cdot k}} \tag{3.10}$$

where C_{D_0} is the zero-lift drag coefficient and K is the induced drag coefficient. Assuming $C_{L,\text{cruise}} = 0.7$ for regional aircraft [153], lift-to-drag ratios are as shown in Table 3.2.

Table 3.2: Lift-to-drag ratios for the DHC-8 Q300 based on different sources.

Parameter	[10]	[87]	Retrofit in [10]
L/D_{cruise}	17.33	13.88	16.81
L/D_{max}	17.79	14.45	17.36

Rietdijk and Selier mention that their drag data is based on [157], where actually a $L/D_{\text{max}} = 15.46$ is shown instead of 17.79. However, their data for L/D might actually originate from the manufacturer. Therefore, the required power levels in this thesis, which are based on Quillet et al. [87], may be conservative. Quillet et al. base their drag calculations on extrapolation of data in the original Aircraft Flight Manual of the DHC-8 Q300.

3.2. Modeling Strategy

In this section, the modeling strategy will be presented. Since the objective is to develop a preliminary design and off-design model, an **object-oriented** approach will be used in **Matlab**. As such, a **steady-state lumped parameter model** suffices for design insights. Assumptions are grounded in validated studies and model components are verified where possible (see Section 4).

An overview of the lumped parameter model is given in Subsection 3.2.1, the optimization strategy is presented in Subsection 3.2.2, and general model limitations are discussed in Subsection 3.2.3.

3.2.1. Lumped Parameter Model Overview

In the literature study in chapter 2 several subsystems are discussed. Relations between these systems can be of the electrical, fluid/gas, thermal or mechanical type. Figure 3.4 shows in a block diagram an overview of the subsystems with corresponding relations. In this diagram:

- Solid blocks or lines represent subsystems or interactions included in the lumped parameter model.
- Dotted blocks or lines represent subsystems or interactions that are excluded from the lumped parameter model.

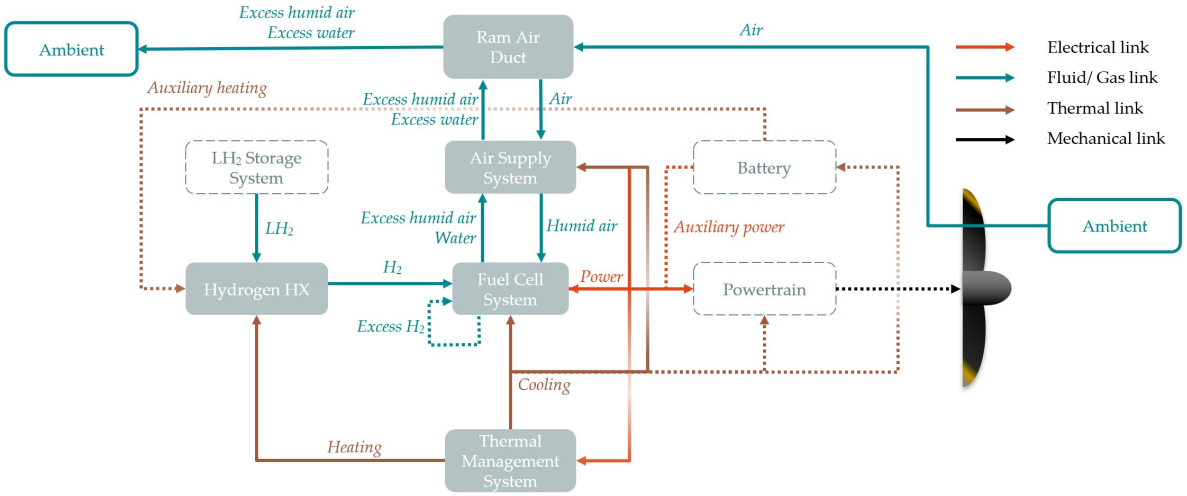

Figure 3.4: Block diagram of the propulsion system.

The fuel cell system is the primary source of electrical power, converting hydrogen and oxygen into electricity, water, and heat. It interacts with the Hydrogen Heat Exchanger (HX) for the hydrogen supply, the air supply system for humid air supply, and exhaust gas and water outflow, the thermal management system for heat dissipation, and the powertrain to deliver electrical power. Excess H_2 can be recirculated using a control mechanism or vented.

The LH_2 storage system stores liquid hydrogen at cryogenic temperatures. It interacts with the hydrogen HX, providing the hydrogen as a liquid at elevated pressure.

The hydrogen HX evaporates and heats the liquid hydrogen to desired input temperature and pressure for the fuel cell system. Waste heat from the fuel cell system is delivered to the hydrogen HX by the thermal management system.

The air supply system provides the necessary amount of humid pressurized air to the fuel cell system. Cooling from the thermal management system is required as the ingested ambient air heats up significantly in the compressor.

Air is ingested into the air supply system via the ram air duct intake. The ram air slows down the air flow before the radiator, possibly reducing overall duct drag by increasing temperature of the ram air and ejecting it through a nozzle, while keeping pressure drop low.

Aside from heating the hydrogen HX, cooling the fuel cell system and cooling the air supply system, the thermal management system is used to provide cooling to the battery and powertrain.

The powertrain consists of DC/AC inverters, a gearbox, electric motors, and other electrical components required to convert power from the fuel cell and battery into mechanical rotation of the propshaft, in turn providing thrust to

the aircraft. Part of the power is also provided to the air compressor and coolant pump.

The battery is necessary to assist the fuel cell system during fast transients, and to provide auxiliary heat to the hydrogen HX during start-up and in the case of freezing issues with the cryogenic H_2.

3.2.2. Optimization Strategy

In this section the overall optimization strategy is discussed. Since the ram air ducts can significantly increase aircraft drag, their frontal area should be minimized. As discussed in Section 3.3, the duct height will be fixed according to the height of the nacelle, leaving the duct width W_{duct} as the primary design variable.

Optimization W_{duct} is based on iterative narrowing of the bounds with convergence checks. A design solution converges when heat rejection from the system is sufficient. Between the bounds for W_{duct} a random guess is made. If the design converges, this is the new upper bound (ub) and a guess of $W_{\text{duct}} = (\text{ub} - \text{lb})/2$ is attempted. If a design does not converge, the current W_{duct} is the new lower bound (lb) and a a guess of $W_{\text{duct}} = (\text{ub} + \text{lb})/2$ is attempted. This continues till the offset between the current guess and the upper bound is smaller than the tolerance.

While this approach can be more time-consuming than using e.g. *fmincon*, the fact that this optimization problem has a double objective (minimizing W_{duct} and reaching design convergence) introduces complexities. With the current method, no weights or penalties have to be adjusted until model performance is as desired. As such, this optimization method is quite robust.

To visualize the optimization method put in place to minimize W_{duct}, an extended design structure matrix (XDSM) architecture is constructed, according to guidelines of Lambe and Martins [158] in Figure 3.5. The optimization is of Gauss-Seidel Multi-Disciplinary Analysis (MDA) type, where a number of analyses are computed in series until a consistent set of state variables is returned by the MDA. The state variable of interest is the pressure drop in the heat exchangers Δp_{HX}, namely in the radiator, intercooler and hydrogen heat exchanger. With guesses for Δp_{HX}, first the ram air duct (RAD) model is solved, giving as output the ram air properties. These ram air properties are then used as input for the fuel cell system (FCS) and air supply system (ASS) analysis, determining the total fuel cell power $P_{\text{FC,total}}$. With fuel cell power and efficiency η_{FC} known, coolant properties can be determined, including a temperature target $T_{\text{c,target}}$. This target is derived from the fuel cell coolant inlet temperature, and includes a margin for the coolant temperature difference in the intercooler.

After sizing the heat exchangers using *fmincon*, the actual temperature out of the radiator $T_{\text{c,actual}}$ is known. While the volume of the radiator is fixed according to the ram air duct width (see Section 3.3), the fins and tubes are optimized to minimize the absolute error:

$$\epsilon_{T_c} = |T_{\text{c,actual}} - T_{\text{c,target}}| \tag{3.11}$$

The optimization constraint is that this error ϵ_{T_c} requires to be smaller than a convergence tolerance. Given W_{duct} and the error ϵ_{T_c}, the optimizer makes a choice for the next iteration. Table 3.3 summarizes the optimization tolerances.

Table 3.3: Error Tolerances

Parameter	Value	Units
HX Pressure Drop Convergence Tolerance, $c_{\Delta p}$	1×10^{-1}	Pa
Fuel cell Power Convergence Tolerance, $c_{P_{\text{FC}}}$	1×10^{-1}	W
Coolant Temperature Convergence Tolerance, c_{T_c}	1×10^{-1}	K
Average Velocity in HX Convergence Tolerance, $c_{u_{0,\text{HX}}}$	1×10^{-4}	m/s
Duct Width Convergence Tolerance, $c_{W_{\text{duct}}}$	1×10^{-2}	m
Fixed Optimization Step Size	1×10^{-2}	-
Max Iterations	20	-

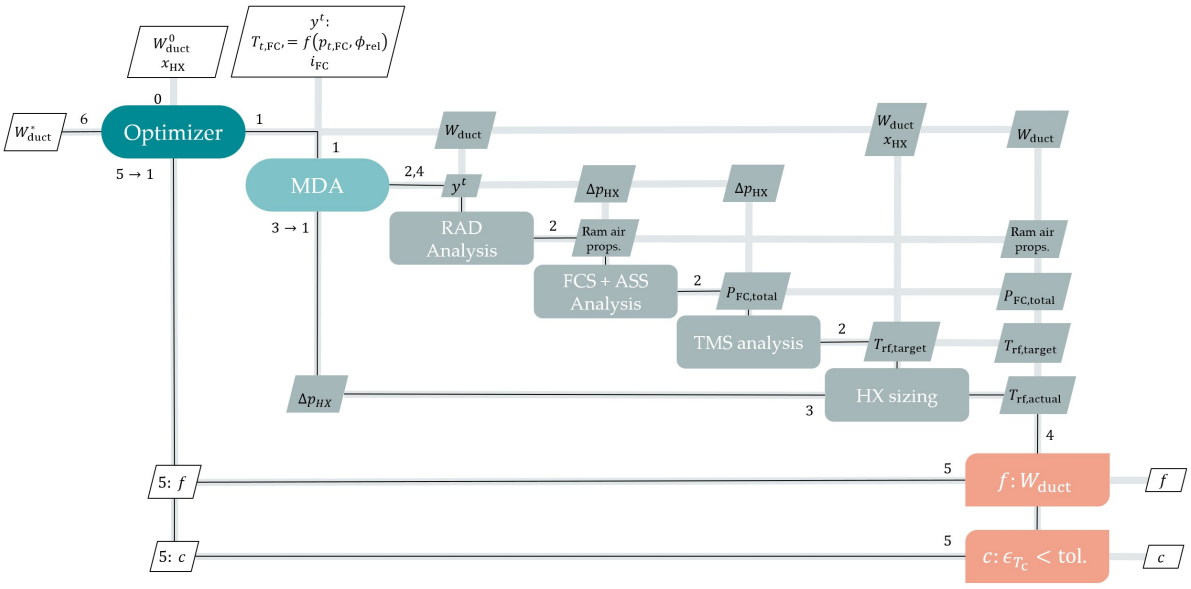

Figure 3.5: XDSM (eXtended Design Structure Matrix) architecture of the optimization strategy devised for W_{duct} and the preliminary sizing of the system.

3.2.3. General Model Limitations

When modeling complex systems, making assumptions always introduces limitations. The general limitations of the preliminary design model are highlighted below:

- The model is limited to steady state analysis. Transient analysis would allow for better fuel flow estimates, thereby affecting range. Payload is then again affected by a change in fuel mass and mostly tank mass. Also, a battery can be sized for fast transients.
- A worst case scenario that is currently not assessed is restart in cold conditions. The freezing point of water-eglycol 40/60 is significantly lower than water (-52.80°C), but as temperature drops below 0°C viscosity increases to more than 20 times that of water (Section 2.4.2). A dynamic analysis could highlight the response time required to restart engines in case of a fall-out. Potentially, battery mass must be increased to provide electric heating.
- Systems such as a battery, high-voltage electronics, control valves and tubing are not included in the preliminary sizing. Therefore, the payload budget includes the weight of these components and not only that for passengers, cargo and crew.
- Currently the point of mininum control velocity is regarded as most demanding during take-off for power and thermal management, based on expert knowledge at NLR. Potentially, the thermal management system might run into problems at start-up and lower speeds, requiring additional components such as fans or variable air intakes.
- The model is of the lumped parameter type, meaning properties inside components are averaged values between in- and outlet.
- Optimization tolerances are taken relatively broad to reduce simulation time of the preliminary sizing process.

3.3. Ram Air Duct Modeling

The ram air duct is a component necessary to house the radiator. In this model, it is assumed that per nacelle there are 2 ducts on each side. If designed carefully, the ram air duct can offset the additional drag by providing a small amount of thrust through the Meredith effect (see section 2.4.3). The station numbering and ram air duct components are visualized in Figure 3.6.

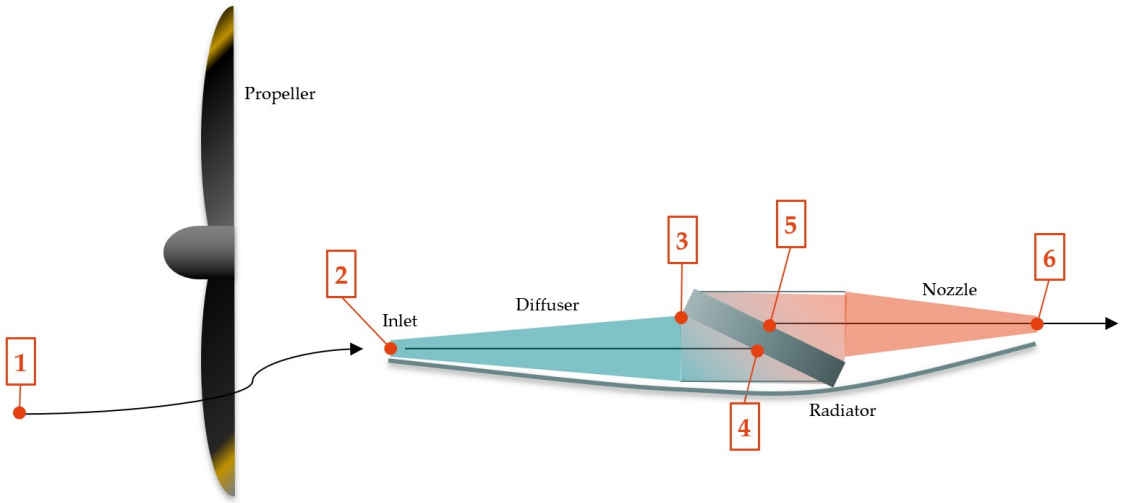

Figure 3.6: Ram air duct components and station numbering.

It is argued by Rietdijk and Selier (2024) that for radiators angled at 65° a straight ram air duct of 0.61x0.4m is necessary, increasing frontal area by 5% [10]. While in their study an ideal radiator is assumed, in this work the more realistic effectiveness-NTU method is implemented (see Section 3.6.5). As a result, when the effectiveness is less than a 100%, the radiator dimensions or flow rates in the radiator must be increased to maintain the overall heat flux. Therefore, the frontal area of the aircraft might be increased by more than 5%. For comparison purposes, initially it is assumed that the diffuser inlet and outlet area are equal, as in the paper by Rietdijk and Selier. At a later stage, this so-called diffuser area ratio AR could potentially be increased to generate a small amount of thrust.

Another factor of influence is the propeller in front of the ram air duct. This causes a velocity increase in the ram air duct from the free-stream conditions. This increase in velocity can be modelled by simple propeller equations [159]:

$$F_T = \frac{P_{\text{shaft}} \cdot \eta_{\text{prop}}}{u_\infty} \quad [\text{N}]$$

$$u_e = \sqrt{u_\infty^2 + \frac{2 \cdot F_{\text{T}}}{\rho_{\text{ambient}} \cdot A_{\text{prop}}}}$$

where η_{prop} is assumed to be 0.84 (Quillet et al. [87]). Shaft power P_{shaft} can be determined using the net required fuel cell output power for each mission scenario (Section 3.1) and the efficiencies for electric motors, gearboxes and inverters, as discussed in Section 2.6.

Realistically, not all air is ingested into the ram air duct inlet. The ratio between the actual ingested air and the air that would be ingested if streamlines were straight, can be called the Mass Flow Ratio MFR. The non-ingested air contributes to spillage drag, decreasing the L/D of the aircraft. Beltrame et al. argue that a mass flow ratio between 0.6-0.7 results in the smallest spillage drag [18]. However, given that the outside air is not modeled in detail, and that the propeller makes complicates the flow at the ram air duct inlet, a $MFR = 1.0$ is assumed for simplicity.

While a detailed drag analysis of the ram air ducts is not included, a rough estimate can be made. Two methods are considered. With the first one, the zero-lift-drag coefficient increases according to the increase in frontal area [10]. The parasite drag is directly affected by the area increase factor f_{duct}, according to:

$$C_D = C_{D_0} \cdot f_{\text{duct}} + k \cdot C_{\text{L}}^2 \tag{3.12}$$

This may be a very optimistic estimate, since the nacelle is assumed to be streamlined, while multiple components of drag are neglected as well as propeller blockage (see 3.3.1).

Alternatively, ram air thrust can be computed, resulting in drag when negative. With the assumption that $AR = 1$, the air velocity in the radiator remains high, causing a significant pressure drop. Therefore, the likelihood of some thrust generation seems small. This hypothesis can be verified by assuming an ideal nozzle, and determining the exit velocity. Thrust is then computed according to [159]:

$$F_{T,\text{duct}} = \dot{m}_{\text{ram air}}(u_{\text{exit}} - u_\infty) \tag{3.13}$$

The exit velocity from the nozzle can be determined given the static-to-total pressure ratio between stations 5 and 6, and the total temperature at station 5.

$$u_{\text{exit}} = \sqrt{2C_p T_{t,5} \cdot \left(1 - \frac{p_{0,6}}{p_{t,5}}^{\frac{\gamma-1}{\gamma}}\right)} \tag{3.14}$$

When the ram air ducts generate thrust in steady flight, propeller thrust may be decreased. On the other hand, additional thrust is required when the ducts generate drag. Although the potential in-/decrease in thrust is included in the model, an indication can be made in terms of the overall thrust ratio OTR:

$$\text{OTR} = \frac{F_{T,\text{ducts}}}{F_{T,\text{aircraft}}} \tag{3.15}$$

Note that this is different from the definition in Beltrame et al. (2024) [18], where TR is defined as the ratio between ram air thrust and gross drag.

In steady symmetric flight, thrust is approximately equal to the drag if the small angle approximation is used for the angle of attack, i.e. $T \approx D$ [160]. This means that:

$$T = D = C_{D_0}\frac{1}{2}\rho_{\text{ambient}}u_\infty^2 S + k \cdot C_L^2\frac{1}{2}\rho_{\text{ambient}}u_\infty^2 S \tag{3.16}$$

Assuming that the ram air ducts thrust only has effect on the parasite or zero-lift drag and not on the lift-induced drag (second term in Equation 3.16), yields the following:

$$\Delta C_{D_0} = -\frac{F_{T,\text{ducts}}}{\frac{1}{2}\rho_{\text{ambient}}u_\infty^2 S}, \tag{3.17}$$

where S = 56.1 m^2, according to Rietdijk and Selier [10].

To model the ram air duct, the following assumptions are implemented:

- $AR = 1.0$. For preliminary sizing of the ram air duct, it is assumed that the diffuser is straight up to the radiator. Possibly, at a later stage, the area ratio can be increased up to $AR = 3.8$, which is the optimal diffuser area ratio for small thrust generation, according to Beltrame et al. [18].
- $\theta = 70°$. This heat exchanger tilt angle maximizes air inflow area, while having small additional pressure drop due to air flow direction change [18]. Beyond this angle pressure drop increases drastically. The pressure drop is assumed to be 15% larger due to the inclination of the radiator, derived from Figure A.1.
- $MFR = 1.0$. Streamlines do not in front of around the inlet.
- The diffuser is assumed to have no losses. The length of the diffuser is therefore not modelled.
- The length of the radiator is assumed to be 65% of W_{duct}, derived from Figure 2.24. Note that duct width is assumed equal to the diffuser outlet width. The radiators are angled into the nacelle.
- The duct height is fixed to $H_{\text{duct}} = 0.61$ m, which is the available space next to the nacelle of the DHC-8 Q300 aircraft [10] (see Appendix B.3 as well).
- The radiators orientation is rotated 90° compared to the publication by Rietdijk and Selier, [10]. Also the ram air duct is assumed to be integrated partly in the nacelle. As such, a slightly larger frontal area is obtained, while minimizing duct width.
- The wall thickness t_{duct} of the duct is assumed as 2 mm [161], with as material Aluminum 2024-T3, often used for fuselage and wing skins.
- The length of the duct L_{duct} is assumed as 4.22 m, according to Figure 2.23.

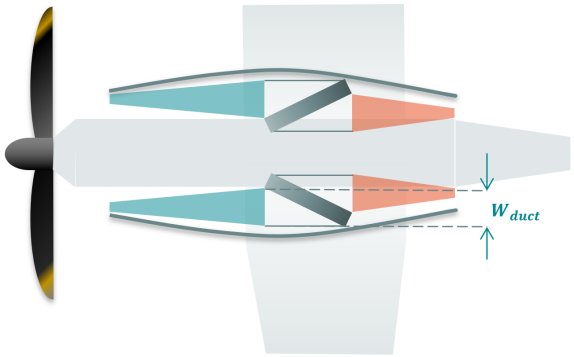

Figure 3.7: Ram air duct integration in the nacelle and duct width.

The parametrization for the ram air duct model and integrated radiator is shown in Figure 3.8. The width of the radiator is directly determined by θ,

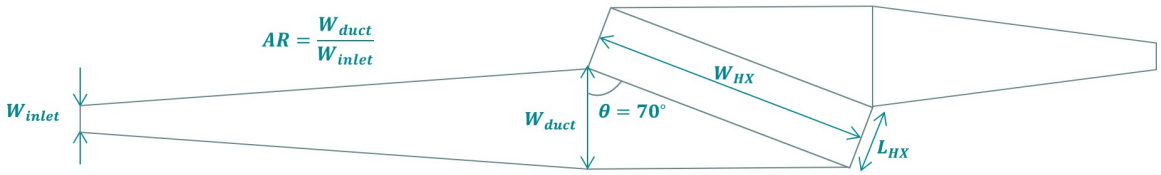

Figure 3.8: Ram air duct parametrization

The mass of the ducts can be estimated, using the geometrical and material assumptions, as:

$$m_{\text{duct}} = \rho_{\text{Alu 2024-T3}} \cdot L_{\text{duct}} t_{\text{duct}} \cdot (H_{\text{duct}} + 2W_{\text{duct}}) \tag{3.18}$$

For further details on calculation of thermodynamic properties of the air inside the ram air duct, see Appendix A.1.

3.3.1. Ram Air Duct Model Limitations

The following factors, which may affect the influence of the ram air duct on drag and thrust of the aircraft significantly, are left out of consideration:

- **Spillage drag** . This is consistent with the assumption of no external diffusion, i.e. a the mass flow ratio MFR = 1. It is uncertain whether this assumption is valid during all mission phases, affecting drag, required power and range.
- The effect of **air inflow angle**. This changes during flight, increasing spillage drag.
- The effects on drag and thrust of the ram air intakes being in the **propeller streamtube** is not considered. **Spillage drag** might be increased and increased propeller blockage can lead to **reduced thrust**. Also, the mass flow through the ducts may be lower than anticipated, as the ideal propeller downstream velocity may not be fully achieved by the time the air reaches the ram air duct inlet. During cruise, the air velocity increase behind the propeller is approximately 6
- **Interference drag** of the ram air ducts with the nacelle and wing is not considered.
- **Skin friction drag** of the duct panels is not considered.
- Also, the adverse effects of **drag during take-off and top-of-climb**, possibly increasing required power, are not assessed.
- **Losses in the diffuser and nozzle** due to boundary layers are neglected and uniform velocity is assumed. In Section 4.1 it is assessed to what extent this assumption is valid.

3.4. Fuel Cell System Modeling

Since the objective of this thesis is not to perform a preliminary design of the fuel cell, but of the balance-of-plant, data from a recent fuel cell model publication is implemented [17]. It provides the most complete data for optimal fuel cell temperature, pressure, current density and air excess ratio, validated for the largest fuel cell (ElringKlinger NM5 300) and air supply system testbed documented in literature [17]. Nevertheless, the reported power (65 kW) is still an order of magnitude smaller than that considered in this thesis.

The fuel cell is assumed to operate at a uniform temperature. As all inlet streams (air and hydrogen) will quickly reach this operating temperature upon entering the fuel cell, the temperature of the inlet streams is modeled equal to the stack operating temperature. While in the reference model, the dew point of the inlet air is 65°C (Figure 2.15), it is assumed that the inlet air has 98% relative humidity at the fuel cell's operating temperature. This simplifies the modeling of humidification. Furthermore, relative humidity is interpolated according to the black line representing the reference model data in Figure 3.9. As such, a relationship between fuel cell temperature, reactant inlet temperature, fuel cell pressure and relative humidity is obtained, for an air excess ratio of $\lambda_{\text{air}} = 1.7$, as shown in Figure 3.9

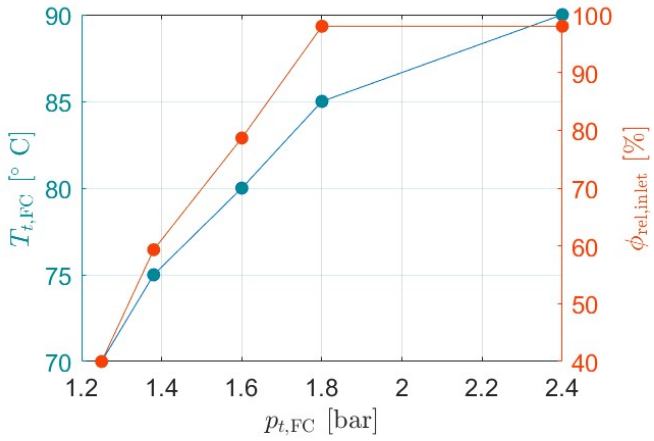

Figure 3.9: Modelled fuel cell inlet temperature, pressure and relative humidity.

Furthermore, data from Figure 2.13 is inter-/extrapolated to generate the data maps shown in Figure 3.10, highlighting the relation between current density i_{FC}, pressure p_{FC} and cell voltage U_{ref}. The data map for power density P/A is obtained by realizing that:

$$P/A = U_{\text{cell}} \cdot i_{\text{FC}} \quad [\text{W/cm}^2] \tag{3.19}$$

In the data maps, the '+' signs represent the original data from the publication by Schröter (2023). Stack voltage and current are converted to cell voltage and current density using the fact that the number of plates is 300 and the active area is 190cm^2.

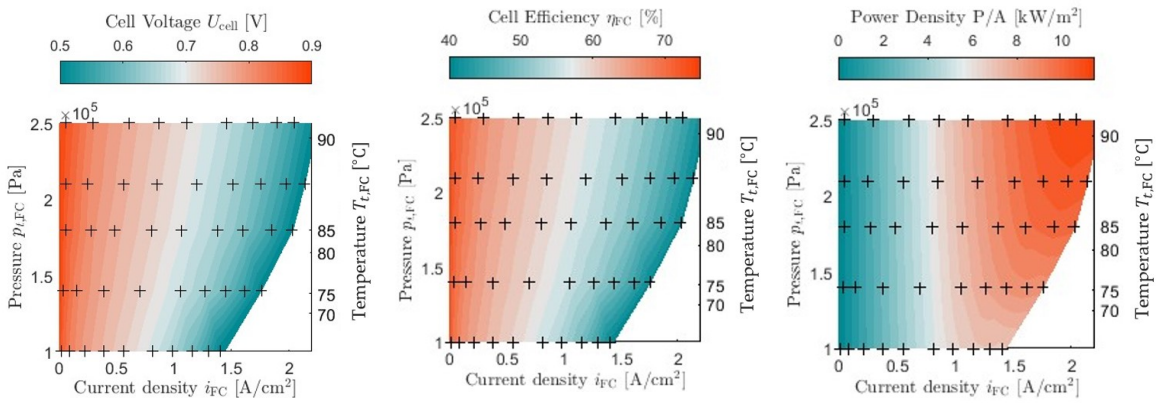

(a) Fuel cell voltage. **(b)** Fuel cell efficiency. **(c)** Fuel cell power density.

Figure 3.10: Performance maps of the ElringKlinger NM5 300 fuel cell, adapted from Schröter (2023) [17]. Adapted data points are shown as '+' signs, while the contours represent the interpolated data.

Fuel cell efficiency is defined by:

$$\eta_{\text{FC}} = \frac{U_{\text{cell}}}{U_{\text{ref}}}; \tag{3.20}$$

where the reference cell voltage of $U_{\text{ref}} = 1.23V$, as in the publication by Schröter [17]. This value corresponds to the higher heating value (HHV) of hydrogen. As such, it is assumed that the water vapor in the exit air condenses, providing a more realistic measure of fuel cell efficiency than when using the LHV [14].

Mass flows of the reactants and products inside the fuel cell are determined taking the LHV of hydrogen, after which mass flow of the other species is determined from the stoichiometry in the fuel cell reaction equation.

$$2H_2 + O_2 = 2H_2O \tag{3.21}$$

$$\dot{m}_{H_2} = \frac{P_{\text{FC}}}{LHV_{H_2}\eta_{\text{FC}}} \tag{3.22}$$

$$\dot{m}_{O_2} = \frac{\dot{m}_{H_2} M_{O_2}}{2M_{H_2}} \tag{3.23}$$

$$\dot{m}_{N_2} = \frac{\dot{m}_{O_2}(1 - f_{O_2})}{f_{O_2} M_{O_2} M_{N_2}} \tag{3.24}$$

$$\dot{m}_{\text{air}} = \lambda_{\text{air}}(\dot{m}_{O_2} + \dot{m}_{N_2}) \tag{3.25}$$

$$\dot{m}_{H_2O} = \frac{\dot{m}_{O_2}}{2} + \dot{m}_{H_2} \tag{3.26}$$

Where $\dot{m}_X$ represents the mass flow of species X in kg/s, P_{FC} the DC power delivered by the fuel cell, M_X the molar mass of species X in g/mole, f_{O_2} the fraction of oxygen in air and λ_{O_2} the air excess ratio.

For calculation of the relative humidity exiting the fuel cell, $\dot{m}_{H_2O}$ is added to the mass fraction of water already present in the flow. Specific calculations for relative humidity can be found in Section 3.5.4.

Total available fuel cell power P_{FC} is determined by taking into account the net power $P_{\text{FC,net}}$ delivered to the powertrain for thrust, and power required for the compressor P_{comp}. As discussed in section 3.6.3, required pump power is negligible compared to the other factors. Other ancillary systems requiring electrical power are also considered to require negligible amounts of power. That gives:

$$P_{\text{FC}} = P_{\text{FC,net}} + P_{\text{comp}} \tag{3.27}$$

Active plate area and fuel cell mass are determined according to [17]. The mass is based on linear extrapolation of the ElringKlinger NM5 stack.

$$A_{\text{FC}} = \frac{P_{\text{FC}}}{i_{\text{FC}}\eta_{\text{FC}}U_{\text{ref}}} \quad [\text{cm}^2] \tag{3.28}$$

$$m_{\text{FC}} = \frac{4.9\ [\text{kg/m}^2]}{10^4} \cdot A_{\text{FC}}[\text{kg}] \tag{3.29}$$

The workflow diagram for the fuel cell system is shown in Figure 3.11.

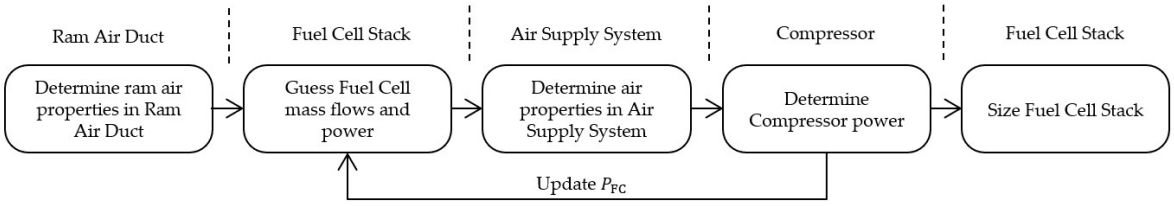

Figure 3.11: Fuel cell system workflow diagram.

3.4.1. Fuel Cell System Model Limitations

The limitations to the fuel cell system model are highlighted below.

- The assumption that the air and hydrogen fuel cell inlet temperatures are approximately valid due to rapid heat transfer within the fuel cell neglects any transient effects or temperature differences in the inlet streams. As a result, the intercooler needs to cool down the air stream less (to the fuel cell temperature instead of to 65°C), reducing its size. Also, humidifier size increases, as air temperature is higher (70-90°C) and more water has to be added to reach 98% humidity.
- The mass of the fuel cell system is based on linear extrapolation of the ElringKlinger NM5 stack data. This fuel cell has a power output an order of magnitude lower than required (65 kW vs. approximately 2 MW). While this fuel cell has relatively high power density at 2.4 kW/kg, compared to current state of the art, larger specific powers might be possible in the near future.
- Hydrogen is assumed to be available at the desired pressure in the fuel cell (equal pressure as the air), as it is stored at about pressure 4 bar. Also, it is currently assumed that the fuel cell data accounts for all losses in the fuel cell, with the input fuel and air entirely reacting.

3.5. Air Supply System Modeling

A general overview of the air supply system is shown in Figure 3.12. Air is assumed to enter via the ram air duct, eliminating the need for an additional inlet on the engine nacelle. Just after the diffuser, air is filtered. Before entering the fuel cell, the air needs to be compressed, especially at altitude as air pressure drops. As air is compressed in the compressor, internal energy and temperature rise, causing a drop in relative humidity and a temperature too high for its use in the fuel cell. For this reason, an intercooler and humidifier are added. As water is produced in the fuel cell, the humidified air can be re-used in the humidifier to make the incoming dry air wet, before being ejected through the nozzle to the environment. Part of the electricity generated by the fuel cell is used to power the compressor. In the following subsections, the models of the various components are discussed in detail.

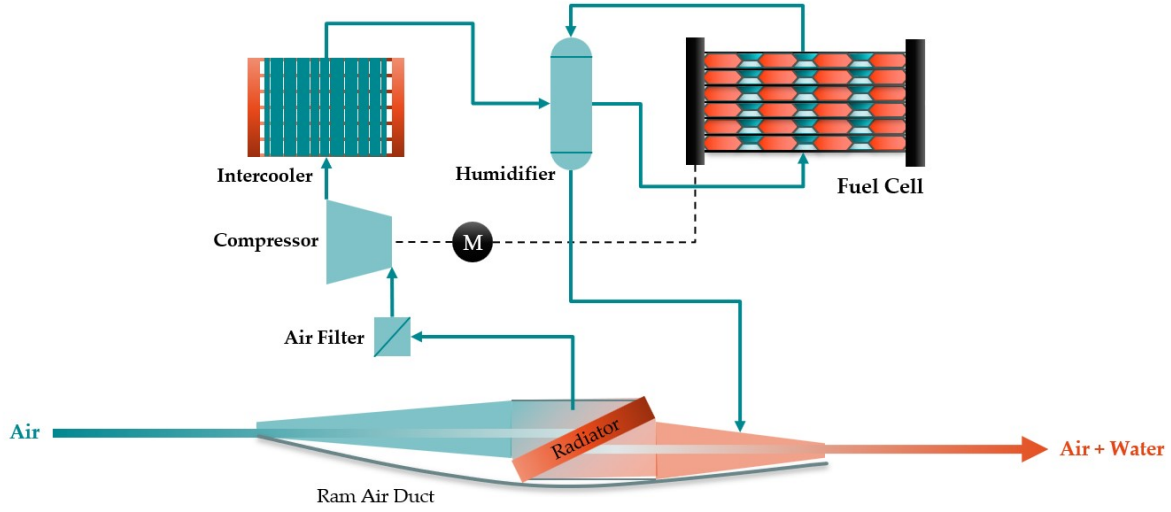

Figure 3.12: Diagram of the air supply system.

A workflow diagram for calculation of the air properties in the air supply system is shown in Figure 3.13. Note that sizing of the intercooler can be done only after sizing the thermal management system, as discussed in Section 3.6.

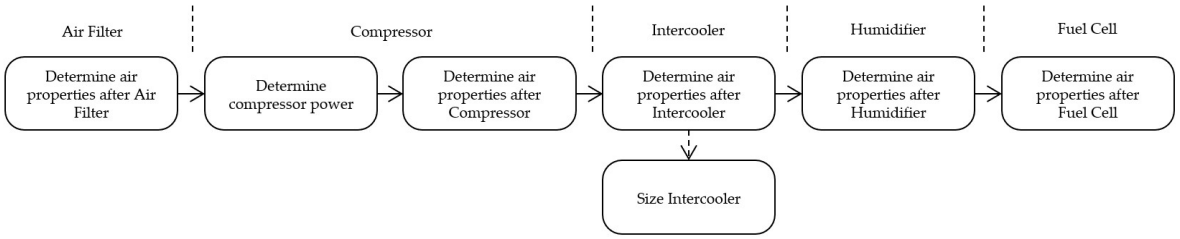

Figure 3.13: Air supply system workflow diagram.

3.5.1. Air Filter Modeling

The air intake of the the air supply system can be placed in the ram air duct after the diffuser. This eliminates the need for additional inlets on the nacelle. Air inlet pressure losses are neglected. Before entering the compressor, air needs to be properly filtered to not damage the fuel cell membrane. One of the few fuel cell grade off-the-shelf air filters are manufactured by Freudenberg [162]. Data for these filters is shown in Figure 3.14.

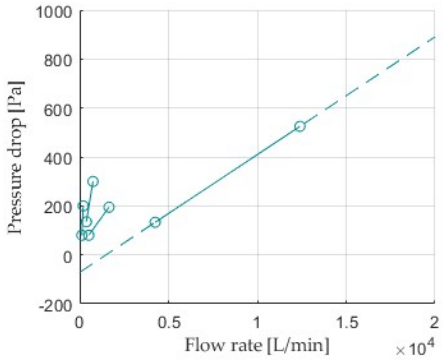

Figure 3.14: Off-the-shelf air filter data

It is assumed that pressure drop can be extrapolated based on data for the largest air filter, which is rated for up to 1.25e4 LPM. For a fuel cell available power output of $2MW$ (half the aircraft), with efficiency of about 50%, the required mass flow of air is about 2 kg/s ≈ 2e6 LPM at the cruise design point 3.1, according to equation 3.25. It is assumed that multiple of these filters are in parallel, only increasing required area and not filter thickness. As such, the pressure drop is kept small with Δp_{filter} =520 Pa at the maximum expected power in top-of-climb conditions.

The mass of the filter is estimated using the following relation [68]:

$$m_{\text{filter}} = 6\ [\text{kg}/(\text{kg}/\text{s})] \cdot \dot{m}_{\text{air}} \tag{3.30}$$

3.5.2. Compressor Modeling

As discussed in Section 2.3.5, a centrifugal compressor is the preferred choice for the air supply system due to its high performance in applications with smaller air flows. It is assumed that one single-stage compressor per nacelle is required. A low-fidelity approach is chosen for the compressor, based on polytropic efficiency definition, which is often used in centrifugal compressor modelling [163]. Compressor efficiency and pressure ratio also vary with on ingested mass flow and rotational speed, but this is neglected. Polytropic efficiency is particularly useful for modeling single stage efficiency, as it is consistent with the actual compression process trajectory in an enthalpy-entropy ($h - s$) diagram, as shown in Figure 3.15.

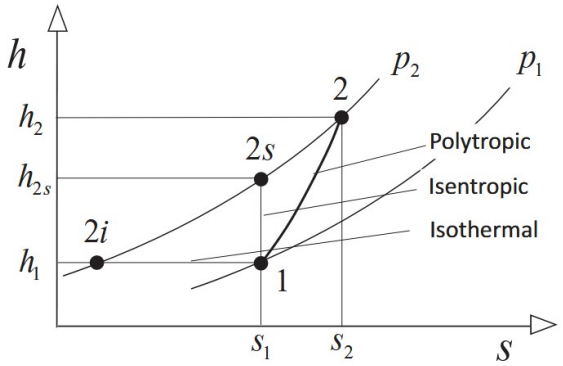

Figure 3.15: Different efficiency definitions for centrifugal compressors.

By knowing the inlet pressure of the compressor, and setting the required outlet pressure equal to the fuel cell inlet pressure minus the losses in the intercooler and humidifier, the required power of the compressor can be determined.

First, the pressure ratio β and isentropic outlet temperature $T_{t,\text{is}}$ are determined.

$$\beta = \frac{p_{t,\text{out}}}{p_{t,\text{in}}} \tag{3.31}$$

$$T_{t,\text{out,is}} = T_{t,\text{in}} \cdot \beta^{\frac{\gamma-1}{\gamma}} \tag{3.32}$$

In reality, the temperature increase will be non-isentropic, adding to the temperature increase. Polytropic efficiencies of close to $\eta_{\text{poly}} = 90\%$ are feasible for high efficiency centrifugal compressors [164]. However, the compressor will have to operate in a wide range of conditions, due to differences in air mass flow and pressure across different mission phases. Therefore a more conservative value of $\eta_{\text{poly}} = 80\%$ is assumed. According to Cohen et al. (1973), polytropic efficiency relates to isentropic compressor efficiency as,

$$\eta_{\text{is}} = \frac{\beta_{\text{comp}}^{\frac{\gamma-1}{\gamma}} - 1}{\beta_{\text{comp}}^{\frac{\gamma-1}{\gamma \cdot \eta_{\text{poly}}}} - 1} \tag{3.33}$$

From this, actual enthalpy and temperature at the compressor outlet ($h_{\text{out}}, T_{t,\text{out}}$) and compressor power P_{comp} are determined according to:

$$h_{\text{out,is}} = C_p \cdot T_{t,\text{out,is}} \tag{3.34}$$

$$h_{\text{out}} = \frac{h_{\text{out,is}} - h_{\text{in}}}{\eta_{\text{is}}} + h_{\text{in}} \tag{3.35}$$

$$T_{t,\text{out}} = \frac{h_{\text{out}}}{C_p} \tag{3.36}$$

$$P_{\text{comp}} = (h_{\text{out}} - h_{\text{in}}) \cdot \dot{m}_{\text{air}} \tag{3.37}$$

To compare mass flow rates between different operating conditions, corrected mass flow is usually computed:

$$\dot{m}_{\text{corr}} = \dot{m}_{\text{air}} \sqrt{\frac{T_{\text{ref}}}{T_{\text{t}}}} \cdot \frac{p_{\text{t}}}{p_{\text{ref}}} \tag{3.38}$$

In cruise, pressure ratios up to 6-7 can be required from the compressor, depending on the fuel cell pressure setting. With estimated mass flow per compressor of up to 2 kg/s (see Section 3.5.1), this means that such a compressor can operate in the transonic regime. This is based on a paper by Zangeneh et al. [165], in which a centrifugal impeller is designed for pressure ratios of 5-6 and a corrected mass flow of > 2 kg/s, which tip Mach numbers of $M > 0.7$. Given a tip radius of 112 mm, a hub radius of 30 mm and a blade height at the exit of 8.7 mm, with material density of 4430 kg/m^3 (Ti6Al4V), the mass of the impeller is about 1.3 kg. The impeller design is visualized in Figure 3.16.

Centrifugal compressor assemblies for fuel cells exist, but for much lower mass flow ratings, such as a compressor by Fischer AG [166] (see Figure 3.17) It is rated for only 200 g/s and 32 kW, but the entire assembly is about 18 kg for a impeller diameter of about 260 mm. Given that this is just larger than the transonic impeller described before, the compressor mass is conservatively estimated at 30 kg.

Figure 3.16: Transonic impeller design by Zangeneh et al. [165].

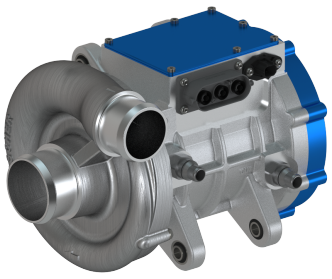

Figure 3.17: 32 kW centrifugal compressor assembly for fuel cells [166].

3.5.3. Intercooler Modeling

From the literature study it became clear that air-to-air and liquid-to-air intercooling systems are both commonly implemented in fuel cell air supply systems. Integrating the intercooler in the coolant cooling loop saves the need for additional cooling air. Also, the coolant will have a larger thermal capacity and heat transfer coefficient than ambient air. This will result in a much lighter intercooler design. Therefore a liquid-to-air intercooler is the preferred choice.

The intercooler is modelled as a heat exchanger with tubes on the coolant side and rectangular fins on the air side. The effectiveness-NTU method for unmixed-unmixed channels is implemented [167] (see Appendix A.2). The intercooler is optimized using constrained gradient-based interior-point minimization (*fmincon* [168]). The objective is to minimize $|T_{\text{out,air}} - T_{t,\text{FC}}|$, i.e. the outlet temperature of the air must be approximately the fuel cell temperature. A tolerance of 0.1 K is considered acceptable to reach the objective. The optimization settings are as follows:

Table 3.4: Intercooler Optimization Settings

Setting	Value
Algorithm	Interior-Point
Function Tolerance	0.1
Optimality Tolerance	0.1
Step Tolerance	0.02

Furthermore, to decrease the simulation time of the duct width optimization problem (see Section 3.2.2), the coolant temperature at the intercooler inlet is assumed to be at a constant delta T below the fuel cell temperature. The maximum heat flow in the intercooler is estimated at

$$Q_{\text{IC}} = \dot{m}_{\text{air}} C_{p,\text{air}} \Delta T_{\text{air}} = 200\text{kW}, \tag{3.39}$$

where,

- $\dot{m}_{\text{air}}$ is estimated to be 2 kg/s at most (see Section 3.5.1
- $C_{p,\text{air}} = 1000$ J/(kg K
- $\Delta T_{\text{air}} = 100$ K.

Using an estimated coolant mass flow $\dot{m}_c$ =60 kg/s per engine and $C_{p,c} = 3300$ J/(kg/K) (see Section 3.6.1), ΔT_c can be approximated at

$$\Delta T_c = \frac{Q_{\text{IC}}}{\dot{m}_c C_{p,c}} = 1K. \tag{3.40}$$

Conservatively, $\Delta T_c = 2$K is assumed.

Figure 3.18 shows the parametrization of the intercooler model. The five design variables are the heat exchanger height H, width W, length L, fin height h_{fins} and fin spacing d_{fins}. Bounds for these design variables are introduced in Section 5.2. Fin thickness t_{fins} and tube thickness t_{tube} are assumed constant at 0.15 mm, common dimensions in heat exchanger manufacturing [118]. Tube diameter t_{tube} can be optimized to minimize pressure drop while maximizing heat transfer coefficient, and is assumed to be at least 1.5 mm [118].

The number of sections, fins and tubes are determined according to the following geometrical relations:

$$N_{\text{sections}} = \frac{H}{2h_{\text{fins}} + d_{\text{tube}} + 2t_{\text{tube}}} \tag{3.41}$$

$$N_{\text{tubes}} = \frac{L}{d_{\text{tube}}} \cdot N_{\text{sections}} \tag{3.42}$$

$$N_{\text{fins}} = \frac{W}{d_{\text{fins}} + t_{\text{fins}}} \cdot N_{\text{sections}} \tag{3.43}$$

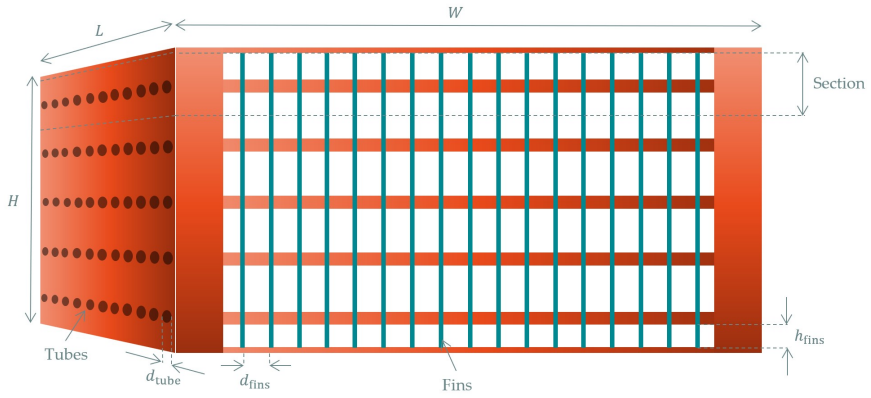

Figure 3.18: Intercooler parametrization.

The heat transfer coefficient and pressure drop in the tubes are modelled using equations in Appendix Section A.3, and for the fin side in Appendix Section A.4. Since the properties inside the intercooler are based on average properties between inlet and outlet, a few iterations are required to make $u_{0,\text{avg}}$, ρ_{avg} and $C_{p,\text{avg}}$ converge. Note that while all fins between sections are connected, the fin height is assumed as visualized in Figure 3.18. A workflow diagram for the intercooler sizing method is shown in Appendix Section B.2.

The density of the Aluminium 3003 alloy, $\rho = 2730\ \text{kg/m}^3$, is used to determine the mass of the fins and tubes. Since the nacelle of the DHC-8 Q300 is 0.8m wide, and the height is approximately 1.4, the dimensions of the intercooler will be limited to 0.8x1.4x0.8m in length, width and height [10].

3.5.4. Humidifier Modeling

Given that the inlet relative humidity of the fuel cell should be near 100% for optimal performance (see Section 3.4), a humidifier is an essential component. Furthermore, the humid flow exiting the fuel cell can be reused effectively. The humidifier increases the relative humidity to the desired inlet value of the fuel cell. The pressure drop is assumed independent of the desired humidity. Also, the device is assumed adiabatic. To determine the pressure drop, data from off-the-shelf humidifiers is used. The largest humidifier currently available is produced by Fumatech, having a pressure drop of 8 kPa for a volume flow of $V = 5000$ LPM [169].

The volume flow for the cruise mission point is several orders of magnitude larger, a rough estimation results in $V = 200,000$ LPM (see Section 3.5.1). It is assumed for pressure drop and mass estimations that the required amount of humidifiers is installed in parallel. This results in the same pressure drop of 8 kPa. For a mass estimation, it is assumed that the surface area required for humidification increases with the square root of the volume flow, while membrane thickness remains fixed. According to data by Fumatech humidifiers, the mass is estimated using:

$$m_{\text{humidifier}} = \sqrt{\frac{6.2\ \text{kg}}{5000\ \text{LPM}} \cdot \dot{V}_{\text{air}}} \tag{3.44}$$

To determine the relative humidity along the air supply system, first the partial pressure of water vapor in the air is determined by:

$$p_{\text{H}_2\text{O}} = \frac{p_{v,\text{air}}}{p_{t,\text{air}}}, \tag{3.45}$$

where $p_{v,\text{air}}$ is the saturation pressure of water vapor in the air and $p_{t,\text{air}}$ is the total pressure. The saturation pressure of water vapor in the air is determined using the Stull empirical relation valid from $T = -17.25°\text{C}$ to $T = 100°\text{C}$ [170].

$$p_{v,\text{air}} = 10^{\left(4.6543 - \frac{1435.264}{T\,[\text{K}] - 64.848}\right)}\ [\text{bar}] \tag{3.46}$$

This relation of temperature and vapor pressure is shown in Figure 3.19 as well.

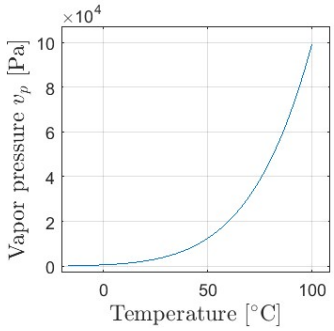

Figure 3.19: Vapor pressure empirical relation from Stull (1947) [170].

Assuming the relative humidity of the outside air constant at $\phi_{\text{rel}} = 50\%$ the mole fraction of water vapor x_{H_2O}, molar mass of moist air $M_{\text{moist air}}$ and mass fraction of water vapor w_{H_2O} can be determined. w_{H_2O} remains constant unless water is added. This gives the following relations:

$$x_{H_2O} = \frac{\phi_{\text{rel}}}{100} \cdot p_{H_2O} \tag{3.47}$$

$$M_{\text{moist air}} = x_{H_2O} M_{H_2O} + (1 - x_{H_2O}) M_{\text{air}} \tag{3.48}$$

$$w_{H_2O} = \frac{x_{H_2O} \cdot M_{H_2O}}{M_{\text{moist air}}} \tag{3.49}$$

3.5.5. Air Supply System Model Limitations

This section highlights the limitations of the air supply system model.

- Air inlet and tubing pressure losses are not modelled, as system layout is unknown in a preliminary design stage. Increased pressure loss might impact the required pressure ratio by the compressor.
- Compressor efficiency is assumed constant. In reality, the compressor can have decreased performance in different operating regimes, especially when operation at different pressure ratios and mass flow is required.
- The mass of the humidifier is based on an increase in humidification membrane area due to increased volume flow, scaling with the square of volume flow per mass. However, the order of magnitude is much larger than the reference off-the-shelf component, potentially resulting in under- or overestimations.

3.6. Thermal Management System Modeling

A general overview of the thermal management system (TMS) for one engine is shown in Figure 3.20. Most of the heat needs to be removed from the fuel cell (O(2 MW)), while a smaller amount of air needs to be cooled in the intercooler (O(200 kW) in cruise). Some of the heat can be rejected by heating and evaporating the hydrogen in the H2HX (O(100 kW)), while the rest of the heat has to be rejected in the radiators (O(1 MW) per radiator).

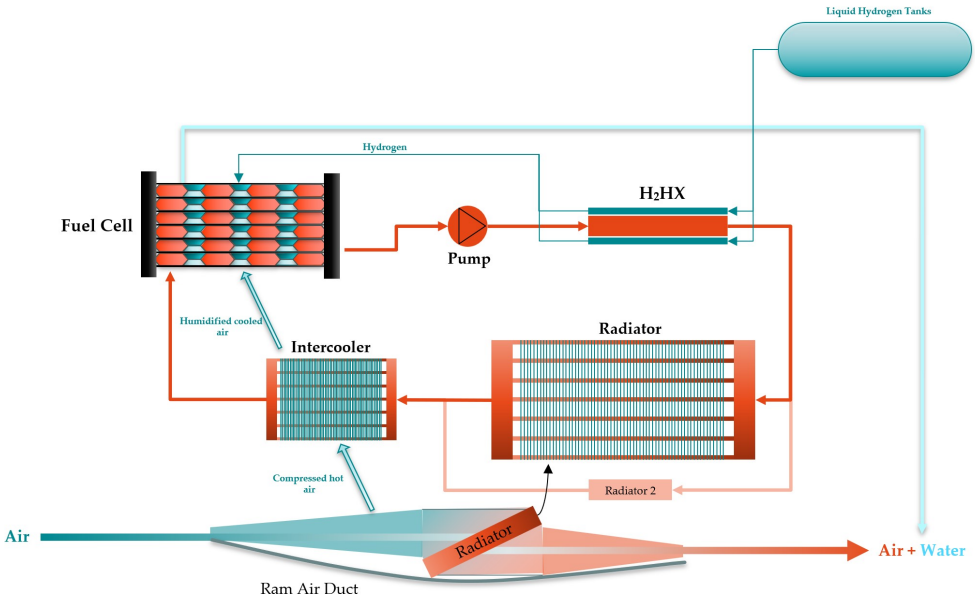

Figure 3.20: Diagram of the thermal management system

The H2HX is placed before the radiator, such that coolant temperature is highest to minimize the risk of freezing due to system malfunctioning. The coolant mass flow is split between the radiators in two ram air ducts on either side of the nacelle. The coolant flow then recombines to cool compressed hot air in an intercooler, before entering the fuel cell. The pump is placed downstream of the fuel cell to lower the coolant pressure between the membranes, lowering mechanical stresses. In the following subsections, the modeling methodology for each component is discussed in more detail.

The addition of an accumulator to the thermal management system is neglected, as well as coolant tubing. Both are assumed to have minimal impact on system mass compared to the main system components. In a two-phase cooling system, the impact of an accumulator would be much larger, due to the difference between phase densities.

A workflow diagram of the TMS model is shown in Figure 3.21. First, temperature increase and heat flux in the intercooler are estimated, based on a coolant mass flow rate guess. Then, the required coolant mass flow rate in the fuel cell is determined, and coolant temperature difference in the intercooler is iterated based on the new mass flow rate. Afterwards, the pump pressure rise is updated from the pressure drop guesses in the components, which are iterated within the overall solver (see Figure 3.5). After determining the temperature differences in the H2HX and radiator, the average temperatures and specific heat coefficients in the components are iterated. Lastly, the radiator can be sized.

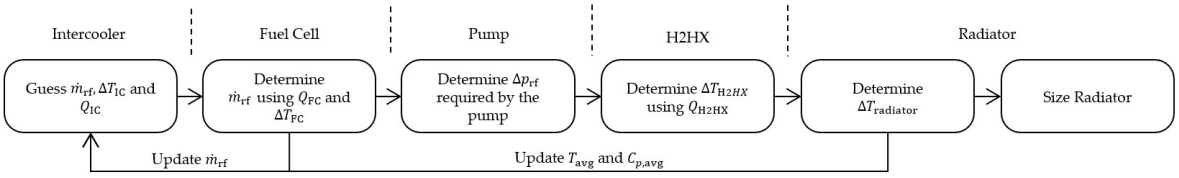

Figure 3.21: Thermal management system workflow diagram.

3.6.1. Coolant Selection

Table 3.5 shows the four best performing cooling fluids and their properties, based on criteria introduced in Section 2.4.2. The coolant properties are modeled using a software called REFPROP, which has a built-in function for Matlab [123]. This analysis was done for a heat load of $Q = 4$ MW, which is near the estimated worst case scenario for the entire aircraft, assuming $\eta_{FC} = 50\%$ (see Section 3.1).

Table 3.5: Comparison of different fluids and their properties.

Fluid Name	Water-Eglycol 50/50	Water-Eglycol 40/60	Methanol	Ethanol
$p_{\text{min, system}}$ [bar]	7.81×10^{-1}	7.06×10^{-1}	3.52	2.23
T_{triple} [°C]	-36.80	-52.80	-97.39	-114.00
T_{crit} [°C]	399.96	405.79	240.38	241.71
C_p [kJ/(kg K)]	3.47	3.31	2.96	2.95
ρ_l [kg/m^3]	1479.00	1479.00	732.98	735.15
μ_l [Pa s]	1.76×10^{-3}	2.04×10^{-3}	2.75×10^{-4}	4.31×10^{-4}
k_l [W/(m K)]	0.461	0.419	0.190	0.154
CTE [1/K]	6.59×10^{-4}	6.63×10^{-4}	1.43×10^{-3}	1.36×10^{-3}
$\dot{m}$ [kg/s]	115.33	120.69	134.97	135.78
$\dot{V}$ [L/s]	77.98	81.60	184.14	184.69
d_{tube} [mm]	172.70	176.20	203.20	203.60
NFPA Health	2	2	1	1
NFPA Flammability	1	1	3	3
NFPA Stability	0	0	0	0
M_{pump}	1.91	1.66	1.00	0.88
$M_{\text{accumulator}}$	3.11	2.82	1.00	1.09
$M_{\Delta p}$	0.62	0.59	1.00	0.95
M_{weighted}	**1.88**	**1.69**	**1.00**	**0.97**

While water-eglycol 50/50 has the highest M_{weighted}, its critical temperature T_{crit} is very close to the ambient temperature at cruise altitude for regional aircraft. Methanol and Ethanol could provide a solution to this, but these fluids have a lower M_{weighted}, relatively high NFPA rating and a minimum operating pressure above desirable fuel cell pressures (1.25 - 2.5 bar).

Therefore, water-eglycol 40/60 presents the best characteristics, with acceptable critical temperature, high figure of merit, low minimum operating pressure and low NFPA. Increasing the mass fraction of Ethylene-Glycol further is not recommended due to increased viscosity (see Section 2.4.2) and smaller M_{weighted}. The GWP of Ethylene-Glycol is not more than 10 times that of CO_2 [171].

3.6.2. Fuel Cell Thermal Modeling

From a thermal perspective, the fuel cell is modelled as a device from which a certain amount of heat Q_{FC} has to be removed, depending only on fuel cell power and efficiency as discussed in Section 3.4. Total heat is then equal to:

$$Q_{FC} = P_{FC}\left(\frac{1}{\eta_{FC}} - 1\right) \tag{3.50}$$

All heat is assumed to be produced within the fuel cell due to the chemical reactions. As such, the assumption is made that products and reactants do not carry in or out any heat. Removal of this heat is required for stable operation. As discussed in Section 3.6.1, Water-Ethylene Glycol is selected as the liquid coolant having the best Figure of Merit, in a 40%/60% ratio to lower the freezing point as much as possible.

Using the assumption from NLR experts that the coolant temperature rise in the fuel cell $\Delta T_{FC,c}$ is generally in the order $10 - 15$K [98], the coolant mass flow $\dot{m}_c$ can be determined.

$$\dot{m}_c = \frac{Q_{FC}}{C_{p,c,avg}\Delta T_{FC,c}} \tag{3.51}$$

To estimate the coolant pressure drop across the fuel cell, an analytical approach is used. Using equations 3.50 and 3.51, with $P_{FC} = 2$ MW, $\eta_{FC} = 50\%$, $\Delta T_{FC,c} = 10$K and $C_{p,c,avg} \approx 3310$ J/(kg K), the coolant mass flow $\dot{m}_c \approx 60$ kg/s. This is in line with the estimated mass flow rate in Section 3.6.1 for $P_{FC} = 4$ MW.

The coolant channels can be modeled as tubes of $D = 0.5$mm, based on data by Graf et al. (2018) [172]. Figure 3.22 shows a individual cells in a fuel cell stack, with coolant channels made from formed metal sheets.

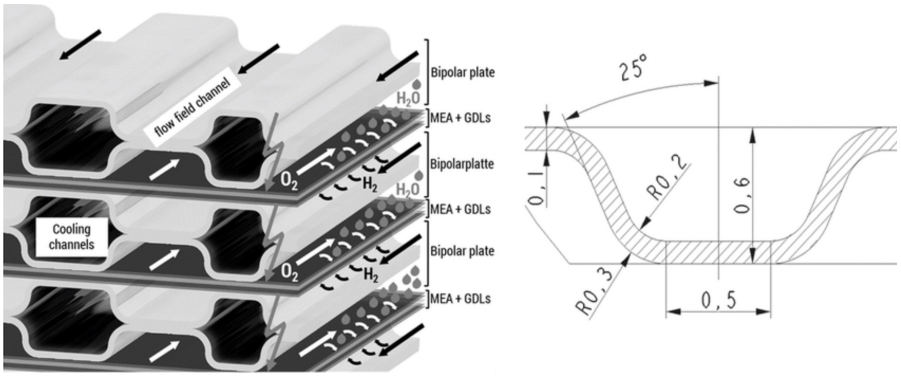

Figure 3.22: Cross-section of formed channels in fuel stack cells. Reproduced from Graf et al. (2018) [172]

Using the fact that the ElringKlinger NM5-300 fuel cell in Schröter (2023) [17] has a power output of 41 kW and dimensions of 0.5 m^2, $N_{cells} \approx 15000$ and the amount of tubes per cell is around 500. Mass flow per coolant tube is then $\dot{m}_{c,\,tube} \approx 0.05$ kg/s

With water-eglycol 40/60 at $T = 90°C$ and $p = 3$ bar, pressure drop can be estimated using conservation of mass and the equations presented in Appendix A.3. Implementing a conservative factor of 2 on the pressure drop,

$$\Delta p_{FC} = 20,000 \quad \text{Pa} \tag{3.52}$$

Although very conservative, the same pressure drop is assumed for the humid air side channels within the fuel cell. Temperature and pressure are approximately equal and water content is formed on the cathode side, having similar density as water-eglycol 40/60.

3.6.3. Pump Modeling

The pump is modelled as a simple device that provides the required pressure rise to the coolant without increasing the temperature. This means that for the coolant the following equation holds.

$$\Delta p_{pump} = \Delta p_{IC} + \Delta p_{FC} + \Delta p_{H2HX} + \Delta p_{radiator} \tag{3.53}$$

The temperature rise in the pump can be assumed to be negligible. The first law of thermodynamics states that

$$Q + W_{in} = \dot{m}\,(h_{out} - h_{in}) \tag{3.54}$$

Assuming an adiabatic pump, there is negligible heat transfer, i.e. $\dot{Q} \approx 0$. Assuming incompressible liquid, the enthalpy change can be written as:

$$\Delta h \approx \frac{\Delta p}{\rho} + C_p \Delta T \tag{3.55}$$

Within the pump model, the temperature rise of water-eglycol 40/60 can be assumed negligible by doing a simple calculation. Firstly, with the pressure drop in the fuel cell (Section 3.4), and an estimated pressure drop in the other heat exchangers of 2000 Pa, a required pressure rise of $\Delta p = 26000$ Pa is estimated for the pump. With $\rho \approx 1000$ kg/m^3 and $c_p \approx 3300$ J/(kg K) at $T = 95°C$ and $p = 3$ bar for water-eglycol 40/60, the following temperature rise ΔT is obtained:

$$\Delta T \sim \frac{\Delta p}{\rho C_p} = 0.0079 \text{ K} \tag{3.56}$$

A quick pump power estimate reveals that this does not have a significant impact on total fuel cell power. Assuming an efficiency of $\eta = 0.8$ and $\dot{m} = 121$ kg/s (see Table 3.5):

$$P_{pump} = \frac{\dot{m}\Delta p_{pump}}{\rho \eta} \approx 3.9 \text{ kW} \tag{3.57}$$

While it is difficult to determine the mass of an aviation-grade pump for the TMS, a rough estimate can be made using linear extrapolation. From industrial pump data provided by [103]:

$$m_{\text{pump}} = \frac{2.3\ \text{kg}}{80\ \text{LPM}} \cdot \dot{V}\ [\text{LPM}], \tag{3.58}$$

where $\dot{V}$ is the volume flow of the coolant in liters per minute. The volume flow for the considered application can be expected to be about 60 times larger, when taking into account $\dot{V}$ in Table 3.5 for water-eglycol 400.

3.6.4. Hydrogen Heat Exchanger Modeling

The Hydrogen Heat Exchanger (H2HX) is modeled as a parallel tube heat exchanger using the effectiveness-NTU method [167]. The equations are summarized in Appendix A.2. The coolant flows through a single larger tube, to minimize the risk of ice formation (see section 2.4.3). The H2HX is optimized using constrained gradient-based interior-point minimization (*fmincon* [168]). The objective is to minimize $|T_{\text{out},H_2} - T_{t,\text{FC}}|$, i.e. the outlet temperature of the hydrogen must be approximately the fuel cell temperature. A tolerance of 0.1 K is considered acceptable. The optimization settings are as follows:

Table 3.6: H2HX Optimization Settings

Setting	Value
Algorithm	Interior-Point
Function Tolerance	0.1
Optimality Tolerance	0.1
Step Tolerance	0.02

The geometry and parametrization are illustrated in Appendix B.1. The model makes use of average properties for the coolant between the inlet and outlet. From verification data provided by NLR [122], it was determined that the length of the HX required to evaporate the hydrogen is less than 3% of the total length. As a result, this evaporative section is excluded from the model but added back into the total HX length afterwards.

Hydrogen properties are modeled using the *'PARAHYD'* option in REFPROP library [123]. When hydrogen is cryogenic, the isomeric spin is in the 'para' state, as shown in Figure 3.23. It is assumed that the fluid does not have sufficient time to convert a fraction to the 'ortho' state as it is evaporated and heated.

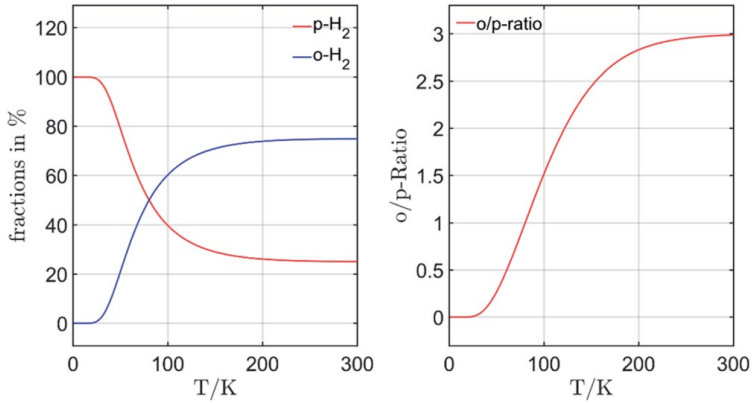

Figure 3.23: Ortho-para hydrogen ratio as a function of temperature. Reproduced from [173].

To determine whether the hypothesis that a hydrogen pump is not required is valid (Section **??**), simple fluid dynamics are implemented. The hydrogen needs to be delivered at a pressure of 2.4 bar and a temperature of 90°C at maximum (see Section 3.4). To estimate the pressure drop of hydrogen from the tank to the fuel cell, the length of the required tubing must be known. The hydrogen tanks are assumed to be located in the back of the aircraft, whereas the fuel cells are located in the nacelle. Using Appendix B.3, this distance is estimated at 10m. To determine the pressure drop in steady-state conditions, first the hydrogen mass flow rate $\dot{m}_{H_2}$ must be estimated. For this a required power of 2 MW (half of the aircraft), a fuel efficiency $\eta = 50\%$ and the lower heating value of hydrogen $LHV \approx 120$ MJ/kg, the fuel mass flow rate is:

$$\dot{m}_{H_2} = \frac{Q_{\text{FC}}}{LHV_{H_2} \cdot \eta_{\text{FC}}} = \frac{2\text{MW}}{120\text{MJ/kg} \cdot 0.5} = 0.033\text{kg/s} \tag{3.59}$$

Conservatively, the mass flow is assumed to be $\dot{m}_{H_2} = 0.04$ kg/s. The inner diameter of the tube is assumed at $d = 100mm$. In Appendix A.8 it was shown that for a Darcy friction factor ranging from 0.002 to 0.004, the expected pressure drop across the tube would be approximately 1860 Pa to 3720 Pa. This shows that a hydrogen tank pressure of approximately 2.5 bar is sufficient for delivery at $p = 2.4$ bar and $T = 90°$C a tube with $L = 10$m and $d = 10$cm. Further modeling of the tubing from tank to H2HX to fuel cell is not included in this work, but it is assumed that the hydrogen stream enters the H2HX as a saturated vapor at 4 bar.

Since the density of hydrogen decreases non-linearly with temperature, and the temperature inside the HX increases logarithmically, using simple average properties for hydrogen is not sufficient. Instead, a logarithmic temperature increase is simulated (see Figure 3.24) to calculate density-based average properties between the inlet and outlet, using the average temperature (see Figure 3.25). This results in an average hydrogen density of $\rho_{\text{avg}} = 0.38$ kg/m^3. A workflow diagram of the H2HX sizing procedure is shown in Appendix Section B.2.

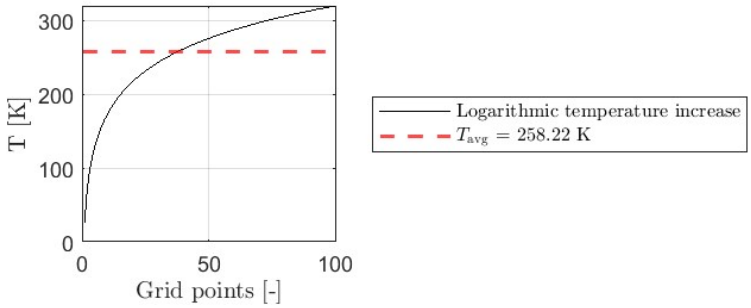

Figure 3.24: Simulated logarithmic temperature increase of hydrogen. The red dotted line indicates the average temperature.

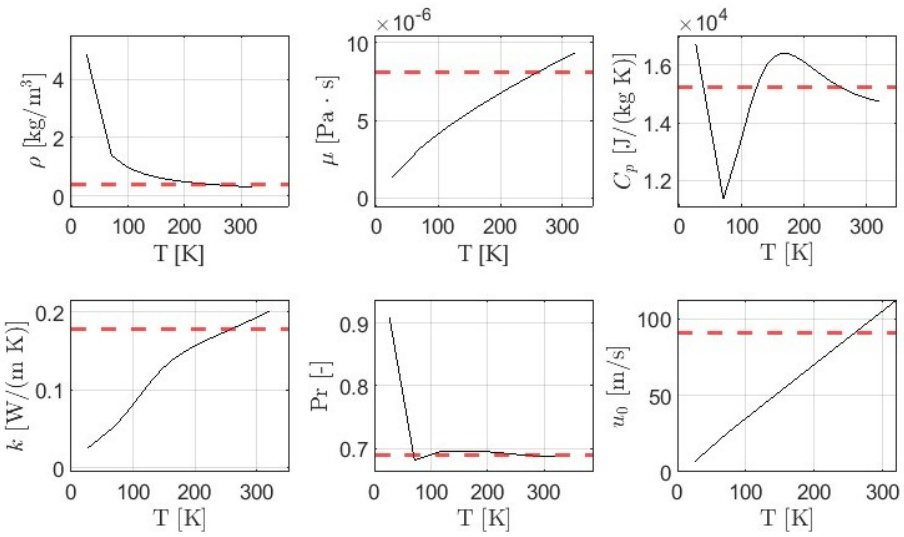

Figure 3.25: Hydrogen properties as a function of the logarithmic temperature increase: Density ρ, dynamic viscosity μ, specific heat coefficient C_p, thermal conductivity k, Prandtl Pr, bulk velocity u_0. The red dotted line indicates the average temperature.

The mass of the heat exchanger is based on the Aluminium 3003 alloy, commonly used in heat exchangers. This alloy has a material density $\rho = 2730$ kg/m^3 and a thermal conductivity $k = 190$ W / (m K). Due to the high thermal conductivity, the wall thermal resistance is assumed to be negligible in this model.

Since it may be desired to maximize the thermal power exchanged in the H2HX, the hydrogen needs to enter as a liquid. Close integration with the liquid hydrogen tanks could allow the hydrogen to remain liquid until entering. In preliminary designs for retrofitted aircraft, the non-integral fuel tanks are sometimes placed sideways (see Figure 2.33). For close integration of the H2HX with the tanks, the maximum length of the H2HX is assumed equal to the cabin width of a DHC-8 Q300 fuselage (2.52m).

3.6.5. Radiator Modeling

The radiator is modelled using the same methodology as the intercooler, as a cross-flow heat exchanger with fins and tubes. The effectiveness-NTU method is implemented as well. However, the direction of heat transfer changes. While the intercooler cools the hot air from the compressor, ram air cools the hotter coolant in the ram air duct. The radiator is optimized using constrained gradient-based interior-point minimization (*fmincon* [168]). The objective is to minimize $T_{\text{out,c}}$, i.e. the outlet temperature of the coolant should be as low as possible. The optimization settings are as follows:

Table 3.7: Radiator Optimization Settings

Setting	Value
Algorithm	Interior-Point
Optimality Tolerance	0.1
Step Tolerance	0.01

As discussed in Section 3.3, the the width and length of the radiator are fixed according to the size of the ram air duct. The height is fixed at $H_{\text{radiator}} = 0.61m$, according to the available space along the nacelle in the DHC-8 Q300. This leaves only two design variables, as the same model as used for the intercooler is adopted: the fin height h_{fin} and fin spacing d_{fins}. Since radiator performance has a large effect on the overall optimization problem of W_{duct}, the diameter of the tube d_{tube} is added as design variable, allowing further optimization of the heat transfer area on the tube side. Bounds for these design variables are introduced in Section 5.2. The workflow diagram of the sizing procedure of the radiator is shown in Appendix Section B.2.

For illustrative purposes, the assumed orientation of the radiator alongside the nacelle of the DHC-8 Q300 is shown in Figure 3.26. This orientation maximizes frontal area, as discussed in Section 3.3.

Figure 3.26: Orientation of the radiator in the ram air duct, alongside the nacelle of the DHC-8 Q300. Image adapted from [174].

3.6.6. Thermal Management System Model Limitations

The most important components of the thermal management system are included in the lumped parameter model, but some limitations are introduced:

- The **coolant temperature increase** in the fuel cell is estimated based on knowledge from fuel cell testing at NLR.
- **Accumulator** sizing is not included in the model. Generally, the impact on single-phase cooling system mass is significantly smaller than for two-phase systems.
- Pressure loss in coolant **tubing** is neglected, since exact integration and placement of the systems cannot be determined. This can result in an underestimation of pressure loss and required pump size. Also, heat loss in the tubing is neglected.
- Not all **properties of water-eglycol 40/60** can be determined by Refprop [123], the following ones have been determined as mass average of the properties of the pure components in the blend: dynamic viscosity μ_{c} and thermal conductivity k_{c}. Refprop can handle density ρ_{c}, enthalpy H_{c} and specific heat capacity $C_{p,\text{c}}$.
- **Variations in hydrogen pressure** during the aircrafts mission are neglected. As the liquid hydrogen is drawn from the tank, supply pressure drops and temperature rises. However, pressure and temperature regulation devices should be able to minimize such deviations.

- In reality a **full vacuum** around the LH2HX is probably not feasible, decreasing the thermal power transferred to the hydrogen. However, close integration with the cryogenic tank might allow for increased system efficiency.
- **Hydrogen evaporation** is not modeled in the H2HX, as the corresponding thermal power is estimated to be small. To verify this assumption, the H2HX model results are compared with those of a more detailed model using data from NLR (see Section 4.4.2).
- What happens in case of **coolant freezing** inside the H2HX is not modeled. Also, water-eglycol becomes more viscous near its freezing point. Freezing prevention is especially important during start-up, restart and shutdown, when coolant temperature can drop significantly below the fuel cell temperature. It is assumed that this can be prevented by battery powered electric heaters, increasing pump speed or partially closing the ram air HXs. The mass of the battery powered elecric heaters inside for example the H2HX is not modelled, but its solid aluminium casing of 1.5 cm should account for the extra mass.

3.7. Powertrain Modeling

Although the Powertrain is not modeled, efficiencies for the electric motors, gearboxes and inverters can be assumed from literature (see Section 2.6), and components masses can be estimated using simple relations. Mass of the electric motors is estimated according to data presented by Andersen et al. (2023) [175]:

$$m_{\mathrm{EM}} = 17\mathrm{kW/kg} \cdot P_{\mathrm{FC,DC}} \cdot \eta_{\mathrm{INV}} \cdot \eta_{\mathrm{EM}}, \tag{3.60}$$

Where $\eta_{\mathrm{EM}} = 0.973$ and $\eta_{\mathrm{INV}} = 0.98$.

Additionally, the mass of the reduction gearbox can be estimated according to a relation presented by Pettes-Duler et al. (2022) [176], assuming $\mathrm{rpm}_{\mathrm{in}} = 12,500$ for aviation grade electric motors [177], and $\mathrm{rpm}_{\mathrm{out}} = 1050$ for the propeller maximum rotational speed [87]:

$$m_{\mathrm{GB}} = \left(\frac{P_{\mathrm{shaft}}}{\mathrm{rpm}_{\mathrm{out}}}\right)^{0.75} \left(\frac{\mathrm{rpm}_{\mathrm{in}}}{\mathrm{rpm}_{\mathrm{out}}}\right)^{0.15} \tag{3.61}$$

An efficiency of $\eta_{\mathrm{gr}} = 0.98$ can be used to estimate P_{shaft}.

3.7.1. Powertrain Model Limitations

- Mass of inverters or other power electronics is not included. Also, battery weight is excluded, as it is difficult to estimate required battery power from steady-state analysis. Transient analysis and reserve requirements would be required to size a battery system.
- Cooling requirements of the powertrain components are not taken into account in the TMS sizing procedure, as the powertrain is very efficient with a combined efficiency of $\eta_{\mathrm{pt}} = 0.906$.

4

Verification & Validation

This chapter presents the verification and validation of the model components discussed in 3. Firstly, the ram air duct model will be treated. Then follow the fuel cell system, air supply system, radiator, intercooler and hydrogen heat exchanger (H2HX) models.

4.1. Ram Air Duct Model Verification

Using data from the publication by Beltrame et al. (2024) [18] for Mach number, velocity and total and static temperature, the properties inside the ram air duct model can be verified. As described in Section 3.3, the ram air duct model includes a flow velocity increase due to a propeller, and assumes that no pre-diffusion occurs. Furthermore, the ram air duct is modeled only up to just before the radiator. To verify the model the following modifications to the ram air duct model need to be implemented:

- Exclude the propeller.
- Include a pre-diffusion mass flow ratio of $\dot{m}_0/\dot{m}_1 = 0.7$. This means that the Mach number before the inlet (station 2) can be determined from:

$$f(M_1) = \frac{M_1}{\dot{m}_{\text{ratio}}} \left(1 + \frac{\gamma - 1}{2} M_1^2\right)^{-\frac{\gamma+1}{2(\gamma-1)}} - M_0 \left(1 + \frac{\gamma - 1}{2} M_0^2\right)^{-\frac{\gamma+1}{2(\gamma-1)}} \tag{4.1}$$

  The total ingested mass flow is then determined by:

$$\dot{m}_{\text{tot}} = \frac{A_{\text{in}} p_{t,2}}{\sqrt{T_{t,2}}} \sqrt{\frac{\gamma}{R}} M_2 \left(1 + \frac{\gamma - 1}{2} M_2^2\right)^{\frac{-(\gamma+1)}{2(\gamma-1)}} \tag{4.2}$$

- Change the mission parameters to $M_0 = 0.78$, $h = 10,000$m and $T_{\text{ISA}} = +15°$C.

The comparison with the results from the lumped parameter model in the publication is illustrated in Figure 4.1. See Appendix A.1 for more details.

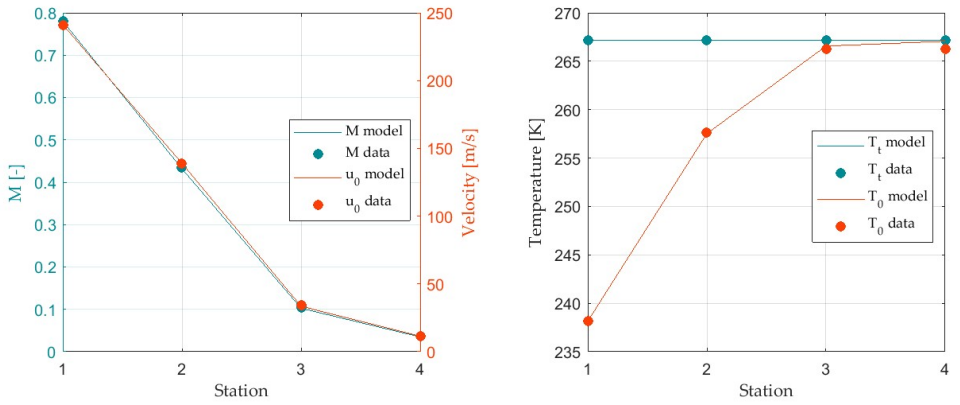

Figure 4.1: Verification of the ram air duct model against data from Beltrame et al. (2024) [18]

It can be concluded that the simplified ram air duct model shows good agreement with the Lumped Parameter Model data in the publication. Only the static temperature T_0 just before the radiator (station 4) is different, since the radiator inlet temperature is assumed equal to the total temperature as air velocity is small.

4.2. Fuel Cell System Model Verification

Since the fuel cell system model is directly based on experimental data and performance characteristics from a Fuel Cell Stack described in a reputable publication (see Section 3.4), further verification using other fuel cell models is deemed unnecessary. The model parameters and performance outputs have already been validated in the source publication, providing a high level of confidence in their accuracy and applicability. As such, efforts in this study are focused on system-level integration and optimization rather than re-verifying the fuel cell subsystem itself.

4.3. Air Supply System Model Verification

For the air supply system, verifying the correct modeling of the compressor is crucial, as it significantly impacts system performance and results. In contrast, components such as the air filter and humidifier primarily contribute to minor pressure drops, making their verification less critical for the overall analysis.

4.3.1. Compressor Model Validation

Important to note is that it is assumed that the compressor can operate at similar efficiency for all operating conditions. In reality, the compressor should be sized for top-of-climb, as required power is highest, resulting in higher air mass flow than other scenarios. Also, the required pressure ratio is larger at increased altitude, although the same as in cruise, obviously.

To get insight in compressor performance in take-off, top-of-climb and cruise, various parameters are summarized in Table 4.1. See Chapter 5 for more insight on sizing of the propulsion system for these mission phases.

Table 4.1: Compressor Performance Across Mission Phases

Parameter	Take-off	Top-of-climb	Cruise
Compressor power (P_{comp})	171 kW	438 kW	221 kW
Pressure ratio (β_{comp})	2.44	4.12	4.12
Air mass flow rate ($\dot{m}_{air}$)	1.40 kg/s	2.34 kg/s	1.19 kg/s
Corrected mass flow rate ($\dot{m}_{corr}$)	1.34 kg/s	1.12 kg/s	0.55 kg/s
Isentropic compressor efficiency ($\eta_{comp,is}$)	0.77	0.76	0.76
Temperature increase (ΔT)	119.6°C	182.4°C	182.4°C

As expected, required performance varies significantly between mission phases. Required mass flow in top-of-climb is almost twice as high as during cruise for the same pressure ratio. In top-of-climb conditions, mass flow is 67% higher than in take-off for a 69% increase in pressure ratio. The different pressure ratios result in a slight difference in isentropic efficiency To verify whether operation under such conditions is possible, comparison with transonic compressor data by Zangeneh et al. (2011) is done [165]. This reference is also used to estimate the mass of the compressor. In Figure 4.2 pressure ratio and efficiency for corrected mass flow are shown.

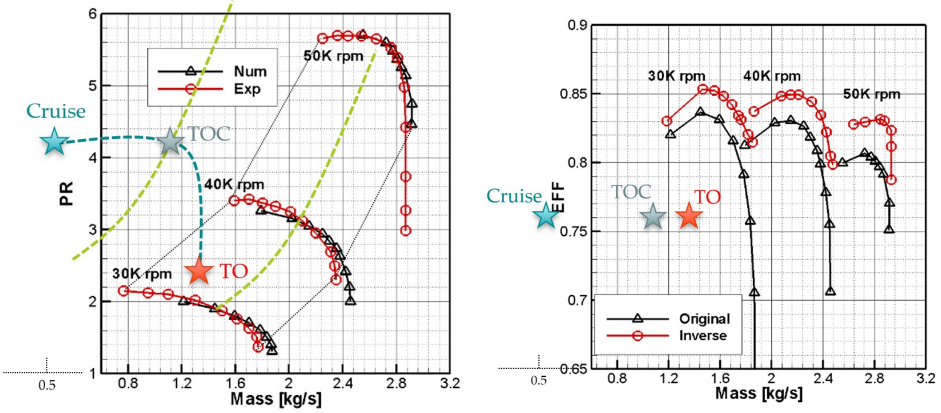

(a) Pressure ratio vs. reduced mass flow.

(b) Compressor power.

Figure 4.2: Compressor performance for different mission phases. Compressor maps are adapted from Zangeneh et al. (2011) [165]. Optimal efficiency is indicated in green, while constant rpm is indicated in blue.

As can be seen, the compressor operating point falls outside of this compressor map in top-of-climb conditions.

This highlights the challenges of compressor design. However, it should be possible to design a compressor with a shifted compressor map, operating at similar rpm in all conditions (blue dotted line). This may potentially result in optimal performance in top-of-climb, but compromised performance in cruise and take-off, as the optimal efficiency line is usually in the middle of the map as indicated in green.

4.4. Thermal Managementent System Verification

Since lumped parameter models are developed for the Radiator, intercooler, and Hydrogen Heat Exchanger (H2HX), their verification is essential to ensure accuracy and reliability. Conversely, the fuel cell and pump are not explicitly modeled; their behavior is instead represented through simplified assumptions, making verification unnecessary.

4.4.1. Radiator and Intercooler Verification

The radiator and intercooler models use the same heat exchanger sizing methodology as described in Sections 3.6.5 and 3.5.3. The radiator component rejects heat of the coolant (water-eglycol 40/60) to the ram air inside the ram air duct. The intercooler component cools air out of the compressor to the required fuel cell inlet temperature, while heating the coolant.

The verification data is provided by NLR [103]. The heat exchanger model can be verified in terms of the following parameters:

- Geometry: while height, width and length are inputs to the model, the number of sections, fins and tubes should match with the verification data.
- Mass: the mass of the fins is provided in the verification data and can therefore be used for verification.
- Overall heat flux.
- Fin velocity $u_{0,fins}$: the heat exchanger in the verification data is assumed to be in free-stream air, increasing air pressure drop. For details, see Appendix A.5.
- Exit temperatures of the air and coolant.

Additionally, it can be checked for the following components whether they are within an acceptable range:

- Pressure drops should be within an acceptable range (Δp < 25,000 Pa), based on consultation with experts at NLR [16].
- Heat transfer coefficients should be within expected ranges for air and the coolant [178]: 4 - 100 (W/(m2K)) for air in air-cooled heat exchangers and 1400 - 2000 (W/(m2K)) for cooling of liquids inside tubes.
- Reynolds numbers should be in the same regime, laminar in this case.

The specific model against which the data is verified uses a different approach:

- While the model in this thesis is based on the effectiveness-NTU method for heat exchangers [167], the NLR model implements a CFD model [179].
- The fluid properties in the model for this thesis are averaged between in- and outlet of the heat exchanger, while the NLR model computes properties on a 20x20 grid using a MacCormack discretization scheme [179].

The table below provides a comparison of the model results and NLR data [103]. Percentual deviations or limits provide insight into the verification.

Table 4.2: Results of the verification exercise for the radiator/intercooler model

Parameter	Actual	Expected	Percentual Difference	Limits
N_{sections}	22	22	0%	-
N_{fins}	7000	6999	0%	-
N_{tubes}	8800	Unknown	-	-
m_{fins} [kg]	15.12	15	0.6%	-
Q_{HX} [W/m^2]	27.29	30	**-9.05%**	-
u_0 (Fins)	16.78	17.8	**-5.7%**	-
$T_{\text{c,out}}$ [K]	330.53	330.54	0%	-
$T_{\text{fluid,out}}$ [K]	324.10	324.05	0%	-
Δp_{fluid} [Pa]	683.80	-	-	<25,000 Pa
Δp_{c} [Pa]	14,536	-	-	<25,000 Pa
U_{c} [W/m^{2}K]	805	-	-	50 - 10000 W/m^{2}K
U_{fluid} [W/m^{2}K]	61.10	-	-	0.5 - 1000 W/m^{2}K
Re_{fluid}	2140	-	-	<2300 (Laminar flow)
Re_{c}	92.6	-	-	<2300 (Laminar flow)

As can be seen, expected heat flux is about 10% lower than in the reference Finned HX. Air velocity deviates about 5%, which also has effect on the pressure drop between the fins. Parameters for which no data is available are within the acceptable range.

4.4.2. Hydrogen Heat Exchanger Verification

The Hydrogen Heat Exchanger (H2HX) methodology is described in Section 3.6.4. Inside the parallel tube heat exchanger, liquid hydrogen is evaporated and heated to the fuel cell inlet temperature, while some of the fuel cell waste heat can be rejected. While the heat transfer fluid (htf) is single-phase in this research, a two-phase condensing heat transfer fluid is used in the verification exercise. Additional equations for this are described in Section A.6. A workflow diagram of the calculation procedure is provided in Appendix Section B.2.

The H2HX model can be verified for the following parameters, with verification data provided by NLR [16].

- The mass of the fins is provided in the verication data.
- Overall heat flux.
- Exit temperatures of the hydrogen and heat transfer fluid.

Additionally, it can be checked for the following components whether they are within an acceptable range:

- Pressure drops should be within an acceptable range (Δp < 25,000 Pa), based on consultation with experts at NLR [16].
- Expected range of the heat transfer coefficient for the the condensing heat transfer fluid is: 2000 - 3000 (W/(m2K)) for condensing R1233ZD(E) [180]. However, heat transfer coefficients for cold gaseous hydrogen could not be found in literature, so additional parameters determining the heat transfer coefficient are presented in 4.3.

The model is verified using data provided by NLR. This data is generated using a different approach:

- While the model in this thesis is based on the effectiveness-NTU method for heat exchangers [167], the NLR model uses a discretized grid. [16].
- While the model in this thesis uses averaged thermodynamic properties between the inlet and outlet to calculate the heat exchanger parameters, the NLR model updates the thermodynamic properties at each grid point.

Results of the verification are provided in Appendix Section B.1. As can be seen, the resulting heat exchanger mass is about 30% less than in the verification data. This is due to a rough approximation of the geometry. While the inside wall thickness is taken equal, outside geometry is roughly approximated and manifolds are neglected. Regarding the heat transfer, this is 15% smaller than expected. This difference can partly be explained by the fact that the heat required for evaporation of the hydrogen is not taken into account. In this case, the heat required for evaporation is about 7.8% of the total heat, considering that the heat needed for evaporation is:

$$\dot{m}_{H_2} = H_{\mathrm{lv}} \Delta \chi \tag{4.3}$$

The remaining 7.2% can be due to inaccuracies regarding fluid properties, versus the discretized model used in the verification data.

The outlet temperature of the heat transfer fluid should remain that at the saturation point for a pressure of 3.9 bar. The heat transfer fluid does not fully condensate, as the quality drops to about 0.1 and the pressure drop is about zero. Also, the heat transfer fluid pressure drop is indeed minimal. Furthermore, the heat transfer coefficient of the heat transfer fluid and pressure drops are within the expected range. The hydrogen gas heat transfer coefficient is relatively large, compared to other gases such as air. While a common range for this heat transfer coefficient is hard to determine, according to the equations in Appendix Section A.3, thermal convective properties of the gaseous hydrogen are as shown in Table 4.3 for the average conditions in the H2HX.

Table 4.3: Hydrogen forced convection heat transfer properties

Average Properties	Value
Bulk velocity u_0 [m/s]	34.9
Tube diameter d_{tubes} [mm]	1.5
Nusselt number Nu [-]	28.3
Reynolds number Re [-]	8661
Thermal conductivity k [W/m/K]	0.13
Heat transfer coefficient U [W/m^2 / K]	2420

4.5. Model Convergence

To assess the performance of the solver, it is essential to perform some model convergence analysis. As summarized in Figure 3.5, the model requires a guess for heat exchanger pressure drops at first. After HX sizing, the actual pressure drops are calculated. These values have to be fed back into the solver for correct recalculation of average properties inside the heat exchangers. The results are shown in 4.3. As can be seen the solver usually converges after 3 iterations, since tolerance for pressure drop deviation between iterations is only 0.1 Pa (see Table 3.3). Note that the radiator air side pressure drop is not included, since it has no effect on convergence of the model in this thesis.

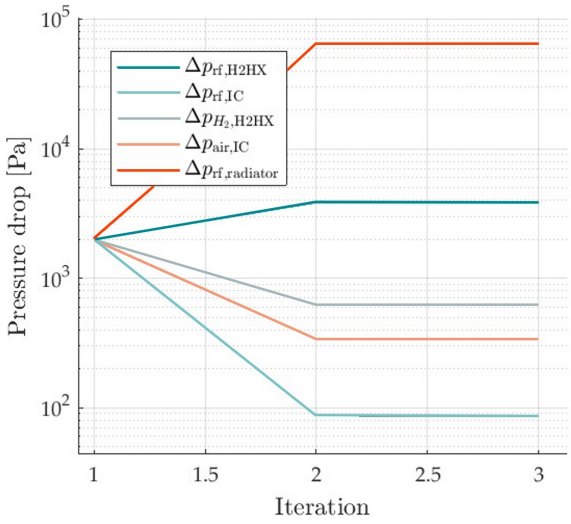

Figure 4.3: Pressure drop convergence in solver.

Results for convergence of average properties inside the radiator, intercooler and H2HX for top-of-climb conditions are shown in Figures 4.4, 4.5 4.6, respectively. Results are shown for outlet velocity and density of the coolant and fluid. As can be seen, more than 10 iterations are required for the components, even though differences between initial and final values are sometimes marginal. Still, computation time is less than a second for 20 iterations, thus the tighter convergence criteria imposed on the outlet temperature of the heat exchanger component models do not have significant impact on the computational efficiency of the overall system model.

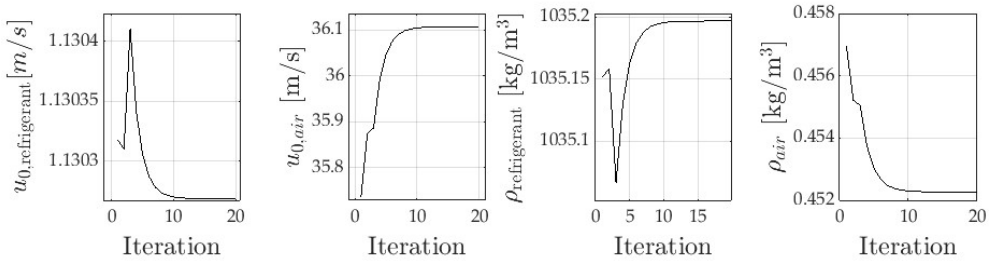

Figure 4.4: Convergence of outlet properties in the radiator.

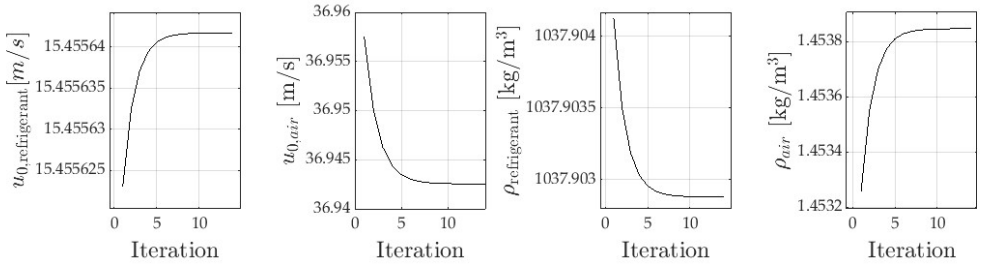

Figure 4.5: Convergence of outlet properties in the intercooler.

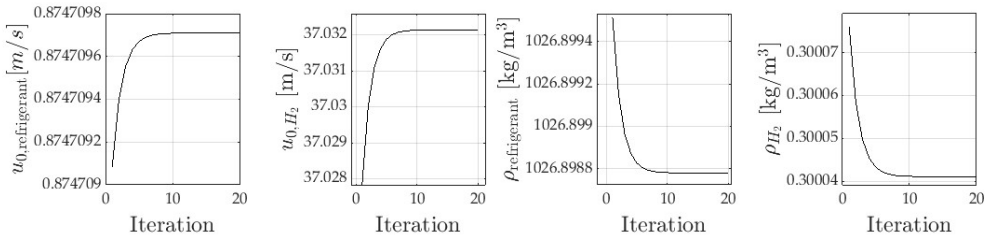

Figure 4.6: Convergence of outlet properties in the H2HX.

While the convergence tolerances on temperature output of the heat exchangers should not allow for values larger than summarized in Table 3.3, it can still occur that heat exchanger sizing results in a local minimum, or the step size is smaller than the tolerance. In that case, the model will converge and move to another design point. Results for the radiator, intercooler and H2HX are shown in Figures 4.7. Note that these results are presented for the sensitivity analysis as performed in Section 5.2. Errors for on- and off-design are shown in the sections afterwards, and influence the selection of optimal design point.

An error $\epsilon < 0$ indicates the heat exchanger is oversized, while a positive error indicates an undersizing. As can be seen the error is mostly below the tolerance of $0.1^c irc$C. Only for the intercooler in top-of-climb conditions the error is sometimes up to 0.5°C. However, the effect on the results is expected to be marginal, considering the overall temperature drop in the intercooler in top-of-climb conditions (ΔT = 143.25°C for $T_{\text{t,FC}}$ = 90°C and $i_{\text{t,FC}}$ = 1.25 A/cm^2).

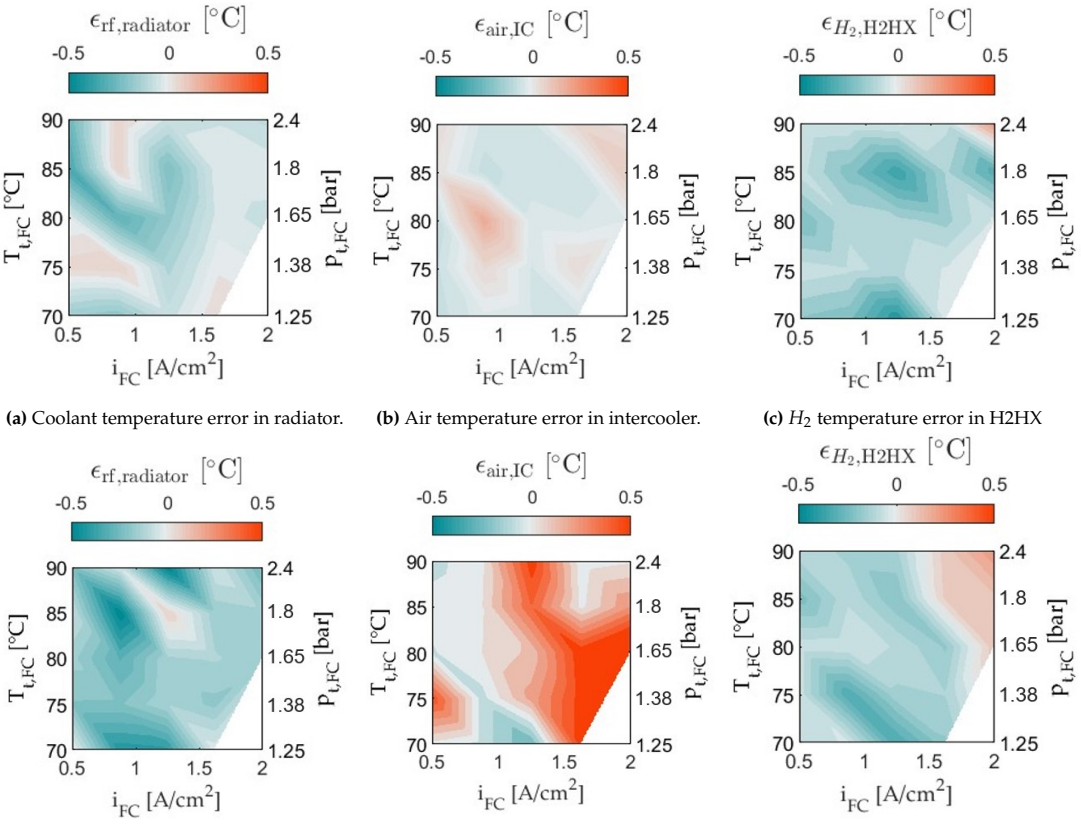

(a) Coolant temperature error in radiator. **(b)** Air temperature error in intercooler. **(c)** H_2 temperature error in H2HX

(d) Coolant temperature error in radiator. **(e)** Air temperature error in intercooler. **(f)** H_2 temperature error in H2HX

Figure 4.7: Results of sensitivity analysis for take-off conditions (a,b,c) and top-of-climb conditions (d,e,f).

5

Results & Discussion

This section will present and discuss the results obtained through the system model simulations and consists of the following sections:

- **A sensitivity analysis.** To address the research questions, the impact of key input parameters on the preliminary design of an LH2FCE aircraft is analyzed. Parameters for the sensitivity analysis are selected and prioritized based on their anticipated influence on model outputs and the level of uncertainty associated with each parameter. The findings from this sensitivity analysis are presented and discussed in Section 5.2.
- **On-design analysis.** The purpose is to determine to what extent the different operating conditions are constraining the design space. This is done in Section 5.3.
- **Off-design analysis**. Performance of the selected designs needs to be tested in other operating conditions. This is performed in Sections 5.4 and 5.5.
- **Design Variations**. Small variations in components or input parameters may lead to improvements compared to the baseline propulsion system architecture. This is discussed in Section 5.7. For the best performing modifications combined, as well as for technological advancements for 2030, system performance is discussed in Section 5.7.2.
- **Discussion and Outlook**. A concluding discussion is provided with an outlook for future research possibilities in Section 5.8.

5.1. Input Parameters for Test Case: DHC-8 Q300

This section describes the values and bounds of input parameters to the model and provides a clarification for the selection of input parameters for the sensitivity analysis. Parameters are first classified based on whether expected impact on model outcome is high, medium or low. Then, an uncertainty score is given to the parameter. If a well-educated guess can be made for the parameter, a value of 1 is given. For input parameters that are, for example, optimized (e.g. HX design variables) or dependent on other input parameters (e.g. relative humidity), the uncertainty score is of level 2. Parameters with the highest uncertainty (level 3) and expected impact will be selected for sensitivity analysis.

A summary is provided in Table 5.1. Parameters with **medium to high** expected impact and higher uncertainty (2-3) include:

- Fuel cell parameters: For fuel cell temperature $T_{t,\text{FC}}$, pressure $p_{t,\text{FC}}$ and current density i_{FC} it is uncertain what the optimal values are. As described in Section 3.4, pressure is a function of temperature, to reach optimal relative humidity ϕ_{rel} at a fixed air excess ratio λ_{air}.
- Ram air duct design parameters: While ram air duct width W_{duct} is an output of the model, ram air duct height H_{duct} and diffuser area ratio AR are fixed according to educated guesses, as discussed in Section 3.3. Also, Mach number at the inlet of the ram air duct M_{inlet} is fixed to the exit Mach number of the propeller, but can be smaller in reality.
- Radiator design parameters: While the volume of the radiator is directly determined by W_{duct}, the other 3 design parameters are optimized within reasonable bounds (see Section 3.6.5).
- Compressor polytropic efficiency η_{poly}: As this has high impact, a conservative estimate is made as described in Section 3.5.2.
- Intercooler and H2HX design variables, which are optimized within bounds. This is discussed in more detail in Section 3.5.3 and Section 3.6.4. Bounds are taken relatively wide, and expected impact on system level results is smaller.
- For coolant temperature $T_{c,0}$ and pressure p_c good assumptions can be made. $T_{c,0}$ is based on the expected temperature rise in the intercooler and fuel cell as discussed in Section 3.5.3. p_c has some influence on pump design, which is why a conservative estimate is made for the pump mass (see Section 3.6.3). Furthermore, the operating pressure has impact on tubing design, but that is not analyzed in this work.

For the remaining input parameters, valid assumptions can be made as discussed in Chapter 3. This includes, among others, the mission parameters, of which the influence is assessed through on-/ and off-design analysis. Concluding, $T_{t,\text{FC}}$ and i_{FC} are selected as sensitivity parameters.

Table 5.1: Parameters and Their Expected Impacts and Uncertainty Scores

Parameter	Range	Expected impact	Uncertainty score
$T_{t,\mathrm{FC}}$	70 – 90°C	High	3
Current density i_{FC}	0.5 - 2.0 A/cm^2	High	3
$p_{t,\mathrm{FC}}$	1.25 - 2.4 bar	High	3
Air excess ratio λ_{air}	$1.7 = f(T_{t,\mathrm{FC}})$	High	2
$\phi_{\mathrm{rel,FC}}$	40 – 98%	High	2
Area ratio diffuser AR	1.0	High	2
$\Delta T_{\mathrm{c,FC}}$	10	High	2
Radiator L	$0.6645 \cdot W_{\mathrm{duct}}$	High	2
Radiator h_{fins}	3 – 20 mm	High	2
Radiator d_{fins}	1 – 5 mm	High	2
Radiator d_{tube}	1 – 5 mm	High	2
Compressor η_{poly}	0.8	High	2
Ram air duct M_{inlet}	Propeller u_e	High	2
Intercooler H	0.2 – 1.4 m	Medium	2
Intercooler W	0.05 – 0.8 m	Medium	2
Intercooler L	0.2 – 1.0 m	Medium	2
Intercooler h_{fins}	3 – 20 mm	Medium	2
Intercooler d_{fins}	1.5 – 3 mm	Medium	2
Intercooler d_{tube}	1 – 5 mm	Medium	2
H2HX L	0.2 – 2.49 m	Medium	2
H2HX r_{in}	50 – 500 mm	Medium	2
H2HX d_{tubes}	3 – 15 mm	Medium	2
$T_{\mathrm{c,0}}$	$(T_{t,\mathrm{FC}} - \Delta T_{\mathrm{c,FC}} - 2)$ K	Medium	2
P_{shaft}	2.28 MW (cruise) - 3.56 MW (TOC)	High	1
η_{prop}	0.84	High	1
D_{prop}	4.1 m	High	1
H_{duct}	0.61 m	High	1
Radiator inclination θ	70°	High	1
HX material	Alu 3003	High	1
Altitude h	0 m (TO) - 7620 m (cruise)	High	1
M_∞	0.11 (TO) - 0.44 (cruise)	High	1
$P_{\mathrm{net,FC}}$	2.5 MW (cruise) - 3.9 MW (TOC)	High	1
T_{ISA}	+30°C	High	1
$U_{\mathrm{ref,FC}}$	1.229	Medium	1
p_{c}	3 bar	Medium	1
$\Delta p_{\mathrm{c,FC}}$	20,000 Pa	Low	1
$\Delta p_{\mathrm{air,\ filter}}$	525 Pa	Low	1
$\Delta p_{\mathrm{air,\ humidifier}}$	8000 Pa	Low	1
$\Delta p_{\mathrm{air,\ FC}}$	20,000 Pa	Low	1
$C_{p,\mathrm{air}}$	1024 J/kg K	Low	1
$\phi_{\mathrm{rel,air}}$	50%	Low	1
ΔT_{pump}	0	Low	1
Hydrogen T_{in}	26	Low	1
Hydrogen p_{in}	p_v(26 K)	Low	1

5.2. Sensitivity Analysis

This section gives the results of the sensitivity analysis, where fuel cell temperature $T_{t,\mathrm{FC}}$ and current density i_{FC} are varied in the range displayed in Table 5.1, to assess their impact on payload and range of a LH2FCE aircraft. Fuel cell pressure $p_{t,\mathrm{FC}}$ has to increase with temperature, to maintain optimal relative humidity in the LT-PEM fuel cell.

The bounds for the duct width are summarized in Table 5.2.

Table 5.2: Duct Width Bounds

Parameter	Value	Units
Lower Bound for Duct Width, $W_{\mathrm{duct,lb}}$	0.2	m
Upper Bound for Duct Width, $W_{\mathrm{duct,ub}}$	1.0	m

Figure 5.1 visualizes the results for take-off and top-of-climb conditions. Infeasible designs fall in the white regions in the chart and are associated with output variables exceeding the set limits. The limit to W_{duct} = 0.61m represents the duct width being equal to the duct height. When m_{PS} >6000 kg, the entire propulsion system mass budget is consumed. This represents a third of the payload budget (3096 kg) allocated by Rietdijk and Selier (2024) [10]. (see Figure 3.2). The propulsion system mass m_{PS} excludes the tank mass, as this cannot be sized until cruise analysis is performed. In any case, the fuel burn of 340 kg/h cannot exceed. Otherwise, the maximum mission fuel mass, as estimated by Rietdijk and Selier, would be consumed within one hour.

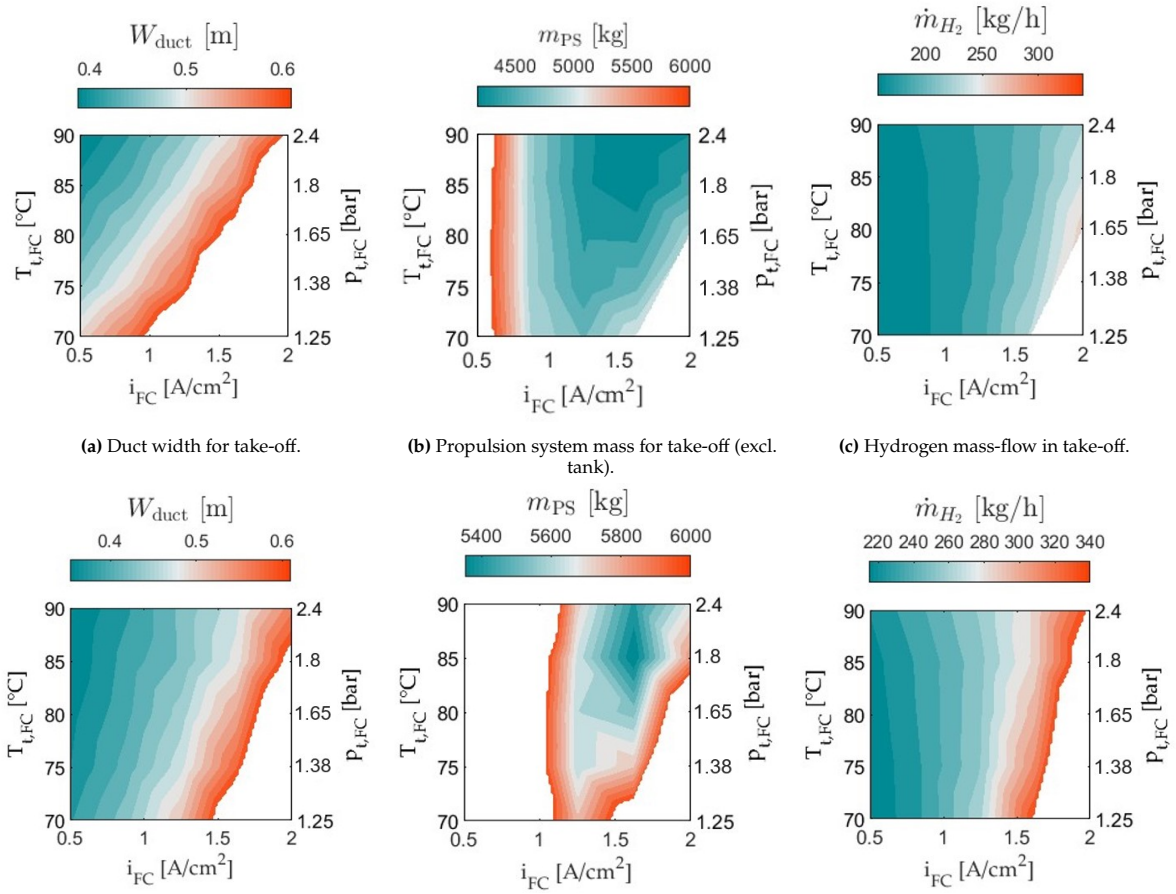

(a) Duct width for take-off.

(b) Propulsion system mass for take-off (excl. tank).

(c) Hydrogen mass-flow in take-off.

(d) Duct width for top-of-climb.

(e) Propulsion system mass for top-of-climb (excl. tank).

(f) Hydrogen mass-flow in top-of-climb.

Figure 5.1: Results of sensitivity analysis for take-off conditions (a,b,c) and top-of-climb conditions (d,e,f).

Selecting the optimal fuel cell **current density** is a trade-off between payload and range. Smaller current density results in a smaller duct width, lower drag and thus a larger lift-to-drag ratio. Additionally, less fuel is used due improved fuel cell efficiency, increasing range. However, at smaller current densities, propulsion system mass increases significantly, reducing available mass for payload.

Similarly, selecting the optimal **fuel cell temperature and pressure** also results in a trade-off between payload and range. A higher temperature results in a larger temperature difference in the radiator, improving heat rejection to the ambient air and reducing required ram air mass flow and duct width, improving the lift-to-drag ratio and range. Additionally, range is increased further as fuel cell efficiency improves with increasing pressure. However, in top-of-climb conditions, increasing fuel cell temperature beyond $T_{t\text{FC}} = 85°\text{C}$ seems ineffective. The higher pressure ratio demanded from the compressor increases fuel cell power, increasing fuel cell mass and reducing payload mass. As a result of increasing fuel cell power, fuel mass flow rate increases slightly for the highest fuel cell temperature and pressures.

When considering duct width W_{duct}, **take-off** conditions are constraining. While demanded fuel cell power is lower and air density increases in take-off conditions, the air velocity is low (40 m/s), resulting in lower mass flow through the radiator. In top-of-climb, the increase in demanded fuel cell power is compensated by the increase in mass flow through the ram air duct, due to increased airspeed (128.5 m/s), even though air density is halved.

When considering propulsion system mass m_{PS}, **top-of-climb** is the constraining operating condition. Depending on the optimal current density, the fuel cell mass increases by up to 1000 kg compared to take-off conditions. As more power is required to compress the air at high altitude, required fuel cell power and size increase, as shown in Figure 5.2. Therefore, top-of-climb conditions are assessed first in on-design, to size the fuel cell. Subsequently, it is assessed whether the TMS can reject the thermal power in take-off conditions. If not, the duct width should be increased.

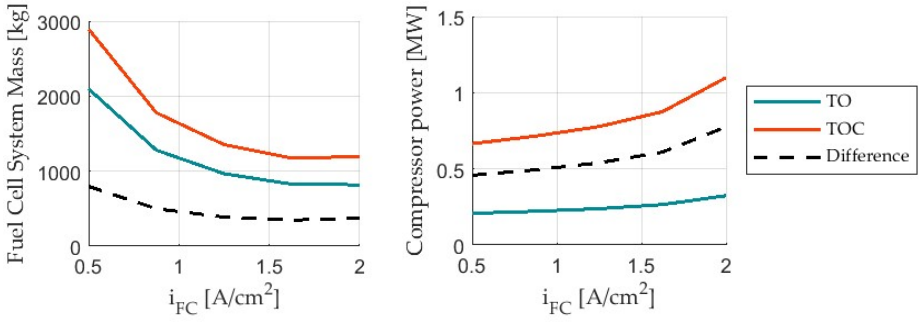

(a) Fuel cell system mass.

(b) Compressor power.

Figure 5.2: Comparison of fuel cell system mass and compressor power between take-off and top-of-climb at $T_{t,\text{FC}} = 90°\text{C}$ and $p_{t,\text{FC}} = 2.4$ bar.

5.3. On-design Analysis: Top-of-climb Conditions

From sensitivity analysis results in Section 5.2 it is clear that the propulsion system has to be sized for **top-of-climb** conditions. Selecting a design solution is a complex decision. One could design for the smallest duct and have a lower fuel mass flow rate, but obtain the heaviest propulsion system. On the other hand, if designing for the smallest mass, a larger duct is obtained and fuel mass flow rate is increased. The result is that either range or payload is compromised, or in the worst case both.

By tackling this design challenge as a multi-objective problem, where no objective is dominant, a Pareto front can be constructed [181]. Fuel mass flow rate is left out of this on-design analysis, as the overall fuel required to reach top-of-climb is expected to be smaller than for cruise. Conversely, W_{duct} and m_{PS} are parameters that drive the design. The Pareto front for all optimized design solutions is shown in Figure 5.3. The upper bounds for W_{duct} and m_{PS} are again set to 0.61 m and 6000 kg, respectively.

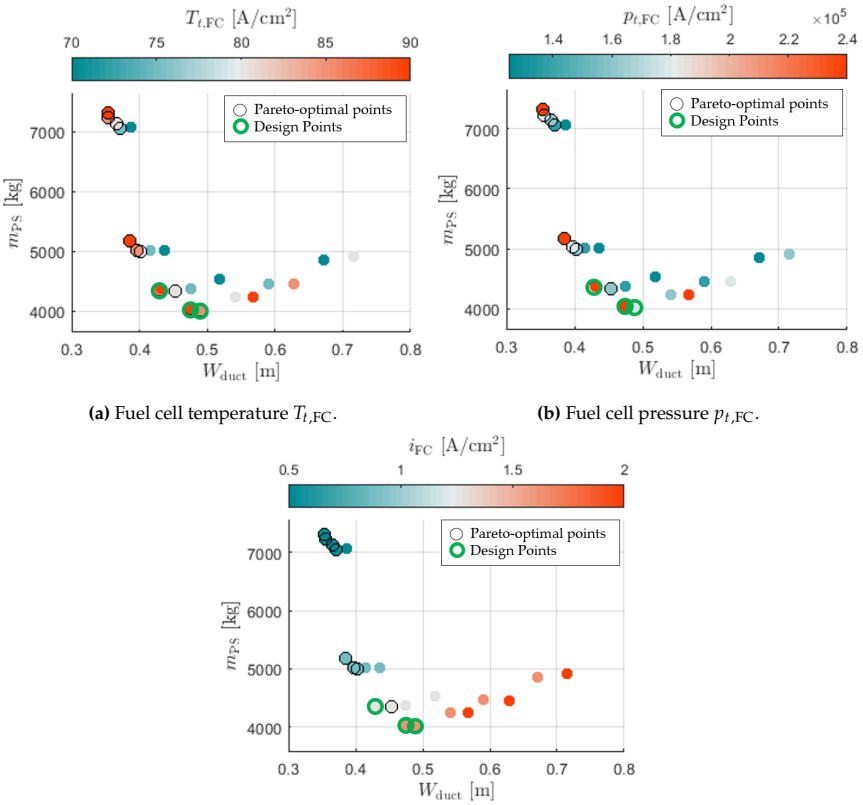

(a) Fuel cell temperature $T_{t,\text{FC}}$.

(b) Fuel cell pressure $p_{t,\text{FC}}$.

(c) Fuel cell current density i_{FC}.

Figure 5.3: Pareto front with non-dominated solutions in W_{duct} and m_{PS} for top-of-climb conditions. Pareto optimal solutions circled in black, design solutions that are selected for further analysis are circled in green.

As can be seen in Figure 5.3, few Pareto-optimal solutions fit the constraints. Highest fuel cell pressure and temperature are not necessarily optimal, as discussed before in Section 5.2, due to the weight penalty to the fuel cell of increased compressor pressure ratio. However, the optimal fuel cell current density seems to be somewhere between $i_{\text{FC}} = 1.25 - 1.625$ A/cm^2, right in the center of the sensitivity range.

Three Pareto-optimal solutions are selected for further analysis. These are highlighted in green in Figure 5.3. Tank mass is not yet included into the propulsion system mass m_{ps}, which can account for up to 1500 kg, given the fuel mass m_{fuel} =340 kg in [10] and a η_{gr} = 23%. Therefore, the mass budget for fuel cell, balance-of-plant and powertrain is about 4000 kg (see Figure 3.2), yielding the design solutions as in Table 5.3.

Table 5.3: Selected design solutions.

Design Solution	m_{PS} [kg]	W_{duct} [m]	i_{FC} [A/cm^2]	Tt_{FC} [°C]	pt_{FC} [bar]
1	5660	0.430	1.25	85	1.8
2	5431	0.475	1.625	90	2.4
3	5353	0.489	1.625	85	1.8

5.4. Off-design Analysis: Take-off Conditions

Given the non-dominant design points from Table 5.3, off-design analysis for take-off can be performed. The required power by the fuel cell system is lowered from 3.9 MW to 3.1 MW (see Table 3.1). Also, the following input parameters are fixed:

- Duct width W_{duct}.
- Fuel cell area (and mass). Current density can be determined by realizing that power density decreases for the same fuel cell area.
- Geometry of the Radiator, Intercooler and H2HX.
- Coolant mass flow $\dot{m}_c$.

Although power required for take-off is smaller than in top-of-climb, so is the mass flow through the radiator. Since required duct width is just slightly smaller in take-off than in top-of-climb, it is assessed whether the TMS can reject all heat in take-off conditions. The system may benefit from a change in fuel cell temperature and pressure setting, so this is included in the analysis.

First, heat exchanger performance is assessed. The duct width W_{duct} may need to be increased if the required coolant temperature cannot be reached in the radiator. Secondly, the take-off fuel mass flow rate is determined as this is crucial for payload and range analysis.

Temperature Discrepancy Calculation

In on-design conditions, the radiator, intercooler and H2HX are sized to obtain the required coolant, air and hydrogen temperature, respectively. To assess system performance in take-off conditions, it is essential to verify whether the required temperature output at the heat exchanger outlets is reached under these operating conditions as well.

The air temperature at the intercooler outlet and the hydrogen temperature at the H2HX outlet correspond to the fuel cell temperature. For the radiator, as discussed in Section 3.5.3, the coolant temperature at the outlet is fixed to $T_{t,\text{FC}} - \Delta T_{t,\text{FC}} - 2\text{K}$, even though the temperature difference across the intercooler might be smaller. In take-off, the magnitude of this offset can be reduced, by realizing that the cooling power is decreased significantly. In take-off, compression power will be significantly less due to the higher ambient pressure, reducing the temperature of air entering the intercooler.

For the same range of $T_{t,\text{FC}}$ and $p_{t,\text{FC}}$ in the on-design analysis, it can than be determined, for each design solution, what the discrepancy is between the actual and target temperature at the heat exchanger outlets. The results are shown in Figure 5.4.

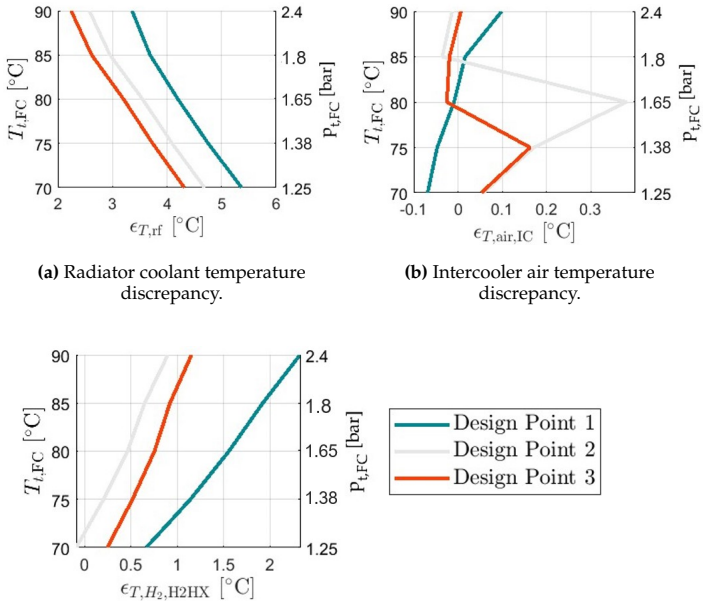

(a) Radiator coolant temperature discrepancy.

(b) Intercooler air temperature discrepancy.

(c) H2HX hydrogen temperature discrepancy

Figure 5.4: discrepancy between actual temperature and required temperature, for different design solutions, in take-off off-design conditions.

As can be seen in Figure 5.4, the coolant temperature discrepancy $\epsilon_{T,c}$ in the radiator gets relatively large, indicating that the ram air cannot reduce the coolant temperature sufficiently. For design solution 3, corresponding to the highest temperature and pressure setting, the discrepancy is smallest $\epsilon_{T,c} \approx 2°C$, as the duct width is larger than for the other design options. The smaller the duct, the larger the temperature discrepancy.

The temperature discrepancies in the intercooler and H2HX are smaller, but not necessarily within the convergence tolerance of 0.1 K (Table 3.3). However, the overall impact on the design is small, as these heat exchangers have a large temperature difference between the hot and cold streams ($\Delta T_{H_2,\text{H2HX}} = 339K$ and $\Delta T_{\text{air,IC}} = 75K$). The mass will therefore increase marginally in a design iteration.

To get the three design solutions to meet the requirement on the radiator thermal load in take-off conditions, the duct width will need to be increased. A small gain in performance was found in setting the $T_{t,\text{FC}} - \Delta T_{t,\text{FC}} - 2K$ to 10K instead of 12K. Since required cooling power in take-off is lower than in top-of-climb, the overall coolant temperature difference can be slightly lower for the same coolant mass rate as in top-of-climb. Also, the cooling power in the intercooler is lower as a lower temperature is reached at the compressor outlet due to the decreased pressure ratio.

Since the temperature discrepancy in the radiator is smallest at $T_{t,\text{FC}} = 90°C$ and $p_{t,\text{FC}} = 2.4$ bar, these must be the take-off fuel cell settings. The corresponding duct widths are shown in Figures 5.5. The recalculated performance of the three design solutions with the larger ram air ducts are presented in Table 5.4.

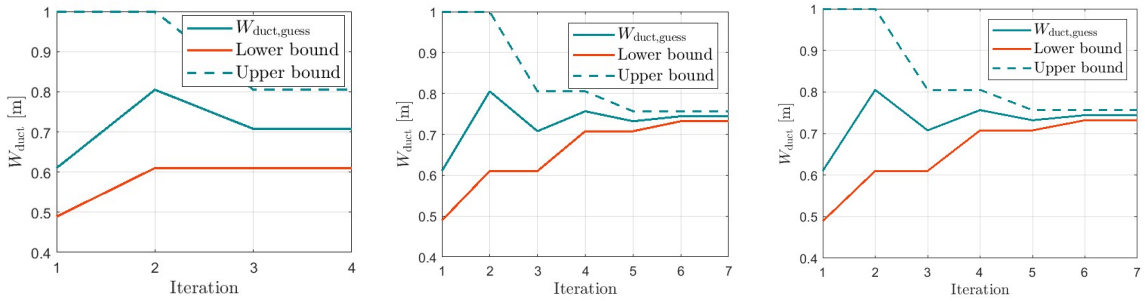

(a) Design solution 1. **(b)** Design solution 2. **(c)** Design solution 3.

Figure 5.5: Duct size required for take-off off design conditions.

Table 5.4: Converged design parameters for take-off (TO) and top-of-climb (TOC) conditions.

Design Solution	m_{PS} [kg]	W_{duct} [m]	i_{FC} [A/cm^2]	Tt_{FC} [°C]	pt_{FC} [bar]	$\dot{m}_{H_2}$ [kg/h]
Conditions			TO / TOC	TO / TOC	TO / TOC	TO/TOC
1	4656	0.708	0.778 / 1.250	90 / 85	2.4 / 1.8	169 / 246
2	4442	0.744	0.923 / 1.625	90 / 90	2.4 / 2.4	174 / 276
3	4429	0.744	0.919 / 1.625	90 / 85	2.4 / 1.8	174 / 286

As can be seen, the duct size, current densities and fuel mass flow rates for design solution 2 and 3 are similar, even though the second design solution has a 13 kg higher mass. Fuel cell size in both designs is approximately the same, however the intercooler is lighter in the third design. Required fuel cell power output can be lower, as the air pressure is smaller. This decreases the required length of the fins in the intercooler, as the compressed air has a lower temperature.

5.5. Off-design Analysis: Cruise Conditions

Given the non-dominant design solutions from Table 5.4, off-design analysis for cruise can be performed. The required power by the fuel cell system is lowered to 2.5 MW overall. As in take-off off-design analysis, the following input parameters remain fixed:

- Duct width W_{duct}.
- Fuel cell area (and mass).
- Geometry of the Radiator, Intercooler and H2HX
- Coolant mass flow $\dot{m}_c$

While the fuel cell is now sized for top-of-clib conditions, where power is highest, and the duct for take-off, where air velocity is lowest, it is expected that cruise will not require a redesign. First, the temperature discrepancies between required and actual temperatures at the heat exchanger outlets are discussed. Afterwards, a payload range estimation for the different design solutions is done for various fuel cell temperatures and pressures. The design that performs best will be selected for further analysis.

Temperature discrepancy Calculation

The temperature deviations in the various HXs estimated by the model with respect to the design requirements for cruise conditions are presented in Figure 5.6. It is clear that the HXs are oversized for all the fuel cell settings considered. The negative values indicate that the coolant in the radiator and air in the intercooler are being cooled too much, requiring adequate regulation. The negative values in the H2HX indicate that the hydrogen is overheated compared to the target. However, the offset is only by a few degrees, while the hydrogen is heated by more than 300°C in total. Therefore, minimal design changes are expected.

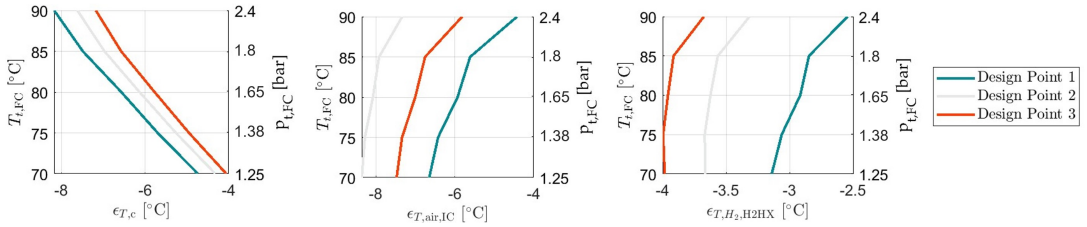

(a) Discrepancy for the coolant temperature output targeted in the radiator.

(b) Discrepancy for the air temperature output targeted in the intercooler.

(c) Discrepancy for the hydrogen temperature output targeted in the H2HX.

Figure 5.6: Discrepancy between actual temperature and targeted temperature, for different design solutions, in cruise off-design conditions. Temperature and pressure is varied while current density is fixed at $i_{\text{FC}} = 0.5$ A/cm^2

Optimal Fuel cell Settings

The optimal fuel cell settings in cruise are determined by searching for the combination of pressure and temperature that maximizes aircraft payload for the given design cruise range. While there is some uncertainty about payload and range calculations as no full mission analysis is performed, a rough estimate can be made using the equations in Section 3.1. Maximum cruise rating for the original DHC-8 Q300 is approximately 1500 km, with a payload of 5300 kg (see Appendix B.4). Using the Breguet range equation, the fuel mass to reach this cruise range can be determined. The lift-to-drag ratio in cruise is estimated to be $L/D_{\text{cruise}} = 13.6$. More details for this estimation can be found in Section 5.6.1. The space left for payload has to account for passengers, cargo, crew and some auxiliary systems that are not included in the weight analysis, such as a battery, high-voltage inverters and tubing.

The analysis is repeated for the three Pareto design solutions selected from Figure 5.3. The results are shown in Figure 5.7.

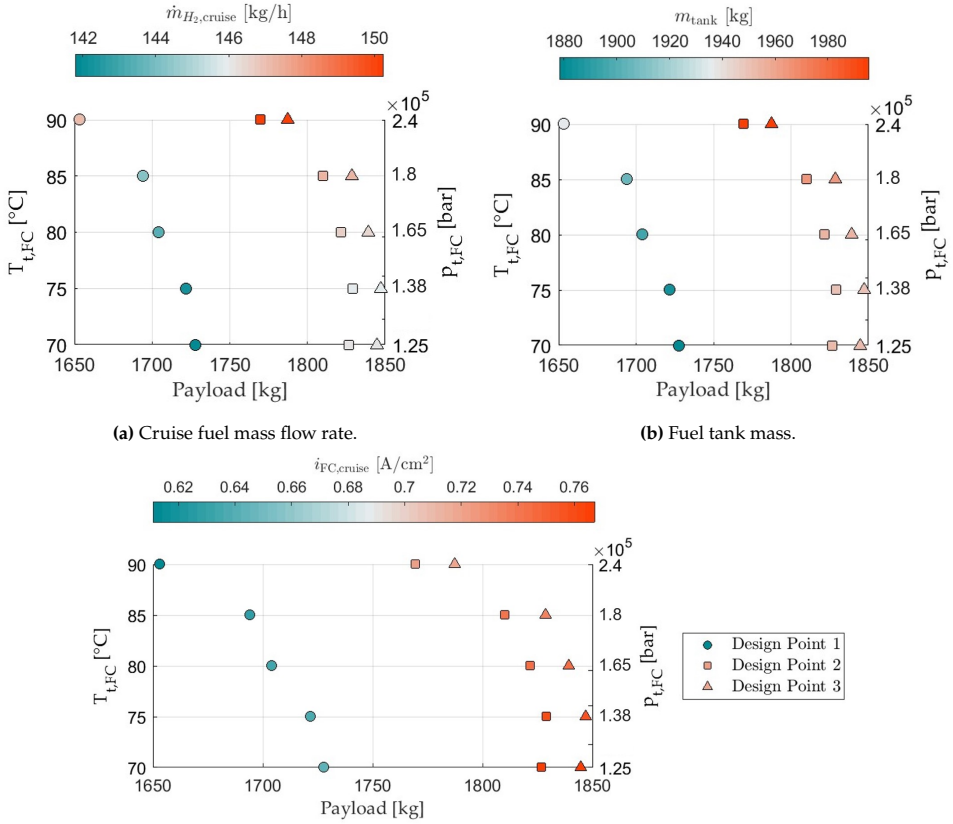

(a) Cruise fuel mass flow rate.

(b) Fuel tank mass.

(c) Fuel cell current density.

Figure 5.7: Payload mass of the retrofitted DHC-8 Q300 for the three Pareto design solutions and a required range of 1500 km as a function of different fuel cell temperature and pressure settings.

In Figure 5.7, fuel mass flow rates in cruise, total liquid hydrogen tank mass and current densities in cruise are visualized by the colors.

Evidently, payload is highest for design solution 3, which is the one featuring the lower propulsion system mass among the selected Pareto design solutions. Although the larger fuel cell in design solution 1 operates more efficiently, and has a lower fuel mass flow rate and lower current density, payload is affected more by the mass of the fuel cell.

The difference in payload between the lowest and highest temperature and pressure setting is small, about 60 kg. Fuel mass flow rate is slightly larger for a higher fuel cell pressure, due to the increase in compressor power. Therefore, fuel and tank mass increase slightly.

The optimal settings thus lie at a lower temperature and pressure for cruise than $T_{t,\text{FC}} = 90°\text{C}$ and $p_{t,\text{FC}} = 2.4$ bar. However, the differences between $T_{t,\text{FC}} = 75°\text{C}$ and 85°C are very small, about 20 kg. Therefore, the optimal setting could be selected considering fuel cell lifetime. As discussed in Section 2.3, increased relative humidity is probably best to prevent damage to the membrane. In that case, $T_{t,\text{FC}} = 85°\text{C}$ and $p_{t,\text{FC}} = 1.8$ bar can be selected, since the corresponding required relative humidity $\phi_{\text{rel,FC}} = 98\%\text{C}$. When reduced operational temperature would have more effect on the lifetime of the membrane, a lower temperature setting can be selected.

Concluding, the optimal design option is solution 3. Furthermore, the optimal fuel cell settings across operating scenarios are known as well as propulsion system mass and duct width. These baseline parameters are presented in Table 5.5.

Table 5.5: Baseline design parameters.

Optimal Design Solution	Design Solution 3
W_{duct}	0.744 m
m_{PS}	4429 kg
Take-off FC setting	$T_{t,\text{FC}} = 90°\text{C}$, $p_{t,\text{FC}} = 2.4$ bar
Top-of-climb FC setting	$T_{t,\text{FC}} = 85°\text{C}$, $p_{t,\text{FC}} = 1.8$ bar
Cruise FC setting	$T_{t,\text{FC}} = 85°\text{C}$, $p_{t,\text{FC}} = 1.8$ bar

5.6. Baseline Design

In this section the results for the baseline design are presented, starting with a drag polar for the design range (1500 km) in Subsection 5.6.1, followed by the mass breakdown in cruise conditions in Section 5.6.2 . Afterwards, ram air duct performance, fuel cell system performance, air supply system performance and thermal management system performance are provided in Sections 5.6.3 to 5.6.6.

5.6.1. Drag Polar Estimation

Before the drag polar of the aircraft is determined, it is assessed whether a small amount of thrust is generated from the ram air ducts in cruise conditions, according to the ΔC_{D_0}-method in Section 3.3. The total thrust for all four ram air ducts at different fuel cell temperatures and pressures is shown in Figure 5.8.

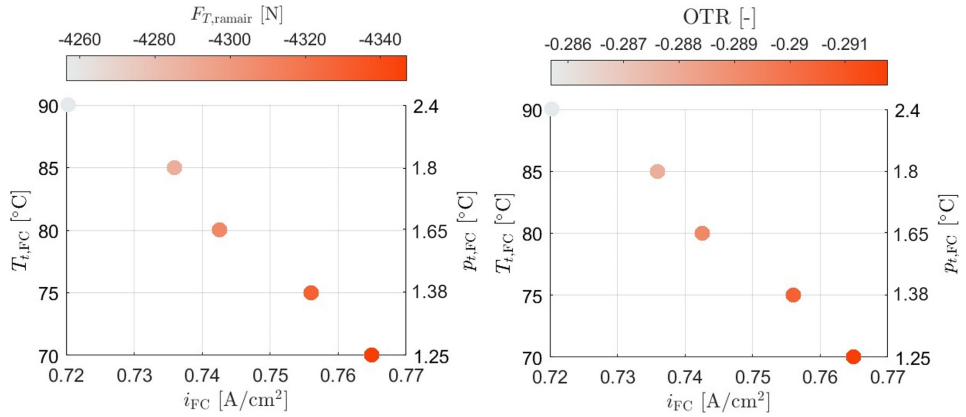

(a) Ram air thrust.

(b) Overall thrust ratio (OTR).

Figure 5.8: Total ram air thrust in cruise at different fuel cell operational settings, according to the ΔC_{D_0}-method (see Section 3.3.

As can be seen in Figure 5.8, fuel cell parameters do not have a large effect on thrust. However, note that thrust and overall thrust ratio (OTR) are **negative**, resulting in a ram air drag in the range of 4250-4350 N, which is almost 30% of the total thrust of the aircraft. Ram air drag is caused by large momentum and pressure losses in the ram air duct, as discussed in Section 5.6.3. In Section 5.7.1, is it analyzed to what extent increasing the diffuser area ratio reduces the drag in cruise associated with the ram air ducts.

Drag polars and lift-to-drag ratios for the different sources and methods, as discussed in Section 3.1.2, are shown in Figure 5.9. The results of the conceptual design performed by Rietdijk and Selier (2024), for a DHC-8 Q300 retrofitted with LH2FCE propulsion, are also shown.

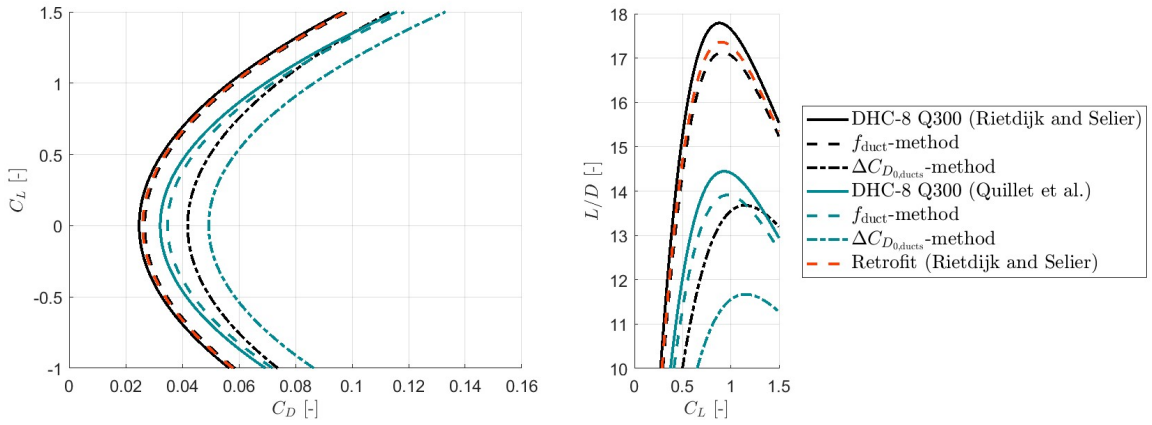

(a) Drag polar.

(b) Lift-to-drag ratio.

Figure 5.9: Drag polar and lift-to-drag ratio for the **original** DHC-8 Q300, based on Rietdijk and Selier (2024) [10] and Quillet et al. (2021) [87]), according to the f_{duct} (Equation 3.12) and $\Delta C_{D_{0,\text{ducts}}}$ (Equation 3.17) methods, and for the conceptual design by Rietdijk and Selier of a DHC-8 Q300 retrofitted with LH2FCE propulsion [10].

As can be seen in Figure 5.9, there is quite a large difference between different sources and methods for the drag polar, and especially the lift-to-drag ratio L/D. An overview of the percentual difference in drag coefficient C_D and L/D for cruise and maximum lift coefficient is shown in Table 5.6.

Table 5.6: Comparison of drag and lift-to-drag characteristics, based on Rietdijk and Selier (2024) [10] and Quillet et al. (2021) [87]), using the f_{duct}-method and ΔC_{D_0}-method. $C_{L_{\text{cruise}}} = 0.7$.

Parameter	Original (Rietdijk and Selier)	f_{duct}-method	ΔC_{D_0}-method	Original (Quillet et al.)	f_{duct}-method	ΔC_{D_0}-method
$C_{D_{\text{cruise}}}$	0.0404	+3.1%	+48.2%	0.0504	+5.0%	+40.0%
C_{D_0}	0.0248	+3.7%	+32.9%	0.0322	+4.0%	+27.0%
L/D_{cruise}	17.3	-4.6%	-29.8%	13.9	-4.8%	-25.4%
L/D_{max}	17.8	-3.7%	-23.1%	14.4	-3.7%	-19.9%

As can be seen in Table 5.6, the magnitude of drag coefficients and lift-to-drag ratios varies significantly across various studies. Whereas the difference in percentual increase between the characteristics based on different original values according to the f_{duct}-method is small, this increases a bit for the ΔC_{D_0}-method. This uncertainty in lift-to-drag ratio has impact on payload and range calculations. Using the equations in Sections 3.1.1 and 3.1.2, the payload for a 1500 km cruise range can be determined for minimum and maximum estimated L/D_{cruise}-ratios in cruise. This is shown in Figure 5.10, along with the result for the average L/D_{cruise}. The percentual decrease in payload from the original payload (5300 kg for a range of 1500 km) of the DHC-8 Q300 is also shown.

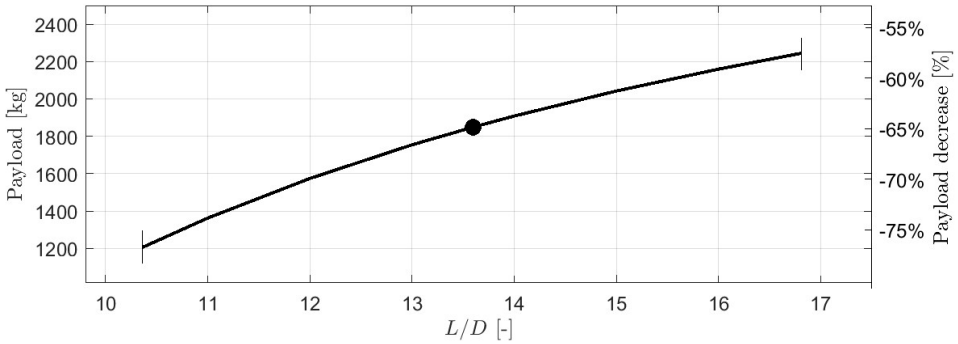

Figure 5.10: Payload uncertainty range due to uncertainty in L/D_{cruise}-ratio for a range of 1500 km, and payload decrease compared to the original DHC-8 Q300.

As can be seen, the uncertainty in payload is quite large, with a difference of 700 kg between the lower and upper bound of the range in Figure 5.10 (58 - 77% payload reduction). Since L/D linearly affects range, increasing fuel mass required to reach the design range, the large uncertainty in payload is not unexpected. The relation between L/D-ratio and payload is slightly non-linear due to the logarithm in Equation 3.3.

While the decrease in payload compared to the original kerosene-powered turboprop is significant, the actual payload may be even lower than estimated here. The increase in drag causes an increase in required thrust, increasing P_{shaft} and P_{FC}, increasing fuel cell size and propulsion system mass. However, as discussed in Section 3.1.2, required power levels for different operating conditions are based on the drag polar from Quillet et al. [87], which may be conservative. The increase in required fuel cell size may therefore be offset by a reduction in required power.

Nevertheless, considering the baseline design solution, the viability of a DHC-8 Q300 aircraft retrofitted with an LH2FCE propulsion system is doubtful at the design range of 1500 km. In the next sections, a mass breakdown for the baseline design will be presented, along with in-depth analyses of the results for each subsystem.

5.6.2. Aircraft Mass Breakdown for a Design Range of 1500 km

A comparison with respect to the DHC-8 Q300 in terms of MTOM breakdown is shown in Figure 5.11 for the original design range of 1500 km (Appendix B.4). As discussed in the previous section, payload is reduced between 58 - 77% for the range of L/D_{cruise}, when comparing results to the kerosene-powered turboprop. Fuel mass reduces between 57 to 69%, as hydrogen is a lighter fuel than kerosene. While hydrogen has 4 times more energy per kg, power-specific fuel consumption increases as propulsion system mass is about 4.3 larger. With the addition of the heavy cryogenic tank system, OEM increases by 35-60%. Specific power in top-of-climb for the propulsion system is reduced from 1.38 kW/kg to 0.62 kW/kg.

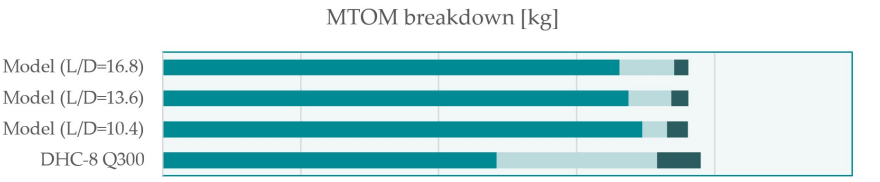

	DHC-8 Q300	Model (L/D=10.4)	Model (L/D=13.6)	Model (L/D=16.8)
OEM	12103	17384	16879	16565
Payload	5814	889	1554	1962
MF	1588	768	617	524

Figure 5.11: MTOM breakdown for a cruise range of 1500 km.

Figure 5.12 shows the mass of the retrofit-ready DHC-8 Q300, with fuel and engine systems removed (5.5% MTOW [10]). Additionally, the individual masses of the propulsion system, payload, fuel, liquid hydrogen tank are shown. The OEM in Figure 5.11 includes the propulsion system, liquid hydrogen tank and DHC-8 Q300 (excluding original turboprop engines and kerosene fuel system) masses.

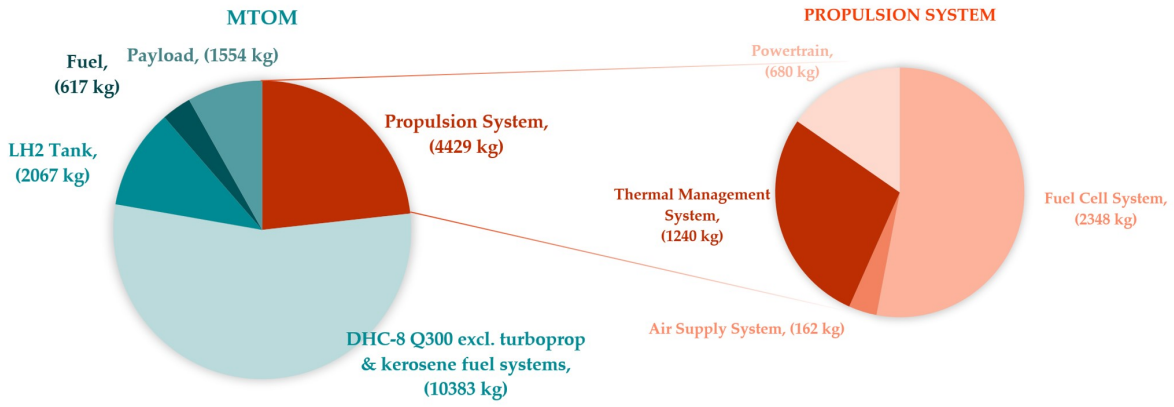

Figure 5.12: MTOM piechart for a design range of 1500 km.

On the left hand side of Figure 5.12, it can be seen that, despite the low fuel mass, the liquid hydrogen tank and propulsion system occupy a significant portion of the MTOM budget, leaving minimal capacity for payload. On the right, the breakdown of the propulsion system shows that the fuel cell system accounts for the largest share, followed by the thermal management system, powertrain, and air supply system."

5.6.3. Ram Air Duct Performance

Figure 5.13 illustrates the total and static temperature and pressure profiles along the ram air duct under various operating conditions. At station 6, the total conditions correspond to the airflow exiting the ram air duct, while the static conditions reflect the ambient environment. When momentum and pressure loss in the ram air duct are significant, the total pressure exiting the ram air duct can be lower than the ambient static pressure.

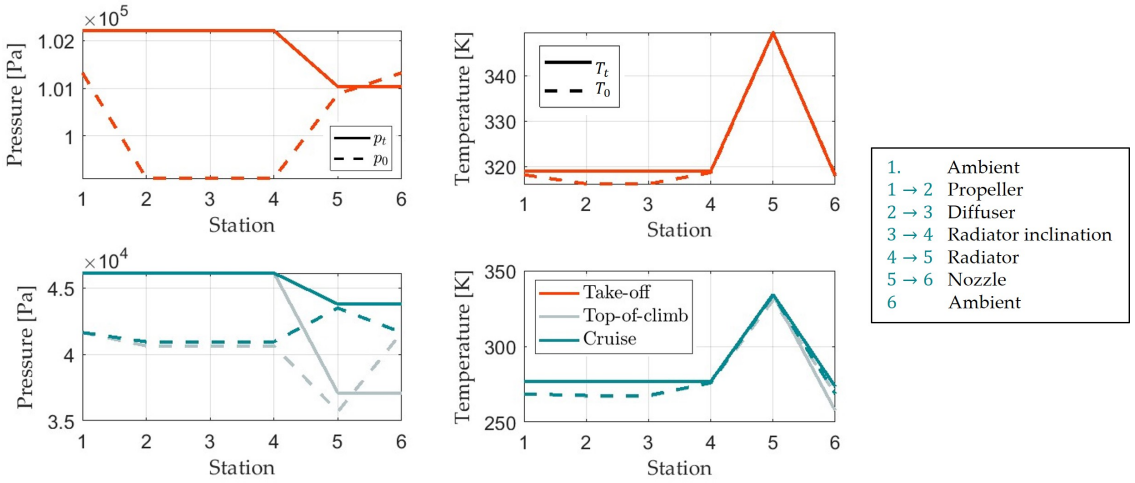

(a) Ram air total and static pressure.

(b) Ram air total and static temperature.

Figure 5.13: Ram air duct properties at station 1 (before propeller) to 6 (nozzle exit), for different operating conditions.

First of all, taking a look at cruise conditions in Figure 5.13, the increase in dynamic pressure and decrease in static pressure due to the propeller is visible (Station $1 \rightarrow 2$) . While properties are constant throughout the straight diffuser, the ram air is slowed and static pressure is increased due to the radiator inclination angle of 70°. This was modeled as an increase in area, but the effect of flow turning was neglected, as this should have minimal as was found in previous studies in literature (see Section 3.3). Pressure drop through the radiator is about 2000 Pa, while temperature increases by about 60K. While a large temperature difference is beneficial for thrust generation, its positive effect is limited by the nozzle pressure ratio NPR≈1.05. As the flow is expanded in cruise, velocity is increased slightly below the original free-stream velocity (128.6 m/s), resulting in the ram air drag as discussed in Section 5.6.1.

However, in top-of-climb conditions, total pressure visibly drops below the ambient pressure at station 6. Performance of the ram air duct should be comparable to cruise conditions, as ambient conditions are equal. However, the amount of heat added to the air flow, as shown in Table 5.7, is much larger. This increases flow momentum, but also increases frictional pressure loss. At the nozzle entrance, total pressure reduces by more than 9000 Pa compared to the free-stream, even though average velocity of the ram air in the radiator fins is about higher than in cruise conditions (71.0 vs. 32.5 m/s).

In take-off conditions, ram air velocity is relatively low, reducing the gap between static and total pressure. As can be seen, the total pressure reduces below the ambient pressure. Therefore, the nozzle pressure ratio NPR<1.0 causes $u_0 \rightarrow 0$ for top-of-climb and take-off conditions. The ideal nozzle is not able to accelerate the flow, as the equation implemented for nozzle exit velocity,

$$u_{\text{exit}} = \sqrt{2C_p T_{t,5} \cdot \left(1 - \frac{p_{0,6}}{p_{t,5}}^{\frac{\gamma-1}{\gamma}}\right)} = \sqrt{2C_p T_{t,5} \cdot \left(1 - \frac{1}{NPR}^{\frac{\gamma-1}{\gamma}}\right)}, \tag{5.1}$$

becomes zero. As a result, ram air drag will be larger in take-off and climb conditions than in cruise. Potentially, stagnation or reversal ov the flow can cause major issues for the TMS. As stated before, this issue may be eliminated by introducing fans in the ram air duct to sufficiently increase total pressure. While further analysis is needed, puller fans within the ram air ducts may be required to sustain sufficient ram air flow in take-off and top-of-climb these conditions.

An overview of Ram Air Duct performance parameters is shown in Table 5.7. This table also reports data for the ram air duct design by Beltrame et al. [18] (see Figure 2.24), to verify the soundness of the estimated drag value in cruise conditions.

Table 5.7: Ram air duct performance parameters across operating conditions.

Parameter	Take-off	Top-of-climb	Cruise	Beltrame et al. (2024), Cruise
Q_{radiator} [kW]	561	1869	992	740
Δp_{duct} [Pa]	1157	9059	2287	1360
$\Delta p_{\text{radiator}}$ [Pa]	1157	9059	2287	760
$u_{\text{fins,avg}}$ [m/s]	16.5	71.0	32.5	11.6
M_∞	0.11	0.39	0.39	0.78
NPR [-]	0.997	0.891	1.051	1.377
D_i [N]	n/a	n/a	n/a	1786
F_T [N]	n/a	n/a	-4288	1872

Comparing the results for cruise conditions between the baseline design and the ram air duct of Beltrame et al., pressure and momentum losses are larger for the baseline design. Pressure drop in the radiator is about 3 times larger, even though losses in the inlet, diffuser and nozzle are neglected. Also, air velocity in the radiator is about 3 times larger, due to the lack of a diffuser. The large pressure loss in the baseline design during cruise causes the nozzle pressure ratio (NPR) to be only slightly larger than 1.0, resulting in large ram air drag. Moreover, in the study by Beltrame et al., inlet drag D_i was determined, which may be, although left out of analysis here, in the same order of magnitude as ram air drag. However, in the design by Beltrame et al., NPR is much larger, resulting in a net thrust. Also, the free-stream Mach number is about twice as much, and the geometrical characteristics of the two ducts are slightly different, making the comparison more difficult, as shown in Table 5.8.

Table 5.8: Comparison of ram air duct design parameters.

Parameter	Baseline design	Beltrame et al. (2024)
W_{duct} [m]	0.744	0.27
L_{duct} [m]	> 2.04	3
θ [deg]	70	70
AR	1.0	3.8
L_{radiator} [cm]	47.9	17.6
Fin type [-]	Straight	Offset strip
h_{fins} [mm]	4	6.5
d_{fins} [mm]	1.5	2

As can be seen in Table 5.8, in the baseline design there is essentially no diffuser (AR = 1.0), while in the design by Beltrame et al. AR = 3.8, resulting in a larger reduction in air velocity and less pressure loss in the radiator. Furthermore, the baseline radiator fins are longer (L_{radiator}), shorter (h_{fins}) and fin spacing d_{fins} is slightly less than in the publication by Beltrame et al., decreasing fin hydraulic diameter and increasing friction loss.

While overall duct length is not determined for the baseline design, the length of the section with the inclined radiator is 1.973 m. When the nozzle and diffuser would scale linearly with the dimensions of the design by Beltrame et al. (see Figure 2.24), the duct length would be about 7 m. This is slightly longer than the current nacelle length of the DHC-8 Q300 (see Appendix B.3 for the dimensions).

Furthermore, the total temperature increase is about 60K at maximum, while 100K is reached in the design by Beltrame et al. This provides another reason for the fact that no thrust generation in the ram air duct is achieved.

5.6.4. Fuel Cell System Performance

In Table 5.9, fuel cell parameters and fuel mass flow rates in different operating conditions are summarized. In Figure 5.14, fuel cell efficiency and power density in take-off, top-of-climb and cruise conditions are highlighted on the fuel cell performance maps.

Table 5.9: Design solution 3 parameters for a range of 1500 km.

Parameter	Take-Off (TO)	Top-of-Climb (TOC)	Cruise	Climb	Other
Tt_{FC} [°C]	90.0	85	85	-	-
pt_{FC} [bar]	2.4	1.8	1.8	-	-
$\dot{m}_{\text{H2}}$ [kg/h]	172	289	147	-	-
i_{FC} [A/cm²]	0.870	1.625	0.736	-	-
η_{FC} [%]	0.605	0.500	0.605	-	-
$m_{\text{H2,cruise}}$ [kg]	-	-	432.6	-	-
$m_{\text{H2,climb}}$ [kg]	-	-	-	97.7	-
$m_{\text{H2,other}}$ [kg]	-	-	-	-	58.9
P_{FC} [MW]	3.44	4.78	2.94	-	-

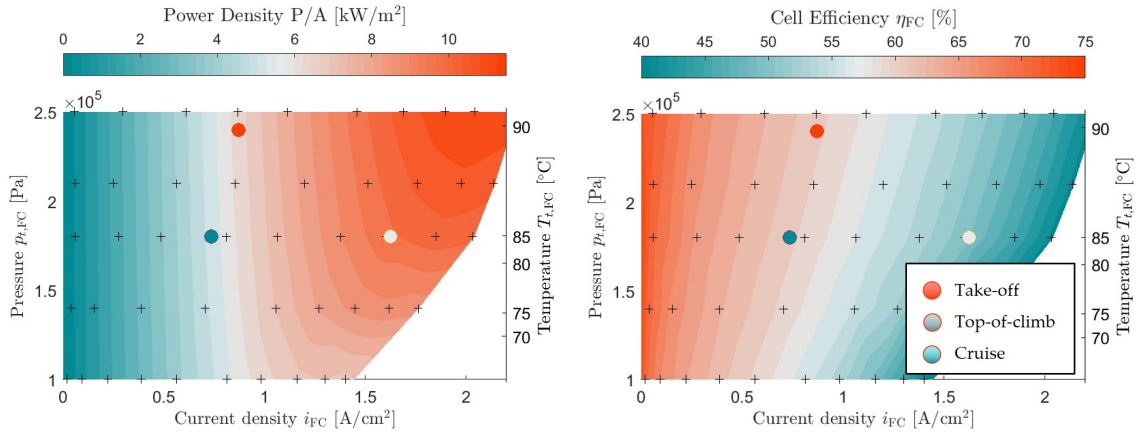

(a) Fuel cell power density.

(b) Fuel cell efficiency.

Figure 5.14: Fuel cell properties across different mission phases, with varying fuel cell settings (current density i_{FC}, pressure $p_{t,FC}$ and temperature $T_{t,FC}$).

As can be seen, different settings are optimal under different ambient conditions and power levels, as discussed before in Sections 5.2-5.5.

For take-off and cruise conditions, the optimal FC settings are those enabling average efficiency and average power density. Power density is maximized for top-of-climb conditions, which is the most power demanding flight phase. This reduces fuel cell efficiency to 50%, which means heat produced is almost 5MW in top-of-climb conditions. Lower fuel cell pressure is beneficial in case of lower ambient pressures, reducing fuel cell temperature to maintain a relative humidity of ϕ_{rel} = 98%. Such a high relative humidity at the fuel cell inlet this high is indicated as essential for fuel cell performance in the literature (see Section 2.3.4).

As can be seen in Table 5.9, fuel mass flow is lowest in cruise, and highest for top-of-climb. This corresponds directly to the required power levels in Table 3.1. Total fuel mass is includes the estimated fuel consumed during climb, cruise, and other mission phases. Fuel required for climb $m_{H_2,\text{climb}}$ was determined from the average fuel mass flow rate in take-off and top-of-climb, and the time to reach cruise altitude. $m_{H_2,\text{climb}}$ is almost a third of $m_{H_2,\text{cruise}}$, highlighting the inefficient usage of the fuel cells at high power density. Fuel required for other mission phases (taxiing, descent, landing, go-around) was assumed 10%.

In reality, the average fuel mass consumed during climb and other mission phases may be higher than estimated here. When $m_{H_2,\text{climb}}$ and $m_{H_2,\text{other}}$ are both increased by 5%, payload is reduced by about 8.7% or 170 kg. This is not only due to increased fuel mass, but also tank mass, which has a relatively low gravimetric efficiency of 23%. This calls for a full mission analysis in further work.

5.6.5. Air Supply System Performance

In this section, performance of the air supply system across different mission phases is discussed. The pressure-enthalpy diagram for the fuel cell air stream from inlet to outlet is shown in Figure 5.15. Note that expansion to ambient conditions from station 7 is not included to highlight the amount of energy remaining in the air stream.

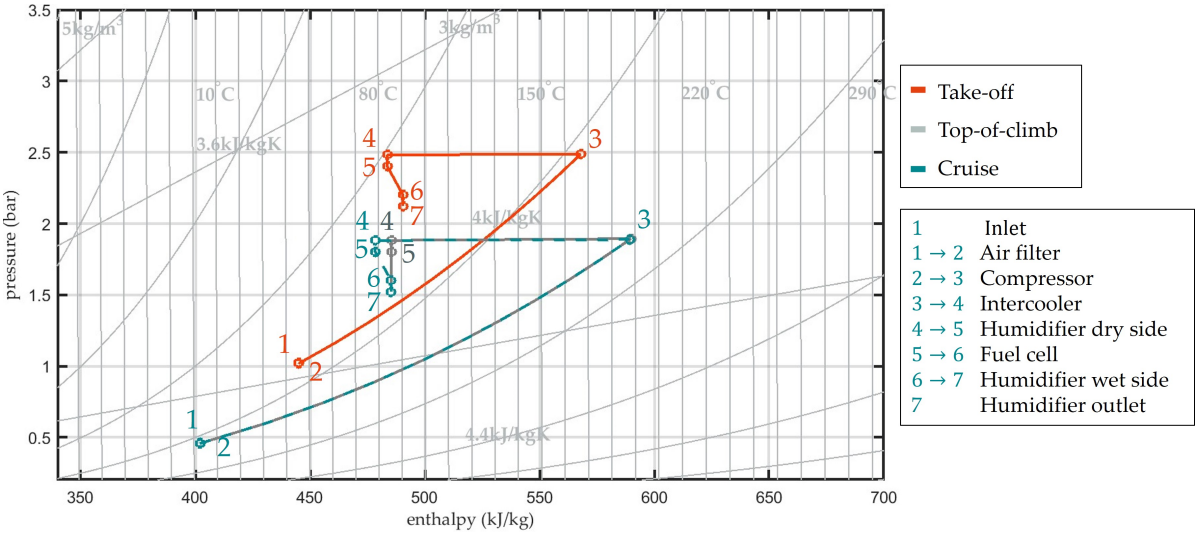

Figure 5.15: Pressure-enthalpy diagram for the air supply system across different mission phases.

First of all, it should be noted that the pressure-enthalpy diagrams for cruise and top-of-climb largely overlap, as fuel cell temperature and pressure are equal and compressor efficiency is assumed constant, as discussed in 5.6.5. Furthermore, note the higher working pressure during take-off conditions, where p = 2.4 bar in the fuel cell (station 5) proved to be optimal.

An intercooler is needed as air temperature rises significantly beyond the desired fuel cell temperature, while pressure is increased in the compressor. Visibly, the intercooler is slightly oversized in cruise and take-off conditions, as was also concluded in Section 5.5, requiring adequate regulation. Notably, pressure drop in the intercooler is negligible, as discussed in Section 5.6.6. Pressure drop along the humidifier was estimated at 8000 Pa (see Section 3.5.4, while pressure drop in the fuel cell was estimated at 20,000 Pa 3.6.2. Also note that the humidifier and fuel cell are assumed isothermal.

At the outlet (station 7), the air is not yet expanded fully to ambient conditions. The total-to-static pressure ratios are shown in Table 5.10, highlighting the potential for power recovery using a turbine. Alternatively, the fuel cell cathode side exhasut air may be used to elevate the ram air pressure in the ram air duct nozzle. However, the difference between corrected fuel cell air mass flow rate and corrected ram air mass flow rate is quite large, as shown in Table 5.10. Therefore, the elevation in total pressure at the nozzle entry will be small, and the positive effect on ram air drag will be marginal.

Table 5.10: Conditions at the air supply system exhaust (station 7) across operating conditions.

Parameter	Take-off	Top-of-climb	Cruise
$p_{t,7}/p_{0,\infty}$ [-]	2.09	3.16	0.76
$\dot{m}_{\text{air supply}}$ [kg/s]	1.40	2.35	1.19
$\dot{m}_{7,\text{ corrected}}$ [kg/s]	2.6	3.16	0.76
$\dot{m}_{\text{ram air, corrected}}$ [kg/s]	33.13	11.77	13.9

Compressor Performance

As shown in Figure 5.15, the pressure ratios to be delivered by the compressor in cruise and top-of-climb conditions are equal, despite the difference in air mass flow. The temperature difference in the compressor is determined by the pressure ratio from Equation 3.32. Since polytropic efficiency is assumed constant, the enthalpy rise is equal for cruise and top-of-climb conditions. The higher P_{comp} observed for top-of-climb is due to an increase in $\dot{m}_{\text{air}}$.

In Figure 5.16, the operating points of the compressor are shown in terms of corrected mass flow, compressor total-to-total pressure ratio and efficiency. Note that detailed compressor design was not performed in this work, so actual efficiency might be higher or lower for the different design solutions. Compressor mass, including electric motor and housing was estimated at 30 kg (Section 3.5.2).

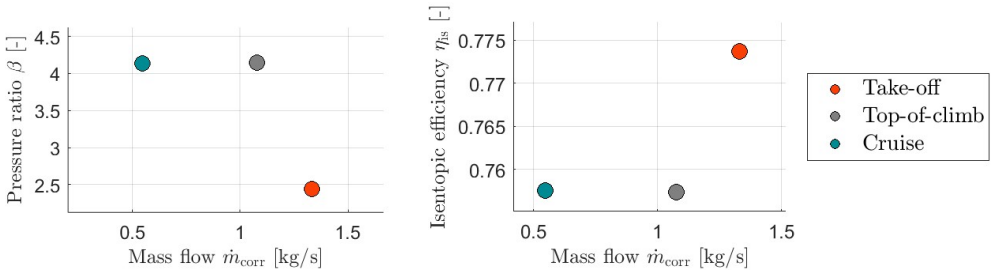

(a) Compressor pressure ratio.

(b) Isentropic compressor efficiency.

Figure 5.16: Compressor pressure ratio and isentropic efficiency vs. corrected mass flow accross different mission phases.

The range of pressure ratios and corrected mass flow as shown in Figure 5.16 seems feasible. However, the isentropic efficiency may be higher than assumed in this model. As discussed in Section 4.3.1, it should be feasible to design a compressor that can operate in these 3 regimes with higher efficiency than reported here. As the compressor operating points for the top-of-climb mission solution lie in between the other scenarios, this should be the on-design solution for the compressor.

Humidifier Performance

In Figure 5.17 the relative humidity and water mass fraction in the air supply system are shown. The assumed inlet relative humidity is 50% for all operating conditions (see Section 3.5.4).

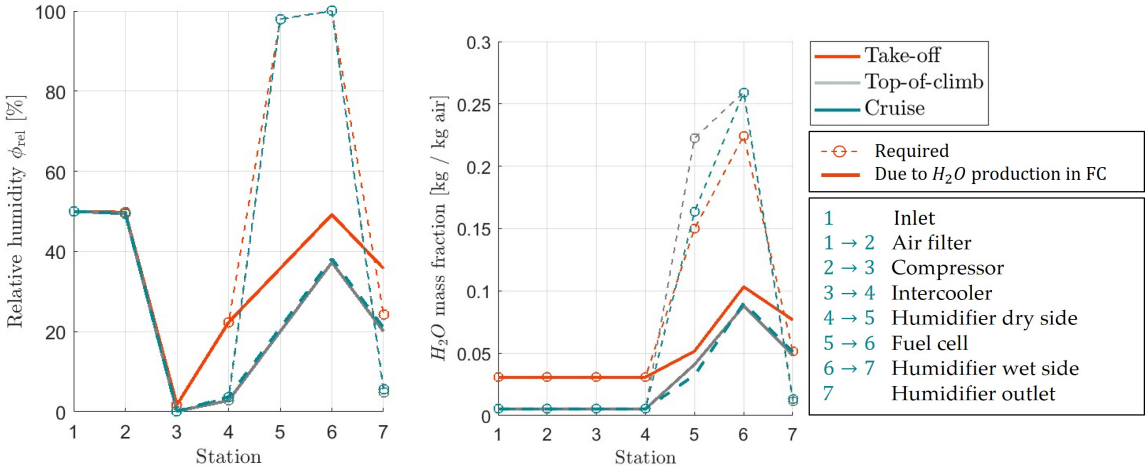

(a) Air relative humidity.

(b) Water mass fraction (kg/kg air).

Figure 5.17: Humidity properties in Air Supply System across different mission phases.

First of all, it can be seen that relative humidity ϕ_{rel} drops significantly within the compressor (station 2 → 3), as temperature is increased significantly. ΔT = 120 °C in take-off and ΔT = 195 °C in cruise and top-of-climb conditions. The increasing pressure increases relative humidity, but the effect on ϕ_{rel} is notably much smaller (see Section 2.3.2). As the intercooler (3 → 4) reduces air temperature to the required fuel cell inlet temperature, relative humidity is slightly increased. Again, despite the difference in $\dot{m}_{air,corr}$, trends are mostly equal for cruise and top-of-climb conditions as enthalpy and pressure are the same. The only difference has its origin in the slightly oversized intercooler in cruise, increasing relative humidity due to a slightly lower temperature before the fuel cell. This also reduces the water mass fraction necessary in the humidifier to reach the high relative humidity.

However, it can be seen that relative humidity is not increased sufficiently, when only considering water production within the fuel cell (station 5 → 6). In this case, the added water in the fuel cell is assumed to be recycled with 100% effectiveness from the humdifier wet side (station 6 → 7), to the humidifier dry side (station 4 → 5). To increase fuel cell inlet relative humidity to the required 98%, adequate water management is required. To have a sufficiently wet membrane in start-up conditions, water must be injected in the humidifier, from a kind of reservoir. Additionally, some water content might be extracted at the outlet (7).

Furthermore, a small difference in relative humidity between the three operating points can be observed. Overall, ϕ_{rel} is slightly larger for take-off conditions. While fuel cell temperature is slightly higher in take-off conditions (ΔT = 5 °C), decreasing ϕ_{rel}, the higher fuel cell pressure increases ϕ_{rel} more (Δp = 60,000 Pa).

Lastly, it can be concluded that a humidifier is required regardless of the ambient relative humidity. Even with very humid air, the reduction in ϕ_{rel} in the compressor is too large to obtain ϕ_{rel}=98% at the fuel cell inlet without any water management. Additionally, extra water must be injected for ϕ_{rel} <80%, as water production inside the fuel cell is not enough to sustain the high required humidity.

5.6.6. Thermal Management System Performance

In this section, the performance of the Thermal Management System (TMS) is discussed. Figure 5.18 shows, for different operating conditions, the pressure and temperature in the mechanically pumped cooling cycle.

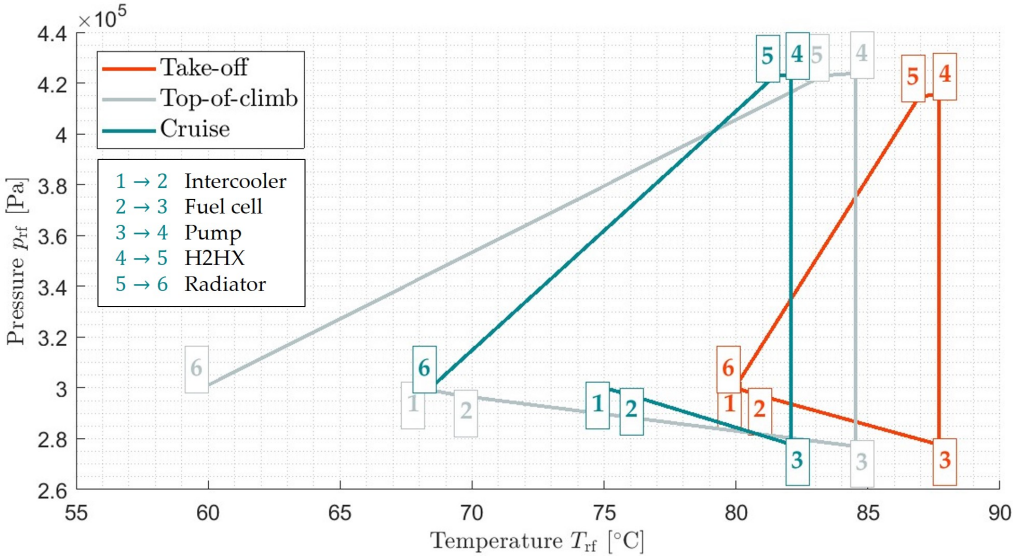

Figure 5.18: Pressure and temperature in the water-eglycol 40/60 cooling loop across different mission phases.

As can be seen in Figure 5.18, for all operating conditions, pressure drop in the radiator (station 5 to 6) is about 1 bar. This is much larger than what was assumed in Chapter 4, where it was decided that pressure drop should be lower than 25000 Pa. This also means that pressure of the coolant, water-eglycol 40/60, must be increased to 4 bar, which should be manageable considering that this is the average water pressure in household water tubing. Pressure is kept lowest in the fuel cell by placing the pump directly behind the fuel cell, thereby limiting stress on the fuel cell membrane. Still, it should be validated that the offset between coolant pressure and air pressure (up to 1.3 bar in cruise and top-of-climb) does not lead to major issues in the fuel cell structural design. A reduction in coolant pressure could lower these stresses.

As a result of the significant pressure drop in the radiator, required pressure rise in the pump is about 1.4 bar for cruise conditions. However, given Equation 3.57, pump power is still very small compared to fuel cell power, as can be seen in Table 5.11. Therefore, the higher pressure drops result in a negligible increase in fuel cell size.

For all operating conditions, coolant temperature is just below the operating temperature of the fuel cell, as expected. For take-off conditions, the offset with $T_{t,\text{FC}}$ is about 2K. When this gap in temperature between the coolant and the fuel cell is reduced further, the width of the duct might be slightly reduced. In cruise, this gap (3K) can also be reduced to increase the temperature difference between the coolant and the ram air. In top-of-climb, this temperature gap is minimal.

Furthermore, it should be noted that there is a temperature discrepancy in top-of-climb and cruise conditions. The offset $\epsilon_{T_{\text{c},6}}$ is summarized in 5.11. As discussed in Section 5.5 as well, the radiator is oversized, requiring adequate regulation. Alternatively, as assessed in Section 5.7, the ram air mass flow can be decreased by implementing a variable inlet and increasing the diffuser area ratio AR. When AR is large enough, it might be possible to reduce drag in top-of-climb and cruise conditions, using the Meredith effect (see Section 3.3).

Fuel cell power and heat production are also shown in Table 5.11. Visibly, the fuel cell is not very efficient in top-of-climb conditions at about 50%, resulting in a large amount of heat to be removed. Still, heat is less effectively removed in take-off conditions, as discussed in Section 5.4, due to the low air mass flow rate.

Table 5.11: Thermal management system performance parameters across operating conditions.

Parameter	Take-off	Top-of-climb	Cruise
$\dot{m}_c$ [kg/s]	48.3	48.3	48.3
P_{pump} [kW]	7.0	7.5	7.4
P_{pump}/P_{FC} [%]	0.41	0.31	0.50
$\epsilon_{T_{c,6}}$ [°C]	-0.04	-8.20	-6.57
P_{FC} [MW]	3.44	4.78	2.95
Q_{FC} [MW]	2.25	4.79	1.92

Radiator Performance

The geometry of the radiator per side of each nacelle is summarized in Table 5.12.

Table 5.12: Radiator geometry specifications for **one** ram air duct.

Parameter	Value	Parameter	Value
Length [m]	0.48	N_{fins} [-]	87020
Width [m]	2.18	N_{tubes} [-]	31650
Height [m]	0.61	$N_{sections}$ [-]	66
h_{fins} [mm]	4.0	d_{fins} [mm]	1.5
t_{fins} [mm]	0.15	d_{tube} [mm]	1.0
t_{tube} [mm]	0.15	Mass [kg]	193

As can be seen, the size of the radiator is significant, and its mass is more than 60% of the total TMS mass (see Figure 5.11). Performance parameters of the radiator are summarized in Table 5.13. Heat rejection percentage in the radiator is determined from the total heat addition in the TMS:

$$Q_{\text{Radiators}}[\%] = \frac{4 \cdot Q_{\text{radiator}}}{2 \cdot Q_{FC} + 2 \cdot Q_{IC}} \cdot 100\% \tag{5.2}$$

Table 5.13: Radiator performance parameters across different mission phases for **one** ram air duct.

Parameter	Take-off	Top-of-climb	Cruise
NTU [-]	1.58	1.49	1.54
Effectiveness ϵ [-]	0.739	0.673	0.731
U_{air} [W/m^2]	83.0	165.0	75.7
UA_{air} [kW]	31.9	61.6	29.2
Δp_{air} [kPa]	1.16	9.06	2.29
U_c [W/m^2]	1495.7	1492.5	1490.7
UA_c [kW]	323.5	322.8	322.5
Δp_c [bar]	1.147	1.229	1.226
$Q_{radiator}$ [kW]	560.9	1867	991.6
$Q_{Radiators}$ [%]	90.4%	141.5%	181.7%

As can be seen, the effectiveness ϵ of the radiator is quite small, as well as the number of transfer units (NTU). Even though h_{fins}, d_{fins} and d_{tube} were optimized within appropriate constraints, length, width and height were fixed according to ram air duct volume constraints. Without these constraints, a longer radiator with a smaller frontal area would potentially result in a higher effectiveness, while also reducing W_{duct}. Alternatively, the inclination angle of the radiator in the ram air duct can be reduced to achieve a similar result. However, this may yield an increase in pressure drop due to the increased fin length. Also, the increased NTU due to increased ϵ may result in a higher mass of the radiator. Concluding, increasing radiator effectiveness is a trade-off between duct width, radiator mass, and ram air pressure drop, each parameter having an effect on payload by impacting drag or weight.

Furthermore, as discussed in Sections 5.6.3 and 5.6.6, the radiator is oversized for top-of-climb and cruise conditions. Heat transfer coeffcients (U_{air} and U_c) are within the expected range as discussed in Section 4.4.1.

Intercooler Performance

The geometry of the intercooler per engine is summarized in Table 5.12.

Table 5.14: Intercooler geometry specifications for **one** engine.

Parameter	Value	Parameter	Value
Length [m]	0.80	N_{fins} [-]	6904
Width [m]	0.49	N_{tubes} [-]	5475
Height [m]	0.41	$N_{sections}$ [-]	24
h_{fins} [mm]	6.6	d_{fins} [mm]	1.6
t_{fins} [mm]	0.15	d_{tube} [mm]	3.5
t_{tube} [mm]	0.15	Mass [kg]	37.5

As can be seen in Table 5.14, when comparing the dimensions of the intercooler with those of the nacelle (WXH = 0.8x1.4, Section 3.5.3), the intercooler should fit within the nacelle. Still, it must be verified whether this is actually feasible in combination with other subsystems.

Performance of the intercooler across different operating conditions is shown in Table 5.15. Notably, effectiveness and NTU are much larger than for the radiator (Table 5.13), as the frontal area-to-length ratio is lower for the intercooler (0.25 vs. 2.77). However, air mass flow is also much larger in the radiator (see Table 5.11), further reducing heat transfer effectiveness. As air is the limiting side of both the radiator and intercooler, a lower mass flow will result in lower $C_{r,min}$, increasing NTU and ϵ (see Appendix A.2).

Table 5.15: Intercooler performance parameters across different mission phases for **one** engine.

Parameter	Take-off	Top-of-climb	Cruise
NTU [-]	3.26	1.96	3.57
Effectiveness ϵ [-]	0.960	0.856	0.971
U_{air} [W/m^2]	98.3	102.1	100.5
UA_{air} [kW]	7.3	7.5	6.9
Δp_{air} [kPa]	0.50	1.22	0.60
U_c [W/m^2]	425	421	423
UA_c [kW]	12.5	12.4	11.5
Δp_c [kPa]	2.32	3.02	2.27
Q_{IC} [kW]	116.6	243.2	131.4

Hydrogen Heat Exchanger

The hydrogen heat exchanger geometry for one engine can be found in Appendix B.1. Note that the hydrogen heat exchanger is sized for one engine. The heat exchangers to warm up the hydrogen stream are assumed to be placed in a separate circuit per engine, for safety considerations. As discussed in Section 2.4.3, these heat exchangers must not be placed in parallel.

To assess to what extent the hydrogen heat exchanger (H2HX) can be used to reject heat from the fuel cell and intercooler and evaporate and heat the hydrogen supply to the fuel cell, heat rejection percentage is defined as:

$$Q_{H2HX}[\%] = \frac{Q_{H2HX}}{Q_{FC} + Q_{IC}} \cdot 100\% \tag{5.3}$$

The results for different fuel cell temperatures and pressures in cruise are shown in Figure 5.19, indicating that different fuel cell settings do not have much influence on H2HX waste heat usage.

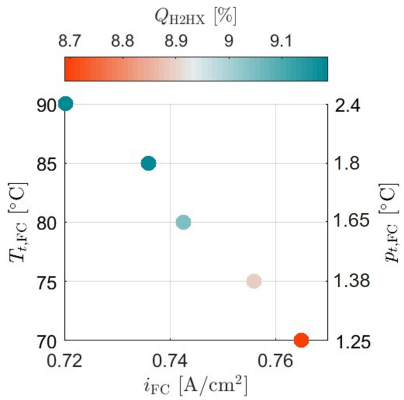

Figure 5.19: Hydrogen heat exchanger waste heat usage in cruise at different fuel cell current density settings.

The performance of the H2HX across different operating condtions is shown in Table 5.16.

Table 5.16: H2HX performance parameters across different mission phases for **one** engine.

Parameter	Take-off	Top-of-climb	Cruise
NTU [-]	6.57	4.83	6.81
Effectiveness ϵ [-]	0.996	0.988	0.997
U_{H_2} [W/m^2]	1195.2	1839.3	1046.1
UA_{H_2} [kW]	4.0	6.2	3.5
Δp_{H_2} [kPa]	3.7	9.3	2.8
U_c [W/m^2]	4778.9	4621.3	4309.6
UA_c [kW]	5.6	5.5	5.1
Δp_c [kPa]	0.9	0.9	0.9
Q_{H2HX} [kW]	119.4	197.1	100.4
Q_{H2HX} [%]	9.6%	7.5%	9.2%

As can be seen in Table 5.16, the percentage of heat rejected to the hydrogen heat exchanger is a little bit higher than expected in Section 2.4.3 (7.5%). While waste heat usage of the H2HX is <10%, it should be mentioned that for instance the cooling power required for the powertrain is not included in the model. This could be as large as 340 kW, given the power in top-of-climb (3.9 MW) and overall powertrain efficiency (91.24%). Since waste heat usage for the H2HX then drops by a marginal amount (to 7.1%), using waste heat for hydrogen fuel conditioning can be considered an efficient strategy to manage a portion of the overall thermal load.

Furthermore, U_c is just higher than the upper bound of the expected range for forced convection using liquid water as coolant (800 - 3000 W/m^2) [178]. It makes sense that water-eglycol 40/60 has a slightly better heat transfer coefficient than water. The average hydrogen heat transfer coefficient U_{H_2} is slightly smaller than in the verification model 4.4.2.

5.7. Design Improvements

To improve the performance of the propulsion system, the impact of small modifications to the baseline design solution or mission are analyzed. The effect of modifications achieved by exploiting state-of-the-art technology is assessed in Section 5.7.1. Then, the combined effects of these technological modifications as well as the impact of technological advancements expected for 2030 are analyzed in Section 5.7.2.

5.7.1. Design Modifications Based on Current Technology

The impact of a few design improvements is assessed, based on what is currently possible. This does therefore not yet include technology projections for coming years. The implemented variations include:

- A **turbine** is added to the air supply system (see Section 2.3.5). The power that can be extracted from the air flow exiting the fuel cell can be approximated using the simple equations in Appendix Section A.7. This results in a compressor power saving of 70.2% fot take-off, 72.3% in top-of-climb and 34.8% in cruise conditions. Equation 3.27 is adapted correspondingly. As such, this will directly affect required fuel cell power and total fuel cell mass.
- The **rate-of-climb (ROC)** can be decreased to 2.5 m/s, reducing required power from 3.9 MW to 3.17 MW in top-of-climb conditions.
- The **flight altitude and flight speed** can be lowered slightly, increasing air density. The chosen cruise conditions include is an altitude of h = 6600 m and u_∞ = 113 m/s. Required power is reduced from 3.9MW to 3.79MW in top-of-climb conditions and from 2.5MW to 2.16MW in cruise conditions.
- **Range** can be sacrificed for **payload**, as is done in the publication by Rietdijk and Selier (2024) [10].

The same procedure to size the propulsion system and to determine the aircraft range is applied for each modification. This means that the propulsion system will be sized for top-of-climb conditions, while the ram air duct width is adapted for take-off. The effects of the five design modifications on payload as a function of the targeted design range are shown in Figures 5.20a and 5.20b. The second figure expresses the relative increase in payload and decrease in range as a percentage of the baseline design. The impact of the uncertainty in L/D_{cruise} on the estimated payload, as discussed in Section 5.6.1, at each design range is also shown for each design modification. While the uncertainty of the baseline design is added as a green semi-transparent box, the upper and lower bounds of the uncertainty associated with each modification are indicated with dashed lines.

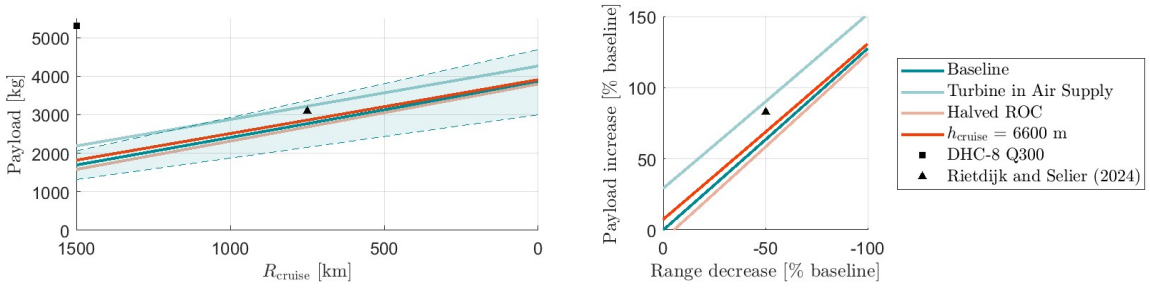

(a) Payload-range limit including uncertainty range.

(b) Percentual payload increase as a function of design range.

Figure 5.20: Impact of modifications to the baseline design, based on current technology.

The effect on propulsion system mass, including the weight of the cryogenic hydrogen tank, of these design changes is shown in Figure 5.21.

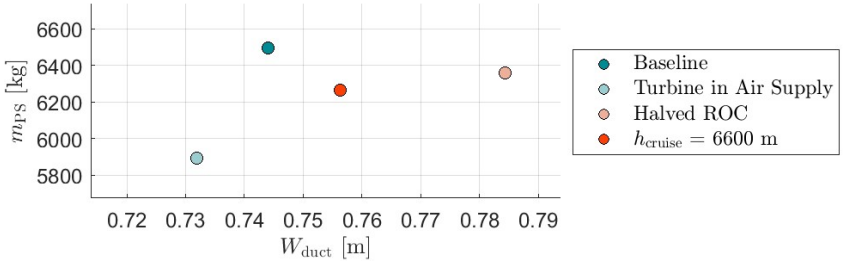

Figure 5.21: Propulsion system mass m_{PS} (including tank mass) and duct width W_{duct} for each design modification.

Firstly, note how the uncertainty in L/D_{cruise} has a larger effect on payload increase or decrease than the design modifications, highlighting the importance of obtaining the correct lift-to-drag ratio to reduce the uncertainty of the design. The following discussion is based on the payload at average $L/D_{\text{cruise}} = 13.6$, at which a payload of 1820 kg is obtained.

The addition of a **turbine** results in promising improvements with respect to the baseline design. Propulsion system mass is decreased by more than 500 kg, due to the reduction in fuel cell size required to drive the compressor in top-of-climb conditions. Furthermore, the required duct width is reduced slightly, as the fuel cell produces less heat at a lower power. At 1500 km, an increase in payload of 29.2%.

Halving the **rate of climb** reduces the fuel cell size and overall propulsion system mass. However, the resulting 3% drop in efficiency at the same take-off power as the baseline design requires the thermal management system (TMS) to dissipate 10% more heat under take-off conditions. This necessitates a larger duct size and increases the TMS mass. This highlights the trade-off between reducing fuel cell size and managing heat dissipation during take-off, a trade-off also observed in the baseline design. Moreover, payload capacity falls below the baseline due to an increase in tank mass. The smaller fuel cell operates less efficiently during cruise, increasing fuel consumption. This suggests that the current fuel cell settings, which were assumed to match those of the baseline design, may not be optimal. Designing the fuel cell for a lower power density could improve efficiency. While this adjustment would slightly increase the fuel cell size, it could enhance overall performance. However, halving the rate of climb doubles the climb time from 25 to 50 minutes, increasing cruise time by 13% (excluding the distance traveled during climb). It is worth noting that the climb phase could be divided into multiple segments starting at a higher rate of climb. For comparison, the DHC-8 Q300 performs its climb in three phases, with an initial climb rate of 1200 ft/min (approximately 6 m/s) and a final climb rate of 1000 ft/min (5 m/s).

Reducing **flight altitude and speed** has only marginal effects on the propulsion system mass, while payload increases by just 7.4%. However, duct size also increases due to the same heat dissipation requirements observed when reducing the rate of climb. Although further reductions in flight altitude could lower the fuel cell mass, they would also necessitate a wider duct. At an altitude of 6600 m, flight time is already extended by 12%, which further increases operational time. In the regional aircraft sector, longer flight times are generally not a compelling alternative, making this approach less viable.

Decreasing range has significant effects on payload, increasing the viability of retrofitted turboprop aircraft as a sustainable alternative at smaller distances. Halving the **range** to 750 km increases payload by about 60.4% to 3118 kg. This is in close agreement with predictions by Rietdijk and Selier, with a difference in estimated payload of less than 1% [10]. However, it is unknown which mass estimates are used by Rietdijk and Selier. Also, estimated fuel weight is a bit lower (40 kg), while estimated propulsion system mass is 20 kg larger. Additionally, mass for a potentially required battery, high-voltage electronics and thermal management and air supply system tubing were for instance not included, which can add O(100 kg).

Aside from these modifications, it is assessed whether **ram air drag** can be reduced efficiently. The following two parameters can be adapted:

- In climb and cruise conditions, the ram air inlet area could be decreased using **adaptable inlet ramps**, narrowing the inlet area. These kind of inlets have been widely implemented in supersonic aircraft such as fighter jets and the Concorde. The increase in **diffuser area ratio** AR slows the air flow down, decreasing the pressure drop in the radiator. The increase in propulsion system weight due to the actuators required to move the panels could be outweighed by generation of a small amount of thrust in top-of-climb and cruise conditions. An example of such a mechanism is shown in Figure 5.22. Another solution could be to integrate extra inlet doors, that can open during take-off and the first part of climb. However, this may increase drag more than with a well-designed variable inlet geometry.

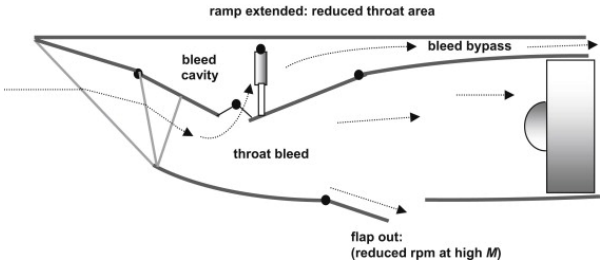

Figure 5.22: Variable intake area mechanism. Reproduced from Sforza (2012) [182]

.

- **An increase in the temperature rise of the airflow in the radiator** may reduce ram air drag. The temperature

rise could be improved when for instance a high temperature PEM fuel cell (HT-PEMFC) is implemented. HT-PEMFC currently have a low technology readiness level (see Section 2.2), but operational temperatures might increase to 180°C . The effect on other components is not considered. While a humidifier is potentially not required, the coolant (water-eglycol 40/60) could potentially be boiling at the increased fuel cell temperature. Equations are shown in Section A.8.

As presented in Figure 5.6, there is a 5°C margin for increasing the diffuser area ratio. This limits mass flow into the ram air duct, reducing cooling power in the radiator. Results for both modifications are shown in Table 5.17, for an area ratio of $AR = 3.0$, without any other changes to the baseline design, and for a fuel cell operational temperature of 180°C.

Table 5.17: Ram air thrust modifications in cruise conditions, for $AR = 3.0$ (scenario 1), $T_{\text{air,radiator}} = 180°C$ and $AR = 3.0$ (scenario 2)

Parameter	Baseline	Scenario 1	Scenario 2
Ram air thrust $F_{\text{t,total}}$ [N]	-2581.5	207.0	991.3
$\Delta p_{t,\text{air}}$ [Pa]	2290	634.9	634.9
u_{fins} [m/s]	32.3	10.33	10.33
$\dot{m}_{\text{air,cruise}}$ [kg/s]	29.4	10.94	10.94

As can be seen, having a variable inlet that could increase AR to 3.0 already improves thrust significantly to over 200 N total in cruise, compared to the baseline design. In case of a drastically increased operating temperature in the radiator, achievable with a HT-PEM fuel cell, combined with the increased AR, ram air thrust is almost tripled.

While this remains a small amount of thrust compared to the 14 kN of thrust required in take-off (4%), the snowball effect of decreased required thrust may provide a reasonable increase in payload. Also, the lift-to-drag ratio is certainly affected, decreasing required cruise fuel mass, thereby increasing payload further.

While thrust is only estimated in cruise, it should be noted that the ram air duct is also oversized in top-of-climb. Although to a lesser extent than during cruise, the aircraft can certainly benefit from an increasing AR during climb.

5.7.2. System Improvement by Combined Modifications and Technological Advancements Expected for 2030

To visualize the impact of the solutions described in the previous section when combined, the analysis is repeated. System sizing is performed for top-of-climb conditions, while the ram air duct width is increased to provide sufficient cooling in take-off off-design conditions.

When combining the modifications that have a large effect and are currently feasible, it can be estimated to what extent payload and range can be increased for a DHC-8 Q300 retrofitted with a LH2FCE propulsion system. The following modifications with large effects are evaluated together:

- **A turbine** is added in the air supply system to reduce compressor power and save fuel cell mass.
- **A variable inlet diffuser** with $AR = 3$ is used in cruise to generate a small amount of thrust.

The resulting system configuration is indicated in the following as "Improved Design". Moreover, to analyze the impact of technological innovations expected for 2030, the following assumptions regarding component performance are made:

- **Specific power of the fuel cell**. Currently a value of 2.04 kW/kg is obtained for the modeled fuel cell stack in top-of-climb conditions. Although Schröter mentions 2.4 kW/kg [17], this value is not reached as power density is not necessarily maximized, as fuel cell efficiency drops in that case. According to predictions by the Aerospace Technology Institute, fuel cell specific power may increase to 9 kW/kg by 2030 (see Section 2.2). This assumes HT-PEM technology.
- **Specific power of the electric motors**: while this is currently estimated at 17 kW/kg based on a publication by MIT, this may increase to 23 kW/kg by 2030 (see Section 2.6).
- **Specific cooling power** of the heat exchangers might be increased towards 10 kW/kg by 2030 (see Section 2.2). This is enabled by HT-PEM techology with an increase in the temperature difference between the coolant of the FC stack and the ambient.
- **Gravimetric efficiency of the liquid hydrogen tanks** may increase significantly up to 61% by 2030. Estimations are based on large integral tanks, while replacing metal vacuum-insulation walls with composite material (see Section 2.5).

These technological advancements are based on a newly designed conceptual regional aircraft and not a retrofitted DHC-8 Q300 [49]. Table 5.18 reports the main assumptions made for the "Improved Design" test case as well those

of a scenario called "Design 2030" where the propulsion system configuration of the "Improved Design" scenario benefits of the technological advancements listed above.

Table 5.18: Comparison of Improved Model results with technological advancements expected for 2030 [54, 146, 66, 139].

Parameter	Improved Design	Design 2030
Fuel cell specific power [kW/kg]	2.04	9
Electric motor specific power [kW/kg]	17	23
Radiator specific cooling power TO [kW/kg]	4.03	10
Intercooler specific cooling power TOC [kW/kg]	2.78	10
H2HX specific cooling power TOC [kW/kg]	2.22	10
Cryogenic tank gravimetric efficiency [%]	23	61

To model 'Design 2030', the 'Improved Model' design parameters will be used as reference. Only the effect of a reduction in system mass is accounted for. A reduction in required duct width can be estimated using the technological advancement in radiator specific cooling power for take-off conditions, and the constraints for radiator volume (see Section 3.3):

$$m_{\text{radiator}} = \rho_{\text{radiator}} \cdot V_{\text{radiator}} = \rho_{\text{radiator}} \cdot 0.61 \cdot 0.65 \cdot W_{\text{duct}} \frac{W_{\text{duct}}}{cos(\theta)}$$

Then, W_{duct} scales with $\sqrt{(m_{\text{radiator}})}$, resulting in a reduction of 36.5%. Results for the 'Improved Design' and 'Design 2030' test cases in terms of feasible payload and range are summarized in Figures 5.23a and 5.23b. In Table 5.19 propulsion system mass and duct width are presented for two test cases.

Table 5.19: Comparison of parameters of the 'Baseline Design', 'Improved Design' and 'Design 2030'.

Parameter	Baseline Design	Improved Design	Design 2030
$m_{\text{PS + tank}}$ [kg]	6364	5823	2040
W_{duct} [m]	0.744	0.738	0.45

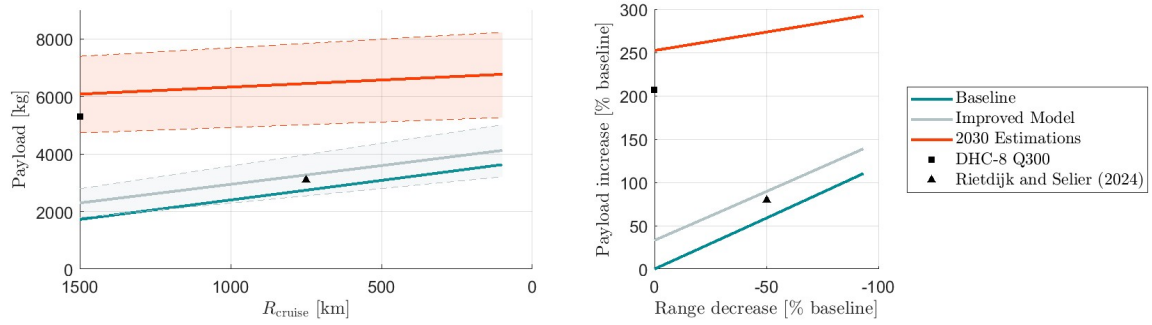

(a) Payload-range limit.

(b) Percentual payload increase a function of design range.

Figure 5.23: Improvements of the 'Improved Model' and 'Design 2030' respect to the baseline design.

First of all, note the large uncertainty in payload in Figure 5.23b due to L/D_{cruise} being uncertain. The analysis of both test cases is based on the average $L/D_{\text{cruise}} = 13.6$.

As can be seen, payload is increased by 33.1% for the Improved Model or about 570 kg. When range is reduced to 750 km, this budget increases to about 3300 kg, still almost 40% below the design payload of the original aircraft. Considering that some systems were not modeled, such as a battery, tubing and high-voltage inverters (Section 3.2.3), it might be possible to reach a design range of 1500 km with approximately the payload estimated by Rietdijk and Selier (3096 kg) [10].

For the 'Design 2030' test case, the payload budget increases beyond that of the original DHC-8 Q300, with an increase of 14.7% for 1500 km. In the worst case, at the lower bound of the uncertainty in L/D_{cruise}, the gap in payload with the reference aircraft is just about 500 kg. However, since ram air drag can be eliminated by using a variable inlet, and as W_{duct} is expected to decrease due to an increase in radiator cooling power, L/D_{cruise} will certainly be larger than the lower bound of L/D_{cruise}. This does not even account for the increased temperature out

of the radiator due to a higher operating temperature with HT-PEM fuel cells. As such, the viability of LH2FCE aircraft for the regional aviation segment is becoming increasingly plausible, provided advancements in specific (cooling) power and gravimetric efficiency continue as projected.

5.8. Discussion and Outlook

Concluding, it has been possible to size the propulsion system of a DHC-8 Q300 retrofitted with a LH2FCE propulsion system, while determining payload and range, based on the required performance and size of the propulsion system in take-off, top-of-climb and cruise.

While there is huge potential for LH2FCE aircraft to establish itself in regional aviation segment and provide a sustainable alternative to kerosene powered aircraft within the coming decade, challenges remain. At the design range of current turboprop aircraft, payload is definitely reduced with current available technology for retrofits, due to relatively low specific power of the propulsion system. Payload is reduced by 58-77% for the selected design solution. There is uncertainty in the L/D-ratio of the reference aircraft, causing large uncertainty in the estimation payload reduction.

While hydrogen is a fuel with 4 times higher energy per mass than kerosene, its energy per volume is about 3 times lower. The tank volume can be reduced significantly by compressing and liquefying hydrogen, but leads to heavy tanks. Cryogenic tanks will need to be integrated with the fuselage (integral tanks) to reduce weight and increase payload. Whereas the engines, fuel tank and fuel systems in turboprop aircraft account for about 5.5% of the MTOM (1048 kg), the LH_2 tank, fuel cell system, thermal management system and air supply system in an aircraft retrofitted with LH2FCE propulsion system account for 34.1% of the MTOM.

Two design modifications to the baseline design solution can lead to increased performance. Firstly, adopting a turbine in the air supply system saves compressor power: about 70% in take-off and top-of-climb conditions, and 35% in cruise. This reduces propulsion system mass and duct size, while increasing the payload by 29.2%. Still, the gap to the original DHC-8 Q300 remains large. Furthermore, when a variable inlet geometry is implemented, the diffuser area ratio can be increased in cruise to eliminate ram air drag. Since the ram air duct is oversized in top-of-climb as well, the same solution can be implemented. However, since cooling power is larger in top-of-climb than in cruise conditions, it might not be possible to increase the diffuser area ratio as much, resulting in some ram air drag still. Including a fan in the ram air duct is therefore recommended for investigation.

However, uncertainties in determination the L/D remain, due to drag from the four ram air ducts. These are most of all required to cool the fuel cell and balance-of-plant during take-off. Under the assumption that these ducts increase C_{D_0} proportionally to the frontal area, the L/D_{cruise} is only decreased by about 3-5% compared to the original aircraft. When ram air drag is taken into account in cruise, which increases C_{D_0} according to $D_{\text{ram air}}/(q_{\text{cruise}}S)$, L/D_{cruise} may be decreased by up to 20-50%. Still, these drag calculations do not include the adverse effects of interference drag, friction drag and propeller blockage, which could lead to a reduction in range. Nevertheless, the large ram air drag may be partially countered by including variable duct geometry such as adjustable inlets, generating a total thrust of about 200N in cruise. Although this is a small amount compared to overall thrust in cruise (4%), ram air drag can be eliminated.

While reducing cruise altitude or the rate-of-climb may appear to be promising design modifications due to the lower power requirements in top-of-climb conditions, the results were not favorable. In both cases, the fuel cell size decreased, reducing the overall propulsion system mass. However, the smaller fuel cell proved less efficient at dissipating thermal power during take-off, as its efficiency dropped by 3% at the same power density as the baseline design. This reduction in efficiency led to a 10% increase in heat dissipation requirements, necessitating a larger TMS and a corresponding increase in duct size and mass. For the reduction in rate-of-climb, payload was actually reduced below the baseline, due to a higher fuel mass flow rate in cruise. The reduction in cruise altitude only provided an increase in payload of 7.4%. Nevertheless, these modifications extended flight time by over 10% in each case, making them less viable as design adjustments.

In a comparative study by Rietdijk and Selier, reaching a design range of 750 km with a payload of 3096 kg is considered to be a viable target in the regional market [10]. Considering the exclusion of some systems (batteries, tubing, high-voltage inverters), reaching the 1500 km design range with a competitive payload (about 3300 kg) appears feasible for refrofits. This means at least 35 passengers can be carried, assuming a passengers weight of 84 kg [183]. A budget of 300 kg remains for the non-modeled systems.

Verification and validation of the heat exchanger models highlighted some model discrepancies (Chapter 4). Radiator heat flux is about 10% smaller than the reference model. When this increase in thermal power is implemented, a reduction in radiator mass may be achieved. On the other hand, H2HX mass is about 30% lower than in the verification data. Since these effects may cancel each other out, and HX mass is only about a quarter of the propulsion system mass (see Section 5.6.2), only the L/D-ratio effects are included in the payload and range uncertainty.

According to estimations by the Aerospace Technology Institute [49] in terms of specific power, cooling power and gravimetric efficiency, performance of current turboprop aircraft can definitely be reached by 2030. While the payload budget increases by 15.9% beyond that of the DHC-8 Q300 at the same design range (1500 km), considerable space is left for the non-modeled systems (~ 1000 kg). When this budget is not entirely filled, LH2FCE aircraft can even outperform current turboprops by 2030. Still, this requires significant research advancements into specific power of fuel cells (2.04 to 9 kW/kg), transition from LT-PEM to HT-PEM, increase in specific power of electric motors (17 to 23 kW/kg), increase in cooling power of heat exchangers (2.22-4.03 to 10 kW/kg) and adoption of composite integral cryogenic hydrogen tanks with increased gravimetric efficiency (23% to 61%).

6

Conclusion & Recommendations

In this chapter, the results and discussions as presented in Chapter 5 are summarized, while answering the research questions proposed in Section 2.7. Furthermore, some recommendations are given regarding the limitations of this work.

6.1. Conclusion

The research question, *'To what extent do fuel cell operational parameters affect payload and range?'* was addressed through sensitivity analysis of **fuel cell temperature, pressure,** and **current density** (Section 5.2). Air stoichiometry and relative humidity were fixed to ensure valid results based on the implemented fuel cell model.

Selecting the optimal current density involves a trade-off: lower **current density** reduces duct width, drag, and fuel consumption, increasing range due to improved efficiency. However, it also increases propulsion system mass, limiting payload capacity. Similarly, optimizing temperature and pressure affects both payload and range. Higher **temperatures** improve radiator heat rejection, reducing ram air mass flow and duct width, while higher **pressures** enhance fuel cell efficiency, further increasing range. However, at top-of-climb conditions, temperatures above $T_{t\text{FC}} = 85°\text{C}$ are less effective, as higher compressor pressure ratios increase fuel cell mass while slightly raising fuel consumption, reducing payload capacity.

The research question, *'What operating conditions constrain the preliminary design of the fuel cell balance-of-plant architecture?'*, was addressed through sensitivity analysis (Section 5.2). The propulsion system should be sized for **top-of-climb conditions** due to higher fuel cell and compressor power requirements, resulting in a larger fuel cell. After completing on-design analysis and selecting design points via a Pareto front, off-design analysis revealed that the ram air duct must be sized for **take-off conditions**. At lower speeds, reduced ram air mass flow outweighs the benefit of higher ambient pressure, leading to an oversized duct in top-of-climb. The best performing Pareto design point showed priority for the lightest propulsion system, as opposed to the smallest duct width. In cruise, the propulsion system remains oversized, improving efficiency and reducing fuel flow. However, specific power of the propulsion system is reduced significantly compared to the reference turboprop, the DHC-8 Q300. A reduction in propulsion system specific power from 1.38 kW/kg to 0.61 kW/kg in top-of-climb conditions reduces the payload budget by 58-77%, depending on L/D_{cruise}. It should be noted that the remaining payload budget has to account for passengers, cargo, crew and some auxiliary systems that are not included in the weight analysis, such as a battery, high-voltage inverters and tubing.

Further insights into the first research question on **fuel cell operational parameters** were provided in Sections 5.3, 5.4 and 5.5. Optimal temperature and pressure settings vary by mission phase:

- In **top-of-climb**, the optimal setting is governed by minimized system mass, at $T_{t\text{FC}} = 85°\text{C}$ and $p_{t\text{FC}} = 1.8$ bar.
- In **take-off** conditions, the optimal setting is governed by the largest temperature difference with the ambient air in the ram air duct, resulting in $T_{t\text{FC}} = 90°\text{C}$ and $p_{t\text{FC}} = 2.4$ bar.
- In **cruise**, the optimal setting depends on the impact on fuel cell lifetime. When decreased operational temperature is desired to improve fuel cell lifetime and maximize payload, $T_{t\text{FC}} = 70°\text{C}$ and $p_{t\text{FC}} = 1.25$ bar can be used. When increased relative humidity is desired for increased fuel cell lifetime, while reducing payload marginally (20 kg), $T_{t\text{FC}} = 85°\text{C}$ and $p_{t\text{FC}} = 1.8$ bar can be selected, resulting in $\phi_{\text{rel}} = 98\%$.

The research question, *'To what extent does ram air duct design affect payload and range?'*, was addressed in Section 5.6.1. Ram air drag may cause a significant decrease in lift-to-drag ratio of 5-30%, directly affecting payload at the design range, depending on the drag calculation method and reference drag polar for the original DHC-8 Q300, for which significant differences were reported in literature. Therefore, the uncertainty in $L/D_{\text{cruise}} = 10.4 - 16.8$ results in payload reduction of 58-77%. Still, these drag calculations do not include the adverse effects of interference drag, friction drag and propeller blockage, which could further reduce payload for the design range. Also, required shaft power was based on the L/D_{cruise} of the original aircraft. While this may further reduce payload, the baseline L/D_{cruise} may be conservative as it was on the lower end of the uncertainty range. The ram air duct proved to be

the only subsystem that had to be sized for take-off off-design conditions (Section 5.4). Four ram air ducts with significant inlet area of 0.61x0.74m were required to cool the radiator adequately at low airspeed and mass flow. As a result, the ducts are oversized duct for top-of-climb and cruise conditions, requiring adequate coolant flow regulation or reduced air flow through the radiator.

The potential to reduce airflow through the ram air ducts in cruise provided the opportunity to answer the research question, *'To what extent can a small amount of thrust be generated from the ram air duct?'* in Section 5.7.1. A variable ram air inlet, increasing AR to 3.0, eliminated ram air drag and **increased ram air thrust to over 200 N**. Additionally, an increase in air temperature out of the radiator, which may be employed when using high-temperature PEM technology in future airborne fuel cell systems, **increased ram air thrust to over 900 N.**

The research question, *''To what extent can a hydrogen heat exchanger be employed to reject heat from the thermal management system?'*, was addressed in Section 5.6.6. Approximately **9% of the heat generated** by the fuel cell and intercooler **can be rejected** in evaporation and heating of the hydrogen fuel. This result showed minimal sensitivity to variations in fuel cell operational temperature and pressure.

The research question, *"To what extent can the addition of turbine enhance payload and range?"*, was answered in Section 5.7.1. It was concluded that the addition of **a turbine** to the air supply system **can save more than 70% compressor power** in top-of-climb and take-off conditions, reducing fuel cell mass. Additionally, about 35% compressor power can be saved in cruise, decreasing fuel mass flow rate. Furthermore, it was determined *"What modifications to the baseline mission can improve payload and range using current technology?"*. **Reducing the rate-of-climb by 50%** and **reducing the cruise altitude to 6600m** proved to have **adverse effects** on duct size. While fuel cell size was decreased, payload was decreased below the baseline for the reduction in rate-of-climb, and only increased by 7.4% for the reduction in cruise altitude. The modifications showed to increase flight time by 10% in each case, making them less viable as design adjustments.

The research question, *'What modifications to the baseline design can improve payload and range, based on technology projections for 2030?'*, was answered in Section 5.7.2. According to projections for 2030, performance of current turboprop aircraft can definitely be reached by 2030. This requires significant research advancements into **specific power of fuel cells** (2.04 to 9 kW/kg), transition from LT-PEM to HT-PEM, increase in **specific power of electric motors** (17 to 23 kW/kg), increase in **specific cooling power of heat exchangers** (2.22-4.03 to 10 kW/kg) and adoption of composite integral cryogenic hydrogen tanks with **increased gravimetric efficiency** (23% to 61%). The payload budget increases by about 15% beyond that of the DHC-8 Q300 at the same design range (1500 km). Considering that this budget is partly filled with the non-modeled systems, the viability of LH2FCE aircraft for the regional aviation segment is becoming increasingly plausible, provided advancements in specific (cooling) power and gravimetric efficiency continue as projected.

Concluding, the main research question *"How are payload and range affected when retrofitting a turboprop aircraft with a liquid hydrogen fuel cell electric propulsion system?"* can be answered. It was concluded in Section 5.8 that **payload is decreased significantly (47-66%), when the design range is that of current turboprop aircraft (1500 km)**, provided a turbine is included in the air supply system and the ram air duct has a variable inlet. However, **reaching a design range of 750 km with a competitive payload (>3000 kg, 35 passengers) appears feasible for retrofits**. This includes a budget of approximately 300 kg for excluded systems in the mass analysis, such as a battery. Additionally, according to projections for 2030, it is plausible that **performance of current turboprop aircraft can be reached by 2030**.

6.2. Recommendations

While the results from lumped parameter analysis give insights on how payload and range are affected when retrofitting a turboprop aircraft with a liquid hydrogen fuel cell electric propulsion system, limitations of the model should be acknowledged to ensure accurate interpretation and to highlight areas for future refinement. Therefore, some important recommendations are made.

First of all, it is recommended that the **lift-to-drag ratio in cruise** is determined accurately, directly affecting payload at the design range. This required an accurate reference L/D_{cruise} for the original DHC-8 Q300, and a **detailed drag analysis** of the **ram air duct** in the wake of the propeller. In this work, the effects of spillage drag, interference drag, air inflow angle, external diffusion, skin friction drag, and reduced thrust due to propeller blockage are not included (Section 3.3.1). Furthermore, the **required shaft power** P_{shaft} should be based on the thrust required to counteract drag from the ram air duct. Adverse effects on the lift-to-drag ratio may be introduced, which is currently estimated to be between 5 to 20% smaller than the reference aircraft. In cruise conditions, ram air drag can be eliminated by introducing a variable inlet, increasing L/D. However, additional estimations in required P_{shaft} and L/D should be performed for top-of-climb and take-off conditons.

Furthermore, it is recommended that **additional operating conditions** are added, such as **initial acceleration in take-off**, before the maximum expected power point (minimum control velocity) (Section 3.2.3). It is uncertain

whether sufficient cooling can be provided at lower power levels and lower mass flows due to decreased air velocity. If not, initial take-off power may need to be reduced, increasing take-off distance. Also, it is uncertain whether the aircraft is able to perform taxiing using the fuel cell system.

The model is limited to steady state analysis (Section 3.2.3). **Transient analysis** would allow for better fuel flow estimates, thereby affecting range. Payload is then again affected by a change in fuel and tank mass. Furthermore, it should be assessed whether the fuel cell can handle high transient loads, and whether the air supply system and thermal management system can respond adequately. The importance of a **battery** can then be highlighted, potentially adding significant mass.

Another mission scenario that may bring challenges is **restart during cold conditions** (Section 3.2.3). The freezing point of water-eglycol 40/60 is significantly lower than water (-52.80°C), but as temperature drops below 0°C viscosity increases to more than 20 times that of water. A dynamic analysis could highlight the response time required to restart engines in case of a fall-out. Potentially, battery mass must be increased to provide electric heating.

Next, it is recommended that a **detailed compressor and turbine analysis** is done. Firstly, it should be verified whether a compressor can efficiently operate across the mission, at different corrected mass flow rates (0.55 - 1.34 kg/s) and pressure ratios (2.44 - 4.12). Efficiency may be maximized for top-of-climb conditions, whereas performance may need to be slightly compromised in cruise and take-off. The operating point of top-of-climb is centered between the other operating conditions, as discussed in Section 4.3.1.

More **detailed analysis** is also recommended for the **heat exchanger** models. The radiator, intercooler and hydrogen heat exchanger (H2HX) models are currently based on the effective-NTU method and averaged properties. Although model prediction are close to those of more details models (see Chapter 4), improvements can be made. Especially in the H2HX model, hydrogen properties such as density and specific heat have non-linear behaviour as temperature increases, an aspect that cannot be captured accurately with an ϵ-NTU based HX model (Section 3.6.4).

Furthermore, it is recommended that a **detailed fuel cell model** is made. The literature data used for the current model assumes inlet streams with slightly lower temperatures (65°C and 98% relative humidity), while the model assumes inlet streams with a temperature equal to the fuel cell stack temperature. Additionally, the assumption that 98% relative humidity improves performance and fuel cell lifetime should be verified. Moreover, a more detailed assessment of heat transfer in the fuel cell to the coolant is necessary, considering heat transfer coefficients, flow characteristics, and channel geometry. The current model assumes that all heat generated by the fuel cell can be transferred to the coolant while maintaining a constant and uniform fuel cell temperature, which may oversimplify actual thermal behaviour.

Regarding thermal management, **powertrain cooling** must be addressed. Although it is estimated that the heat load is only 8.7% compared to the fuel cell in top-of-climb conditions, this can impose additional cooling challenges. Especially during take-off conditions, more air mass flow might be required through the ram air ducts.

Furthermore, it is recommended that adequate water management is installed to maintain high relative humidity in the fuel cell. As discussed in 5.6.5, produced water is not sufficient to maintain balance.

Lastly, **sizing of a battery** is recommended. This component may be vital to support the fuel cell system under high transient loads, such as in take-off. A battery may add significant mass, but the order of magnitude is difficult to estimate. Also, auxiliary components such as high-voltage electronics, tubing and variable ram air inlet actuators should be included in analysis. When the mass of these components is added to the operational empty weight of the reference retrofit, it can be determined how many passengers such an aircraft can carry across the design range.

References

[1] D.S. Lee et al. "The contribution of global aviation to anthropogenic climate forcing for 2000 to 2018". In: *Atmospheric Environment* 244 (2021). DOI: 10.1016/j.atmosenv.2020.117834.

[2] E. S. van der Sman et al. "Destination 2050". In: (2020). Publisher: Netherlands Aerospace Centre NLR. URL: http://hdl.handle.net/10921/1555.

[3] ATAG. *Waypoint 2050*. Air Transport Action Group (ATAG), 2021. URL: https://aviationbenefits.org/media/167417/w2050_v2021_27sept_full.pdf.

[4] Fuel Cells {and} Hydrogen 2 and Clean Sky 2. *Hydrogen-powered aviation: a fact based study of hydrogen technology, economics, and climate impact by 2050*. Publications Office of the European Union, 2020. ISBN: 978-92-9246-342-7. URL: https://data.europa.eu/doi/10.2843/471510.

[5] Tom Koehler. "Boeing makes history with flights of Fuel Cell Demonstrator Airplane". In: (2008). URL: https://cdn.archilovers.com/projects/43ae05e9-c1be-4065-a15c-f3038bcb9dec.pdf.

[6] G. Romeo et al. "ENFICA-FC: Design of transport aircraft powered by fuel cell & flight test of zero emission 2-seater aircraft powered by fuel cells fueled by hydrogen". In: *International Journal of Hydrogen Energy* 38.1 (Jan. 2013), pp. 469–479. DOI: 10.1016/j.ijhydene.2012.09.064.

[7] H2Fly. *World's First Flight of Liquid Hydrogen Aircraft*. H2FLY. 2023. URL: https://www.h2fly.de/2023/09/07/h2fly-and-partners-complete-worlds-first-piloted-flight-of-liquid-hydrogen-powered-electric-aircraft/.

[8] ZeroAvia. *ZeroAvia Successfully Completes Initial Dornier 228 Flight Test Campaign*. 2023. URL: https://zeroavia.com/complete-flight-test/ (visited on 12/11/2023).

[9] Universal Hydrogen. *Universal Hydrogen Successfully Completes First Flight of Hydrogen Regional Airliner*. 2023. URL: https://hydrogen.aero/press-releases/universal-hydrogen-successfully-completes-first-flight-of-hydrogen-regional-airliner/ (visited on 12/08/2023).

[10] B. Rietdijk, M. Selier, and Conscious Aerospace. "Architecture Design for a Commercially Viable Hydrogen-Electric Powered Retrofitted Regional Aircraft". In: 34th ICAS Congress. Vol. Aircraft Design and Integrated System (Applications). Florence, 2024. URL: https://www.icas.org/ICAS_ARCHIVE/ICAS2024/data/preview/ICAS2024_1090.htm.

[11] *ZEROe | Airbus*. Sept. 10, 2024. URL: https://www.airbus.com/en/innovation/energy-transition/hydrogen/zeroe (visited on 11/26/2024).

[12] E.J. Adler and J.R.R.A. Martins. "Hydrogen-powered aircraft: Fundamental concepts, key technologies, and environmental impacts". In: *Progress in Aerospace Sciences* (2023). DOI: 10.1016/j.paerosci.2023.100922.

[13] G. Onorato, P. Proesmans, and M. F. M. Hoogreef. "Assessment of hydrogen transport aircraft: Effects of fuel tank integration". In: *CEAS Aeronautical Journal* (2022). DOI: 10.1007/s13272-022-00601-6.

[14] Ryan O'Hayre et al. *Fuel Cell Fundamentals*. John Wiley & Sons, Ltd, 2016. DOI: 10.1002/9781119191766.fmatter.

[15] P.C. de Boer. "Employing Liquid Hydrogen for Fuel Cell Heat Recovery in Aircraft". In: (2024). URL: https://repository.tudelft.nl/record/uuid:61c71c50-f77e-42d0-b37b-e00c7747e414.

[16] A. te Nijenhuis and A Pauw. *D3.1 - Modelling and design of the hydrogen condtioning and distribution system*. Project: 101101998 - HyPoTraDe - HORIZON-JU-Clean_Aviation-2022-01. 2023.

[17] J. Schröter. "Fuel cell air supply for hydrogen electric propulsion systems in aircraft applications". Dissertation. Universität Ulm, 2023. DOI: 10.18725/OPARU-49048.

[18] F. Beltrame et al. "Optimal design of a ram air cooling duct housing the condenser of an airborne ORC WHR unit". In: GPPS Chania 24. 2024. DOI: 10.33737/gpps24-tc-107.

[19] S. Gudmundsson. "The Anatomy of the Propeller". In: *General Aviation Aircraft Design*. Elsevier, 2014. DOI: 10.1016/B978-0-12-397308-5.00014-3.

[20] J. Mukhopadhaya. *Performance Analysis of Fuel Cell Retrofit Aircraft*. White paper. Washington, D.C.: International Council on Clean Transportation, 2023. URL: https://theicct.org/wp-content/uploads/2023/08/Aircraft-retrofit-white-paper-A4-v3.pdf.

[21] European Commission. *Flightpath 2050 :Europe's vision for aviation : maintaining global leadership and serving society's needs*. LU: Publications Office of the European Union, 2011. URL: https://data.europa.eu/doi/10.2777/50266.

[22] European Commission. "Council Regulation (EU) No 558/2014 of 6 May 2014 establishing the Clean Sky 2 Joint Undertaking". In: Brussels, 2014.

[23] UNFCCC. *The Paris Agreement*. URL: https://unfccc.int/process-and-meetings/the-paris-agreement.

[24] European Commission. *The European Green Deal*. 2019. URL: https://commission.europa.eu/strategy-and-policy/priorities-2019-2024/european-green-deal_en.

[25] Clean Aviation. *Strategic Research and Innovation Agenda (SRIA)*. URL: https://www.clean-aviation.eu/strategic-research-and-innovation-agenda-sria.

[26] IATA. *Net-Zero Carbon Emissions by 2050*. URL: https://www.iata.org/en/pressroom/pressroom-archive/2021-releases/2021-10-04-03/.

[27] Airbus. *What is sustainable aviation fuel (SAF)?* 2022. URL: https://www.airbus.com/en/sustainability/respecting-the-planet/decarbonisation/sustainable-aviation-fuels.

[28] IATA. *Developing Sustainable Aviation Fuel (SAF)*. 2021. URL: https://www.iata.org/en/programs/environment/sustainable-aviation-fuels/.

[29] M.D. F. Shahriar and A. Khanal. "The current techno-economic, environmental, policy status and perspectives of sustainable aviation fuel (SAF)". In: *Fuel* (2022). DOI: 10.1016/j.fuel.2022.124905.

[30] Rafael Belo Duarte et al. "A bibliometric analysis on sustainable aviation fuels: core technologies, challenges and trends". In: *Universal Journal of Carbon Research* (2023). DOI: 10.37256/ujcr.1220234147.

[31] S. Baumeister, T.K. Simic, and E. Ganic. "Emissions reduction potentials in business aviation with electric aircraft". In: *Transportation Research Part D* (2024). DOI: https://doi.org/10.1016/j.trd.2024.104415.

[32] R.E. Wolleswinkel et al. "A New Perspective on Battery-Electric Aviation, Part I: Reassessment of Achievable Range". In: *Proceedings of the AIAA SCITECH 2024 Forum* (2024). DOI: 10.2514/6.2024-1489.

[33] R. de Vries et al. "A New Perspective on Battery-Electric Aviation, Part II: Conceptual Design of a 90-Seater". In: *Proceedings of the AIAA SCITECH 2024 Forum* (2024). DOI: 10.2514/6.2024-1490.

[34] Pipistrel. *Velis Electro*. Pipistrel. 2024. URL: https://www.pipistrel-aircraft.com/products/velis-electro/.

[35] Eviation. *Aircraft – Eviation*. 2024. URL: https://www.eviation.com/aircraft/.

[36] J. Mukhopadhaya and Brandon Graver. "Performance analysis of regional electric aircraft". In: (2022). Publisher: International Council on Clean Transportation. DOI: 10.13140/RG.2.2.30087.16803.

[37] I. Staack, Alejandro Sobron, and Petter Krus. "The potential of full-electric aircraft for civil transportation: from the Breguet range equation to operational aspects". In: *CEAS Aeronautical Journal* (2021). DOI: 10.1007/s13272-021-00530-w.

[38] N. Thonemann et al. "Towards sustainable regional aviation: Environmental potential of hybrid-electric aircraft and alternative fuels". In: *Sustainable Production and Consumption* (2024), S2352550924000137. DOI: 10.1016/j.spc.2024.01.013.

[39] V. Sosounov and V. Orlov. "Experimental turbofan using liquid hydrogen and liquid natural gas as fuel". In: *26th Joint Propulsion Conference*. Joint Propulsion Conferences. American Institute of Aeronautics and Astronautics, 1990. DOI: 10.2514/6.1990-2421.

[40] Airbus Deutschland GmbH. *Liquid hydrogen fuelled aircraft - system analysis (CRYOPLANE)*. CORDIS | European Commission. 2002. URL: https://cordis.europa.eu/project/id/G4RD-CT-2000-00192.

[41] A. Schwander. *Bei Tupolew fand die Wasserstoff-Zukunft vor 30 Jahren statt*. strom-online. 2021. URL: https://strom-online.ch/bei-tupolew-fand-die-wasserstoff-zukunft-vor-30-jahren-statt/.

[42] H.G. Klug and R. Faass. "CRYOPLANE: hydrogen fuelled aircraft — status and challenges". In: *Air & Space Europe* 3.3 (2001). DOI: 10.1016/S1290-0958(01)90110-8.

[43] N. Lapeña-Rey et al. "First Fuel-Cell Manned Aircraft". In: *Journal of Aircraft* (2010). DOI: 10.2514/1.42234.
[44] *Boeing's chief sustainability officer: 'We can't count on hydrogen-powered commercial flights before 2050'*. Fortune. 2023. URL: https://fortune.com/2023/01/26/boeings-chief-sustainability-officer-we-cant-count-on-hydrogen-powered-commercial-flights-before-2050/.
[45] *Bombardier Q Series*. 2018. URL: https://web.archive.org/web/20180416074022/https://commercialaircraft.bombardier.com/content/dam/Websites/bombardiercom/supporting-documents/BA/Bombardier_Q%20Series_Final.pdf.
[46] H. Degirmenci et al. "Challenges, prospects and potential future orientation of hydrogen aviation and the airport hydrogen supply network: A state-of-art review". In: *Progress in Aerospace Sciences* (2023). DOI: 10.1016/j.paerosci.2023.100923.
[47] *HYPORT: the first green hydrogen production and distribution station in Europe has opened | ENGIE*. Engie.com. 2023. URL: https://www.engie.com/en/news/hyport-green-hydrogen.
[48] K.M. Spencer and C.A. Martin. *Investigation of Potential Fuel Cell Use in Aircraft*. Technical Report IDA Document D-5043. Insitute for Defence Analysis (IDA), 2013. URL: https://www.ida.org/-/media/feature/publications/i/in/investigation-of-potential-fuel-cell-use-in-aircraft/d-5043.ashx.
[49] *FlyZero Zero Carbon Emission Aircraft Concepts*. Aerospace Technology Institute, 2022. URL: https://www.ati.org.uk/wp-content/uploads/2022/03/FZO-AIN-REP-0007-FlyZero-Zero-Carbon-Emission-Aircraft-Concepts.pdf.
[50] Q. Chen et al. "Thermal management of polymer electrolyte membrane fuel cells: A review of cooling methods, material properties, and durability". In: *Applied Energy* (2021). DOI: 10.1016/j.apenergy.2021.116496.
[51] Toyota. *Introducing the all-new Toyota Mirai*. 2020. URL: https://newsroom.toyota.eu/introducing-the-all-new-toyota-mirai/.
[52] G. Polek. *Airbus Unveils 'Podded' Engine Design for ZEROe Program | AIN*. 2020. URL: https://www.ainonline.com/aviation-news/air-transport/2020-12-15/airbus-unveils-podded-engine-design-zeroe-program.
[53] *Universal Hydrogen tests 1MW fuel cell propulsion system with liquid hydrogen*. Aerospace Testing International. 2024. URL: https://www.aerospacetestinginternational.com/news/electric-hybrid/universal-hydrogen-tests-1mw-fuel-cell-propulsion-system-with-liquid-hydrogen.html.
[54] *Fuel Cells Roadmap Report*. Aerospace Technology Institute, 2022. URL: https://www.ati.org.uk/wp-content/uploads/2022/03/FZO-PPN-COM-0033-Fuel-Cells-Roadmap-Report.pdf.
[55] J. Larminie and A. Dicks. *Fuel cell systems explained*. 2nd. Wiley, 2003. DOI: 10.1002/9781118706992.
[56] M.D. Fernandes et al. "SOFC-APU systems for aircraft: A review". In: *International Journal of Hydrogen Energy* (2018). DOI: 10.1016/j.ijhydene.2018.07.004.
[57] E. Waddington, J.M. Merret, and PhJ.illip J. Ansell. "Impact of LH2Fuel Cell-Electric Propulsion on Aircraft Configuration and Integration". In: *AIAA AVIATION 2021 FORUM*. AIAA AVIATION Forum. American Institute of Aeronautics and Astronautics, 2021. DOI: 10.2514/6.2021-2409. URL: https://arc.aiaa.org/doi/10.2514/6.2021-2409.
[58] Q. Yuan et al. "Performance Analysis and Optimization of SOFC/GT Hybrid Systems: A Review". In: *Energies* (2024). Number: 5 Publisher: Multidisciplinary Digital Publishing Institute. DOI: 10.3390/en17051265.
[59] M.A. Azizi and J. Brouwer. "Progress in solid oxide fuel cell-gas turbine hybrid power systems: System design and analysis, transient operation, controls and optimization". In: *Applied Energy* (2018). DOI: 10.1016/j.apenergy.2018.01.098.
[60] A. Hagen, H. Langnickel, and X. Sun. "Operation of solid oxide fuel cells with alternative hydrogen carriers". In: *International Journal of Hydrogen Energy* (2019). DOI: 10.1016/j.ijhydene.2019.05.065.
[61] H. Liu et al. "Comparative study of fuel types on solid oxide fuel cell – gas turbine hybrid system for electric propulsion aircraft". In: *Fuel* (2023). DOI: 10.1016/j.fuel.2023.128426.
[62] T. Choudhary et al. *Thermodynamic Modeling of Blade Cooled Turboprop Engine Integrated to Solid Oxide Fuel Cell: A Concept*. SAE International, 2018. DOI: 10.4271/2018-01-1308.
[63] M. Zhou et al. "Modeling the Performance Degradation of a High-Temperature PEM Fuel Cell". In: *Energies* (2022). Number: 15 Publisher: Multidisciplinary Digital Publishing Institute. DOI: 10.3390/en15155651.
[64] *HyPoint - we make zero emission air transport possible*. URL: https://hypoint.com/.
[65] Luchtvaart in Transitie. *Embraer waterstof-demonstratievliegtuig*. 2023. URL: https://luchtvaartintransitie.nl/project-item/embraer-demovliegtuig/.
[66] *Thermal Management Roadmap Report*. 2022. URL: https://docplayer.net/232086780-Thermal-management-roadmap-report-fzo-ppn-com-published-march-2022.html.
[67] J. Jiang et al. "Optimization of Operating Parameters on Proton Exchange Membrane Fuel Cells for Efficiency". In: *Journal of Undergraduate Chemical Engineering Research* (2021). URL: https://bpb-us-e1.wpmucdn.com/you.stonybrook.edu/dist/f/2071/files/2021/05/pgs-63-71.pdf.
[68] RVO and Netherlands Aerospace Centre - NLR. *CATHINCA*. RVO.nl. 2023. URL: https://www.rvo.nl/subsidies-financiering/tsh-vliegtuigmaakindustrie/geselecteerde-projecten.
[69] B. Blunier and A. Miraoui. "Air management in PEM fuel cells: State-of-the-art and prospectives". In: 2007 International Aegean Conference on Electrical Machines and Power Electronics (ACEMP) and Electromotion '07. Bodrum, Turkey: IEEE, 2007. DOI: 10.1109/ACEMP.2007.4510510.
[70] F. Barbir. "PEM Fuel Cells". In: *Fuel Cell Technology: Reaching Towards Commercialization*. Ed. by N. Sammes. Springer, 2006. ISBN: 978-1-84628-207-2. DOI: 10.1007/1-84628-207-1_2.
[71] Y. Kim et al. "A polyoxometalate coupled graphene oxide–Nafion composite membrane for fuel cells operating at low relative humidity". In: *Journal of Materials Chemistry A* (2015). DOI: 10.1039/C5TA00182J.
[72] O.S. Ijaodola et al. "Energy efficiency improvements by investigating the water flooding management on proton exchange membrane fuel cell (PEMFC)". In: *Energy* (2019). DOI: 10.1016/j.energy.2019.04.074.
[73] L. Fan, Zhengkai Tu, and Siew Hwa Chan. "Recent development of hydrogen and fuel cell technologies: A review". In: *Energy Reports* (2021). DOI: 10.1016/j.egyr.2021.08.003.
[74] D.G. Sanchez et al. "Effect of the Inlet Gas Humidification on PEMFC Behavior and Current Density Distribution". In: *ECS Transactions* (2014). ISSN: 1938-5862, 1938-6737. DOI: 10.1149/06403.0603ecst.
[75] Q. Yan et al. "Effect of sub-freezing temperatures on a PEM fuel cell performance, startup and fuel cell components". In: *Journal of Power Sources* (2006). DOI: 10.1016/j.jpowsour.2006.02.075.
[76] M. Schröder et al. "Optimal operating conditions of PEM fuel cells in commercial aircraft". In: *International Journal of Hydrogen Energy* (2021). DOI: 10.1016/j.ijhydene.2021.07.099.
[77] H Kim et al. "Effects of key operating parameters on the efficiency of two types of pem fuel cell systems (High-Pressure and Low-Pressure operating) for Automotive Applications". In: *Journal of Mechanical Science and Technology* (2005). DOI: 10.1007/BF02919185.
[78] Dietmar Filsinger, Gen Kuwata, and Nobuyuki Ikeya. "Tailored Centrifugal Turbomachinery for Electric Fuel Cell Turbocharger". In: *International Journal of Rotating Machinery* (2021). Ed. by Gerard Bois. DOI: 10.1155/2021/3972387.
[79] G. Romeo et al. "Air Cooling of a Two-Seater Fuel Cell–Powered Aircraft: Dynamic Modeling and Comparison with Experimental Data". In: *Journal of Aerospace Engineering* (2012). Publisher: American Society of Civil Engineers. DOI: 10.1061/(ASCE)AS.1943-5525.0000138.
[80] C. Werner, l. Busemeyer, and J. Kallo. "The impact of operating parameters and system architecture on the water management of a multifunctional PEMFC system". In: *International Journal of Hydrogen Energy* (2015). DOI: 10.1016/j.ijhydene.2015.02.012.
[81] Green Car Congress. *Toyota details design of fuel cell system in Mirai; work on electrode catalysts*. 2016. URL: https://www.greencarcongress.com/2016/04/20160419-toyota.html.
[82] S. Campanari et al. "Performance Assessment of Turbocharged Pem Fuel Cell Systems for Civil Aircraft Onboard Power Production". In: *Journal of Engineering for Gas Turbines and Power* (2008). DOI: 10.1115/1.2772636.
[83] J. Hoeflinger and P. Hofmann. "Air mass flow and pressure optimisation of a PEM fuel cell range extender system". In: *International Journal of Hydrogen Energy* (2020). DOI: 10.1016/j.ijhydene.2020.07.176.

[84] S. Abuelsamid. *Bosch To Invest $1.3 Billion In Hydrogen Technology By 2025*. Forbes. Section: Cars & Bikes. 2022. URL: https://www.forbes.com/sites/samabuelsamid/2022/06/07/bosch-to-invest-13b-in-hydrogen-technology-by-2025/.

[85] A. Scoccimarro. "Preliminary design methods for the thermal management of fuel cell powered aeroengines". In: (2023). URL: https://repository.tudelft.nl/islandora/object/uuid%3A9a16e0f8-722d-4a17-9f79-96cea2de6906.

[86] Tom Hoogerdijk. "Aircraft Integration of Air-Based Thermal Management Systems for Propulsive Fuel Cell Systems". In: (2023). URL: https://repository.tudelft.nl/islandora/object/uuid%3A592ad30f-93b3-4d01-9fec-9786616dd9c4.

[87] D. Quillet et al. "Parallel Hybrid-Electric Powertrain Sizing on Regional Turboprop Aircraft with Consideration for Certification Performance Requirements". In: AIAA AVIATION 2021 FORUM. Aug. 2, 2021. DOI: 10.2514/6.2021-2443.

[88] A. Fly and R.H. Thring. "A comparison of evaporative and liquid cooling methods for fuel cell vehicles". In: *International Journal of Hydrogen Energy* (2016). DOI: 10.1016/j.ijhydene.2016.06.089.

[89] R.C. van Benthem et al. *Hydrogen Drone Research Aircraft*. NLR - Royal Netherlands Aerospace Centre, 2020. URL: https://www.nlr.org/wp-content/uploads/2022/04/NLR-TP-2020-041.pdf.

[90] G. Zhang and S.G. Kandlikar. "A critical review of cooling techniques in proton exchange membrane fuel cell stacks". In: *International Journal of Hydrogen Energy* (2012). DOI: 10.1016/j.ijhydene.2011.11.010.

[91] H.J. van Gerner et al. "Fluid selection for space thermal control systems". In: 44th International Conference on Environmental Systems. ICES, 2014. URL: http://hdl.handle.net/2346/59591.

[92] R. C. van Benthem et al. *Development of a Mechanically Pumped Fluid Loop for 3 to 6 kW Payload Cooling*. SAE International, 2009. DOI: 10.4271/2009-01-2350.

[93] J. van Es et al. "Mini Mechanically Pumped Loop Modelling, Design and Tests for standardized CubeSat thermal control". In: *50th International Conference on Environmental Systems*. ICES, 2021. URL: https://hdl.handle.net/2346/87057.

[94] M.H.S. Bargal et al. "Liquid cooling techniques in proton exchange membrane fuel cell stacks: A detailed survey". In: *Alexandria Engineering Journal* (2020). DOI: 10.1016/j.aej.2020.02.005.

[95] M.C. Ellis and R.C. Kurwitz. "Development of a Pumped Two-phase System for Spacecraft Thermal Control". In: 46th International Conference on Environmental Systems. ICES, 2016. URL: http://hdl.handle.net/2346/67645.

[96] Y. Lasbet et al. "A chaotic heat-exchanger for PEMFC cooling applications". In: *Journal of Power Sources* (2006). DOI: 10.1016/j.jpowsour.2005.08.030.

[97] T. Luten. *Characterization of the Onset of Boiling for Ammonia in Minichannels*. Publisher: University of Twente. Dec. 22, 2022. URL: https://essay.utwente.nl/93859/.

[98] H.J. van Gerner and Netherlands Aerospace Centre - NLR. *Coolant temperature gradient in airborne fuel cells*. Personal Communication. May 2024.

[99] E.J. Choi, J.Y. Park, and M.S. Kim. "Two-phase cooling using HFE-7100 for polymer electrolyte membrane fuel cell application". In: *Applied Thermal Engineering* (2019). DOI: 10.1016/j.applthermaleng.2018.11.103.

[100] R.W. Morse et al. "Critical heat flux and the dryout of liquid film in vertical two-phase annular flow". In: *International Journal of Heat and Mass Transfer* (2021). DOI: 10.1016/j.ijheatmasstransfer.2021.121487.

[101] *Brava project*. BRAVA. URL: https://brava-project.eu/partner/nlr/.

[102] The Engineering ToolBox. *Ethylene Glycol Heat-Transfer Fluid Properties*. 2003. URL: https://www.engineeringtoolbox.com/ethylene-glycol-d_146.html.

[103] T. Luten and Netherlands Aerospace Centre - NLR. *Air Pressure Drop in a Straight-fin Heat Exchanger in Free-stream Conditions*. Personal Communication. May 2024.

[104] E.W. Lemmon, M.L. Huber, and M.O. McLinden. "NIST Standard Reference Database 23: Reference Fluid Thermodynamic and Transport Properties-REFPROP, Version 9.1". In: *NIST* (2013). Last Modified: 2021-06-02T18:30-04:00 Publisher: Eric W. Lemmon, Marcia L. Huber, Mark O. McLinden. URL: https://www.nist.gov/publications/nist-standard-reference-database-23-reference-fluid-thermodynamic-and-transport.

[105] *EASA Certification Specification for Engines*. EASA, 2007. URL: https://www.easa.europa.eu/en/downloads/1651/en.

[106] *NFPA 704 Standard Development*. 2024. URL: https://www.nfpa.org/codes-and-standards/nfpa-704-standard-development/704.

[107] European Commission. "Regulation (EU) 2024/573 of the European Parliament and of the Council of 7 February 2024 on fluorinated greenhouse gases, amending Directive (EU) 2019/1937 and repealing Regulation (EU) No 517/2014". In: (2024). URL: https://eur-lex.europa.eu/eli/reg/2024/573/oj.

[108] M.F. Ahlers. "Aircraft Thermal Management". In: *Encyclopedia of Aerospace Engineering*. John Wiley & Sons, Ltd, 2011. DOI: 10.1002/9780470686652.eae046.

[109] B.T. Schiltgen and J. Freeman. "Aeropropulsive Interaction and Thermal System Integration within the ECO-150: A Turboelectric Distributed Propulsion Airliner with Conventional Electric Machines". In: 16th AIAA Aviation Technology, Integration, and Operations Conference. American Institute of Aeronautics and Astronautics, June 13, 2016. DOI: 10.2514/6.2016-4064.

[110] F. W. Meredith. *Cooling of aircraft engines with special reference to ethylene glycol radiators enclosed in ducts*. Accepted: 2014-10-21T12:03:22Z. H. M. Stationery Office, 1935. URL: https://reports.aerade.cranfield.ac.uk/handle/1826.2/1425.

[111] G. Aceto. *In the P-51 Mustang's Wake*. 2019. URL: https://www.historynet.com/in-the-mustangs-wake/.

[112] L. Piancastelli, L. Frizziero, and G. Donnici. "The Meredith Ramjet: An Efficient Way to Recover the Heat Wasted in Piston Engine Cooling". In: (2015). URL: https://www.enginehistory.org/Installations/MeredithRamjet.pdf.

[113] *P-51 Gunfighter*. Commemorative Air Force. URL: https://commemorativeairforce.org/aircraft/22.

[114] D. Kozulovic. "Heat Release of Fuel Cell Powered Aircraft". In: GPPS Chania20. 2020. DOI: 10.33737/gpps20-tc-99.

[115] M.R. Nichols. *Investigation of flow through an intercooler set at various angles to the supply duct*. 1942. URL: https://ntrs.nasa.gov/citations/19930093676.

[116] L. Henriksson et al. "Experimental Investigation of Heat Transfer Rates and Pressure Drops through Compact Heat Exchangers - Where the Heat Exchanger is Angled Relative to the Incoming Airflow -". In: *International Journal of Automotive Engineering* (2015). DOI: 10.20485/jsaeijae.6.1_7.

[117] *Microtubes - Innovation in Heat Exchangers*. Mezzo Technologies. URL: https://mezzotechnologies.com/why-microtubes/.

[118] H. Lim, U Han, and H. Lee. "Design optimization of bare tube heat exchanger for the application to mobile air conditioning systems". In: *Applied Thermal Engineering* (2020). DOI: 10.1016/j.applthermaleng.2019.114609.

[119] H. Kellermann et al. "Design and Optimization of Ram Air–Based Thermal Management Systems for Hybrid-Electric Aircraft". In: *Aerospace* (2021). Number: 1 Publisher: Multidisciplinary Digital Publishing Institute. DOI: 10.3390/aerospace8010003.

[120] *CAeS integrates hydrogen fuel cell technology into Islander nacelle*. 2024. URL: https://pilotweb.aero/news/caes-integrates-hydrogen-fuel-cell-technology-into-islander-nacelle/.

[121] *CAeS successfully integrates hydrogen fuel cell technology into an aircraft*. The Engineer. 2024. URL: https://www.theengineer.co.uk/content/news/caes-successfully-integrates-hydrogen-fuel-cell-technology-into-an-aircraft/.

[122] A.K. te Nijenhuis and Netherlands Aerospace Centre - NLR. *Hydrogen Heat Exchanger employing Fuel Cell Waste Heat*. Personal Communication. June 2024.

[123] NIST. *REFPROP wrapper MATLAB*. GitHub. 2023. URL: https://github.com/usnistgov/REFPROP-wrappers/blob/master/wrappers/MATLAB/legacy/refpropm.m.

[124] A. Brenk et al. "The effect of geometrical modifications to a shell and tube heat exchanger on performance and freezing risk during LNG regasification". In: *International Journal of Heat and Mass Transfer* (2020). DOI: 10.1016/j.ijheatmasstransfer.2020.120247.

[125] A. S. J. van Heerden et al. "Aircraft thermal management: Practices, technology, system architectures, future challenges, and opportunities". In: *Progress in Aerospace Sciences* (2022). DOI: 10.1016/j.paerosci.2021.100767.

[126] Tekang Wang, Colin Britcher, and Preston Martin. "Surface heat exchangers for aircraft applications - A technical review and historical survey". In: 37th Aerospace Sciences Meeting and Exhibit. Reno,NV,U.S.A.: American Institute of Aeronautics and Astronautics, 1999. DOI: 10.2514/6.1999-119.

[127] Hariharan Kallath et al. "Computational Study on the Aerodynamics of a Surface-Heated Wing for Thermal Management". In: *AIAA Journal* (2020). Publisher: American Institute of Aeronautics and Astronautics. DOI: 10.2514/1.J059220.

[128] H. Kellermann, A.L. Habermann, and M. Hornung. "Assessment of Aircraft Surface Heat Exchanger Potential". In: *Aerospace* (2020). Number: 1 Publisher: Multidisciplinary Digital Publishing Institute. DOI: 10.3390/aerospace7010001.

[129] Q. Su et al. "A review of loop heat pipes for aircraft anti-icing applications". In: *Applied Thermal Engineering* (2018). DOI: 10.1016/j.applthermaleng.2017.11.030.

[130] R. Hann et al. "Experimental Heat Loads for Electrothermal Anti-Icing and De-Icing on UAVs". In: *Aerospace* (2021). DOI: https://doi.org/10.3390/aerospace8030083.

[131] S. Schaefer et al. "Integration of a Cooling System Architecture with a Skin Heat Exchanger for High Thermal Loads in Fuel Cell Powered Aircraft". In: International Refrigeration and Air Conditioning Conference. Purdue University, 2022. URL: https://docs.lib.purdue.edu/iracc/2347/.

[132] H. Lohse-Busch et al. *Technology Assessment Of A Fuel Cell Vehicle: 2017 Toyota Mirai*. Argonne National Lab, 2018. DOI: 10.2172/1463251. URL: https://www.osti.gov/biblio/1463251.

[133] G Brewer. "Aviation usage of liquid hydrogen fuel—prospects and problems". In: *International Journal of Hydrogen Energy* (1976). DOI: 10.1016/0360-3199(76)90011-2.

[134] F. Troeltsch et al. "Hydrogen Powered Long Haul Aircraft with Minimized Climate Impact". In: AIAA AVIATION 2020 FORUM. 2020. DOI: 10.2514/6.2020-2660.

[135] T. Burschyk et al. "Liquid hydrogen storage design trades for a short-range aircraft concept". In: *CEAS Aeronautical Journal* (2023). DOI: 10.1007/s13272-023-00689-4.

[136] G. Onorato. "Fuel Tank Integration for Hydrogen Airliners". PhD thesis. 2021. URL: https://repository.tudelft.nl/islandora/object/uuid%3A5700b748-82c6-49c9-b94a-ad97c798e119.

[137] F. Friedmann et al. "Design studies for a light aircraft wing with highly integrated load-bearing hydrogen tanks using multi-objective optimization methods". In: *Proceedings of the Institution of Mechanical Engineers, Part G: Journal of Aerospace Engineering* (2023). Publisher: IMECHE. DOI: 10.1177/09544100231155697.

[138] C.A. Saias et al. "Assessment of hydrogen fuel for rotorcraft applications". In: *International Journal of Hydrogen Energy* (2022). DOI: 10.1016/j.ijhydene.2022.06.316.

[139] *Cryogenic Hydrogen Fuel System and Storage Roadmap Report*. Aerospace Technology Institute, 2022. URL: https://www.ati.org.uk/wp-content/uploads/2022/03/FZO-PPN-COM-0027-Cryogenic-Hydrogen-Fuel-System-and-Storage-Roadmap-Report.pdf.

[140] *Hydrogen Aircraft Powertrain and Storage Systems (HAPSS)*. Conscious Aerospace. 2024. URL: https://www.consciousaerospace.com/technology.

[141] F. Michel. "On-board equipment for liquid hydrogen vehicles". In: *International Journal of Hydrogen Energy* (1998). DOI: 10.1016/S0360-3199(97)00044-X.

[142] P. C. de Boer, A. J. de Wit, and R. C. van Benthem. "Development of a Liquid Hydrogen-Based Fuel Cell System for the HYDRA-2 Drone". In: AIAA SciTech 2022 Forum. Publisher: Netherlands Aerospace Centre NLR. NLR- Netherlands Aerospace Centr, 2021. URL: https://hdl.handle.net/10921/1596.

[143] M. Harris. *Universal Hydrogen takes to the air with the largest hydrogen fuel cell ever to fly*. TechCrunch. 2023. URL: https://techcrunch.com/2023/03/02/universal-hydrogen-takes-to-the-air-with-the-largest-hydrogen-fuel-cell-ever-to-fly/.

[144] Martin Hepperle. *Electric Flight – Potential and Limitations*. German Aerospace Center, 2012. URL: https://elib.dlr.de/78726/1/MP-AVT-209-09.pdf.

[145] Henry Andersen et al. "Design and Manufacturing of a High-Specific-Power Electric Machine for Aircraft Propulsion". In: *MIT News* (2023). Accepted: 2023-06-07T16:09:26Z. URL: https://dspace.mit.edu/handle/1721.1/150869.

[146] *Electrical Propulsion Systems Roadmap Report*. Aerospace Technology Institute, 2022. URL: https://www.ati.org.uk/wp-content/uploads/2022/03/FZO-PPN-COM-0030-Electrical-Propulsion-Systems-Roadmap-Report.pdf.

[147] W. Affonso et al. "System architectures for thermal management of hybrid-electric aircraft - FutPrInt50". In: *IOP Conference Series: Materials Science and Engineering* (2022). DOI: 10.1088/1757-899X/1226/1/012062.

[148] J.K. Noland, R. Mellerud, and C. Hartmann. "Next-Generation Cryo-Electric Hydrogen-Powered Aviation: A Disruptive Superconducting Propulsion System Cooled by Onboard Cryogenic Fuels". In: *IEEE Industrial Electronics Magazine* (2022). DOI: 10.1109/MIE.2022.3174332.

[149] L. Ybanez et al. "ASCEND: The first step towards cryogenic electric propulsion". In: *IOP Conference Series: Materials Science and Engineering* (2022). DOI: 10.1088/1757-899X/1241/1/012034.

[150] F. Grilli et al. "Superconducting motors for aircraft propulsion: the Advanced Superconducting Motor Experimental Demonstrator project". In: *Journal of Physics: Conference Series* (July 1, 2020). DOI: 10.1088/1742-6596/1590/1/012051.

[151] *De Havilland DHC-8-300 blank illustration templates – Norebbo*. 2024. URL: https://www.norebbo.com/de-havilland-dhc-8-300-blank-illustration-templates/.

[152] Eurocontrol. *Aircraft Performance Database*. 2024. URL: https://contentzone.eurocontrol.int/aircraftperformance/.

[153] P-J Dewitte. *Required Shaft Power for a DHC-8 Q300 in Cruise, Take-off and Top-of-climb*. Personal Communication. 2024.

[154] W. Lammen, P-J Dewitte, and E. Scheers. *Retrofitted Hydrogen-Electric Propulsion Aircraft: Performance Simulation of Critical Operating Conditions - [v1]*. 2024. URL: https://www.preprints.org/manuscript/202412.0611/v1 (visited on 12/16/2024).

[155] De Havilland Canada. *Owner's & Operator's Guide: Dash 8 & Q Series*. 2009. URL: https://www.aircraft-commerce.com/wp-content/uploads/aircraft-commerce-docs/Aircraft%20guides/DASH%208%20&%20Q%20SERIES/ISSUE63_DASH8SPECS.pdf.

[156] G. Vonhoff. "Conceptual Design of Hydrogen Fuel Cell Aircraft: Flying on hydrogen for a more sustainable future". PhD thesis. 2021. URL: https://repository.tudelft.nl/islandora/object/uuid%3A8bd63dec-b67b-496b-92bc-3d5c07ff859f.

[157] Raffi Babikian, Stephen P. Lukachko, and Ian A. Waitz. "The historical fuel efficiency characteristics of regional aircraft from technological, operational, and cost perspectives". In: *Journal of Air Transport Management* (2002). DOI: 10.1016/S0969-6997(02)00020-0.

[158] A.B. Lambe and J.R.R.A. Martins. "Extensions to the design structure matrix for the description of multidisciplinary design, analysis, and optimization processes". In: *Structural and Multidisciplinary Optimization* 46.2 (Aug. 2012), pp. 273–284. DOI: 10.1007/s00158-012-0763-y. (Visited on 09/04/2024).

[159] NASA. *Propeller Thrust*. URL: https://www.grc.nasa.gov/www/k-12/airplane/propth.html.

[160] G.J.J. Ruijgrok. *Elements of airplane performance (second edition)*. Delft Academic Press, 2009. URL: https://repository.tudelft.nl/record/uuid:9ff3c7e0-e221-4d8f-bf9e-e144d3cacdc1.

[161] L.J. van Dongen. "Modelling and Guidelines for Ram Air Ducts Using the Meredith Effect". PhD thesis. 2024. URL: https://resolver.tudelft.nl/uuid:2702f50e-44e6-4369-8807-f38aa6b4c7de.

[162] *Fuel Cell Solutions*. Freudenberg Filtration Technologies. 2024. URL: https://www.freudenberg-filter.com/en/products/automotive/fuel-cell-solutions/.

[163] M. Casey and C. Robinson. *Radial Flow Turbocompressors: Design, Analysis, and Applications*. Cambridge University Press, 2021. DOI: 10.1017/9781108241663.

[164] J. Cook and A/ Espinoza. "Turbomachinery & Pump Symposia 2024: Emerging Technologies in the Spotlight". In: *Turbomachinery Magazine* (2024). Publisher: MJH Life Sciences. URL: https://www.turbomachinerymag.com/view/centrifugal-vs-reciprocating-compressor.

[165] M. Zangeneh et al. "Optimization of 6.2:1 Pressure Ratio Centrifugal Compressor Impeller by 3D Inverse Design". In: ASME 2011 Turbo Expo: Turbine Technical Conference and Exposition. ASMEDC, 2011. DOI: 10.1115/GT2011-46505.

[166] *Fischer Fuel Cell Compressor AG | FISCHER Fuel Cell Compressor AG*. 2024. URL: https://www.fischer-fuelcell-compressor.com/.

[167] F.P. Incropera et al., eds. *Fundamentals of heat and mass transfer*. Wiley, 2007. URL: https://charlaenlamesadelcasino.wordpress.com/wp-content/uploads/2014/01/fundamentals-of-heat-and-mass-transfer-incropera.pdf.
[168] Mathworks. *fmincon*. 2024. URL: https://nl.mathworks.com/help/optim/ug/fmincon.html.
[169] *Humidifier modules ecomate*. Fumatech. URL: https://www.fumatech.com/en/products/humidifier-modules-ecomate/.
[170] D.R. Stull. "Vapor Pressure of Pure Substances. Organic and Inorganic Compounds". In: *Industrial & Engineering Chemistry* (1947). Publisher: American Chemical Society. DOI: 10.1021/ie50448a022.
[171] Q. Yang et al. "Optimal integration design of sustainable ethylene glycol production process considering economic benefit and environmental impact". In: *Journal of Cleaner Production* (2023). DOI: 10.1016/j.jclepro.2023.136540.
[172] M. Graf et al. "Virtual Manufacturing as Tool for Material and Process Developments and Optimizations". In: *Journal of Mechanical Engineering* (2018). URL: https://jmeche.uitm.edu.my/wp-content/uploads/bsk-pdf-manager/4_SI_5_4_ID_145_368.pdf.
[173] G. Buntkowsky et al. "Recent advances in the application of parahydrogen in catalysis and biochemistry". In: *RSC Advances* (2022). DOI: 10.1039/D2RA01346K.
[174] Asurnipal. *Olympic_Bombadier_Q400*. 2019. URL: https://commons.wikimedia.org/wiki/File:Olympic_Bombadier_Q400_NextGen_SX-OBD-kos_airport-03ASD.jpg.
[175] *MIT team developing 1MW motor for electric aviation*. Green Car Congress. 2023. URL: https://www.greencarcongress.com/2023/06/20230620-mit.html.
[176] M. Pettes-Duler, X. Roboam, and B. Sareni. "Integrated Optimal Design for Hybrid Electric Powertrain of Future Aircrafts". In: *Energies* (2022). DOI: 10.3390/en15186719.
[177] *Electric motors for aircraft*. E-Mobility Engineering. 2023. URL: https://www.emobility-engineering.com/electric-motors-aircraft/.
[178] S.M. Sohel Murshed. "Introductory Chapter: Electronics Cooling — An Overview". In: *Electronics Cooling*. InTech, 2016. DOI: 10.5772/63321.
[179] H.J. van Gerner and N. Braaksma. "Transient modelling of pumped two-phase cooling systems: Comparison between experiment and simulation". In: 46th International Conference on Environmental Systems. ICES, 2016. URL: https://ttu-ir.tdl.org/server/api/core/bitstreams/c733765a-c469-4ac9-8cde-cc40fd6bf691/content.
[180] J.K. Mendizábal et al. "Enhanced internal condensation of R1233zd(E) on micro- and nanostructured copper and aluminum surfaces". In: *International Journal of Heat and Mass Transfer* (2023). DOI: https://doi.org/10.1016/j.ijheatmasstransfer.2023.124012.
[181] P. Ngatchou, A. Zarei, and M.A. El-Sharkawi. "Pareto Multi Objective Optimization". In: *Proceedings of the 13th International Conference on, Intelligent Systems Application to Power Systems* (2005). DOI: 10.1109/ISAP.2005.1599245.
[182] P.M. Sforza. "Turbine Engine Performance and Component Integration". In: *Theory of Aerospace Propulsion*. Elsevier, 2012. DOI: 10.1016/B978-1-85617-912-6.00009-8. URL: https://linkinghub.elsevier.com/retrieve/pii/B9781856179126000098.
[183] *EASA review of standard passenger weights*. 2022. URL: https://www.easa.europa.eu/en/newsroom-and-events/news/easa-review-standard-passenger-weights-2022-shows-no-significant-change.
[184] H.R. Dodiya et al. "Experimental Investigation of Surface Roughness for AA 3003-0 Aluminium Alloy Using Single Point Incremental Forming". In: *Materials Today: Proceedings* (2021). DOI: 10.1016/j.matpr.2021.03.659.
[185] Y. S. Muzychka and M. M. Yovanovich. "Laminar Forced Convection Heat Transfer in the Combined Entry Region of Non-Circular Ducts". In: *Journal of Heat Transfer* (2004). DOI: 10.1115/1.1643752.
[186] R. K. Shah and Dušan P. Sekulić. *Fundamentals of heat exchanger design*. John Wiley & Sons, 2003. DOI: 10.1002/9780470172605.
[187] Ya Cengel, Rh Turner, and R Smith. "*Fundamentals of Thermal-Fluid Sciences*". In: *Applied Mechanics Reviews* (2022). DOI: 10.1115/1.1421126.
[188] M.M. Shah. "An Improved and Extended General Correlation for Heat Transfer During Condensation in Plain Tubes". In: *HVAC&R Research* (2009). DOI: 10.1080/10789669.2009.10390871.
[189] H. Müller-Steinhagen and K. Heck. "A simple friction pressure drop correlation for two-phase flow in pipes". In: *Chemical Engineering and Processing: Process Intensification* (1986). DOI: 10.1016/0255-2701(86)80008-3.
[190] NASA. *Power Turbine Thermodynamics*. 2021. URL: https://www.grc.nasa.gov/www/k-12/airplane/powtrbth.html.
[191] *DHC-8 Q300 Airport Planning Manual*. Bombaridier Aerospace, 2001. URL: https://customer.aero.bombardier.com/webd/BAG/CustSite/BRAD/RACSDocument.nsf/51aae8b2b3bfdf6685256c300045ff31/ec63f8639ff3ab9d85257c1500635bd8/$FILE/ATT3MP36.pdf/D8300-APM.pdf.

A

Additional Equations

A.1. Calculations for Ram Air Duct Conditions

In this section the equations used for the ram air inside the ram air duct are presented. In the following sections, subscripts $T_{0,n}$ and $T_{t,n}$ represent the static and total conditions, respectively.

Free-stream Conditions (1)
For free-stream conditions, the density and velocity are determined based on the Mach number.

$$\rho_{t,1} = \rho_{\text{ambient}}, \quad \rho_{0,1} = \rho_{\text{ambient}} \quad \text{, for } M < 0.3 \text{ (incompressible flow)} \tag{A.1}$$

$$\rho_{t,1} = \frac{\rho_{\text{ambient}}}{\left(1 + \frac{\gamma-1}{2} M_1^2\right)^{\frac{-1}{\gamma-1}}}, \quad \rho_{0,1} = \rho_{\text{ambient}} \quad \text{, for } M > 0.3 \text{ (compressible flow)} \tag{A.2}$$

The static temperature, pressure, and velocity are given by:

$$T_{0,1} = T_{\text{ambient}}, \quad p_{0,1} = p_{\text{ambient}} \tag{A.3}$$

$$u_{0,1} = M_1 \sqrt{\gamma R T_{\text{ambient}}} \tag{A.4}$$

The stagnation temperature and pressure are calculated as:

$$T_{t,1} = T_{\text{ambient}} \left(1 + \frac{\gamma - 1}{2} M_1^2\right) \tag{A.5}$$

$$p_{t,1} = p_{\text{ambient}} + \rho_{0,1} \frac{u_{0,1}^2}{2} \tag{A.6}$$

Inlet Conditions after Propeller (2)
The Mach number far downstream of the the propeller exit is:

$$M_2 = \frac{u_e}{\sqrt{\gamma R T_{\text{ambient}}}} \tag{A.7}$$

It is assumed that this velocity also applies at the Ram Air Duct inlet. Depending on M_2, the density and stagnation conditions are again determined by Equation A.1.
Temperature and pressure are updated as follows:

$$T_{0,2} = \frac{T_{t,2}}{1 + \frac{\gamma-1}{2} M_2^2} \tag{A.8}$$

$$p_{0,2} = p_{t,2} \left(1 + \frac{\gamma - 1}{2} M_2^2\right)^{-\frac{\gamma}{\gamma-1}} \tag{A.9}$$

The total mass flow rate is:

$$\dot{m}_{\text{tot}} = \frac{A_{\text{in}} p_{t,2}}{\sqrt{T_{t,2}}} \sqrt{\frac{\gamma}{R}} M_2 \left(1 + \frac{\gamma - 1}{2} M_2^2\right)^{\frac{-(\gamma+1)}{2(\gamma-1)}} \tag{A.10}$$

Conditions after Diffuser (3)
In the ideal isentropic diffuser, the area ratio is used to solve for the downstream Mach number, M_3, by solving:

$$f(M_3) = \frac{M_3}{A_{\text{ratio}}} \left(1 + \frac{\gamma - 1}{2} M_3^2\right)^{-\frac{\gamma+1}{2(\gamma-1)}} - M_2 \left(1 + \frac{\gamma - 1}{2} M_2^2\right)^{-\frac{\gamma+1}{2(\gamma-1)}} \tag{A.11}$$

Density, temperature, and pressure conditions are updated as:

$$\rho_{0,3} = \rho_{0,2}, \quad \rho_{t,3} = \rho_{t,2} \tag{A.12}$$

$$T_{0,3} = \frac{T_{t,3}}{1 + \frac{\gamma-1}{2} M_3^2}, \quad u_3 = M_3 \sqrt{\gamma R T_{0,3}} \tag{A.13}$$

The pressure increase after the diffuser is calculated as:

$$\Delta p_0 = C_{\text{pressure}} \cdot q_2, \quad p_{0,3} = p_{0,2} + \Delta p_0 \tag{A.14}$$

Where the (ideal) coefficient of pressure C_{pressure} is determined with the diffuser area ratio AR:

$$C_{\text{pressure}} = 1 - \frac{1}{AR^2} \tag{A.15}$$

Conditions before Radiator (4)
To calculate conditions at the Ram Air Heat Exchanger, we again solve the Mach number using the area ratio with equation A.11 and update other parameters similarly. The change in flow angle is unaccounted for.

Conditions after the Radiator (5)
Due to the inclination angle of the radiator, the total pressure drop will be about 15% larger than the frictional pressure drop between the fins (see Section A.4), as derived from Figure A.1 [115].

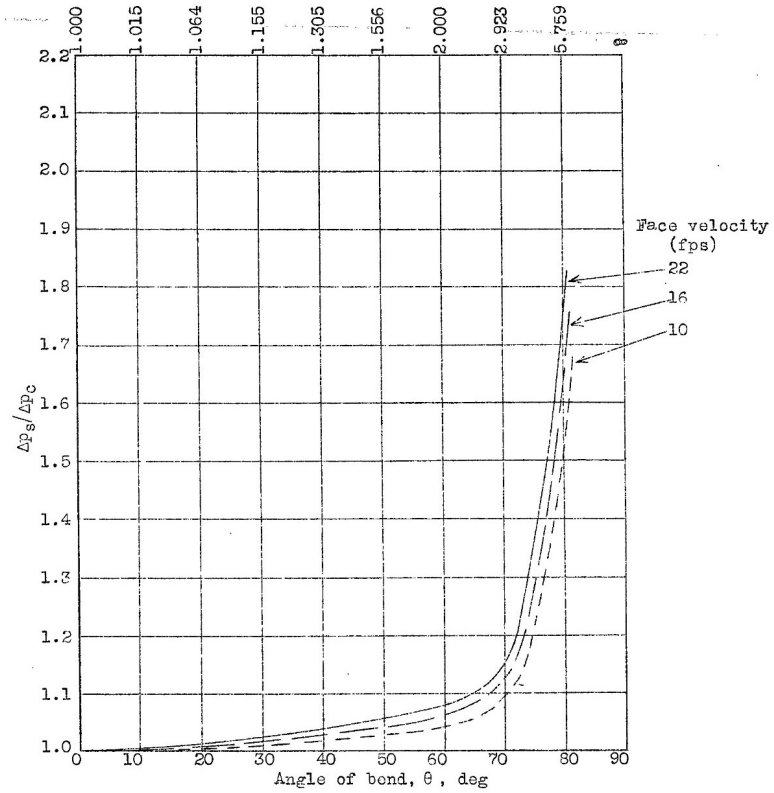

Figure A.1: Variation of the pressure-drop ratio of the system with the angle of bend of the approach duct. Intercooler height-width ratio, 0.644; standard air. Adopted from Nichols (1942) [115].

A.2. Effectiveness-NTU Method

This appendix provides a step-by-step explanation of the calculations and assumptions used in the effectiveness-NTU method for the unmixed cross-flow heat exchanger, used in the Intercooler and Radiator models (see Section 3.5.3 and Section 3.6.5, respectively). Also, the equations for parallel tube heat exchanger implemented in the Hydrogen Heat Exchanger (H2HX) model are provided 3.6.5.
The heat capacity rate for each fluid/gas is given by:

$$C = \dot{m} \cdot C_{p,\text{avg}} \tag{A.16}$$

The capacity rate ratio is then defined as:

$$C_r = \frac{C_{\text{min}}}{C_{\text{max}}} \tag{A.17}$$

For a condensing fluid, as modelled for H2HX verification, the heat capacity rate $C = \infty$, giving $C_r = 0$.
The overall heat transfer coefficient UA_{overall} is given by:

$$UA_{\text{overall}} = \frac{1}{\left(\frac{1}{(UA)_1} + \frac{1}{(UA)_2}\right)} \tag{A.18}$$

The number of transfer units (NTU) is calculated as:

$$\text{NTU} = \frac{UA_{\text{overall}}}{C_{\text{min}}} \tag{A.19}$$

The effectiveness for an unmixed-unmixed cross-flow heat exchanger is given by:

$$\text{Cross-flow:} \quad \epsilon = 1 - \exp\left(\frac{1}{C_r} \cdot \text{NTU}^{0.22}\left(\exp(-C_r \cdot \text{NTU}^{0.78}) - 1\right)\right) \tag{A.20}$$

$$\text{Parallel flow:} \quad \epsilon = \frac{1 - \exp\left(-\text{NTU} \cdot (1 + C_r)\right)}{1 + C_r} \tag{A.21}$$

The heat transfer rate Q for the heat exchanger is then determined by:

$$Q = \epsilon \cdot C_{\text{min}} \cdot \left|T_{1,\text{in}} - T_{2,\text{in}}\right| \tag{A.22}$$

A.3. Heat Transfer Coefficient and Pressure Drop in a Tube

This section details the equations used to calculate heat transfer and pressure drop in the refrigerant flow within the tubes of a heat exchanger [167]. The area of the tube is simply $A_{\text{tube}} = \pi/4 d_{\text{tube}}^2$. The Reynolds number for the refrigerant is calculated as follows:

$$\text{Re} = \frac{\rho_{\text{avg}} \cdot u_{0,\text{avg}} \cdot d_{\text{tube}}}{\mu} \tag{A.23}$$

For turbulent flow, the friction factor is determined using the Haaland equation, which is an explicit approximation of the Colebrook equation:

$$f_{\text{turbulent}} = \left(-1.8 \log_{10}\left(\frac{e}{d_{\text{tube}} \cdot 3.7} + \frac{6.9}{\text{Re}}\right)\right)^{-2}, \tag{A.24}$$

where the surface roughness of the fins is assumed to be $e = 3.5\mu$m [184]. If the Reynolds number is below 2300, the Nusselt number is assumed to be:

$$\text{Nu} = 3.55 \tag{A.25}$$

For Reynolds numbers above 2300, the Nusselt number is calculated using the Gnielinski relation:

$$\text{Nu} = \frac{f_{\text{turbulent}}}{8} \cdot (\text{Re} - 1000) \cdot \frac{\text{Pr}}{1 + 12.7\left(\frac{f_{\text{turbulent}}}{8}\right)^{1/2}\left(\text{Pr}^{2/3} - 1\right)} \tag{A.26}$$

where Pr is the Prandtl number of the refrigerant.
The heat transfer coefficient U for the refrigerant in the tube is then calculated as:

$$U_{\text{tube}} = \frac{\text{Nu} \cdot k}{d_{\text{tube}} \cdot 2} \tag{A.27}$$

where k is the thermal conductivity of the refrigerant, and the division by 2 accounts for the calculation over half the tube wall area. The heat transfer in the tube region is calculated as:

$$(UA)_{\text{tube}} = U_{\text{tube}} \cdot A_{\text{tube}} \cdot N_{\text{tubes}} \tag{A.28}$$

For laminar flow, the friction factor is given by:

$$f_{\text{laminar}} = \frac{64}{\text{Re}} \tag{A.29}$$

A smoothing function is introduced to transition between laminar and turbulent flow:

$$\sigma = \frac{1}{1 + \exp\left(-\frac{\text{Re}-2400}{200}\right)} \tag{A.30}$$

The overall friction factor is then computed as:

$$f = (1 - \sigma) \cdot f_{\text{laminar}} + \sigma \cdot f_{\text{turbulent}} \tag{A.31}$$

For the assumed surface roughness and a tube diameter of 1 mm, the Moody diagram with smoothing function is visualized in Figure..

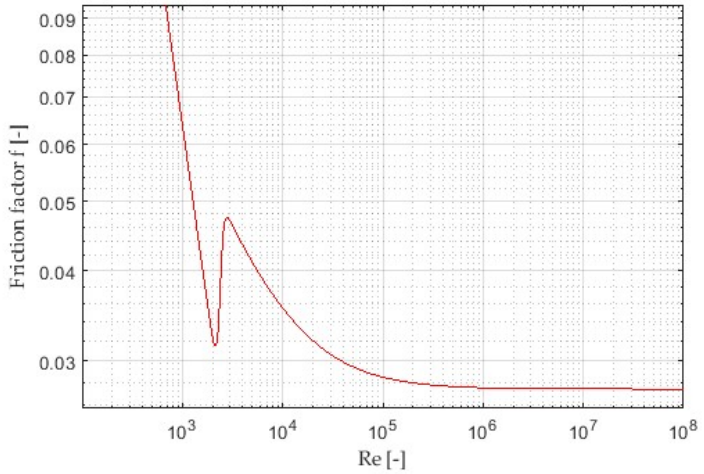

Figure A.2: Moody diagram for a surface roughness of 3.5 micron and a tube diameter of 1 mm.

Finally, the pressure drop across the tube is calculated using the Darcy-Weissbach equation:

$$\Delta p = f \cdot \frac{L_{\text{tube}}}{d_{\text{tube}}} \cdot \frac{\rho_{\text{avg}} \cdot u_{0,\text{avg}}^2}{2} \tag{A.32}$$

A.4. Heat Transfer Coefficient and Pressure Drop Between Rectangular Straight Fins

This section describes the calculations for the heat transfer coefficient and the pressure drop across rectangular straight fins in a heat exchanger [167]. The geometry of the fins is visualized in Figure A.3.

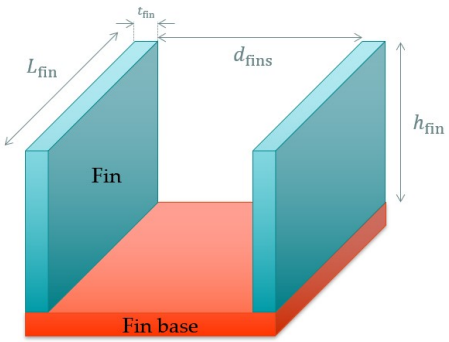

Figure A.3: Fin geometry.

Heat Transfer Coefficient Between the Fins

The heat transfer area of the fins is defined as:

$$A_{fin} = (d_{fins} + h_{fins}) \cdot L_{fin} \tag{A.33}$$

The Reynolds number for the fluid flow between the fins is given by:

$$\mathrm{Re} = \frac{\rho_{avg} \cdot u_{0,avg} \cdot d_{eff,fins}}{\mu}, \tag{A.34}$$

where the fin effective hydraulic diameter is determined by,

$$d_{eff,fins} = \frac{4 d_{fins} h_{fins}}{2 h_{fins} + d_{fins}} \tag{A.35}$$

If the Reynolds number is below 2300, the Nusselt number is determined as:

$$\mathrm{Nu} = 7.55 + \frac{0.024 \cdot d_{dimless}^{-1.14}}{1 + 0.0358 \cdot \mathrm{Pr}^{0.17} \cdot d_{dimless}^{-0.64}} \tag{A.36}$$

where $d_{dimless}$ is the dimensionless distance defined as:

$$d_{dimless} = \left(\frac{z}{L_{fin}}\right) \cdot \mathrm{Re} \cdot \mathrm{Pr} \tag{A.37}$$

For Reynolds numbers above 2300, the Nusselt number is given by:

$$\mathrm{Nu} = \frac{f_{turbulent}}{8} \cdot (\mathrm{Re} - 1000) \cdot \frac{\mathrm{Pr}}{1 + 12.7 \left(\frac{f_{turbulent}}{8}\right)^{1/2} \left(\mathrm{Pr}^{2/3} - 1\right)} \tag{A.38}$$

The heat transfer coefficient for the fluid flowing over the fins is then calculated as:

$$U_{fin} = \frac{\mathrm{Nu} \cdot k}{d_{eff,fins}} \tag{A.39}$$

where k is the thermal conductivity of the fluid. The heat transfer coefficient and pressure drop in the finned region of the heat exchanger are calculated assuming fully developed turbulent flow. This assumption is valid if the channel length-to-tube spacing ratio L/d_{fins} and channel length-to-fin height ratio L/h_{fins} exceed 10. The effectiveness of the fins is calculated based on the heat transfer coefficient in the finned region:

$$(UA)_{fin} = U_{fin} \cdot A_{fin} \cdot \eta_{fin} \cdot N_{fins} \tag{A.40}$$

where:

- h_{fin} is the convective heat transfer coefficient on the fluid side of the fins,
- A_{fin} is the fin surface area,
- η_{fin} is the fin efficiency,
- N_{fins} is the number of fins.

The efficiency of the fins, η_{fin}, is calculated using:

$$\eta_{fin} = \frac{\tanh(m_{fin} \cdot h_{fins})}{m_{fin} \cdot h_{fins}}, \tag{A.41}$$

where,

- The fin effectiveness is defined as $m_{\text{fin}} = \sqrt{\frac{h \cdot P}{k \cdot A_c}}$
- The fin perimeter is defined as $P = L_{\text{fin}} \cdot 2 + t_{\text{fin}} \cdot 2$
- The cross-sectional area of the fin is defined as $A_c = L_{\text{fin}} \cdot t_{\text{fin}}$

Frictional pressure drop between the fins

To calculate the frictional pressure drop across the fins, a publication by Muzychka (2004) is used [185]. First the Reynolds number considering the entry effects:

$$\text{Re}_A = \frac{\rho_{\text{avg}} \cdot u_{0,\text{avg}} \cdot d_{A,\text{fin}}}{\mu} \tag{A.42}$$

where $d_{A,\text{fin}}$ is an alternative hydraulic diameter of the fins:

$$d_{A,\text{fin}} = \sqrt{d_{\text{fins}} h_{\text{fins}}} \tag{A.43}$$

The dimensionless length is defined as:

$$L_{\text{dimless}} = \frac{L/d_{A,\text{fin}}}{\text{Re}_A} \tag{A.44}$$

The friction factor for laminar flow, accounting for entry effects, is calculated using:

$$f_{\text{laminar}} = \frac{4 f_{Re}}{\text{Re}_A} \tag{A.45}$$

where f_{Re} is obtained from the correlation:

$$f_{Re} = \left(\frac{3.44}{\sqrt{L_{\text{dimless}}}} \right)^2 + \left(\frac{12}{\sqrt{\epsilon}(1+\epsilon)(1 - \frac{192\epsilon}{\pi^5} \tanh(\frac{\pi}{2\epsilon}))} \right)^2 \tag{A.46}$$

where ϵ is defined as:

$$\epsilon = \frac{d_{\text{fins}}}{h_{\text{fins}}} \tag{A.47}$$

Just as for the friction factor in tubes, the turbulent friction factor is determined using equation A.24, and a smoothing function is applied (equation A.31). The overall pressure drop across the fins is again calculated using the Darcy-Weissbach equation with average density and bulk velocity (A.32).

A.5. Pressure drop and air velocity for heat exchanger in free-stream conditions

For a radiator subjected to air flow in free-stream conditions, the pressure drop between the fins should be balanced by the increase in static pressure before the radiator [103].

$$\Delta p_{\text{fins}} = \Delta p_0 \tag{A.48}$$

The increase in static pressure is driven by the difference between dynamic pressure in the free-stream and between the fins:

$$\Delta p_0 = q_\infty - q_{\text{fins}} = 1/2 \rho_\infty (u_\infty^2 - u_{\text{fins}}^2) \tag{A.49}$$

The pressure drop between the fins (core) consists of three parts, as shown in Figure A.4 [186]. The effect of momentum change on pressure drop due to changes in density are neglected.

$$\Delta p_{\text{total}} = \Delta p_{\text{entrance}} + \Delta p_{\text{friction}} + \Delta p_{\text{exit}} \tag{A.50}$$

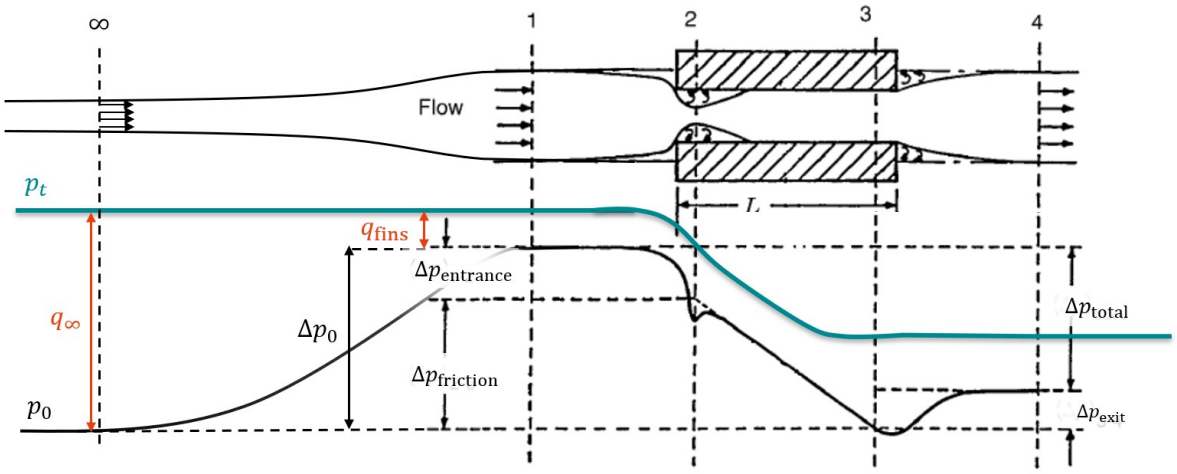

Figure A.4: Pressure distribution between the fins in a heat exchanger in free-stream conditions. Adapted from [186] in consultation with [103].

This combines into the following formula, implementing entrance and exit losses of $K = 1.0$ and $K = 0.5$ [187], respectively.

$$\Delta p_{\text{total}} = \left(f \frac{L_{HX}}{d_h} + K_{\text{entrance}} + K_{\text{exit}} \right) \frac{\rho_{\text{air}} u_{\text{fins}}^2}{2} \tag{A.51}$$

Now, there are two equations and two unknowns ($\Delta p, u_{0,\text{fins}}$) which can be solved for.

A.6. Heat Transfer Coefficient and Pressure Drop for a Condensing Fluid

The heat transfer coefficient and pressure drop for two-phase condensing flow can be determined using Shah's correlation (2009) [188] and the Muller-Steinhagen and Heck correlation (1986) [189], respectively.

Heat Transfer Coefficient for Two-Phase Condensing Flow

Subscripts v refer to the vapor state of the two-phase flow, while subscripts l refer to the liquid state. LS indicates calculation of a parameter assuming only liquid in the tube. GT indicates calculation of the fluid assuming the total mass flowing as a vapor.
First, mass flux G and reduced pressure p_{reduced} can be determined from,

$$G = \frac{\dot{m}}{A_{\text{cross, inner}}} \tag{A.52}$$

$$p_{\text{reduced}} = \frac{p}{p_{\text{crit}}} \tag{A.53}$$

Then the Prandtl number Pr_{LS} and Nusselt number Nu_{LS} are determined using

$$\text{Pr}_{LS} = \frac{C_p \cdot \mu_l}{k_l} \tag{A.54}$$

$$\text{Nu}_{LS} = 0.023 \cdot \text{Re}_{LS}^{0.8} \cdot \text{Pr}_{LS}^{0.4} \tag{A.55}$$

Then, the parameters J_g, Z and Re_{GT} determine the flow regime of the condensing flow. In the faster flowing regime, heat transfer is driven by laminar film condensation.

$$J_g = \frac{\chi G}{\sqrt{g D \rho_v (\rho_v - \rho_l)}} \tag{A.56}$$

$$\text{Re}_{\text{GT}} = \frac{GD}{\mu_v} \tag{A.57}$$

$$Z = \left(\frac{1}{\chi} - 1 \right)^{0.8} p_{\text{reduced}}^{0.4}, \tag{A.58}$$

where χ is the vapor quality of the flow. $\chi = 0$ for all liquid, and $\chi = 1$ for all vapor. Shah defines the following heat transfer coefficients to be used in different regimes:

$$U_{LS} = \frac{\mathrm{Nu}_{\mathrm{LS}} \cdot k_l}{D_{\mathrm{in}}}$$

$$U_I = U_{\mathrm{LS}} \cdot \left(1 + \frac{3.8}{Z^{0.95}}\right) \cdot \left(\frac{\mu_l}{\mu_v}\right)^{0.0058+0.557 \cdot p_{\mathrm{reduced}}}$$

$$U_{\mathrm{Nu}} = 1.32 \cdot \mathrm{Re}_{\mathrm{LS}}^{-1/3} \cdot \left(\frac{\rho_l(\rho_l - \rho_v) g k_l^3}{\mu_l^2}\right)^{1/3}$$

Then there are two flow regimes:

$$\text{if } J_g \geq 0.98 \cdot (Z + 0.263)^{-0.62}$$
$$\Rightarrow U = U_I \tag{A.59}$$
$$\text{elseif } J_g < 0.98 \cdot (Z + 0.263)^{-0.62} \text{ and } \mathrm{Re}_{GT} > 35000$$
$$\Rightarrow U = U_I + U_{\mathrm{Nu}} \tag{A.60}$$

Pressure Drop for Two-Phase Flow

To implement the Muller-Steinhagen and Heck correlation, the pressure drop for the flow assuming pure liquid state, and assuming pure vapor state need to be determined (see Section A.3). The combined pressure drop is then:

$$\Delta p = \left(\Delta p_l + 2 \cdot (\Delta p_v - \Delta p_l) \cdot x\right) \cdot (1 - x)^{1/3} + \Delta p_v \cdot x^3 \tag{A.61}$$

A.7. Turbine Power

To determine the compressor power recovered by the turbine from the hot fuel cell exhaust flow, first the expansion between fuel cell outlet and the ambient is determined [190]:

$$\Delta p_{t,\mathrm{turb}} = \frac{p_{t,\mathrm{FC,out}}}{p_{0,\mathrm{ambient}}} \tag{A.62}$$

This is an idealization as the hot fuel cell air will first pass the humidifier wet side and potentially a water separator. Also, it might not be entirely possible to expand the flow fully to ambient conditions due to different mission conditions, requiring a pressure control valve.

$$T_{t,\mathrm{turb,is}} = T_{t,\mathrm{in}} \cdot \Delta p_{t,\mathrm{turb}}^{\frac{\gamma-1}{\gamma}} \tag{A.63}$$

The turbine efficiency is determined similarly to compressor efficiency from polytropic efficiency [163]:

$$\eta_{\mathrm{turb}} = \frac{1 - \Delta p_{t,\mathrm{turb}}^{\frac{\gamma-1}{\gamma}}}{1 - \Delta p_{t,\mathrm{turb}}^{\frac{\gamma-1}{\gamma \cdot \eta_{\mathrm{poly}}}}} \tag{A.64}$$

The isentropic enthalpy after expansion is:

$$H_{\mathrm{turb,is}} = H_0 + C_p \cdot T_{t,\mathrm{turb,is}} \tag{A.65}$$

The actual enthalpy change with turbine efficiency is then:

$$H_{\mathrm{out}} = H_{\mathrm{in}} - (H_{\mathrm{in}} - H_{\mathrm{turb,is}}) \cdot \eta_{\mathrm{turb}} \tag{A.66}$$

The output total temperature is then:

$$T_{t,\mathrm{out}} = \frac{H_{\mathrm{out}} - H_0}{C_p} \tag{A.67}$$

The power generated by the turbine is then:

$$P_{\mathrm{turb}} = (H_{\mathrm{in}} - H_{\mathrm{out}}) \cdot \dot{m}_{\mathrm{air}} \tag{A.68}$$

A.8. Thrust for Increased Temperature Gradient in the Radiator

Mass flow for increased temperature gradient $\Delta T^{'}$ can be determined from:

$$\dot{m}_{\text{ram air}} = \frac{Q_{\text{radiator}}}{\rho C_p \Delta T'} \tag{A.69}$$

Thrust is computed according to [159]:

$$T_{\text{nozzle}} = \dot{m}_{\text{ram air}}(u_{\text{exit}} - u_{\infty}) \tag{A.70}$$

The exit velocity from the nozzle can be determined given the static-to-total pressure ratio between stations 5 and 6, and the total temperature at station 5.

$$u_{\text{exit}} = \sqrt{2C_p T'_{t,5} \cdot \left(1 - \frac{p_{0,6}}{p_{t,5}}^{\frac{\gamma-1}{\gamma}}\right)} \tag{A.71}$$

Pressure Drop of Hydrogen from Tank to Fuel Cell

The velocity v of the hydrogen flow can be determined using the mass flow rate equation:

$$u = \frac{\dot{m}}{\rho \cdot A} \tag{A.72}$$

where:

- $\dot{m}_{H_2} = 0.04\,\text{kg/s}$.
- $\rho_{H_2} = 0.2665\,\text{kg/m}^3$ is the density of hydrogen at $p = 4$ bar and $T = 90°\text{C}$,
- $A = \frac{\pi d^2}{4}$ is the cross-sectional area of the tube ,with $d = 100mm$.

Substituting the values, the steady-state velocity is calculated as:

$$u = 19.11\,\text{m/s}. \tag{A.73}$$

The pressure drop Δp can be determined using the Darcy-Weisbach equation [167]:

$$\Delta p = f \cdot \frac{L}{d} \cdot \frac{\rho \cdot u^2}{2}, \tag{A.74}$$

where:

- f is the Darcy friction factor (assumed between 0.002 and 0.004),
- $L = 10\,\text{m}$ is the length of the tube,
- $d = 0.1\,\text{m}$ is the assumed inner diameter of the tube,
- $\rho = 0.2665\,\text{kg/m}^3$ is the hydrogen density,
- $v = 19.11\,\text{m/s}$ is the velocity.

For a Darcy friction factor ranging from 0.002 to 0.004, the expected pressure drop across the tube would be approximately 1860 Pa to 3720 Pa, which shows that a hydrogen tank pressure of approximately 2.5 bar is sufficient for delivery at $p = 2.4$ bar and $T = 90°\text{C}$ a tube with $L = 10\text{m}$ and $d = 10\text{cm}$.

B

Additional Diagrams

B.1. Hydrogen Heat Exchanger

This appendix will not be included in the publicly available version due to confidentiality reasons. Please do not distribute.

B.2. Heat Exchanger Workflow Diagram

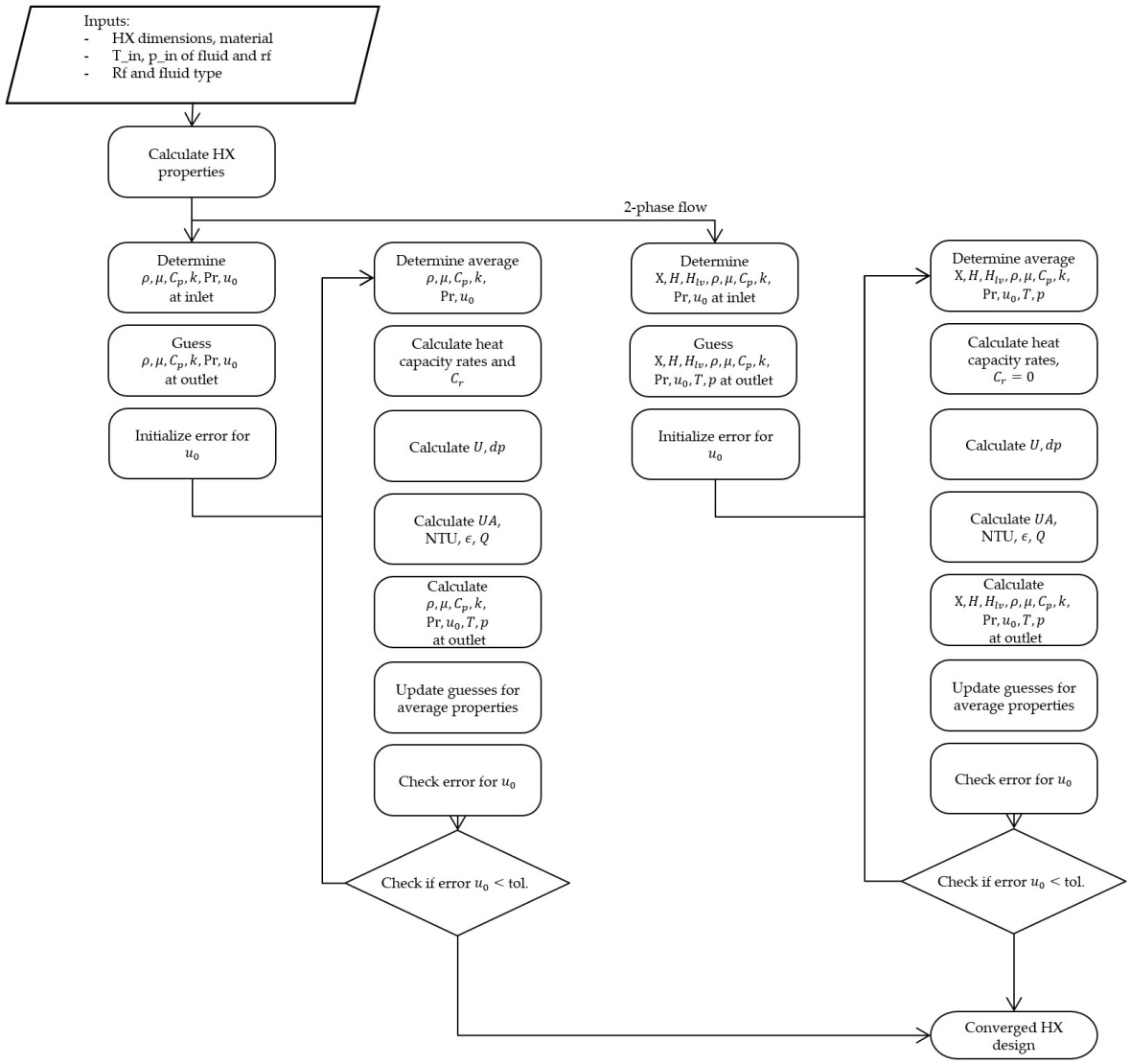

Figure B.1: Heat Exchanger workflow diagram.

B.3. DHC-8 Q300 Dimensions

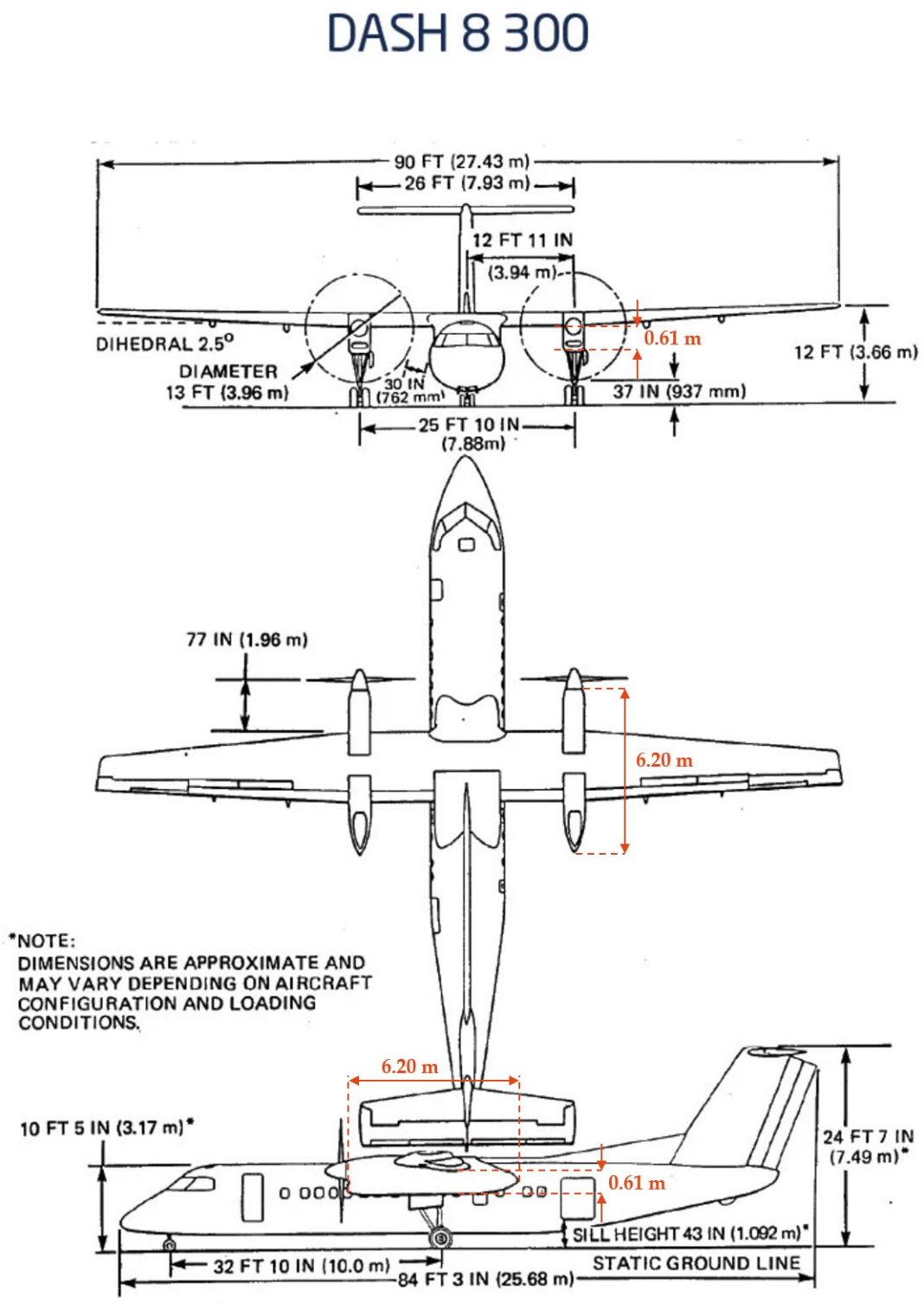

Figure B.2: DHC-8 Q300 dimensions, reproduced from the Airport Planning Manual [191].

B.4. DHC-8 Q300 Payload Range Diagram

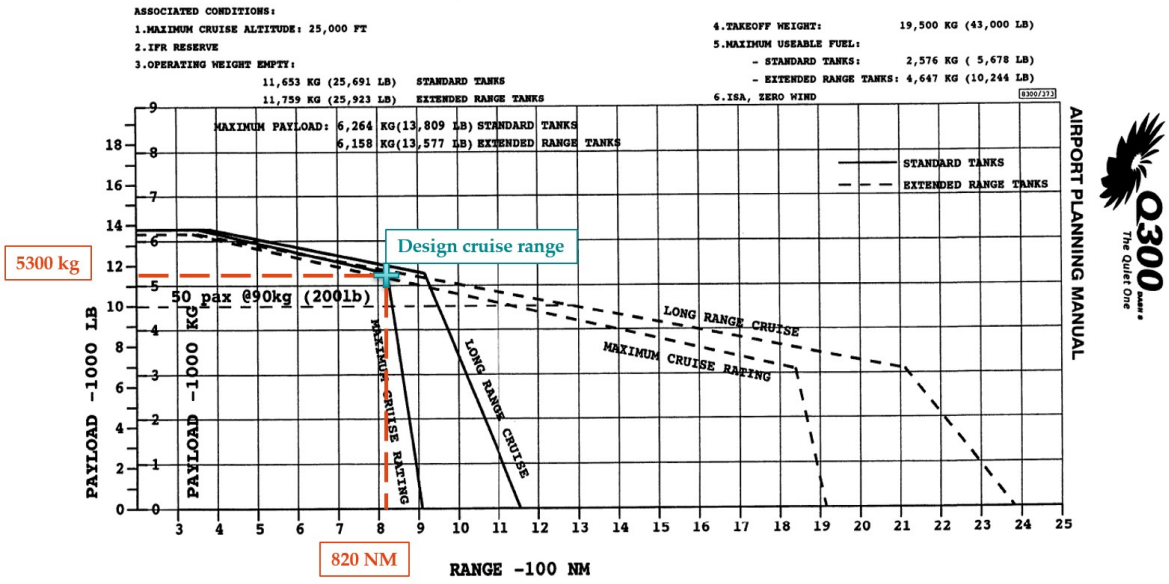

Figure B.3: DHC-8 Q300 payload range diagram, reproduced from the Airport Planning Manual [191].